The modification of graphene band structure by periodic potential perturbation

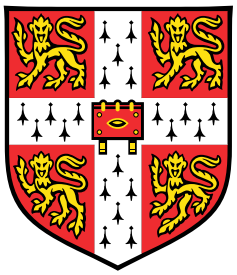

Qifang Wan

Department of Engineering
University of Cambridge

This thesis is submitted for the degree of
Doctor of Philosophy

Newnham College

November 2020

Declaration

This thesis is the result of my own work and includes nothing which is the outcome of work done in collaboration except as declared in the Preface and specified in the text. It is not substantially the same as any that I have submitted, or, is being concurrently submitted for a degree or diploma or other qualification at the University of Cambridge or any other University or similar institution except as declared in the Preface and specified in the text. I further state that no substantial part of my thesis has already been submitted, or, is being concurrently submitted for any such degree, diploma or other qualification at the University of Cambridge or any other University or similar institution except as declared in the Preface and specified in the text. It does not exceed the prescribed word limit for the Engineering Degree Committee of 65,000 words including appendices, bibliography, footnotes, tables and equations and has fewer than 150 figures.

Qifang Wan
November 2020

Abstract

The modification of graphene band structure by periodic potential perturbation

Qifang Wan

Monolayer graphene has been under the spotlight of research since its discovery in 2004, due to its unusual properties such as massless Dirac fermions, exceptional tensile strength, ultrahigh thermal conductivity, superior charge carrier mobility, remarkable optical properties etc. Graphene-based devices are expected to be promising building blocks in nanotechnology for a range of applications. However, it has no intrinsic band gap which means that graphene FETs will have a very low on/off ratio. Several groups have tried to introduce a band gap in graphene artificially, such as etching graphene into nanoribbons. This thesis suggests the possibility to modify graphene's band structure from appropriately engineered periodic potential patterns.

Ferroelectrics is widely applied in everyday technologies, such as non-volatile memories and medical imaging, due to the presence of spontaneous polarisation in the material and that being reversible by an externally applied electric field. A ferroelectric material PZT ($PbZr_xTi_{1-x}O_3$), is utilised in this work to produce 1D periodic potentials. A piece of single crystal thin film PZT undergoes domain engineering to create periodic potentials. With single layer graphene transferred on top, this structure qualifies as an 1D electrostatic graphene superlattice (EGSL), whose effect is measurable as a broadening of the current valley near the CNP point and variations in conductance on the gate sweep curve.

A PZT-graphene device is designed, fabricated, and electrically characterised at different temperatures. The device size is kept around 300$\sim$400nm to ensure coherence transport of electrons in the device. A unique room temperature fabrication process is developed and put in use. Evidence of a bandgap is observed, and the measurements prove to match theoretical predictions on the 1D electrostatic graphene superlattice effect.

I would like to dedicate this thesis to my loving parents and friends.

Acknowledgements

I would like to express my heartfelt thanks to Prof. Colm Durkan for the inspiring, instructive, patient supervision, the encouragement and advice he has provided throughout my time as his student. I have been extremely grateful to him for giving me the opportunity to work in his group.

I wish to thank Dr Ahmed Kursumovic and Prof Judith McManus-Driscoll's, from Department of Materials Science & Metallurgy, University of Cambridge for supplying the single crystal PZT thin films used in this work.

I would like to acknowledge Dr. Nan Wang, Dr. Zhuocong Xiao, Dr. Maria Kaimaki, Dr. Atif Aziz, Dr. Juan Antonio Rubio-Lara, Dr. Cuong Danh Do, Dr. Magali Ferro, Dr. Allison R. Cadore, Dr. Victor Serdio, AbdulAziz AlMutairi for technical help and fruitful discussions.

I would like to express my gratitude to the China Scholarship Council for their financial support.

Finally I would like to thank all my colleagues in the Nanoscience Center, the CAPE building, the Graphene Centre, the Maxwell Center for emotional and social support.

Table of contents

List of figures

List of tables

Chapter 1

Introduction

Monolayer graphene, whose charge carriers are massless Dirac fermions, has exceptional properties such as exceptional tensile strength [18, 19], ultrahigh thermal conductivity [20, 21], superior charge carrier mobility [22–24], remarkable optical properties [25]. Graphene-based devices are expected to be promising building blocks in nanotechnology for a range of applications. However, an inevitable issue with graphene FETs is the poor on/off ratio due to no intrinsic bandgap. Several groups have tried to introduce a bandgap in graphene artificially, such as etching graphene into nanoribbons [26], and introducing strain profiles [27]. This work suggests the possibility to modify graphene's band structure from appropriately engineered periodic potential patterns.

The work aims to experimentally explore the effect of periodic potential modulation on the band structure of graphene. The Kronig-Penney model [28–33] (see subsection 1.1.3) implies that periodic potentials (resulted from the lattice ions) give rise to the electronic band structure with energy gaps. Thus, will artificial periodic potentials created beneath a singe layer of material without band gap, lead to a band gap in that material? The work in this thesis is to test this idea, solve fabrication challenges along the way, and work out the influence such potentials have on the electronic band structure.

In Chapter 1, section 1.1 introduces the concept of band gap in general including why it is important and where it originates from. It also covers the knowledge of band structure for Schrödinger's electrons and massless Dirac fermions in graphene. Section 1.2 focuses on graphene's band structure and relevant characteristics. Section 1.3 includes a literature review on previous experimental efforts in opening an energy gap in monolayer graphene. Section 1.4 demonstrates theoretical predictions of graphene band structure modification using the method detailed in this thesis i.e., electrical periodic potentials.

Chapter 2 concentrates on a multiferroic material called Lead Zirconate Titanate (stoichiometrically $PbZr_xTi_{1-x}O_3$, PZT in short). It was chosen to realise the underlying periodic

potentials, as it exhibits spontaneous polarisation and is ferroelectric (see section 2.1). It is possible to perform domain engineering via electrical excitation. Previous research papers within the group proved in theory that domains of nanometer size can be achieved. In this chapter, ferroelectric domain engineering is explored to form 1D and 2D periodic potentials via Piezoresponse Force Microscopy (PFM). The challenge is that the periodic potential perturbation in the Kronig Penney model are at atomic length scales, which is difficult to achieve. This chapter explores how to produce consistent periodicities.
Chapter 3 reports the fabrication process of the graphene-PZT integrated device. Despite the above advantages of the two materials chosen in this work, it is however not deniable that they are two very distinct materials that do not relate to each other. Attempting to combine them in one device poses significant challenges in nano fabrication. Piezoelectric Force Microscopy (PFM) is used to pattern potentials on a single crystal PZT thin film. As ferroelectric domains depolarise at elevated temperatures, one of the challenges is to develop a room-temperature fabrication process. Secondly, the device size is kept around 300$\sim$400nm, in order to ensure coherent transport of charge carriers in the device. A few dozens of devices are fabricated on a single PZT substrate in each batch. To make sure the above patterned graphene strips sit on the corresponding patterned potentials, a unique alignment method is developed in this chapter.
Chapter 4 discusses electrical characterisation results for the PZT-graphene device, which confirms with theories and predictions that periodic potentials lead to the band structure modification of graphene monolayer and create minibands. In this chapter, observations on critical evidence from gate voltage sweep curves are presented and analysed. Minizone boundaries (MB) and minibands are computed based on parameters in the experiment. Overlapping the modelled MB map with experimental data demonstrates the match between the theory and experiment.

1.1 The concept of band structure

This section describes the concept of band gap. Subsection 1.1.1 outlines the application of band gap in electronic devices. Subsection 1.1.2 introduces Schrödinger's equation and the nearly-free electron model. Subsection 1.1.3 uses the Kronig-Penney model to derive the electronic band structure for a crystal lattice. Subsection 1.1.4 discusses the application of Kronig-Penney model to massless Dirac fermions.

1.1.1 The significance of a band gap

According to electrical conductivity, materials can be classified into roughly four groups: insulators (such as diamond), metals (such as gold, silver and copper), semimetals (such as bismuth and graphite) and semiconductors (such as silicon and germanium). Every crystal contains electrons. It is the way how the internal electrons respond to an applied electric field that differentiates materials and divide them into the above four groups. Electrons in crystals are arranged in energy bands, as shown in Figure 1.1, separated by regions where no electron state exist.

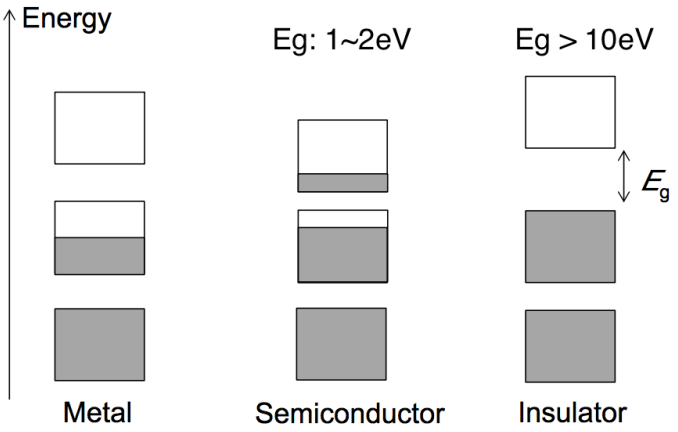

Fig. 1.1 Schematic electron occupancy of energy bands for a metal, semiconductor and insulator. Figure sourced from [1]

For metals, one or more bands are partially filled. The Fermi energy is located within one band or several overlapping bands. For insulators, the energy bands are either completely empty or full [1]. The forbidden regions between the uppermost entirely filled band (valence band) and the next entirely empty band (conduction band) are called band gaps. The band gap in insulators is very large (usually exceeds $\sim$10eV), which makes it almost impossible for an electron to jump from valence band to conduction band, hence blocking electricity flow. Regarding semiconductors, one or two bands are slightly filled or empty [1]. Band gaps in semiconductors refer to regions between two partially filled bands. They are the product of interactions between wavelike conduction electrons and ion cores of crystal lattice. Introducing extra charges, by doping or field effect, manipulates the total number of electrons in energy bands. Therefore, the conductivity of these materials can be modified, which is the basis for semiconductor electronic devices. The size of bandgap in conventional semiconductors is in the range of 1$\sim$2eV. For example at 300K, silicon and gallium arsenide possess a bandgap of 1.14eV and 1.43eV respectively [34]. There are also wide bandgap

semiconducting materials, whose bandgap generally falls between 2∼6eV [35]. For example, diamond has a bandgap of 5.5eV [1].
The idea of band gap helps understand and harness semiconductors for electronic device applications. Silicon, a common material for photovoltaic modules, has a band gap just wide enough so electrons can easily jump across it when being excited by photons from sunlight. This process creates extra electrons and holes at the positive and negative junctions of the cell where they form part of an electric field and cause conduction of electricity. Such a process in reverse also has an application called LED. Semiconducting materials emit light as a result of electronic excitation, whose colour is determined by the band gap. Band gap is also the key to the on/off switching operation in transistors. Energy needed to excite one electron from the valence band to the conduction band for conduction is defined by the size of the band gap. In order to have a clear contrast between on and off states to avoid errors, semiconductors used in transistor components need to have large enough band gaps. Wide band gap materials are also used for power electronics applications for a high breakdown voltage and thermal stability.

1.1.2 The Schrödinger equation

Classical physics regarding electrical conductivity was built upon the Drude model, which relies on Maxwell-Boltzmann statistics. It is based on the principle that particles are "identical but distinguishable". By late 19th century, physics was regarded as a well-developed science with only very few problems to be sorted out. Within those remaining problems, which later led to the establishment of quantum physics, there were black body radiation, Compton modified scattering and the photoelectric effect.
After Rayleigh-Jean Law failed to explain the experimentally measured black body radiance curve, in 1900 Max Plank proposed a concept named "quanta". In summary this means a discrete amount of energy, and its value is the product of the later famous h constant and the radiation frequency v, i.e. $E = hv = \hbar\omega$. Albert Einstein was inspired by this idea, and later considered light as particles carrying a discrete amount of energy (photon), so as to decode the photoelectric effect in 1905.
In 1913, the simple atomic model suggested by Niels Bohr successfully worked out the discrete lines of the hydrogen spectrum. It was significant at the time as it assumed discrete energy values of orbitals and transitions between energy levels to take place when absorbing or emitting a photon. In 1924, Louis de Broglie discovered that not only light has particle characteristics (as suggested by Einstein), but particles also have wave characteristics, hence

the concept of wave-particle duality. The momentum of a photon p

$$p = \frac{h}{\lambda} = \hbar\omega \tag{1.1}$$

In 1926, Erwin Schrödinger found a wave equation to describe the electron behaviour [36–41].

$$-\frac{\hbar^2}{2m}\nabla^2\phi = i\hbar\frac{\partial\phi}{\partial t} \tag{1.2}$$

where the wave function ϕ is normalised to unit probability. Equation (1.2) is the time dependent Schrödinger equation with zero potential. It describes a system that is evolving with time. A more generalised version takes into considerations the electromagnetic vector potential $\mathbf{A}_{(\vec{\mathbf{r}},t)}$ and scalar potential $A_{0(\vec{\mathbf{r}},t)}$. Using the momentum operator $\hat{\mathbf{p}}$,

$$\left[i\hbar\frac{\partial}{\partial t} - \frac{1}{2m}\,|\,\hat{\mathbf{p}}_{(\vec{\mathbf{r}},t)} + e\mathbf{A}_{(\vec{\mathbf{r}},t)}|^2 + eA_{0(\vec{\mathbf{r}},t)} \right] \psi_{(\vec{\mathbf{r}},t)} = 0 \tag{1.3}$$

There is also the time independent Schrödinger equation that describes stationary states

$$-\frac{\hbar^2}{2m}\frac{d^2\psi_n}{dx^2} = \varepsilon_n\psi_n$$

This subsection hereafter will show where band gaps originate from and subsection 1.1.3 will give a simple derivation of the electronic band structure using Kronig-Penney model. The **free electron model** describes a single electron of mass m as a plane wave with a wavefunction $\psi_n(x)$. The energy ε_k of a free electron

$$\varepsilon_k = \frac{\hbar^2}{2m}\vec{k}^2 = \frac{\hbar^2}{2m}\left({k_x}^2 + {k_y}^2 + {k_z}^2\right)$$

The free electron model assumes a free electron gas. It assumes that conduction electrons travel freely throughout the crystal. So the solution to the above wave equation is for a system of only one electron. The model neglects the interaction between conduction electrons as well as that of conduction electrons with ions of the crystal lattice. To understand the concept of band gap, it is necessary to extend the free electron model to account for the effect of periodic lattice of a crystal. The nearly-free electron model emerges and solves the puzzle between insulators and semiconductors, while revealing other useful properties of electrons under electric field, e.g. the effective mass m^*. Bragg reflection of electrons is a characteristic feature of wave propagation for crystal lattices and is the origin of band gaps [1]. Assume

that the lattice constant for a crystal is a, Figure 1.2 shows the band structure for (a) an entirely free electron and (b) a nearly-free electron within a crystal of lattice constant a. For the nearly-free electron, the first Brillouin zone is shown with a corresponding energy gap at wavevector $k = \pm\pi/a$. Below the energy gap is the first allowed band and above it is the second allowed band. The electron wavefunctions at $k = \pm\pi/a$ consist of equivalent electron waves traveling in opposite directions. A wave traveling to the left is Bragg-reflected to the right and vice versa. And at each subsequent Brillouin zone, i.e $k = \pm 2\pi/a, \pm 3\pi/a$ and etc, Bragg reflection will reverse the traveling direction of the wave to produce a wave going neither left or right i.e., a standing wave.

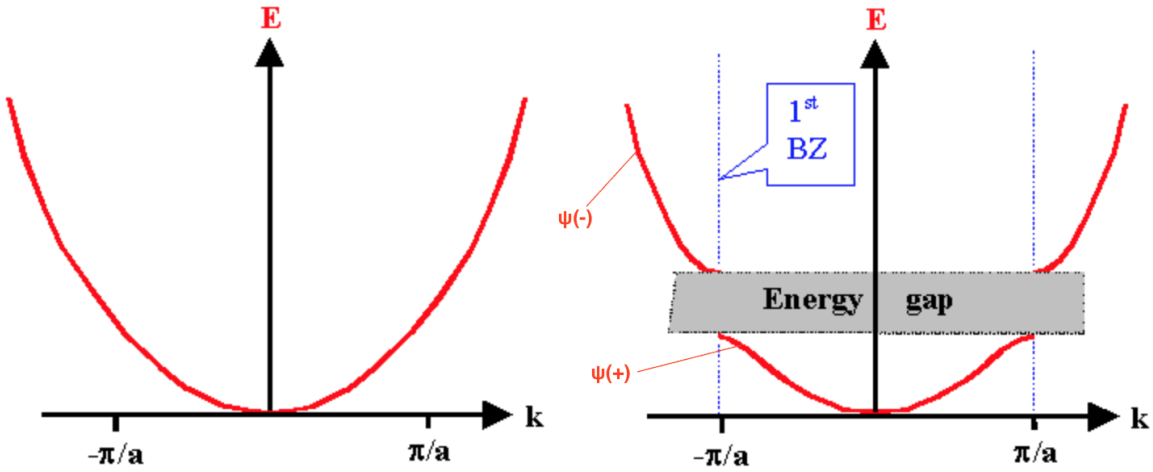

Fig. 1.2 (a) Energy ε versus wavevector k for a free electron; (b) Energy versus wavevector for an electron in a crystal of lattice constant a. Figure sourced from [1]

A time-independent state of an electron is represented by two different standing waves. The two standing waves are formed by two equal but opposite traveling waves of wavevector $k = \pm\pi/a$,

$$\psi(+) = exp(\frac{i\pi}{a}x) + exp(-\frac{i\pi}{a}x) = 2\,cos(\frac{\pi}{a}x)$$
$$\psi(-) = exp(\frac{i\pi}{a}x) - exp(-\frac{i\pi}{a}x) = 2i\,sin(\frac{\pi}{a}x)$$

To look at how those two standing waves result in a band gap, the probability density ρ of an electron within the lattice is:

$$\rho = \psi * \psi = |\psi|^2$$

For wavefunction $\psi(+)$ and $\psi(-)$, the probability density:

$$\rho(+) = |\psi(+)|^2 \propto cos^2(\frac{\pi x}{a})$$
$$\rho(-) = |\psi(-)|^2 \propto sin^2(\frac{\pi x}{a})$$

Figure 1.3 plots $\rho(+)$ and $\rho(-)$. In the lower half of the schematic is the electrostatic energy variation that a conduction electron experiences in the field of lattice ion cores. The potential energy in the case of a positive ion is negative, so that the force between them is attractive [1]. It can be seen that $\psi(+)$ and $\psi(-)$ pile up electrons at different regions, such that two waves have different values of potential energy. $\psi(+)$ piles up electrons on the cores of positive ions, hence lowers the potential energy in comparison with the average potential energy seen by a travelling wave. $\psi(-)$ piles up electrons in-between the ion cores, hence raises the potential energy in comparison with the average potential energy seen by a travelling wave. Averaging those three electron probability distribution, it is found that $\rho(+)$ is lower than that of the traveling wave while $\rho(-)$ is higher. The energy gap is equal to the difference between energies of $\rho(+)$ and $\rho(-)$.

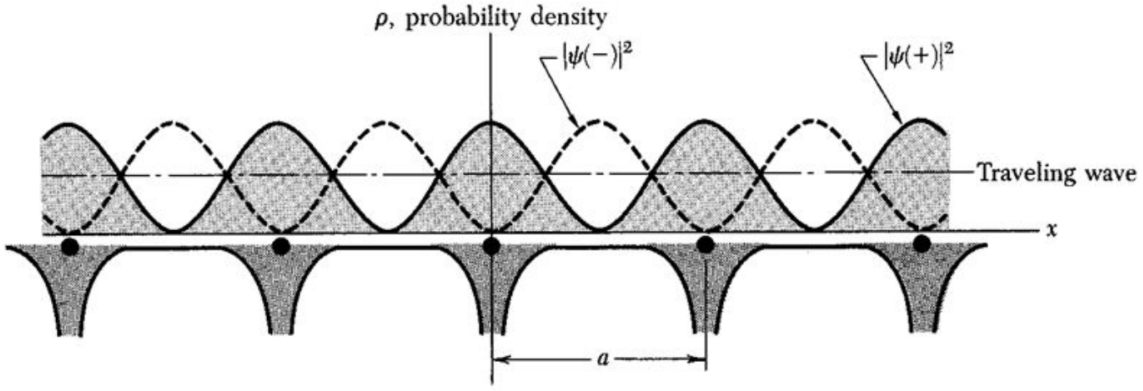

Fig. 1.3 Probability density distributions $\rho(+)$ and $\rho(-)$ of an electron for wavefunctions $\psi(+)$ and $\psi(-)$ with potential energy variation in the field of lattice ions. $\rho(+)$ concentrates electrons on the positive ion cores while $\rho(-)$ piles up electrons in-between the ion cores. The energy gap is equal to the difference between energies of $\rho(+)$ and $\rho(-)$. Figure sourced from [1]

1.1.3 The Kronig-Penney model

The second half of subsection 1.1.2 describes where band gaps originate within the crystal lattice. This subsection will derive the electronic band structure by modelling ions within the lattice as periodic potentials - using the Kronig-Penney model. Figure 1.4 demonstrates the periodic potential situation introduced by Kronig and Penney. Square shaped finite potential wells of width a and periodicity $a+b$ have uniform heights of U_0. This model simulates the periodic potential that a conduction electron experiences in the field of ion cores within a crystal periodic lattice [42]. In this case, the lattice constant corresponds to the width of the potential well a, and b is the diameter of ion cores. In reality, b should be much smaller than a ($b \ll a$) and the energy barrier is infinite compared to the potential energy of an electron in the crystal i.e., $U_0 = \infty$.
From conservation of kinetic and potential energy we have the wavefunction ψ as:

$$-\frac{\hbar^2}{2m}\frac{d^2\psi}{dx^2} + U_{(x)}\psi = \varepsilon\psi \tag{1.4}$$

where $U_{(x)}$ is the potential energy and ε is the energy eigenvalue. In Figure 1.4 in the region $0 < x < a$ where potential potential experienced by the electron $U = \infty$, solution to the wavefunction is:

$$\psi = Ae^{iKx} + Be^{-iKx} \tag{1.5}$$

Substitute the second derivative $\frac{d^2\psi}{dx^2}$ and the original wavefunction back to equation (1.4), the potential energy of the electron is:

$$\varepsilon = \frac{\hbar^2 K^2}{2m}, \; so \quad K = \frac{\sqrt{2m\varepsilon}}{\hbar} \tag{1.6}$$

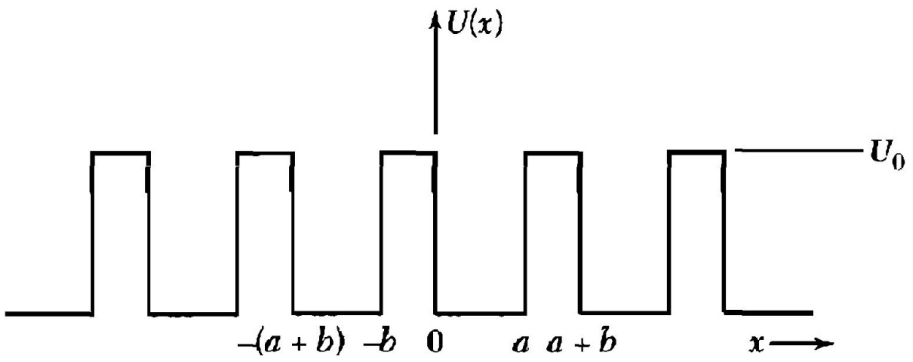

Fig. 1.4 Periodic potential situation introduced by Kronig and Penney. Figure sourced from [1]

In Figure 1.4 in the region $-b < x < 0$ where the potential experienced by the electron $U = U_0$, solution to the wavefunction is:

$$\psi = Ce^{Qx} + De^{-Qx} \tag{1.7}$$

and the electron potential energy is:

$$\varepsilon = U_0 - \frac{\hbar^2 Q^2}{2m}, \; so \quad Q = \frac{\sqrt{2m(U_0 - \varepsilon)}}{\hbar}$$

Bloch's theorem shows that solutions for the Schrödinger equation for a periodic potential problem should be the form of:

$$\psi_{\vec{k}}(\vec{r}) = u_{\vec{k}}(\vec{r})\, exp(i\vec{k} \cdot \vec{r})$$

where $u_{\vec{k}}(\vec{r})$ is of the same periodicity as the crystal lattice, so $u_{\vec{k}}(\vec{r}) = u_{\vec{k}}(\vec{r} + \vec{a})$. Apply Bloch's theorem here, the solution for region $a < x < a+b$ is:

$$\psi(a < x < a+b) = u(a < x < a+b)\, exp(ika)$$

and the solution for region $-b < x < 0$ is:

$$\psi(-b < x < 0) = u(-b < x < 0)\, exp(-ikb)$$

Apply Bloch's theorem with potential periodicity $a+b$, $u(a < x < a+b) = u(-b < x < 0)$ and we have the following relationship:

$$\psi(a < x < a+b) = \psi(-b < x < 0)\, e^{ik(a+b)} \tag{1.8}$$

Solve equations (1.8), (1.7) and (1.5) together, knowing that ψ and $\frac{d\psi}{dx}$ are continuous functions at boundaries $x = 0$ and $x = a$, and make use of the periodicity relationship where $\psi(a) = \psi(-b)$. The resulting solution is very complicated. A simplified version is obtained by assuming a mathematical limiting case where $b = 0$ and $U_0 = \infty$. $Q \gg K$ and $Qb \ll 1$ is also deduced from the limit [1]. It can be found that:

$$\frac{P}{Ka} sin Ka + cos Ka = cos ka\,, \qquad P = \frac{Q^2 ba}{2} = \frac{mba(U_0 - \varepsilon)}{\hbar^2} \tag{1.9}$$

On the RHS of equation (1.9), k originates from the Bloch's function and corresponds to the wavenumber. For the case of $P = 3\pi/2$, Figure 1.5 plots the LHS function $\frac{P}{Ka} sin Ka + cos Ka$

with respect to $Ka(=\frac{a\sqrt{2m\varepsilon}}{\hbar})$. The solution of the above equation is obtained via a graphical method by drawing the range of the RHS function $cos\,Ka$. Because -1 $\leq cos\,Ka$ (LHS) $\leq$ +1, the solutions to the RHS are those parts of the curve lying between -1 and 1, annotated by two red dashed lines +1 and -1. The allowed values of Ka are highlighted as red solid lines. The solutions are symmetric around the y axis.

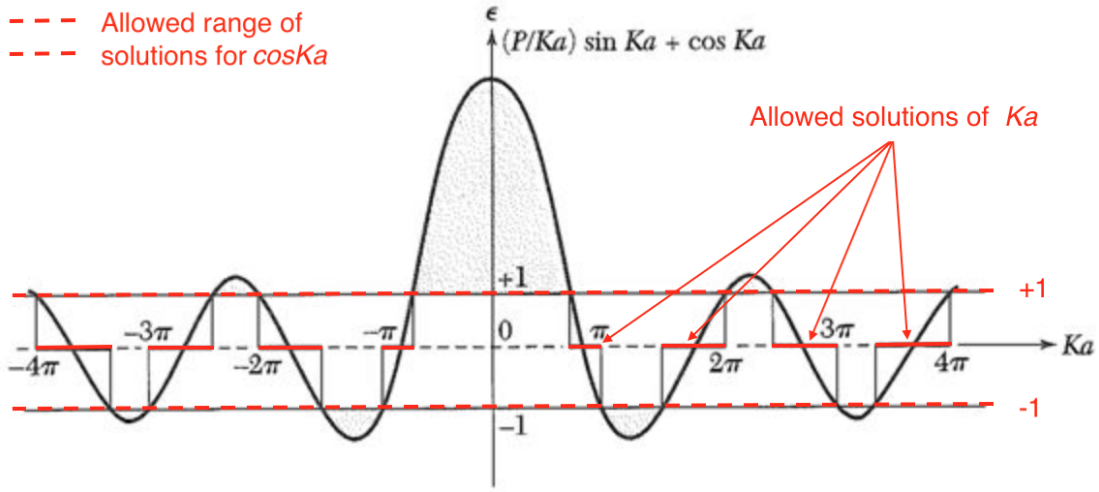

Fig. 1.5 Plot of the function $\frac{P}{Ka}sin\,Ka + cos\,Ka$ at $P = 3\pi/2$. The allowed range of solutions for $cos\,Ka$ is annotated by region between red dashed lines +1 and -1. The allowed solutions of Ka are highlighted as red solid lines. Figure sourced from [1]

Figure 1.6 plots the allowed electron energy bands in the wavenumber k space, with energy gaps at $\pm\pi/a$, $\pm 2\pi/a$, $\pm 3\pi/a$.... The vertical axis values are calculated in units of $\frac{\hbar^2\pi^2}{2ma^2}$. This work aims to experimentally demonstrate the situation in this model. Square shaped finite potential wells of width a, periodicity $a+b$ and uniform height U_0 can be emulated by periodic potential arrays produced on PZT thin film. The concepts of polarisation and domain switching will be elucidated in Chapter 2. Starting with a region with the same polarisation direction, an opposite polarisation direction is introduced at patterned locations. The region of opposite polarisation directions to that of the primitive region represent the bottoms of potential wells. And the periodicity of those patterned regions corresponds to the periodicity $a+b$ in the model. The height of finite potential wells corresponds to the surface potential difference between the primitive region and the patterned locations.

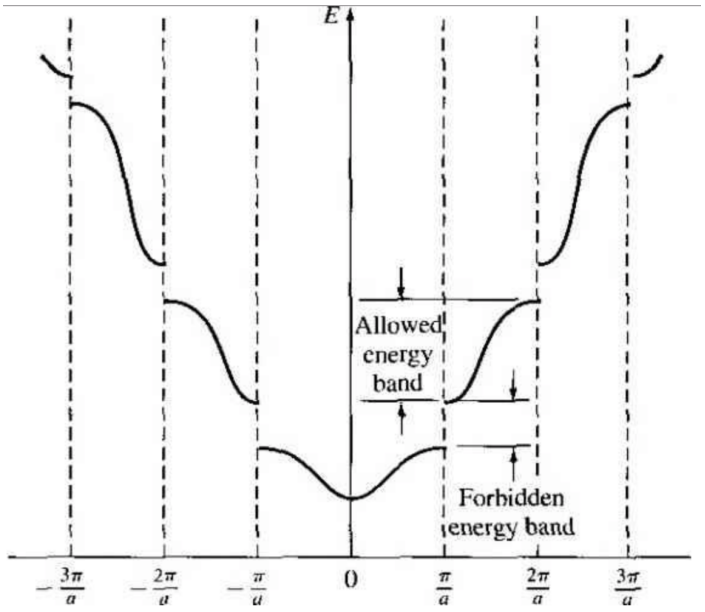

Fig. 1.6 Energy versus wavenumber plot for Kronig-Penney model at $P = 3\pi/2$. Figure sourced from [1]

1.1.4 Massless Dirac fermions

The charge carriers in graphene follow the Dirac equation and have spin 1/2. They are called massless Dirac fermions, behave relativistically, and travel at a fermi velocity $\sim 10^6$ m/s. The energy spectrum of graphene is linear and gapless close to the Dirac points (section 1.2). The chiral nature of the massless fermions leads to unexpected behaviours under periodic potentials. The charge carrier propagation through a graphene superlattice is anisotropic. In extreme cases, the group velocities can be reduced to 40% of its original value in one direction but unchanged in another direction [17]. More details on graphene properties and band structure will be discussed in section 1.2. Barbier *et al* studies the behaviour of massless Dirac fermions in a 1D Kronig-Penney type potentials. Numerical results of the dispersion relation and density of states for 2-dimensional Dirac fermions in the presence of 1D periodic potentials, are appropriate to graphene. Such a 1D potential barrier is shown in Figure 1.7. The x-direction is parallel to the wavevector component k_x.

The charge carriers in graphene are governed by Dirac equation which will be discussed in more details in section 1.2. The light speed is replaced by fermi velocity and zero mass is applied to the equation,

$$[c\,(\,\vec{\sigma}\cdot\hat{p}\,) + m\,c^2\,\sigma_z]\,\Psi = (E - V)\,\Psi \tag{1.10}$$

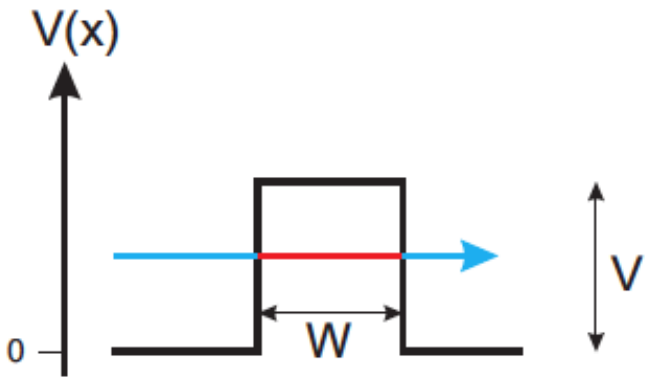

Fig. 1.7 1D potential barrier V(x) of height V and width W. The x-direction is parallel to the wavevector component k_x. Figure sourced from [2].

where $\vec{\sigma} = (\sigma_x, \sigma_y)$ and σ_z are the Pauli matrices. Barbier *et al* first calculated the transmission coefficient T of massless fermions through a single potential barrier of height V and width W, as shown in Figure 1.7. A contour plot of the transmission is shown in Figure 1.8. It can be seen that, if the electrons are at normal incidence to the barrier i.e. $k_y = 0$, the transmission $T(k_x,k_y)$ is equal to 1. This phenomenon is called Klein tunnelling, a result of chirality of the carriers which prevents them from being reflected by the barrier [2]. Figure 1.9 displays slices of the contour plot of Figure 1.8, at $k_y = 0$ and 0.05nm^{-1}. The figure demonstrates clearly that the transmission at $k_y = 0$ is perfect.
They then consider a 1D superlattice - periodic structures consisting of N identical units of length L. Each unit includes a rectangular barrier of width *a* and a rectangular well of width *b*, so L = a + b. Figure 1.10 (top) shows the first two minibands of the energy dispersion relation for a 1D graphene superlattice. The first miniband is between $\pm\frac{\pi}{L}$, and the second miniband is between $\pm\frac{\pi}{L}$ to $\pm\frac{2\pi}{L}$. In contrast to the non-relativistic Kronig-Penney case, the energy dispersion E depends on the wavevector component k_x at a fixed k_y. For $k_y = 0$, the linear dispersion relation $E(k_x, 0) = v_F\hbar k_x$ of graphene is not affected by the periodic potentials, as a consequence of Klein tunnelling. The energy E is shifted by $\frac{V}{2} = 50\text{meV}$.
Figure 1.10 (bottom) shows three slices of curve of the 3D energy dispersion model at the top, for $k_y = 0$ (red solid), 0.066nm^{-1} (green dashed) and 0.132nm^{-1} (blue dash-dotted). The first miniband in the first quadrant, i.e. k_x between 0 and $\frac{\pi}{L}$ and positive E axis, is plotted. Notice that when k_y increases from 0 to 0.066nm^{-1}, an energy gap starts to appear at the first minizone boundary $\frac{\pi}{L}$. The gap is enlarged when k_y goes up to 0.132nm^{-1}. The energy gaps at the first minizone boundary $k_x = \frac{\pi}{L}$ are marked by green and blue arrows for $k_y = 0.066\text{nm}^{-1}$ and 0.132nm^{-1} respectively.

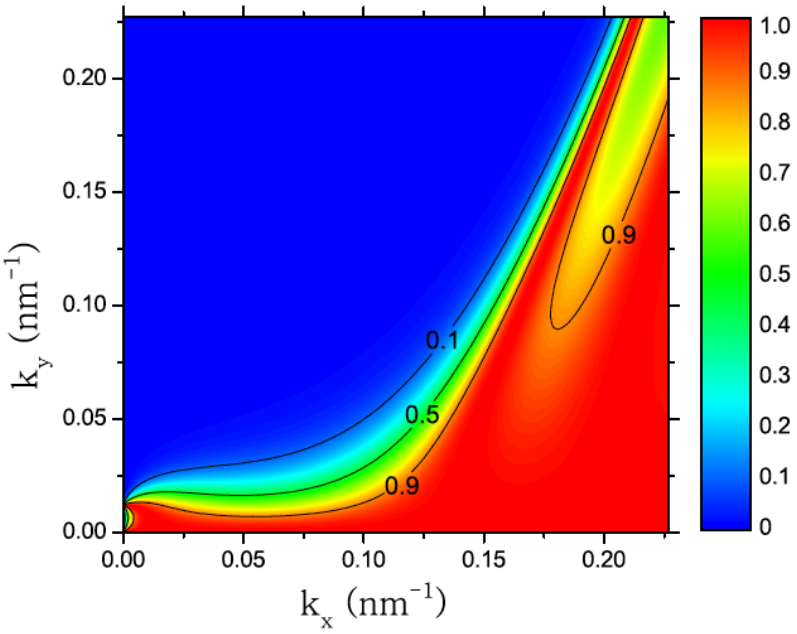

Fig. 1.8 Contour plot of transmission T of massless relativistic electrons through a barrier with V = 50meV, $v_F = 10^6$m/s, and W = 50nm. Figure sourced from [2]

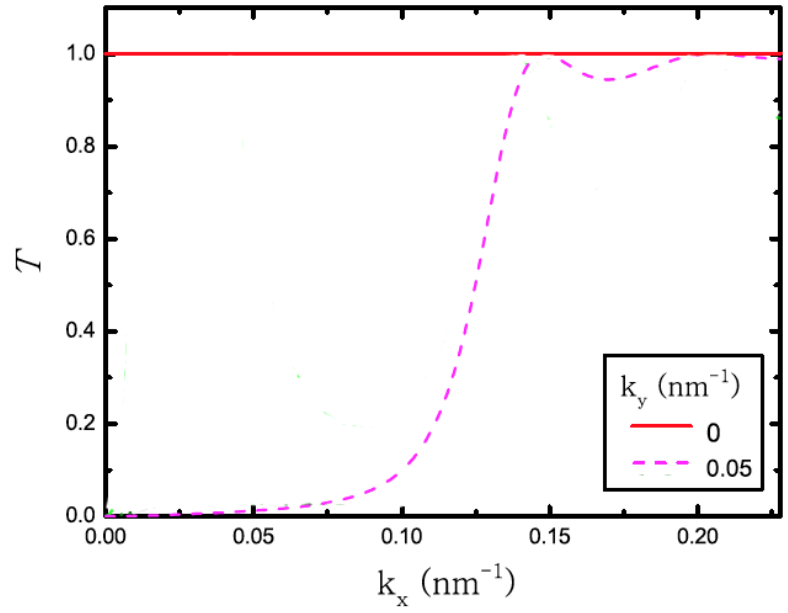

Fig. 1.9 Plot of slices of the transmission coefficient for electrons solid red and dashed magenta curves taken at constant $k_y = 0$ and $k_y = 0.05$nm^{-1} from Figure 1.8. The transmission at $k_y = 0$ is perfect. Figure sourced from [2]

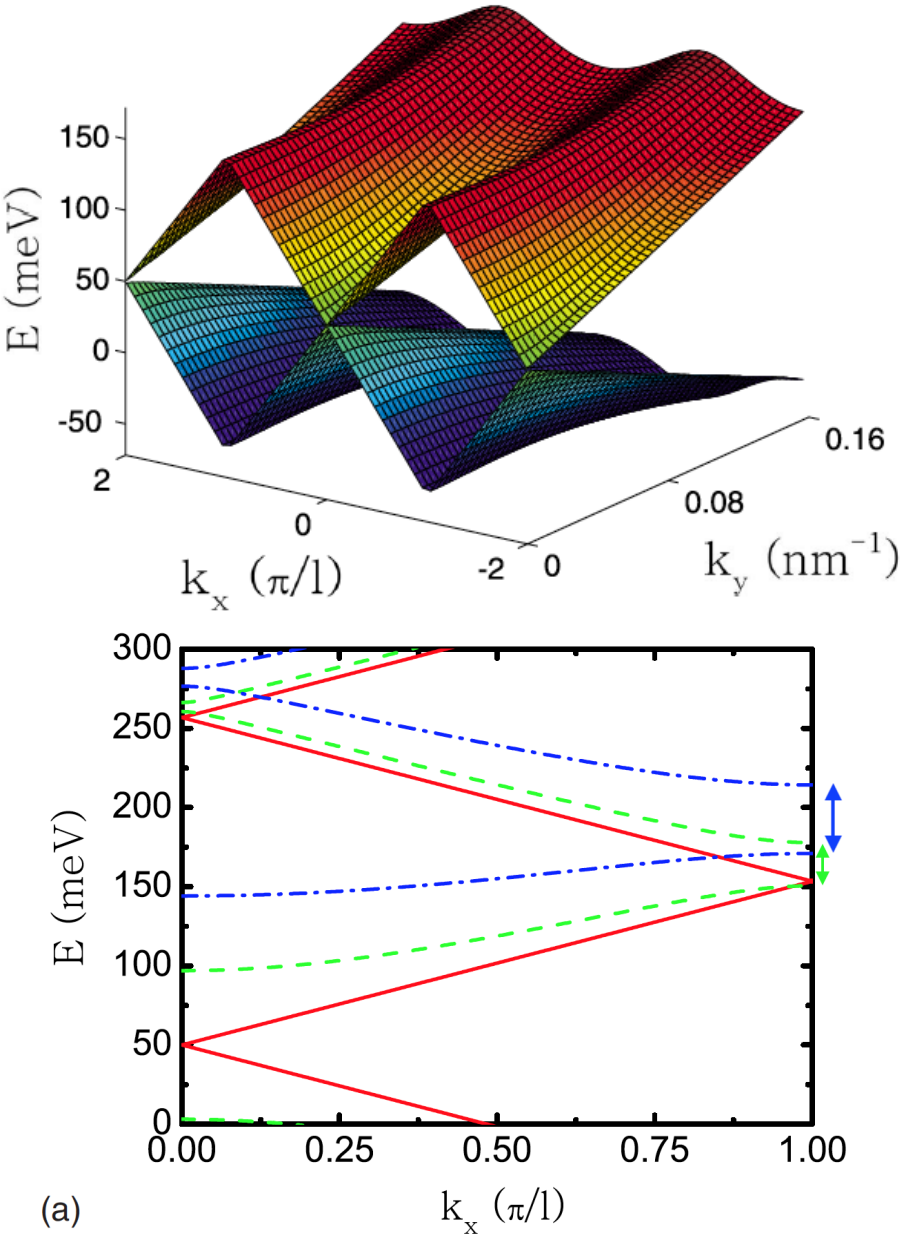

Fig. 1.10 Top: dispersion relation in a 1D graphene SL. Only the first two bands are shown for L = 20nm, a = b =10nm, V = 100meV. Bottom: slices of the top dispersion relation for constant k_y = 0, 0.066, 0.132 nm^{-1} for the solid red, dashed green, and dash-dotted blue curves, respectively. The k_x axis is numbered by integers of $\frac{\pi}{L}$. The first miniband is between $\pm\frac{\pi}{L}$, and the second miniband is between $\pm\frac{\pi}{L}$ to $\pm\frac{2\pi}{L}$. The energy gap at the first minizone boundary $k_x = \frac{\pi}{L}$ is marked by green and blue arrows respectively. Figure sourced from [2]

1.2 The band structure of graphene

Graphene, a single atom thick layer of honeycomb carbon structure, was first described theoretically in 1947 [43]. However, no one believed it would be possible to create a stable 2D sheet of atoms until 2004, when graphene was first separated from bulk graphite by micromechanical cleavage [44]. Graphene's unique properties come from the collective interactions between electrons and the honeycomb lattice. Its interweaving sublattices and linear band structure are demonstrated in subsection 1.2.2. Subsection 1.2.3 introduces Dirac equation that governs the charge carrier behaviour in graphene. The existence of massless electrons is also shown. They are called massless Dirac fermions. Those quasiparticles behave as if the speed of light is $10^6 m/s$, 2 orders smaller than its value in vacuum; such that the relativistic effects can be observed without using particle accelerators. One of which is Klein tunnelling, also discussed in subsection 1.2.3. Lastly, subsection 1.2.4 touches on a few advantages of graphene as a novel material.

1.2.1 The chemical bonding

The Heisenberg uncertainty principle (1927) states: it is impossible to define with absolute precision, at the same time both the position and the momentum of an object.

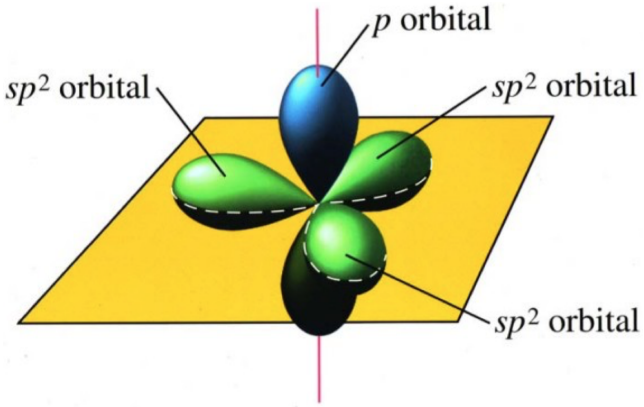

Fig. 1.11 An sp^2 hybridised carbon atom. Figure sourced from [45]

This quantum mechanics rule was later used to develop molecular orbital (MO) theory, one of the two fundamental theories in chemistry, to explain chemical bonding. According to the MO theory, electrons are placed in atomic orbitals in order, starting from s orbital to p, d, f, g, h, i ... orbitals. Graphene is a single layer of carbon atoms. Being the 6th element, an isolated carbon has an electron configuration $1s^2\ 2s^2\ 2p^2$. A $1s$ orbital electron has a very low energy, less than $-250eV$ compared to the vacuum level.

Putting an infinite number of carbon atoms on a single plane, electrons reorganise themselves to form three identical orbitals, called sp^2 hybrids. That is to say, the carbon atom promotes one electron from the $2s^2$ energy orbital, to fill the $2p_z$ energy orbital. So the electron configuration becomes $1s^2\ 2s^1\ 2p_x^1\ 2p_y^1\ 2p_z^1$. The sp^2 hybrids are made of $2s$, $2p_x$ and $2p_y$ orbitals, shown in Figure 1.11. They arrange themselves as far apart as possible on a plane, at 120° to each other. Those are called σ orbitals and are tightly bonded to the atom. Between every two carbon atoms (spaced at 1.42 Åfor graphene), a sigma (σ) bond is formed along the internuclear axis - reason for graphene's exceptional structural rigidity. The remaining $2p_z$ orbital is at right angle to the plane, classified as π orbital. Electrons in π orbital allow creations of weak π bonds with neighbours, accounting for the conduction in graphene lattice. Every π bond results in two π energy bands called bonding and anti-bonding π bands in the Brillouin zone.

1.2.2 The tight-binding model

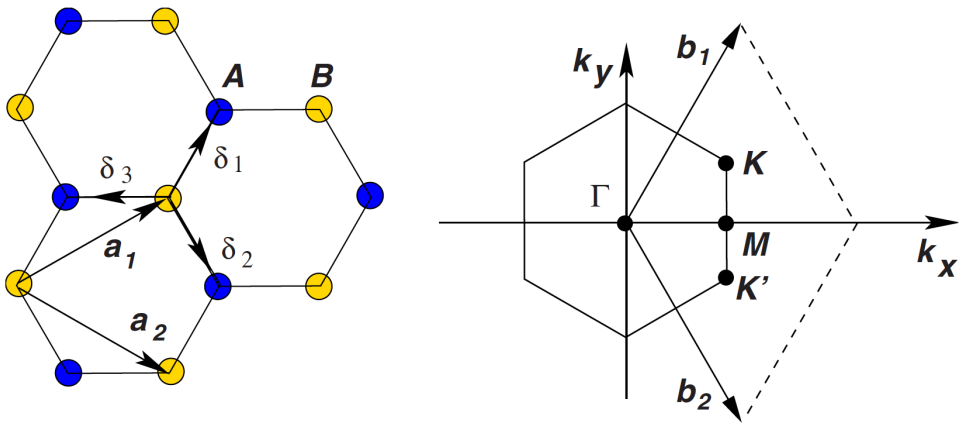

Fig. 1.12 Graphene honeycomb lattice and its Brillouin zone. Left: graphene lattice structure, made of two interpenetrating triangular sublattices A and B. $\vec{a}_1$ and $\vec{a}_2$ are the lattice unit vectors. $\vec{\delta}_i$, i = 1, 2, 3 are the nearest neighbour vectors. Right: the corresponding Brillouin zone. The Dirac cones are located at the K and K' points. Figure sourced from [46]

The tight binding model is a molecular orbital model that can be used to derive the band structure for graphene. Figure 1.12 shows the lattice structure of graphene and the corresponding Brillouin zone. The two triangular sublattices A and B interpenetrate each other and construct a hexagonal lattice structure. The graphene lattice can be viewed with a two-atom basis (A and B) per unit cell. This is a result of the σ bond (formed from sp^2 orbitals) between two carbon atoms. Such a crystal lattice structure gives an additional degree of freedom to an

electron, named pseudo spin, its orbital wavefunction can sit on different sublattices of the honeycomb lattice.

Considering an arbitrary atom A_0 in the A sublattice, there are three nearest neighbours B_{1j}, i.e. B_{11}, B_{12}, B_{13}. The carbon-carbon distance a ≈ 1.42 Å. The lattice vectors $\vec{a}_1$ and $\vec{a}_2$ are written as

$$\vec{a}_1 = \frac{a}{2}\begin{pmatrix} 3 \\ \sqrt{3} \end{pmatrix} \qquad \vec{a}_2 = \frac{a}{2}\begin{pmatrix} 3 \\ -\sqrt{3} \end{pmatrix}$$

Figure 1.12(b) shows the reciprocal graphene lattice. Reciprocal space, namely the k-space or momentum space, is the space where the Fourier transform of a space dependent function is represented. This is analogous to the frequency domain being the space to represent Fourier transform of a time dependent function. A reverse Fourier transform takes us back to the real space from reciprocal space. A plane wave can be written as an oscillating term $e^{i(kx-\omega t)}$, k is the wavevector and ω is the angular frequency. The periodicity oscillates with $kx = 2\pi$. Hence for a given space, k and x are reciprocal to each other, i.e. $k = \frac{2\pi}{x}$. The primitive vectors $\vec{a}$ and reciprocal vectors $\vec{b}$ satisfy the following relationship:

$$\begin{cases} \vec{a}_i\vec{b}_i = \vec{a}_j\vec{b}_j = 2\pi \\ \vec{a}_i\vec{b}_j = \vec{a}_j\vec{b}_i = 0 \quad \text{when} \quad i \neq j \end{cases}$$

Hence, the reciprocal lattice vectors $\vec{b}_1$ and $\vec{b}_1$ can be written as

$$\vec{b}_1 = \frac{2\pi}{3a}\begin{pmatrix} 1 \\ \sqrt{3} \end{pmatrix} \qquad \vec{b}_2 = \frac{2\pi}{3a}\begin{pmatrix} 1 \\ -\sqrt{3} \end{pmatrix}$$

In Figure 1.12b, the two points K and K' at the corner of the Brillouin zone are named Dirac points. They are not equivalent to each other, and correspond to different sublattices. Their locations are given as

$$\mathbf{K} = \begin{pmatrix} \frac{2\pi}{3a} \\ \frac{2\pi}{3\sqrt{3}a} \end{pmatrix} \qquad \mathbf{K'} = \begin{pmatrix} \frac{2\pi}{3a} \\ -\frac{2\pi}{3\sqrt{3}a} \end{pmatrix}$$

The three position vectors between A_0 and B_{11}, B_{12}, B_{13} are δ_1, δ_2 and δ_3. They connect two nearest-neighbouring carbon atoms in real space.

$$\delta_1 = \frac{a}{2}\begin{pmatrix} 1 \\ \sqrt{3} \end{pmatrix} \qquad \delta_2 = \frac{a}{2}\begin{pmatrix} 1 \\ -\sqrt{3} \end{pmatrix} \qquad \delta_3 = a\begin{pmatrix} -1 \\ 0 \end{pmatrix}$$

The six position vectors to the next-nearest neighbours in real space are

$$\delta_1' = \pm\vec{a}_1 \qquad \delta_2' = \pm\vec{a}_2 \qquad \delta_3' = \pm(\vec{a}_2 - \vec{a}_1)$$

The tight binding Hamiltonian for electrons in graphene considers that they can hop to nearest- and next-nearest neighbours, while assuming translational invariance i.e., an infinite graphene sheets. In equation (1.11), t is the nearest-neighbour hopping energy (between different sublattices) and t' is the next-nearest-neighbour hopping energy (within the same sublattice). The electronic energy bands are derived

$$\begin{aligned} E_{\pm}(\mathbf{k}) &= \pm t\sqrt{3+f(\mathbf{k})} - t'f(\mathbf{k}) \\ f(\mathbf{k}) &= 2\cos(\sqrt{3}k_y a) + 4\cos(\frac{\sqrt{3}}{2}k_y a)\cos(\frac{3}{2}k_x a) \end{aligned} \tag{1.11}$$

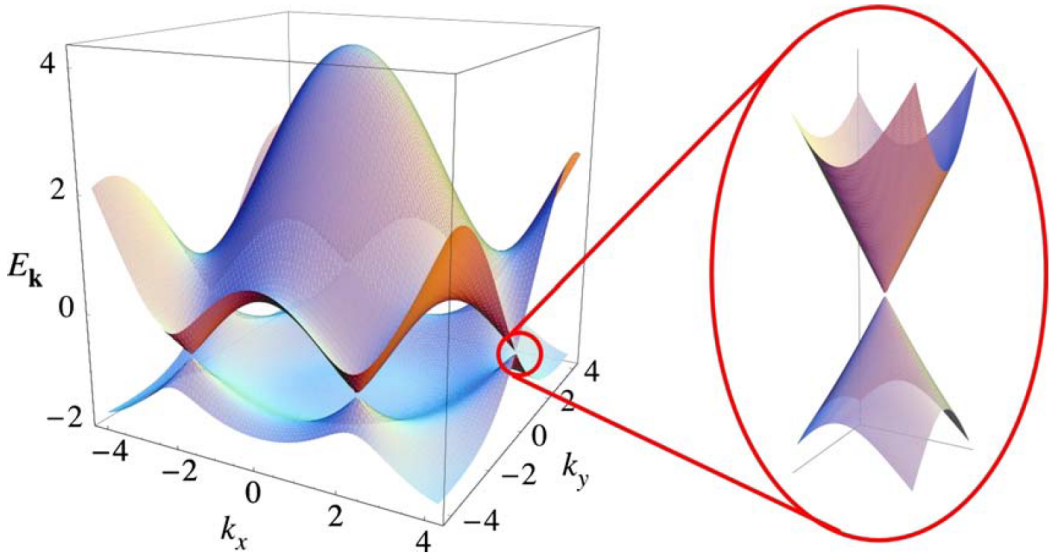

Fig. 1.13 Electronic dispersion in the honeycomb lattice. Left: energy spectrum in units of t for finite values of t and t'. t = 2.7eV and t' = -0.2t. Right: zoom in of the energy bands close to one of the Dirac points. Figure sourced from [46]

The plus sign refers to the upper (π*) band and the minus sign refers to the lower (π) band. Figure 1.13 shows the band structure of graphene over the whole Brillouin zone, for t = 2.7eV and t' = -0.2t. The vertical E_k axis is in units of t. With finite values of t', π and π* bands are asymmetric. This band structure casts a difference from those of a metal or semiconductor. The intersection of valence (lower half - π energy bonding band) and conduction band (upper half - π^* energy anti-bonding band) in the vicinity of Brillouin zone edges means zero band gap at the Dirac points, where the Fermi energy lies. Further away from the Dirac points, it exhibits cosine like eigenvalues of energy. The figure inset is a zoom in of the energy

spectrum in proximity to one of the Dirac points K or K'. The energy dispersion near the Brillouin zone corners is linear in momentum, it follows $E(\mathbf{k}) = \pm\hbar v_F \mathbf{k}$ where electrons moves at a constant speed given by the fermi velocity $v_F \approx c/300$. The wavevector $\mathbf{k}$ is defined with respect to the Dirac point K (or K'). For pristine graphene, the position of Dirac points coincides with the charge neutrality point (CNP). Two carbon atoms in the unit cell of graphene both contribute one electron to the two bands. This makes the Fermi energy E_F lie precisely at the half-filled band [47].

The linear dispersion is a consequence of the symmetry requirements of A/B sublattices and is independent of any approximation in consideration [43, 48]. This is in line with the Dirac equation when applying to graphene specifically, which will be demonstrated in the next subsection. Fermions inside graphene follow a conical energy spectrum. In other words, an electron with energy E that originates from the positive direction branch of the spectrum propagates in this branch of spectrum. A hole with energy $-E$ originates from the negative direction branch of the spectrum and propagates in the negative direction branch. At zero temperature zero doping, the valence band is completely filled and conduction band is completely empty. The Fermi level stays at the Dirac point, also called the charge neutrality point. The Fermi level will be shifted once doping or temperature change is introduced.

1.2.3 Charge carriers - massless Dirac fermions

Graphene is one of the two-dimensional condensed matter systems whose charge carriers mimic ultrarelativisitc particles. They are called massless Dirac fermions in quantum electrodynamics [49–53]. The discovery of graphene offered an opportunity of testing quantum electrodynamics theories in a low-energy system. One of them is Klein tunnelling, which is the perfect tunnelling of relativistic fermions through potential barriers [54]. In this subsection, I will show that electrons are massless near the Dirac points, and discuss Klein tunnelling.

In quantum mechanics, a particle with large momentum enters the terrain of relativity. They are no longer described by Schrödinger's equation and physicists in 1920s began to search for an equation that governs such particles. It is intuitive to start from the energy momentum relationship $E = \sqrt{c^2p^2 + m^2c^4}$, which can be written as

$$E^2 - c^2p^2 - m^2c^4 = 0$$

Simple factorisation gives,

$$(E + \alpha cp + \beta mc^2)(E - \alpha cp - \beta mc^2) = 0$$

where the following relationship holds to keep the above factorisation true

$$\alpha^2 = 1 \qquad \beta^2 = 1 \qquad \alpha\beta + \beta\alpha = 0 \tag{1.12}$$

Applying the widely accepted substitutions $E \to i\hbar\frac{\partial}{\partial t}$ and $p \to -i\hbar\frac{\partial}{\partial x}$ to the right factor,

$$\left(i\hbar\frac{\partial}{\partial t} - \alpha c(-i\hbar\frac{\partial}{\partial x}) - \beta mc^2 \right) \Psi_{(x,t)} = 0 \tag{1.13}$$

It is clear that the coefficient relationships in equation (1.12) can only hold if α and β are both matrices. Starting from one dimension,

$$\alpha = \sigma_x = \begin{bmatrix} 0 & 1 \\ 1 & 0 \end{bmatrix} \qquad \beta = \sigma_z = \begin{bmatrix} 1 & 0 \\ 0 & -1 \end{bmatrix}$$

The wavefunction in equation (1.13) also becomes a column vector, called a spinor

$$\left[i\hbar\frac{\partial}{\partial t} - \sigma_x c(-i\hbar\frac{\partial}{\partial x}) - \sigma_z mc^2 \right] \begin{pmatrix} \Psi_{1(x,t)} \\ \Psi_{2(x,t)} \end{pmatrix} = 0 \tag{1.14}$$

Equation (1.14) is called the Dirac equation for a free spin $\frac{1}{2}$ particle in one dimension. To generalise it to two dimensions, another Pauli matrix is needed. Using momentum operator $\hat{p_x}$ and $\hat{p_x}$,

$$\left[i\hbar\frac{\partial}{\partial t} - c(\sigma_x\hat{p}_x + \sigma_y\hat{p}_y) - \sigma_z mc^2 \right] \Psi_{(x,y,t)} = 0 \tag{1.15}$$

$$\text{where} \qquad \sigma_y = \begin{bmatrix} 0 & -i \\ i & 0 \end{bmatrix}$$

Note that two dimensions have involved all three Pauli matrices $\sigma_x(\alpha_x)$, $\sigma_y(\alpha_y)$ and $\sigma_z(\beta)$. In order to generalise it to three dimensions and for the factorisation to hold true, four 4×4 matrices should be defined. They are α_x, α_y, α_z and β, which satisfy the following relationship

$$\alpha_i^2 = 1 \quad \beta^2 = 1 \quad \alpha_i\alpha_j + \alpha_j\alpha_i = 0 \quad \alpha_i\beta + \beta\alpha_i = 0 \qquad \text{where } i, j = x, y, z \text{ and } i \neq j$$

Such that the Dirac equation for a free particle in 3 dimensions is

$$\left[i\hbar\frac{\partial}{\partial t} - \alpha_i\, c\, \hat{\mathbf{p}}_{(\vec{\mathbf{r}},t)} - \beta mc^2 \right] \Psi_{(\vec{\mathbf{r}},t)} = 0 \tag{1.16}$$

However, free particles are rare in physics. A particle is likely to be placed in electromagnetic vector potentials $\mathbf{A}_{(\vec{\mathbf{r}},t)}$ and scalar potential $A_{0(\vec{\mathbf{r}},t)}$. In analogy to Schrödinger equation (1.3) in subsection 1.1.2, a more generalised version takes the form

$$\left[i\hbar\frac{\partial}{\partial t} - c\left(\alpha_i\left(\hat{\mathbf{p}}_{(\vec{\mathbf{r}},t)} + e\mathbf{A}_{(\vec{\mathbf{r}},t)}\right)\right) - \beta mc^2 + eA_{0(\vec{\mathbf{r}},t)} \right] \Psi_{(\vec{\mathbf{r}},t)} = 0 \tag{1.17}$$

The charge carriers in graphene mimic Dirac fermions. Moreover, they are massless. The mass of electron at rest m_e is 1.6×10^{-9} kg. However, the effective mass of charge carriers is different in different materials according to their band structures. For example, the effective mass of electrons in GaAs is $m^* = 0.067m_e$. The unique band structure of monolayer graphene leads to zero effective mass of charge carriers. Starting with Plank-Einstein relationship,

$$E = \hbar w \tag{1.18}$$

Hence,

$$\partial w = \frac{1}{\hbar}\partial E$$

The group velocity is given by

$$v_g = \frac{\partial w}{\partial k} = \frac{1}{\hbar}\frac{\partial E}{\partial k} \tag{1.19}$$

The momentum is given by

$$p = m^* v_g$$

and

$$p = \hbar k$$

Therefore, the effective mass is

$$m^* = \frac{\hbar k}{v_g} \tag{1.20}$$

Summing equation (1.19) and (1.20),

$$m^* = \frac{\hbar^2 k}{\frac{\partial E}{\partial k}} \tag{1.21}$$

According to the band structure of graphene, at the charge neutrality point $k = 0$ while $\frac{\partial E}{\partial k} =$ constant. Hence, the effective mass of charge carriers in graphene

$$m^* = 0$$

In other words, charge carriers in graphene are able to travel ballistically. This leads to a mobility value which can be as high as 200,000 $cm^2V^{-1}s^{-1}$ [22–24]. Subsection 1.2.4 will discuss the advantages of graphene. With zero effective mass, the Dirac equation that governs electrons and holes within graphene is reduced to a much simpler form. Starting from the energy momentum relationship,

$$\begin{aligned} E^2 &= c^2p^2 + \cancel{m^2c^4} \\ E_{\vec{\mathbf{p}}} &= \pm v_f \, \vec{\mathbf{p}}_{(x,y)} \end{aligned} \tag{1.22}$$

where v_f is the fermi velocity of the electrons in graphene. It could be as low as $8.5 \times 10^5 m/s$ [55]. It could also reach as high as $3 \times 10^6 m/s$ in suspended graphene [56]. The Dirac equation gives a linear dispersion relation for fermions in graphene, which agrees with the results from the tight binding model at low wavenumber. Those massless quasiparticles cast great opportunities to explore relativistic effects such as Klein tunnelling without the use of a particle accelerator. Klein tunnelling in quantum electrodynamics, refers to the perfect transmission of electrons through large and wide potential barriers. A high enough barrier is either realised by using a heavy nucleus ($Z > 137$) or by producing ultrahigh electric field ($\sim 10^{16} V/cm^{-1}$) [57]. With graphene, an electric field of $10^5 V/cm^{-1}$ is sufficient to observe electron tunnelling [58].

Stacked schematics in Figure 1.14 shows how quasiparticles in graphene pass through a potential barrier of height V_0 and width D. The energy bands (green and red) associated with sublattices A and B intercept at the Dirac point. Shifts in Fermi level (dotted lines) is demonstrated across such a barrier - it lies in the conduction band outside the barrier and the valence band inside the barrier. The pseudo spin σ keeps a fixed direction along the spectrum, parallel (antiparallel) to the direction of wavevector $\mathbf{k}$. The transmission probability T is plotted in Figure 1.15 as a function of the electron incident angle [58]:

The barrier is always transparent to electrons with incident angles close to normal incidence $\phi = 0°$, which is unique to massless Dirac fermions and directly related to Klein tunnelling in quantum electrodynamics [58]. The perfect tunnelling is explained by the matching in pseudo spin σ directions before and after the barrier, as illustrated in Figure 1.14(a). Charge carriers in either red or green branch can only be scattered into states within the same branch. Scattering from one branch to the other is prohibited by the absence of the pseudo spin flip process. The process requires short-range potential acting differently on A and B sublattices, hence is very rare [58].

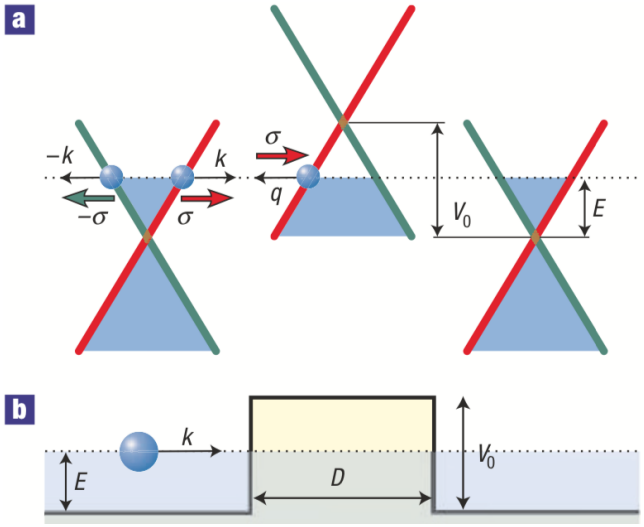

Fig. 1.14 (a) Linear energy spectrum of quasiparticles in graphene at low Fermi Energy ($E < 1eV$). (b) Potential barrier of height V_0 and width D. Shifts in Fermi level (dotted lines) is demonstrated across such a barrier. Figure sourced from [58]

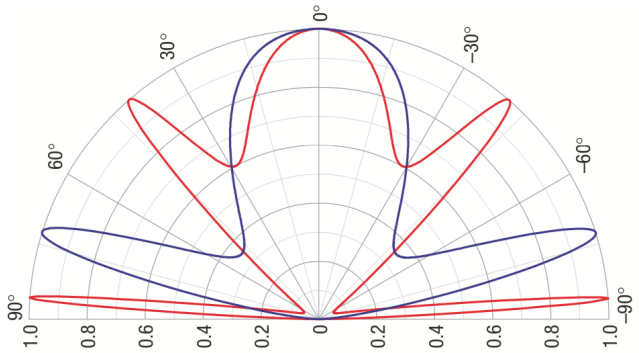

Fig. 1.15 Transmission probability T across a 100nm wide barrier as a function of the incident angle ϕ for graphene. Fermi energy of incident electrons $\approx 80\,meV$ and $\lambda \approx 50\,nm$; barrier heights $V_0 = 200\,meV$ (red curve) and $V_0 = 285\,meV$ (blue curve). Figure sourced from [58]

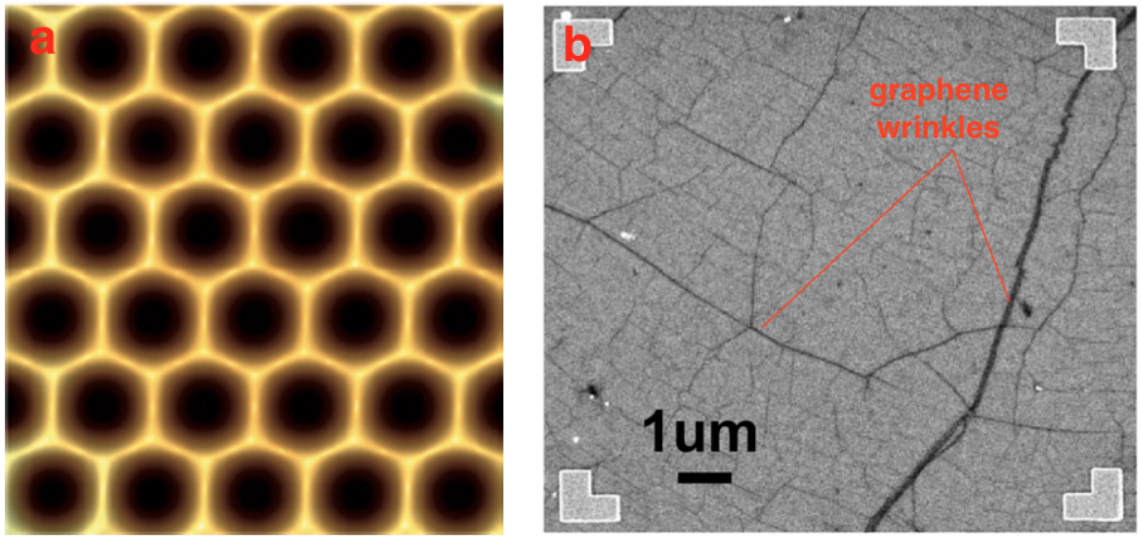

Fig. 1.16 (a) Graphene honeycomb lattice structure [3]. (b) SEM image of graphene on SiO_2/Si substrate [4].

1.2.4 Advantages of graphene

Monolayer graphene is continuous and demonstrates exceptional strength, with a tensile strength of $130GPa$ and Young's modulus Y measured at $\sim 1TPa$ [18]. The high lateral stiffness is contrasted with its low vertical stiffness. The small thickness $t \sim 0.34$nm makes graphene the softest possible material against transverse deflection [19]. The van der Waals force between graphene and the substrate is very weak. This is one of the reasons that cause wrinkles and conical cusps on graphene samples, as shown in 1.16(b). Subsequent fabrication processes of a graphene device usually involve wet transfer (see section 3.4) of the single layer graphene to a target substrate. Graphene will conform to any surface under the influence of attractive van der Waals forces. A Si/SiO_2 substrate with a $300nm$ or $100nm$ SiO_2 layer is standard for many experiments as the single layer graphene is distinguishable on these substrates by the optical microscope.

Thermal Conductivity Theoretical calculations have suggested in plane ultrahigh thermal conductivities [20, 21], due to the sp^2 bonding between carbon atoms. The room-temperature thermal conductivity of suspended graphene is in the range of 4840 - 5300 W/mK determined by confocal micro-Raman spectroscopy [59]. It surpasses carbon nanotubes and is among the most conductive materials known. With the size of electronic devices being decreased continuously, the power dissipation density in those circuits is increasing. Such evolution raises the importance of materials that can conduct heat efficiently. Being a potential thermal

management material, graphene's excellent heat conduction property provides extra motivation for proposed electronic applications, such as integration with nanoscale silicon CMOS technology as well as beyond-CMOS devices and circuits [59]. It also increases the range of graphene applications in optoelectronics, photonics and bioengineering. However others have demonstrated graphene's poor thermal coupling with substrates such as SiO_2 [60]. It is not only the contacts and interfaces which remain significant heat dissipation bottlenecks [61], but also graphene's edge perturbations that can tune the material's thermal conductivity. The latter phenomenon is largely amplified in graphene nanoribbons etched by electron beam lithography [62]. After all, it is graphene's 2D honeycomb lattice structure that gives it the extraordinary thermal properties

Electrical Conductivity and Mobility The 2D electrons in graphene can travel large distances (submicrometer) without being scattered [46]. It makes graphene a promising candidate for very fast electronic components and tiny interconnects (down to nanometer scale width) in electronic circuits. This property is so unique that no other material of atomic thickness is known to be even poorly metallic or continuous under ambient conditions [22]. It was possible to switch the conducting channel between 2D electron and hole gases by simply varying the gate voltage - making effectively a field effect transistor. Furthermore, it was found experimentally that graphene has extremely high charge carrier mobility. A mobility of 200,000 cm^2/Vs is achievable in suspended graphene at room temperature, given no extrinsic disorder [22–24] - higher than any known semiconductor. This is attributed to extremely low electron-phonon scattering rates from temperature dependence of electron transport. However, externally introduced disorders will modify the atomic bonding between carbon atoms and cause re-hybridisation of σ and π orbitals. Furthermore, defects are scattering centres that change electron trajectories [63, 64]. In total, it will disrupt the isotropic and linear dispersion relationship near Dirac points in the vicinity of those disorders[65], leading to an overall drop in mobility.

Transparency and Flexibility Currently, graphene is visible on very few substrates. Oxidised silicon with typically 300 nm SiO_2 was found in 2007 to be one of those few substrates [25, 66], and is commonly used since then. The transparency of graphene casts some difficulties for researches, on the other hand is beneficial for applications. Transparent electrodes for displays and solar cells are two huge implications for the industry. There is a prospect of replacing the ITO (Indium Tin Oxide) film with low-cost graphene based coating. This can remove the uncertainty about indium's availability and cost. Graphene also displays high level flexibility and possesses a large surface to volume ratio. Adding these two advantages

with the aforementioned ones, graphene is a promising candidate for flexible electronics and gas/bio sensors for diagnostics.

1.3 The state of the art - ways to open a band gap in graphene

This section reviews several methods from the literature that have been proved to create an energy gap in graphene at the Dirac point. With exceptional electrical properties, industry has a high expectation on graphene-based devices. However, an inevitable issue with them is the poor I_{on}/I_{off} ratios. The conductance of bulk graphene monolayer is finite at low temperature even for zero carrier density [47, 50]. In other words, it is impossible to turn off such a device because thermal energy and fluctuations can produce enough charge carriers. This considerable "leakage" current causes poor on/off ratios that are typically 1 or 2 [67], not even near the performance of a logic device whose on/off ratio is typically at least 10^6. This is undesirable for electronic devices such as transistors, which require a zero-conductance state. Further development is ultimately prohibited by the material's lack of an appreciable bandgap. Researchers have explored various ways to open a bandgap for graphene, in order to implement the material in electronic devices. It has been well understood from theory and simulations that bilayer graphene has a parabolic instead of linear band structure. It is proved that an electric field can induce a bandgap in bilayer graphene and the gap size is dependent on the electric field magnitude [68]. Regarding a graphene monolayer, a bandgap can be introduced if the symmetry between the layers are broken [69, 70]. This section focuses on research efforts from the literature on opening an energy gap for monolayer graphene, which are divided into three categories: lateral confinement (subsection 1.3.1), periodic modulation of the graphene lattice (subsection 1.3.2), and introduction of strain profiles (subsection 1.3.3).

1.3.1 Lateral confinement - nanoribbons

Nano-lithography has motivated a great deal of research into graphene nanoribbons (GNRs). Graphene monolayers are etched along one specific direction to produce patterned graphene strips, with nanometers in width. Due to quantum confinement, GNRs are no longer semi-metallic [71]. They possess various remarkable properties and are potential candidates for future carbon-based nanoelectronics [72–76]. It was predicted that GNR widths need to be $2 \sim 3\,nm$ in order to produce a band gap similar to that of Ge ($0.67\,eV$) or InN ($0.7\,eV$). While for a bandgap similar to Si ($1.14\,eV$), InP ($1.27\,eV$) or GaAs ($1.43\,eV$), the width has to be further reduced to $1 \sim 2\,nm$. Any GNR wider than $8\,nm$ presents a maximum band gap of $0.3\,eV$ [77]. Graphene's two different edge shapes i.e. armchair and zigzag (shown in Figure 1.17), both produce quasiparticle band gaps in the range of $0.5 \sim 3.0\,eV$ for ribbon width $0.4 \sim 2.4\,nm$ [78]. Some researchers later stated that only armchair edges are predicted to open a band gap [79, 80].

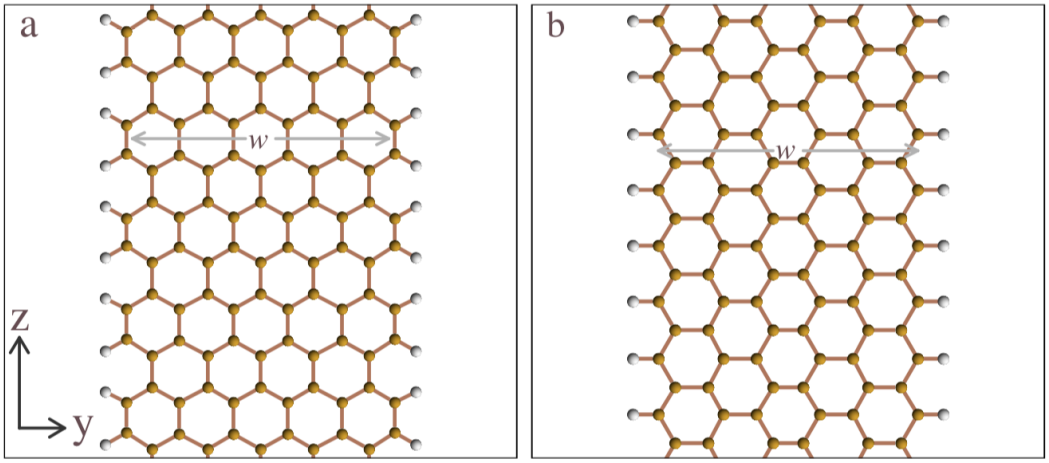

Fig. 1.17 Graphene's two edge shapes (a) Armchair (b) Zigzag. Figure sourced from [78]

Chen *et al.* in IBM T.J. Watson Research Center and Kim's group in Columbia University first demonstrates this concept successfully in parallel. They both use e-beam lithography with negative resist, and oxygen plasma etching to make GNRs less than 50 nm from mechanically exfoliated bulk graphene [81, 26, 82]. As channels of field effect transistors, Chen infers that the narrowest 20 nm ribbons led to a confinement-induced band gap of the order of 30 meV. It is also found that both edge scattering and trapped charges in the substrate greatly affect the transport properties and minimum conductivity of the GNRs [81]. Regarding results from Kim's group, a band gap as high as 200 meV is achieved by etching GNRs to $\sim 15\,nm$. They also agree that detailed edge structure account more than the overall crystallographic direction for determining the properties of the GNRs [26, 82]. Figure 1.18 shows their experiments with different widths of GNRs.

Encouraged by previous predictions on wider band gaps from sub-10 nm GNRs, more researchers are growing GNRs using a different approach to go beyond the lithographic limit. Dai's group first develops a chemical route to derive GNRs directly from bulk graphite. The solution-phase-derived ribbons have smooth, well-defined edges, and can be below 10 nm. From room-temperature electrical transport experiments, all sub-10 nm GNRs can be made into graphene FETs with on-off ratios of about 10^7 [83]. Hicks *et al.* takes advantage of the atomically ordered interactions between graphene and the SiC substrate to grow GNRs on patterned SiC steps. Graphene was forced to bend and ribbons of hundreds of micrometers long are topographically defined by using pre-patterned SiC trenches. This scalable bottom-up method allowed them to produce graphene ribbons with a precisely defined width within a few graphene lattice constants ($\sim 1.4\,nm$), which feature a gap energy of $> 0.5\,eV$ [84]. Later research even revealed a band gap of 1 eV in free standing nano ribbons between pinned

regions on the terraces[85]. GNRs are connected to metallic graphene sheets seamlessly on both of its sides, which also suggests new electronic device architecture.

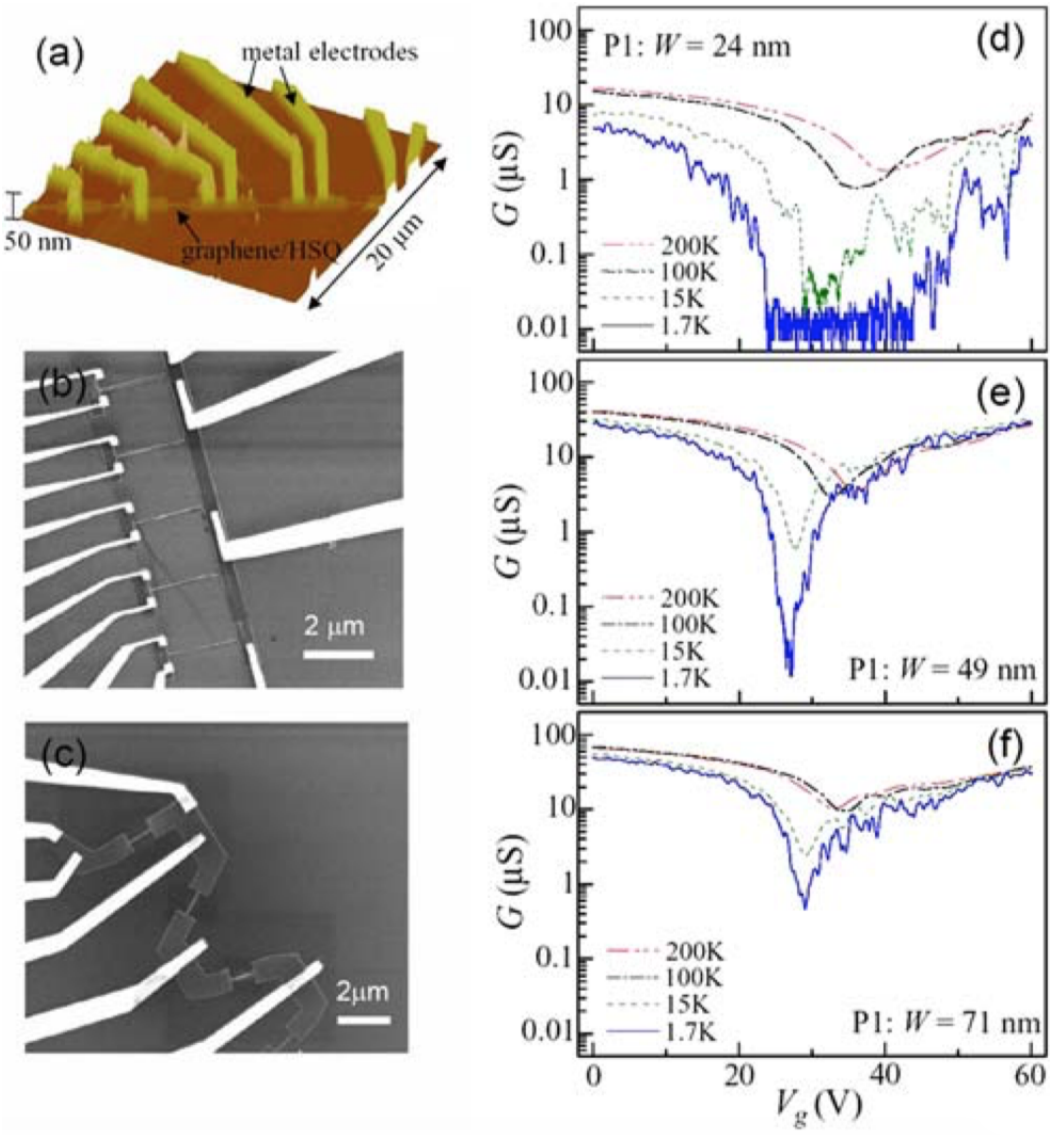

Fig. 1.18 (a) AFM images of GNRs in set P3. (b) SEM image of GNRs of varying widths in set P1. (c) SEM image of GNRs of uniform width in different relative crystallographic directions in set D2. (e)-(f) Conductance of GNRs (set P1, width 24 *nm*, 49 *nm*, 71 *nm*) as a function of gate voltage at different temperatures. Figure sourced from [26]

1.3.2 Periodic modulations of the graphene lattice

Subsection 1.1.3 discusses that electrons in a periodic crystal lattice develops a band structure that is determined by atomic bonding, symmetry and potential magnitude associated with

lattice points. Applying external electrostatic fields and imposing artificial periodic potentials can go beyond the constraints of naturally occurring atomic crystals and further modify the intrinsic material's band structure [86–89].

It is predicted that a bandgap of graphene can be induced and tuned by periodic modulations of the graphene lattice [90–92]. Balog *et al.* patterned atomic hydrogen adsorbates onto the Moiré superlattice positions of graphene grown on Ir (111) substrate. A Moiré superlattice forms from the small difference between the lattice constants of the two crystals. Their idea was rationalised by density functional theory (DFT) calculations that hydrogenation of graphene results in a bandgap opening, the most extreme case being the wide band gap semiconductor graphane [93]. Half-hydrogenated graphene carries a band gap of $430\,meV$ [94]. It was believed that a regular pattern of hydrogen-covered regions results in a confinement of potential for charge carriers in the pristine graphene regions [95]. In a limiting case, the very confinement leads to an increased uncertainty in electron momentum. The formation of such a superlattice structure of graphene-like islands induced a room-temperature bandgap in the material which can be as large as $450\,meV$ [95]. The STM (scanning tunnelling microscopy) and ARPES (angle-resolved photoemission spectroscopy) results constitute experimental support for a band gap from periodic lattice modulations. This concept is potentially applicable to fabricating graphene electronics as the band gap is produced at the Dirac point and is of sufficient size.

A new approach integrates dielectric substrate patterning with graphene and strongly alters graphene's band structure while preserving its high mobility. The patterned dielectric superlattice shown in Figure 1.19 (periodicity as low as $35\,nm$) - van der Waals heterostructure was observed to develop fractal mini-gaps of the Hofstadter spectrum [96]. The results demonstrated a non-Moiré patterned superlattice as the new platform for synthetic band structure engineering.

Periodic perturbations in the lattice structure is explored by other researchers. One example is substrate-induced gaps for graphene supported on SiC, though their existence is being heavily debated [97], and ferroelectric $Pca21$ HfO_2 substrate [98]. Zhou *et al.* (2007) found that a bandgap of approximately 0.26 eV is present when the graphene is grown epitaxially on SiC substrate. The gap size decreases as the graphene grows thicker, and approaches zero when the graphene thickness exceeds four layers [99]. They attributed this opening of bandgap to the graphene-substrate interaction that breaks the inversion symmetry. Self-assembled supramolecular lattice was also deployed to make van der Waals heterostructures to modulate graphene's band structure and electronic properties [100].

A recent article published in March 2017 shows the size of SiC substrate-induced bandgap to be more than 0.5 eV [101], referred to as a "buffer" layer method. They anneal SiC(0001)

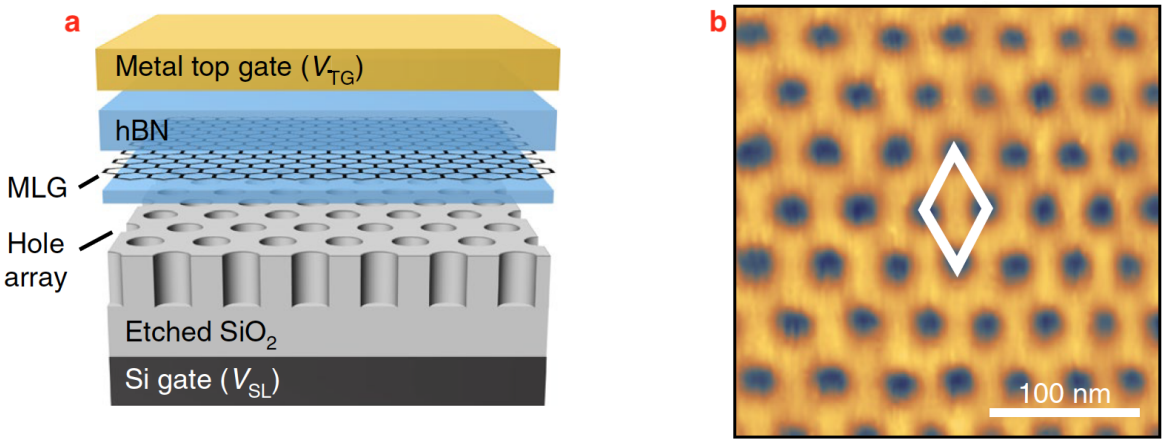

Fig. 1.19 (a) Schematic of a final device: highly doped Si wafer - periodic array of SiO_2 holes - hBN-encapsulated monolayer graphene - hall bar and metal contacts. (b) Variation of the DOS imaged directly through an STM measurement of tunnelling current, dI/dV, of a device with exposed graphene under $V_{superlattice}$= - 25 V. Figure sourced from [96]

below the optimal temperature to grow graphene by atomic layers. This buffer layer is shown to be semiconducting with different electronic properties from normal graphene. Further annealing produces another graphene layer below the existing buffer layer. So the existing buffer layer converts to a conducting graphene layer with a new buffer layer below it in contact with the SiC substrate. They find that the buffer layer is not completely pinned to the substrate, by STM characterisation. It is only pinned at some precise locations and in between those pinning regions, the buffer layer and the substrate is separated by 1.5 nm. Nonetheless, the whole buffer layer system exhibits a bandgap, as well as those decoupled regions. They attributes the opening of bandgap in the π band to a nanoscale super-periodicity [101].

1.3.3 The introduction of strain profiles

Another early focus to open a bandgap is by introducing strain profile into the structure. Simulation results shows that strain distributions strikingly modified the graphene band structure near the Fermi level [27]. They deploy density functional theory (DFT) and find that graphene with symmetrical strain distribution conserves its zero bandgap property. While asymmetrical strain distribution results in the appearance of bandgap near Fermi level. Results show a maximum bandgap of 486 meV as the strain increases up to 12.2% parallel to the C-C bonds direction. The bandgap only increases to 170 meV as the strain increases to 7.3% if the strain direction is perpendicular to C-C bonds [27].

As heterostructure rises to be a new paradigm in materials design, another atomically thin van der Waals crystal boron nitride (BN) is used to encapsulate graphene. It is demonstrated

that applying hydrostatic pressure to BN-encapsulated graphene can decrease their interlayer spacing by more than 5% [102]. Small rotation angle between the layers raise substantially the effectiveness of the moiré superlattice and modifies the electronic characteristics. Furthermore, a linear increase in the induced band gap was observed at increasing strain profile. Atomic scale lattice deformations cause both out-of-plane and in-plane corrugations and break the sublattice symmetry of graphene, resulting in finite effective mass term in the Dirac Hamiltonian which opens a sizeable band gap as large as $250\,meV$ [102].

1.4 Graphene band structure modification by periodic potential perturbation

Section 1.4 will discuss the theoretical predictions that support this work. The charge carriers in single layer graphene are chiral, relativistic, and massless particles. The Fermi velocity within the crystal lattice is v_F = c /300 $\approx$ 10^6m/s. The energy dispersion near the Dirac point (K or K') follows a linear relationship to wavevector. The absence of an energy gap at the Dirac point and the chiral nature of the electronic states in graphene is the fundamental reason for some unusual behaviours such as Klein tunnelling, i.e. perfect transmission of electrons through a potential barrier, upon normal incidence to the barrier. This means that the modification of the graphene band structure from periodic potentials is not as simple as in the Kronig-Penney model. The general Kronig-Penney model has been discussed in section 1.1 and the specific case applied to massless Dirac fermions in subsection 1.1.4. Barbier *et al* studied the effect on graphene band structure from a single 1D square barrier. It is found that the transmission T of massless fermions through a square barrier depends on both components of the wavevector, k_x and k_y. Considering a 1D electrostatic superlattice that is constructed by 1D periodic square barriers, their computation illustrates the emergence of minibands, where the energy gap between neighbouring minibands is again affected by both k_x and k_y.

This section will demonstrate theoretical predictions of graphene band structure modification resulting from electrical periodic potentials. Louie's group considered the situation where additional periodic potentials is applied to graphene, which results in anisotropic behaviours of massless Dirac fermions. Chirality, or pseudo spin that is to do with electron orbital wavefunction staying in different trigonal sublattices of honeycomb lattice, lies at the root of all the following properties [17].

If the spatial period of graphene superlattice is much larger than the nearest-neighbour carbon-carbon distance $\sim$1.42Å, the scattering of a state near one Dirac point (K) to the other Dirac point (K') does not occur. K and K' are inequivalent in the crystal lattice, hence two inequivalent Dirac cones exist for the energy dispersion surface of graphene. Considering only one Dirac cone is sufficient in the analysis [17]. Furthermore, the condition also implies that there is no energy gap opening at the Dirac point [103–105], unlike those methods discussed in section 1.3. To investigate charge carrier behaviours in a 1D electrostatic graphene superlattice (Figure 1.20b), they calculated the group velocities, energy dispersions, and energy gap openings at the minizone boundary (MB) through effective Hamiltonian formalism proposed by P.R.Wallace [43].

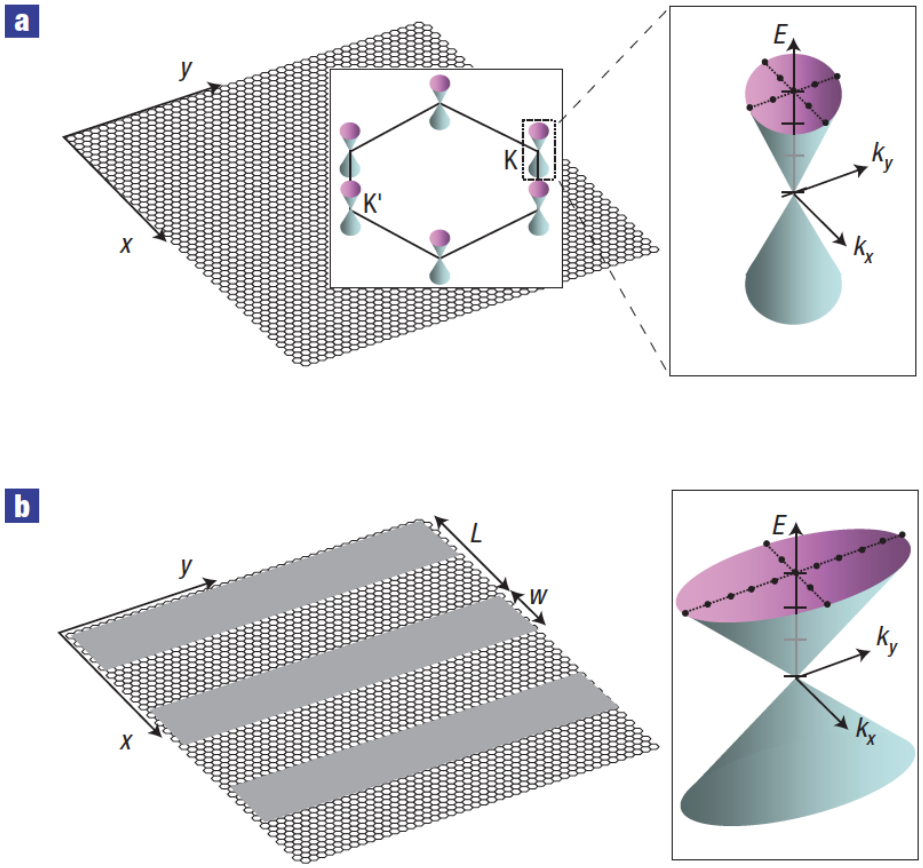

Fig. 1.20 Graphene superlattices and anisotropic Dirac cones. a, Schematic diagram of pristine graphene. Inset: The Brillouin zone of graphene and Dirac cones centred at Dirac points K and K' (left), and the linear energy dispersion near one Dirac point of charge carriers in graphene (right). b, 1D graphene superlattice formed by a Kronig–Penney type of periodic potential along the $\hat{x}$ direction (period L and barrier width w). The potential is U_{1D} in the grey regions and zero outside. Inset: Energy dispersion of graphene charge carriers in 1D superlattice. Figure sourced from [17]

Figure 1.20 shows Dirac cones for pristine graphene and that affected by 1D graphene superlattice. In Figure 1.20b, the periodic potential array has a spatial period L, barrier width w and potential U_{1D}. The energy spectrum along any line in the wavevector $\vec{k}$ space with respect to the Dirac point is linear, yet with different group velocities parallel and normal to the barriers. The periodic potential is in the x-direction in the figure, the group velocity $v_{\parallel}$ for a carrier moving in this direction is not renormalised. While for a particle moving in y direction, which is perpendicular to the periodic potential propagation, the group velocity $v_{\perp}$ is reduced the most. According to Louie group's model, when an external periodic potential is applied to graphene, the group velocity of energy states is renormalised (to v_k).

The renormalisation effect is anisotropic, strongly dependent on the direction of **k**, length parameters L and w, and potential U_{1D}.
Figure 1.21 demonstrates the anisotropic velocity renormalisation in 1D graphene superlattice. It illustrates the dependence between the renormalised group velocity and the polar angle θ_k which is the polar angle between **k** and the direction of periodic potential $\hat{x}$. Under the condition $U_{1D} = 0.5eV$, L = 10nm, w = 5nm, the group velocity v_k can be reduced to less than 40% of the original value v_0 along directions θ_k = 90° and 270° i.e., when wavevector **k** is perpendicular to the periodic potential direction. It retains v_0 along directions θ_k = 0°, 180° and 360° i.e., when **k** is parallel to the periodic potential direction (Klein tunnelling).

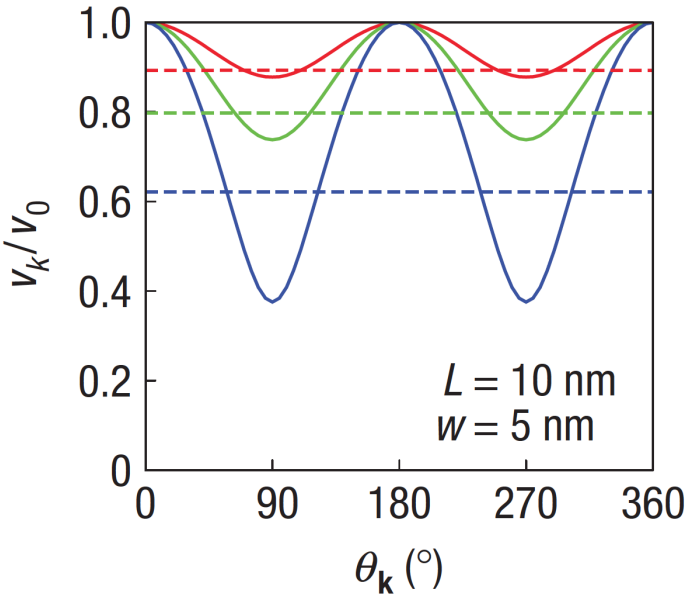

Fig. 1.21 Solid line - the component of charge carrier group velocity parallel to the direction of wavevector **k**, v_k in units of Fermi velocity in graphene v_0 versus θ_k, the polar angle between **k** and the direction of periodic potential $\hat{x}$. Dashed line - same variables for non-chiral fermions in a superlattice with identical properties to those in graphene. Red, green and blue lines refer to U_{1D} = 0.2eV, 0.3eV, 0.5eV respectively. Figure sourced from [17]

Note that the results here are counter-intuitive, as the group velocity of charge carriers in graphene is not modulated while it is crossing the hurdles, but is hugely reduced when it is moving parallel to them. The absence of renormalisation to velocity parallel to the 1D periodic potential comes from the chiral nature of the charge carriers in graphene. The resulting anisotropic behaviours apply to the cases of a single potential barrier and a finite number of barriers [17]. The anisotropy in energy dispersion of 1D graphene superlattice provides an idea to realise graphene nanoribbons in a non-destructive way.

The energy dispersion spectrum of 1D graphene superlattice is worked out. Miniband emergence is learnt as well as energy gap openings at the minizone boundaries (MB), shown in Figure 1.22a. It should be noted that the gap openings happen at the minizone boundaries (certain k points), instead of the original Dirac points. A conventional 1D superlattice results in a gap opening at the MB that is constant and independent of the direction of **k**. The situation for a 1D graphene superlattice is complicated, in that the energy gap disappears when **k** is parallel to the direction of periodic potential ($k_y = 0$), and the size of energy gap depends on the direction of wavevector **k**. The strong anisotropic behaviours do not happen for a non-chiral fermion superlattice system with otherwise identical properties such as linear energy dispersion, shown in Figure 1.22b (dashed lines). Therefore, it is the chirality (or pseudo spin) in graphene that generates such anisotropy in energy gap openings.

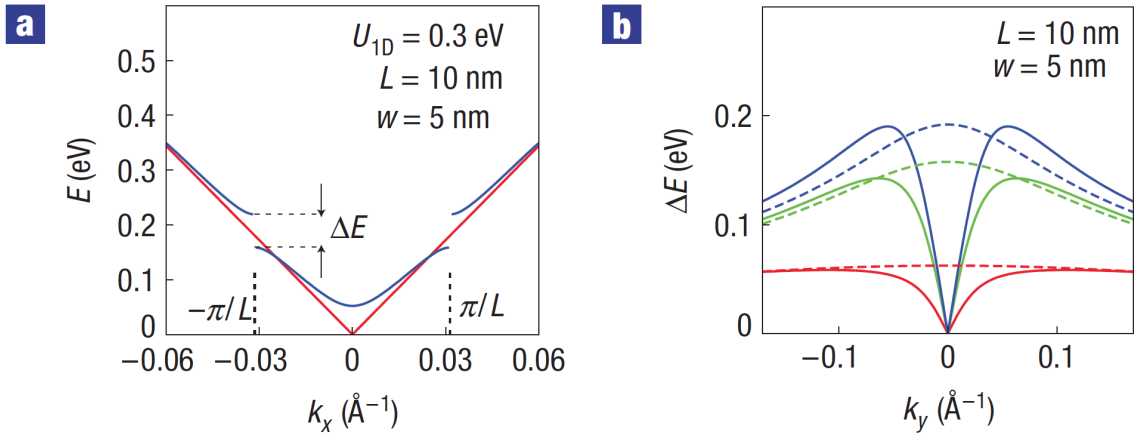

Fig. 1.22 Energy gap at the superlattice Brillouin zone or minizone boundary (MB) of a 1D graphene superlattice. a, U_{1D} = 0.3eV, L = 10nm and w = 5nm. Energy of charge carriers in a 1D graphene superlattice versus the component of the wavevector k_x at a fixed k_y. Dashed vertical lines indicate minizone boundaries ($k_x = \pm\frac{\pi}{L}$). ΔE is the energy gap at the minizone boundary for a given k_y. Red and blue lines correspond to k_y being zero and 0.012 Å^{-1}, respectively. b, ΔE versus k_y for charge carriers in graphene (solid lines) and that of non-chiral fermions in a superlattice with identical properties to those in graphene (dashed lines). Red, green and blue lines refer to U_{1D} = 0.1eV, 0.3eV, 0.5eV respectively. Figure sourced from [17]

From the above simulations, Park *et al.* [17] are able to plot the 3-dimensional energy dispersion of charge carriers in a 1D graphene superlattice in Figure 1.23. The first (red and black) and second (blue and pink) minibands of the Dirac cone above vertex are shown. The components of **k**, k_x and k_y are taken with respect to the Dirac point. The first minizone boundary (MB) is at $k_x = \pm 0.031$Å^{-1}. Arrows represents the points where the energy gap disappear, at $k_y = 0$. This model clearly demonstrates the dependence of energy gap openings

(at the minizone boundary) on both components of wavevector **k**, and will be revisited in Chapter 4.

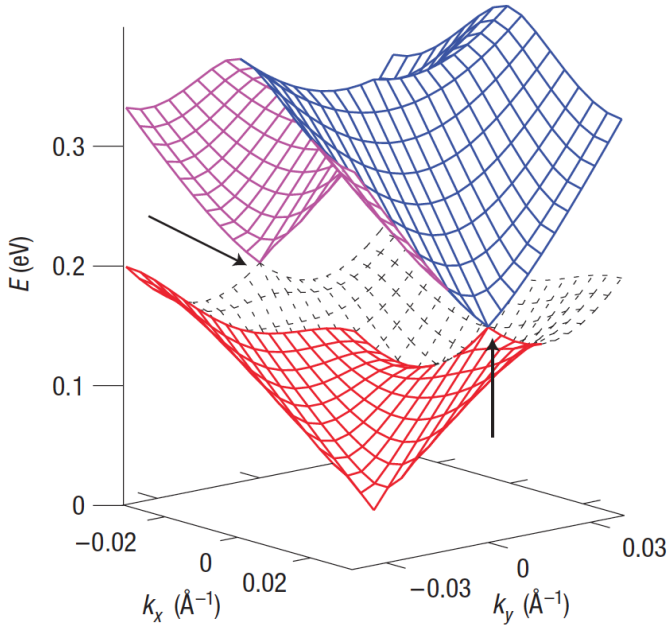

Fig. 1.23 Energy dispersion of charge carriers in 1D graphene superlattice. U_{1D} = 0.3eV, L = 10nm, w = 5nm. The first (red and black) and second (blue and pink) minibands of the Dirac cone above vertex are shown. The components of **k**, k_x and k_y are taken with respect to the Dirac point. Figure sourced from [17]

Other systematic studies [106, 5] also revealed that the electron transmission through a 1D electrostatic graphene superlattice (EGSL) can be modulated readily by changing the superlattice parameters: well and barrier widths, incident energy, angle of the electron wavevector, as well as the number of periods of EGLs. The modulation reflects in the conductance, appearing as conductance peaks as shown in Figure 1.24 (a)(c)(e) where the peaks are highlighted in grey. The amplitude of those oscillations are more pronounced as the number of barriers NB increases.

To explain the origin of conductance oscillations in 1D EGSLs and its relation to the confined states, the electronic band structure of graphene is computed. Figure 1.24 (b)(d)(f) shows the miniband structure formation on bound states caused by the 1D electrostatic graphene superlattice. Allowed values of energy are plotted versus the transverse wave vector k_y. Red arrows indicate the onset and end of the miniband, while blue arrows point to the degeneration (narrowing) of miniband. The narrowing of energy minibands are unique to electrons in graphene, annotated by blue arrows. The opening and degeneration of energy minibands is directly connected to the location of the peaks in the conductance. The onset and end of the

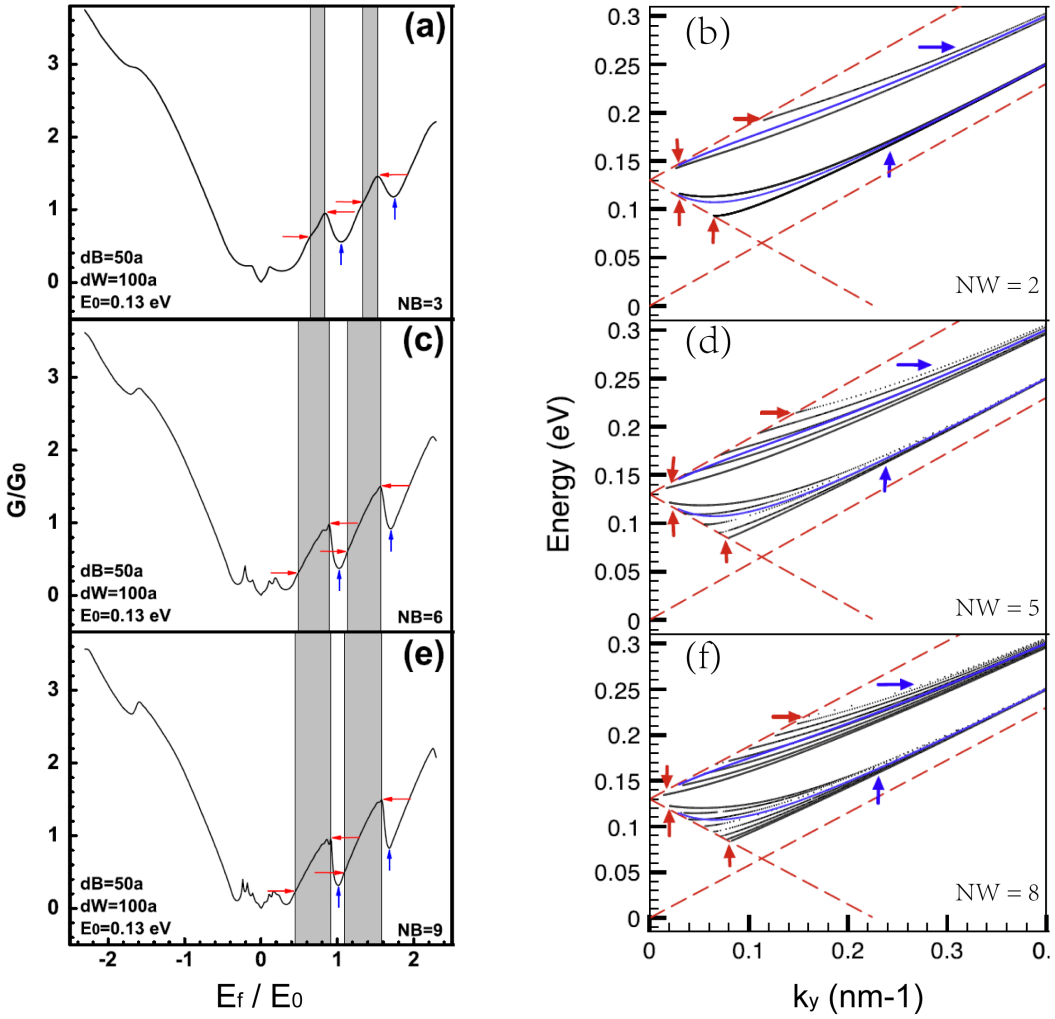

Fig. 1.24 Left column (a)(c)(e): Conductance in EGSLs for different number of barriers versus the Fermi energy E_F. Superlattice parameters: barrier width dB = 50a and well width dB = 100a, barrier height E_0 = 0.13eV. a $\approx$ 1.42Å, is the carbon-carbon distance in graphene. The shaded stripes and red arrows highlight the regions of start and end of the energy minibands, while the blue arrows represent the degeneration (narrowing) of the minibands. The Fermi energy is normalized to the height of the barriers E_0, while the conductance is given in terms of G_0. The number of barriers NB = 3, 6, 9 in (a), (c), (e) respectively.
Right column (b)(d)(f): Spectrum of confined states in EGSLs for different number of wells (NW) versus the wavevector component k_y. The height E_0 and width of barriers dB and wells dW are the same as in the left column. The red arrows state the onset and end of the miniband, while the blue ones mark the degeneration (narrowing) of them. The number of wells NW = 2, 5, 8 for (b)(d)(f) respectively. Figure sourced from [5]

minibands (red arrows) refer to the starting and falling edges of the conductance oscillating regions highlighted in grey. Hence, the oscillatory behaviour in conductance is directly related to the opening of energy minibands, which is a result of the multi-barrier structure constructed by the electrostatic graphene superlattice. In the superlattice for Schrödinger's electrons, barriers split the parabolic energy band to form minibands. This is also the case for Dirac fermions in graphene, the difference is that the original energy band is linear instead of parabolic. The miniband structure shows the spectrum of allowed values of energy. The number of bound states should increase as the number of barriers increases due to the interference of states between wells. It can be seen from Figure 1.24 that the number of created minibands (indicated by black lines) goes up as the number of wells (NW) increases in the superlattice parameter.

1.5 Summary

In this chapter, section 1.1 introduces the basic band structure knowledge of Schrödinger's electrons as well as the chiral and massless Dirac fermions in graphene. The chemical bonding in graphene crystal lattice was discussed in section 1.2, along with the resulting unusual properties such as zero mass of charge carriers and chirality, which then leads to multiple advantages of graphene as an engineering material. Section 1.3 reviews several methods from the literature that have been proved to create an energy gap in graphene at the Dirac point. The periodic potential method detailed in this work was not reported experimentally in the literature before, in order to modify the band structure of graphene and create minibands not at the Dirac point. Section 1.4 presents theoretical predictions on the modification of graphene band structure from 1D periodic potential perturbations, which supports this work and provides a starting point to further analysis detailed later in this thesis.

1.6 Previews for subsequent chapters

The following three chapters will demonstrate how the theories outlined in section 1.4 are realised experimentally, using a PZT-graphene integrated device. Figure 1.25 shows the 3-dimensional model for a PZT-graphene integrated device in this work. In this design, the PZT single crystal grown on $SrTiO_3$ provides a reasonably flat surface, such that the graphene monolayer can conform to the surface where a periodic potential (indicated by orange and green cuboids) is patterned. Electrons in the graphene monolayer therefore experience the perturbation caused by the periodic potential beneath, and this forms the aforementioned 1D

electrostatic graphene superlattice (1D-EGSL). The addition of two electrodes (drain and source) represents connection points to the 1D-EGSL for electrical measurements.

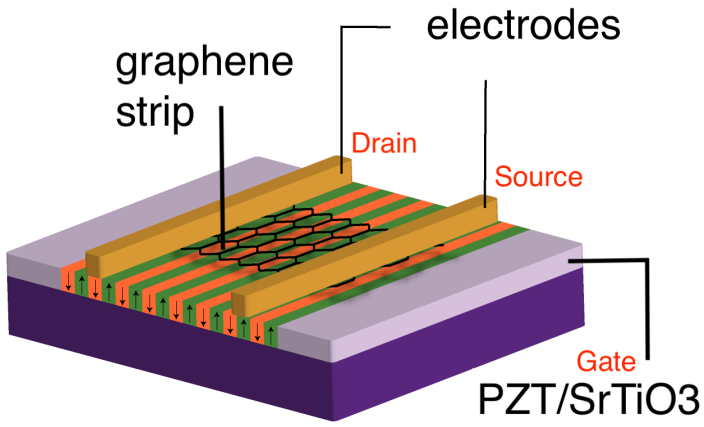

Fig. 1.25 The 3-dimensional model for a PZT-graphene integrated device in this project.

PZT, as a ferroelectric material, is utilised in this work to produce 1D periodic potentials. Chapter 2 will discuss the basics of this material, as well as the steps taken to create and optimise 1D periodic potentials in PZT. It is patterned by Piezoresponse Force Microscopy (PFM) to make periodic domains with opposite polarisation directions. Domains with opposite polarisation directions, when measured by Kelvin Probe (KPFM), exhibits surface potentials of opposite signs.

Chapter 3 reports the PZT-graphene integrated device fabrication process. Above PZT is the single layer graphene, which is wet transferred to the PZT substrate then etched into individual strips for batch device making. Electrodes and pads are manufactured above the single layer graphene. Integrating PZT and single layer graphene in one device is an intricate process, along which a few challenges were overcome.

Chapter 4 will reveal the electrical measurement results from the PZT-graphene integrated device, as well as some difficulties in measurements which further worsen the device yield rate. The theoretically predicted locations of minizone boundary (MB) were computed, as well as the size of energy gap at each MB for specific parameters in this work. Section 4.5 matches those predictions with the measured data.

The band structure of a crystal lattice originates from the interactions of electrons with potentials. To realise an electrostatic graphene superlattice using a graphene-PZT integrated device, the size of the device has to be decided first. Since graphene nano-ribbons fabricated using the same processes possess a mean free path as large as 220nm at room temperature [107], we expect that at low temperature e.g. 10K, it will be larger. Therefore the distance

from one electrode to another is kept between 300∼400nm for all fabricated devices, below the expected mean free path of graphene under low temperature. This ensures that electrons travelling from one electrode to another are transmitting coherently. They travel with the same phase throughout the journey they see the periodic potentials. The periodic potentials underneath is the only factor that will affect their behaviour throughout the journey from one electrode to the other. Thus, it is only the created electrostatic superlattice that accounts for any change in electron transmission in the device. The second factor that shall be taken into account is the theoretical minimum ferroelectric domain size, which is 20nm∼40nm [11]. The coherence requirements together with the ferroelectric material limit, determined that there are only a few barriers/wells in such PZT-graphene devices.

Chapter 2

Domain Engineering

This chapter will focus on the application of ferroelectric domain engineering to Lead Zirconate Titanate. Ferroelectric domains and domain switching will be introduced in section 2.1. The concept of polarisation and therefore hysteresis are discussed. The reading and writing of ferroelectric domains via Piezoresponse Force Microscopy (PFM) will be discussed in section 2.2. This section includes some basics regarding the Atomic Force Microscopy (AFM) of which PFM operates under the contact mode. The amplitude and phase of a PFM signal is analysed in this section, which contains information regarding the corresponding polarisation that leads to the signal. Section 2.3 talks about the energy dynamics in the engineered ferroelectric domains, its relationship to the applied electric field and the critical domain size.

In this work, the PZT surface is poled (by PFM) to form periodic domains of opposite directions of polarisation. The steps taken to create and optimise 2D periodic domains and 1D periodic domains are demonstrated in section 2.4 and 2.5 respectively. The goal of those two sections is to reduce the distance between points (2D) and strips (1D), by experimenting with different lithography conditions. Section 2.6 tackles the potential decay problem in this work, using the Kelvin Probe Force Microscopy (KPFM). The bound charges induced in artificial domains display a periodic surface potential profile, which is measurable under KPFM. The whole domain engineering step is carried out under ambient conditions, thus water molecules landing on the surface give rise to hydrolysis. This flattens the surface potential profile and reduces the difference between the high and low potential values. The resulting time decay of surface potential will be discussed in this section.

2.1 Ferroelectric materials

Lead Zirconate Titanate, stoichiometrically $PbZr_xTi_{1-x}O_3$ is a multiferroic material. It displays ferroelectric, ferroelastic and pyroelectric properties. It is the ferroelectric nature of the material that is of interest here. This section will discuss the concept of polarisation, as an electrical coupling phenomenon. The corresponding characteristic unit - domain and domain switching behaviour are also introduced and will be discussed in section 2.3.
All crystals can be classified into one of 32 different classes, according to several symmetry elements, e.g. center of symmetry and axis of rotation. Those 32 point groups are a subdivision of the seven basic crystal systems that are classified according to the symmetry of the crystal unit cell. In Figure 2.1, 11 groups are centrosymmetric. That is to say a uniform stress field will result in a uniformly distributed pattern of displaced charge movement. The remaining 21 groups are non-centrosymmetric crystals i.e., the original structure and the inverted one are not identical [108]. This is necessary for piezoelectricity to exist. Those 21 groups are called dielectric materials. Dielectrics are electrical insulators which have a wide band gap. Free movement of electrical charges across the lattice is prohibited by the band gap. Out of the 21 non-centrosymmetric dielectrics, 20 groups are piezoelectrics. Direct piezoelectric effect was discovered in the 19th century when scientists found that an applied stress induces electric field within some materials [109].
Some piezoelectrics have a single polar axis and are called pyroelectric. They develop spontaneous polarisation which remains as permanent dipoles in the crystal structure, within a given temperature range. The polarisation changes with temperature, and this response is known as pyroelectricity. Some pyroelectric materials are ferroelectrics. The criterion for a material to qualify as ferroelectric is (i) the presence of spontaneous polarisation and (ii) that being reversible by an externally applied electric field [110, 111]. The ferroelectric effect was discovered in 1920 by Valasek when he was studying Rochelle salt [112, 113]. Ferroelectric materials are often used for their piezoelectric properties, the high electromechanical coupling and electrostriction they exhibit [114]. The additional functionality of reversible polarisation is mostly exploited in memory storage device.
Regarding the origin of ferroelectricity, assume a unit cell within a single crystal of homogenous polarisation distribution, under no external stress. Figure 2.2 shows the perovskite unit cell of $PbTiO_3$. If the temperature is above the Curie temperature ($T > T_c$), the crystal is in the cubic form with Ti ion in the center of the unit cell. When $T < T_c$ the crystal undergoes a phase transition, from cubic to tetragonal. The free energy G demonstrates the stability of the displacement of the central Ti ion in the crystal structure [7]. In the tetragonal phase, the Ti ion can only be at one of the two off-center positions (stable displacements) along the

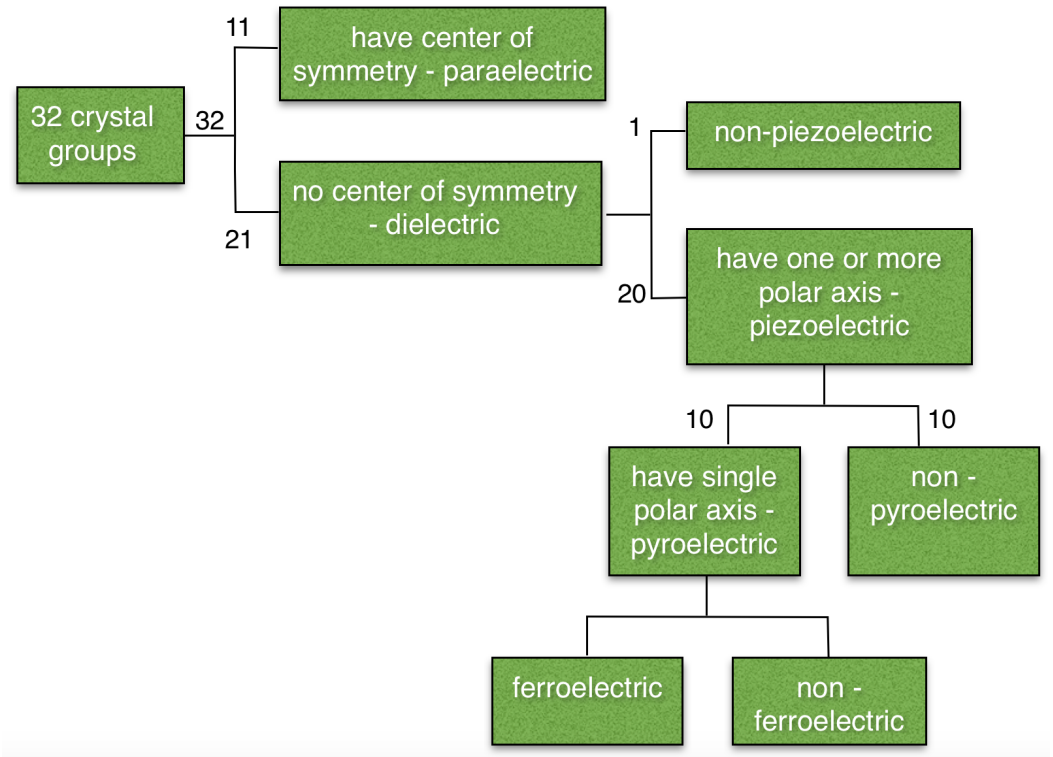

Fig. 2.1 Crystal classification of 32 crystal groups

x_3 axis. Those two locations correspond to the two minima points on the free energy curve versus Ti displacement in (c). This results in hysteresis behaviours in Figure 2.3.
Figure 2.3(a) shows the curve of free energy G versus polarisation P, the two energetically favourable points are at $\pm P_r$ which are called remnant (spontaneous) polarisation. Spontaneous polarisation in ferroelectric materials arises from the primitive asymmetric alignment of negative and positive charges. Figure 2.3(b) demonstrates ferroelectric domains with distinguishable polarisation. Neighbouring dipoles align to the same direction in order to reduce free energy, whereas a less ordered state is preferred by the thermodynamic entropy [115]. These two competing factors cause neighbouring unit cells to align dipoles to the same orientation. Distinguishable regions of different polarisations are called ferroelectric domains. They are separated by domain walls. For a (001) PZT film the polarisation direction is out of plane and points either up or down.
When an electric field is applied dielectric materials respond by slightly shifting the positive and negative charges in opposite directions i.e., changing local polarisations. Each action results in an individual dipole moment $\vec{p}$ [109]. The polarisation in a local area $\vec{P}$ is hence equal to the sum of those individual dipole moments per unit volume, where $\vec{p}$ and $\vec{P}$ are

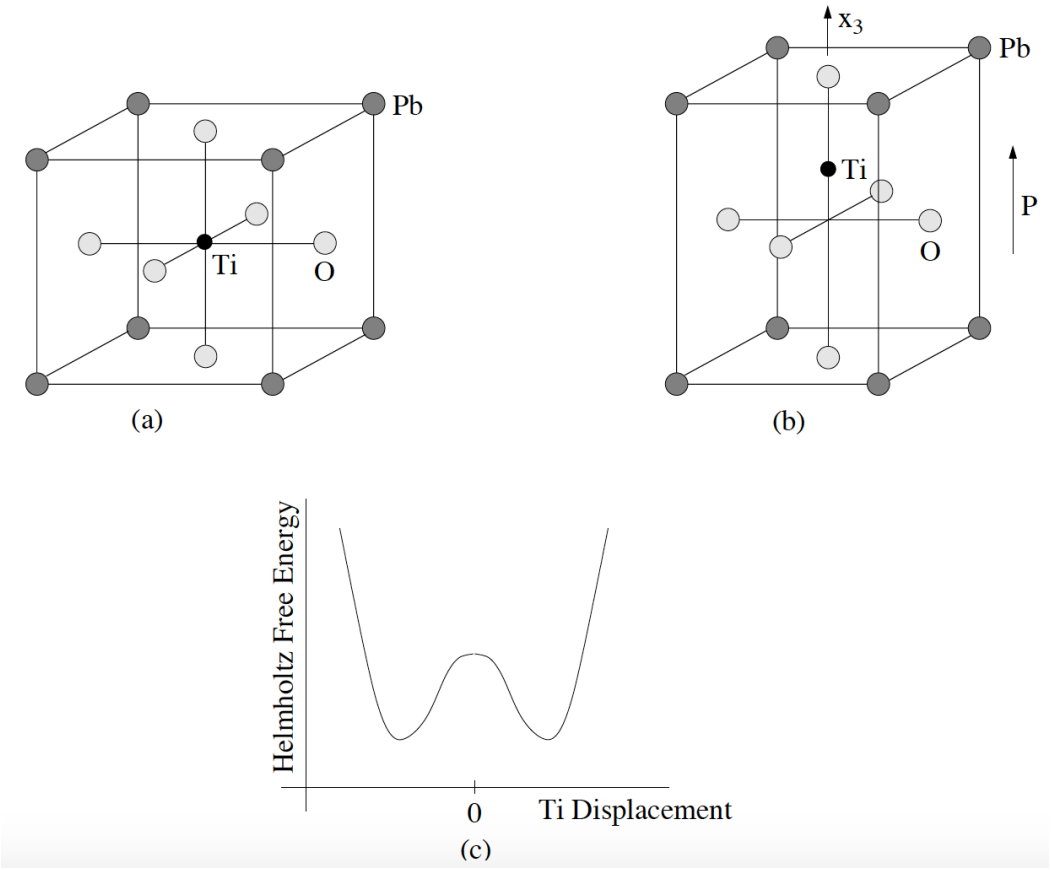

Fig. 2.2 (a) Perovskite structure of $PbTiO_3$ in the cubic form above Curie temperature T_c. (b) Tetragonal structure of $PbTiO_3$ for temperature below T_c. (c) Helmholtz free energy as a function of Ti position along the x_3 axis. Figure sourced from [6]

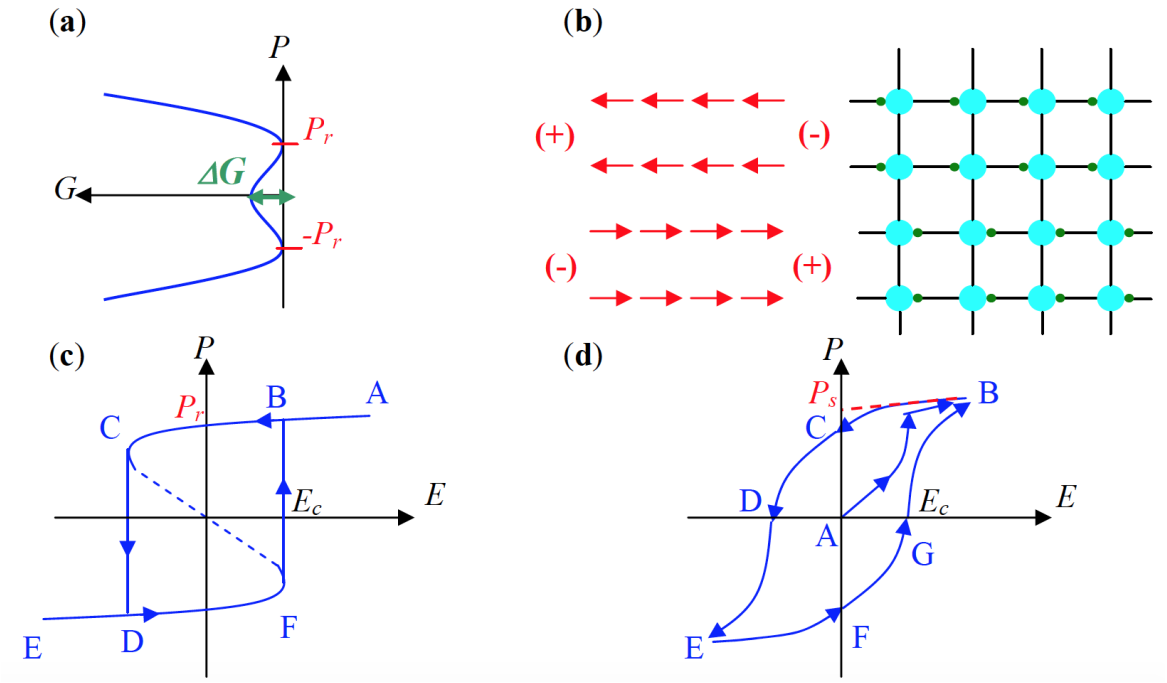

Fig. 2.3 Hysteresis behaviours in ferroelectrics. (a) The free energy G versus polarisation P. $\pm P_r$ are the two stable thermodynamic state, with a barrier of ΔG in between; (b) Ferroelectric domains with distinguishable polarisation; (c) Hysteresis loop ABCDEFBA in a single domain, the path CF is forbidden. The coercive field E_c and the remnant (spontaneous) polarisation P_r are labelled; (d) Hysteresis loop BCDEFGB in real ferroelectrics. AB takes place only during phase transition. The saturation polarisation P_s can be extrapolated in the saturation regime. Figure sourced from [7]

vector quantities:

$$\vec{P} = \frac{\sum_{k=1}^{n} \vec{p}_i}{V} \tag{2.1}$$

Figure 2.3(c) shows the hysteresis loop (polarisation P versus electric field E) ABCDEFBA of a single ferroelectric domain. There exists remnant (spontaneous) polarisation P_r at zero applied electric field. The hysteresis loop intercepts with the E axis at E_c, which is called the coercive field. Unlike most dielectric materials, the relation between P and E is not linear and features a saturation regime. A smoothened hysteresis loop BCDEFGB in real ferroelectrics is shown in Figure 2.3(d). The external applied energy is transferred to both depolarising the unit cells within a domain, and to overcoming the domain wall energy [7]. As a result, different domains can grow or shrink at different rates under the same electric field. Collectively, those behaviours are observed as a smoothened hysteresis loop compared to the single domain one.

2.2 Piezoresponse Force Microscopy

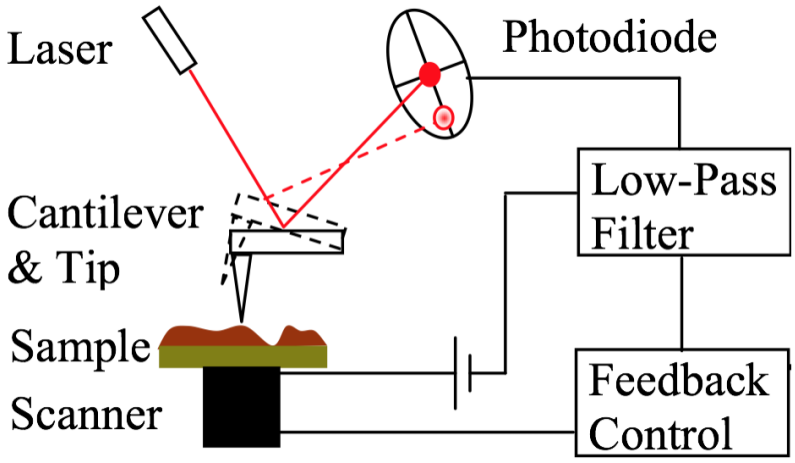

Fig. 2.4 Schematic of Atomic Force microscopy and topography imaging. As the cantilever (tip at the end) approaches the sample, the laser is aligned to reflect the cantilever to the center of photodiode. During the scan, cantilever bending leads to a deviation in the differential signal of the photodiode which is then low-pass-filtered. Such signal is passed through a feedback loop which is to maintain a constant force between the tip and the sample. The output of the feedback loop provides information on the tip-sample interactions, hence forming a topography image. Figure sourced from [8]

Piezoresponse force microscopy is a widely implemented solution in investigating nano domains in ferroelectric materials, a method based on atomic force microscopy [116–118, 7].

AFM is widely used for surface profiling experiments, the schematic shown in Figure 2.4. The AFM cantilever, fixed at one end, features a sharp tip placed at the other end. During the scan, this tip is brought to the vicinity of the sample and the interactions between atoms of tip and the sample surface via van der Waals forces result in cantilever deflections [119, 120]. In the meantime, the laser beam is aligned to reflect from the cantilever to the center of the photodiode.
The cantilever deflection yields a differential signal in the photodiode array, which is fed through a low-pass filter and input to a feedback loop. The feedback loop maintains a constant force between the tip and the sample. The output of the feedback loop is used to map the tip-sample interactions as a function of position (x,y) and forms a surface topography image [121–123]. The typical spring constant of the cantilever is in the range of $0.001 \sim 100$N/m and cantilever deflections of picometer order can be detected [8]. Non-destructive imaging in AFM is possible.
The AFM is able to operate in three working modes:

1. Contact mode. In this mode the tip is in contact with the sample surface. The force between the tip and sample surface is kept constant by keeping a constant deflection of the cantilever. The static deflection is used as the feedback signal [124, 125]. PFM operates in this mode.

2. Non-contact mode. In this mode, the tip is oscillating above its resonance frequency with a small amplitude that keeps it further from the sample surface. When the tip starts to interact with the van der Waals forces on the surface, the resonant frequency changes to lower values [118]. The interaction-force gradient is kept constant by the feedback loop

3. Tapping mode. In this mode, the tip is oscillating just below its resonance frequency. The oscillation amplitude is above 10nm. The tip moves between being in contact and not in contact with the surface hence is the combination of the previous two modes. When the tip starts to interact with the surface, the oscillation amplitude changes so the feedback signal in tapping mode is the amplitude deviation [118]. This is the most commonly used mode of AFM.

In the last decade, PFM has established its position as a primary imaging and non-destructive characterisation techniques of ferroelectric materials on the nanoscale [123, 126]. The domain distribution is imaged based on the inverse piezoelectric effect. Domains with different polarisation direction generates different piezoresponse. PFM carries out domain imaging at the same time when AFM does topography imaging. Domain imaging does not

interfere with the AFM feedback control system. It is a piezoresponse imaging technique, based on the detection of local electromechanical vibrations of the ferroelectric sample caused by external ac signal [127]:

$$V_{tip} = V_{dc} + V_{ac} cos\omega t \tag{2.2}$$

An ac field is applied to a cantilever tip coated with conductive materials e.g. Platinum. The tip is in contact with a ferroelectric thin film sitting on a conductive surface that acts as a bottom electrode. The resonance frequency of the conductive tip (>50kHz) is much greater than that from the AFM low-pass filter (1kHz) [7]. In other words, the applied voltage does not interfere with the AFM electronic feedback control hence the corresponding piezoresponse image is independent from the topography image. As all ferroelectrics are piezoelectric, the external ac field E causes the sample surface to deform (strain s) via inverse piezoelectric effect $s = d_{33} \cdot E$ with an amplitude in picometer order [128, 129], d_{33} is the piezoelectric coefficient. The cantilever tip interacts with the deforming thin film at each scanning point due to linear piezoelectric response, which then yields cantilever deflection. A modulated signal is produced by the laser spot reflection, from the cantilever and reflected into the photodiode array, is detected by the PFM at frequency ω using a lock-in amplifier. This detected tip vibration signal is usually referred to as piezoresponse A [127]:

$$A = A_0 + A_{1w} cos(\omega t + \varphi) \tag{2.3}$$

where A_{1w}, the piezoresponse amplitude of the surface is detected as the first harmonic component. φ is the piezoresponse phase of the surface. The phase difference between the piezoresponse and the *ac* modulation voltage maps the local polarisation orientation and ferroelectric domain distribution [11, 130]. A_{1w} being the piezoresponse amplitude, is also proportional to the piezoelectric coefficient. The piezoresponse signal locked at frequency ω is superimposed on that from the low-passed topography imaging signal which is then filtered. AC voltage is deployed rather than DC in order to avoid abrupt piezoresponse of a thin film. The resulting strain s is very small and the signal frequency is much higher than that of the electronic noise of the system (50Hz). In this way, the PFM signal is periodically oscillating and locked at a frequency much higher than ambient noise.

Consider a polarisation that is purely out-of-plane and an external electric field along the sample thickness axis, as shown in Figure 2.5. Assume that the material is PZT, whose d_{33} is positive. If the local polarisation is in the same direction as the applied electric field (c^- direction here) the material elongates, and the measured piezoresponse will be in phase with the ac modulation voltage. In other words, the phase difference between two signals is 0°. If

the local polarisation is in the opposite direction to the applied field (c^+ direction here) the material contracts, when the measured piezoresponse is out of phase with the applied field, 180° phase difference between piezoresponse and the modulation voltage. The resulting cantilever movement is vertical in both cases.

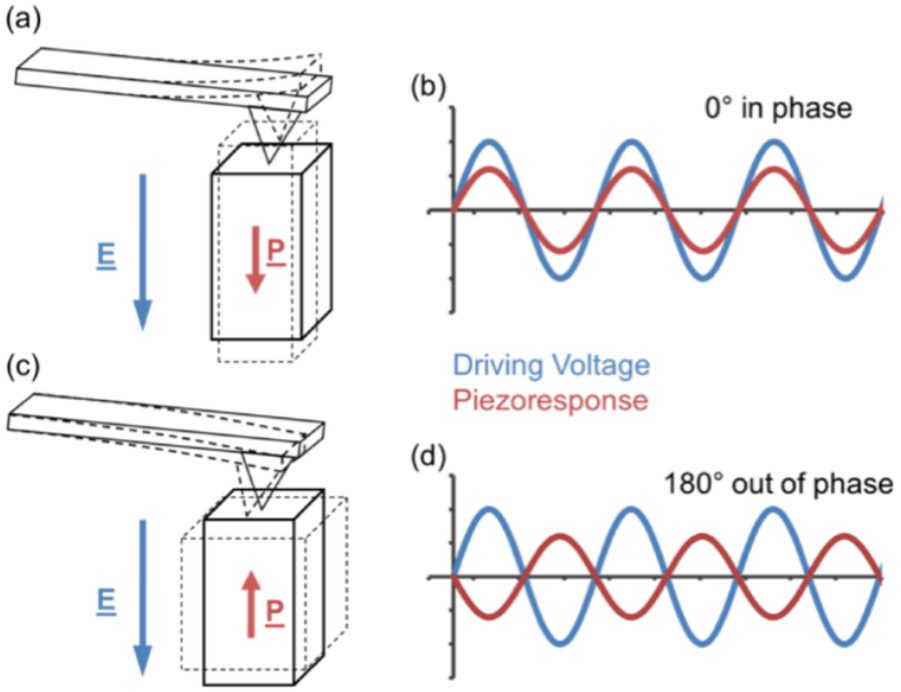

Fig. 2.5 Detection of out-of-plane polarisation component. (a) The applied electric field is in the same direction as the local polarisation direction, thus the driving voltage is in phase with the resulting piezoresponse. (b) The applied electric field is in the opposite direction to the local polarisation direction, thus the driving voltage is 180° out of phase against the resulting piezoresponse. Figure sourced from [9]

Phase φ: For two domains with opposite polarisation directions, their piezoelectric coefficients d_{33} are of opposite polarity. Under an applied electric field, one domain expands while the other shrinks. Locking-in to the phase of the cantilever driving voltage, it is possible to characterise out-of-plane polarisation from phase φ, and thus map the ferroelectric domains. In this way, two domains with opposite polarisation directions will be imaged by PFM as having 180° phase difference.

Amplitude A_{1w}: The amplitude A_{1w}, which is always positive, is directly related to the piezoelectric coefficient d_{33} of the local domain. At the domain boundary, neighbouring domains act to cancel the effect of each other, which leads to zero piezoresponse signal. For two domains with opposite polarisation directions, the amplitude signal A_{1w} will be constant within both domain, except at the domain wall.

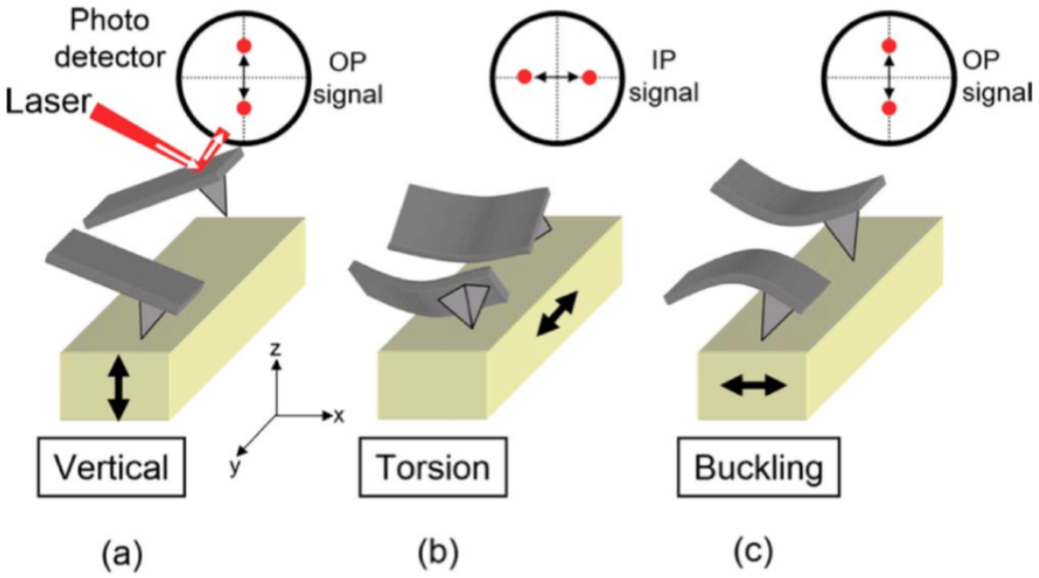

Fig. 2.6 Cantilever movement with out-of-plane and in-plane polarisation. The polarisation direction in (a) is out-of-plane, while it is in-plane in (b)transverse (c)longitudinal. The corresponding piezoresponse leads to cantilever (a)vertical motion, (b)torsion (c) buckling. Figure sourced from [10]

An electric field that acts on the material along its thickness also produce an in-plane polarisation shown in Figure 2.6 (b)(c). In-plane polarisation has two components, transverse (perpendicular to the cantilever) and longitudinal (along the cantilever). Longitudinal polarisation results in buckling i.e. vertical movement of the cantilever, similar to the out-of-plane polarisation. In both cases, the laser beam reflected photodiode signal fluctuates in the top and bottom parts of the photodiode. Therefore, vertical PFM allows detection of both out-of-plane polarisation and in-plane longitudinal polarisation. On the other side, the transverse polarisation results in a periodic torsion and lateral movement of the cantilever. The cantilever torsion gives rise to a difference between the signals collected in the left and right parts of the photodiode. By recording the ac difference in the signal between the left and right areas of the photodiode, one can map the in-plane polarisation of the sample. This method is called in-plane, or lateral PFM [131]. Out-of-plane PFM usually provides stronger signals than in-plane PFM. The former is more popular in PFM experiments traditionally, while the latter is only sought for when supplementary data on in-plane domain distribution is needed. It is therefore worth mentioning that the PFM in this work refers to out-of-plane PFM.

2.3 Engineered ferroelectric domains

Section 2.2 demonstrates how PFM images ferroelectric domains. This section will discuss how to write a ferroelectric domain and the energy dynamics involved in forming an engineered domain. A DC voltage is applied between the PFM tip and the thin film, the latter sits on a conductive surface which is connected to ground. As the tip scans across the ferroelectric surface in a planned course, an electric field is applied along the way. Given that the electric field is higher than the coercive field of the material, the application of opposite voltages results in domains of opposite polarisation directions. Once the surface is poled, PFM images engineered domains in the same manner as the intrinsic ones. Figure 2.7 shows a poled ferroelectric domain on a single crystal PZT thin film of 50nm thickness. The dark coloured region poled at -10V is surrounded by intrinsic ferroelectric domains. The electric field is sufficient to change the polarisation direction within the poled domain compared to that of its surrounding region, hence showing a relative dark colour. The resulted polarisation direction of the dark region (right) is out-of-plane. The applied electric field is in the opposite direction to the local intrinsic polarisation direction out-of-plane (left) i.e., 180° out of phase as discussed in Figure 2.5.

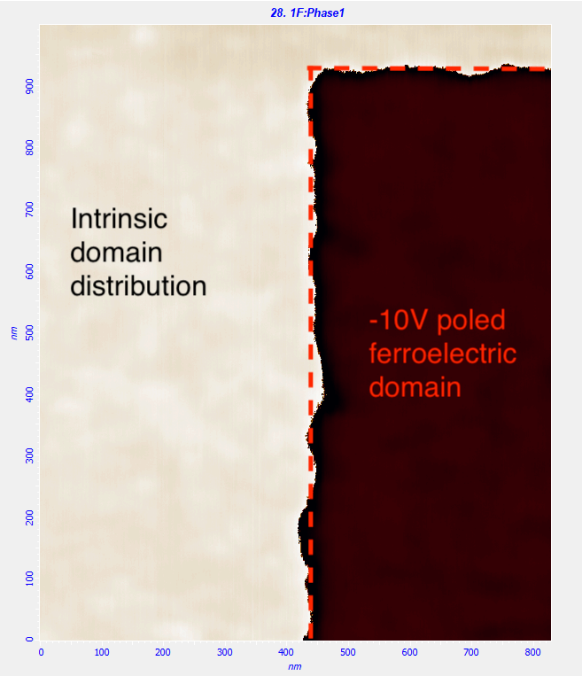

Fig. 2.7 PFM phase image for a PZT single crystal thin film of 50nm thickness, image size $0.83\mu m \times 1\mu m$. A region (within dashed line) poled at -10V is surrounded by intrinsic ferroelectric domains.

Domains under certain size (the critical size) are energetically unstable and cannot exist. There are several different factors taking apart in the formation of ferroelectric domain. Consider a ferroelectric material with spontaneous polarisation P_s subject to external electric field E_a, and the formation of a prolate spheroidal domain of radius r (minor axis) and length l (major axis). In favour of the expansion of a ferroelectric domain of dimension r and l from nonexistence, work done by the external field is the product of the dipole moment (from both itself and its image charge hence $2P_s$) and the electric field i.e., E_a ($2P_s$) ($\frac{2}{3}\pi r^2 l P_s$) [132]. As the domain grows larger, the domain wall dissipates more and more energy in the expansion. Domain wall energy (σ_w per unit area) is counteracting the domain formation, as well as the depolarisation energy U_d [11, 132]. U_d, the third term in formula 2.4, is resulted from the divergence of polarisation along the domain wall. Landauer first calculated this term as the integral of the product between depolarisation field E_d and the resulting deviation ΔD_d ($=4\pi P_s$) caused by E_d [132]. The total energy involved in the process is

$$U = -\frac{4}{3}\pi r^2 l E_a P_s \quad + \quad \sigma_w A \quad + \quad \frac{16\pi {P_s}^2}{3\varepsilon_a \varepsilon_c} r^2 l' (\eta^2 - 1)\Big(\frac{1}{2}\eta\, ln(\frac{\eta+1}{\eta-1}) - 1\Big) \qquad (2.4)$$

$$\text{where} \qquad l' = l\sqrt{\frac{\varepsilon_a}{\varepsilon_c}} \qquad \eta = \frac{l'}{\sqrt{l'^2 - r^2}}$$

where A is the surface area of the domain and ε_a, ε_c are the dielectric constants along major and minor axes respectively. The second term is due to domain wall energy and the third term is the depolarisation energy U_d. According to the above equation, a domain below a critical size is unstable in terms of energy, implying that critical values of r_c and l_c exist for a certain material and the application of a certain electric field. Domains smaller than this critical size are unstable and will disappear on removal of the electric field. Durkan's calculations show that there is a saddle point energy U for the critical radius r_c and length r_c [11]

$$r_c = \frac{15\sigma_w \pi}{48 E_a P_s} \qquad l_c = \left(\frac{5\sqrt{5}}{12} \frac{\sigma_w \pi^2}{{r_c}^2} \sqrt{\frac{U_d}{(\frac{4}{3}E_a P_s \pi)^2}} \right)^2 \qquad (2.5)$$

The domain wall area under the assumption of prolate spheroidal geometry is $\pi^2 rl/2$ [132]. For example, consider a domain where r = 40nm and l = 100nm, the domain wall area is $1.97\times10^{-14}\text{m}^2$. It can be seen that the larger is the applied electric field, the smaller will be the critical domain size. As one increases the dc voltage applied between the tip and the thin film, there comes a point where the associated electric field is greater than the coercive filed of the local domain. From this bias above, stable ferroelectric domains can be written by

PFM lithography. After the writing finishes, one can use PFM to image the written domain by mapping the piezoresponse magnitude and phase.

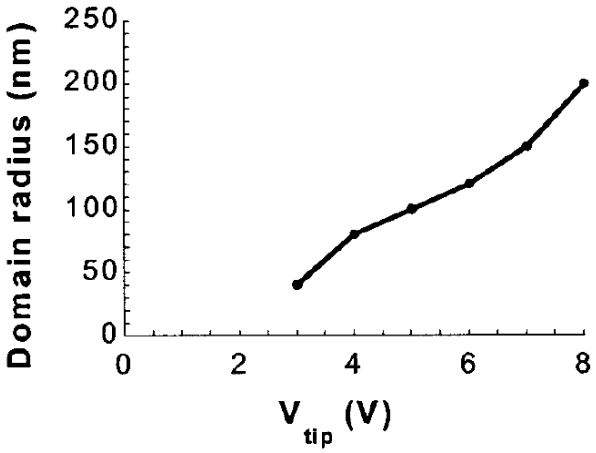

Fig. 2.8 Measured dependence of domain radius on writing voltage. Figure sourced from [11]

Durkan *et al*. measured the critical domain radius by a range of writing voltages, shown in Figure 2.8. As the writing voltage increases, the electric field from the tip spreads out more, hence does the domain radius. The minimum radius of domain they have succeeded in writing and subsequently imaging is 40nm [11]. They also found that longer writing pulses lead to larger domains.

While the piezoresponse signal is affected by the strain resulted from the applied electric field, the controllable parameter of PFM is the applied dc voltage V_{tip}. The relation between the applied dc voltage and the associated electric field applied to the PZT surface is complicated. It is affected by film thickness, the local dielectric constant, and the tip geometry [7]. The electric field is not homogeneous in the material. Durkan *et al* modelled the actual displacement ($D = \varepsilon_0 \varepsilon_r E$) field distribution in the PZT near the tip, shown in Figure 2.9. This calculation assumes there is a gap, d, between the tip (radius R) and the sample surface, which forms a parallel plate capacitor of thickness t. The effective electric field within PZT is

$$E = \frac{V}{t} = \frac{q}{A\varepsilon_0 \varepsilon_r} \tag{2.6}$$

where $q = CV_{tip}$ is the surface charge and A is the area of the capacitor. The tip sample capacitance is $C = \frac{2\pi\varepsilon_0 R^2}{\frac{t}{\varepsilon_r} + \frac{d}{\varepsilon_{gap}} + R}$. From the above geometry, electric field varies spatially to a large extent. From the displacement field distribution, it is possible to calculate the critical domain size as a function of the tip bias. Results are plotted in Figure 2.10, for different tip radii R = 50nm, 100nm, 150nm. The distance from the tip to the PZT surface is chosen as d

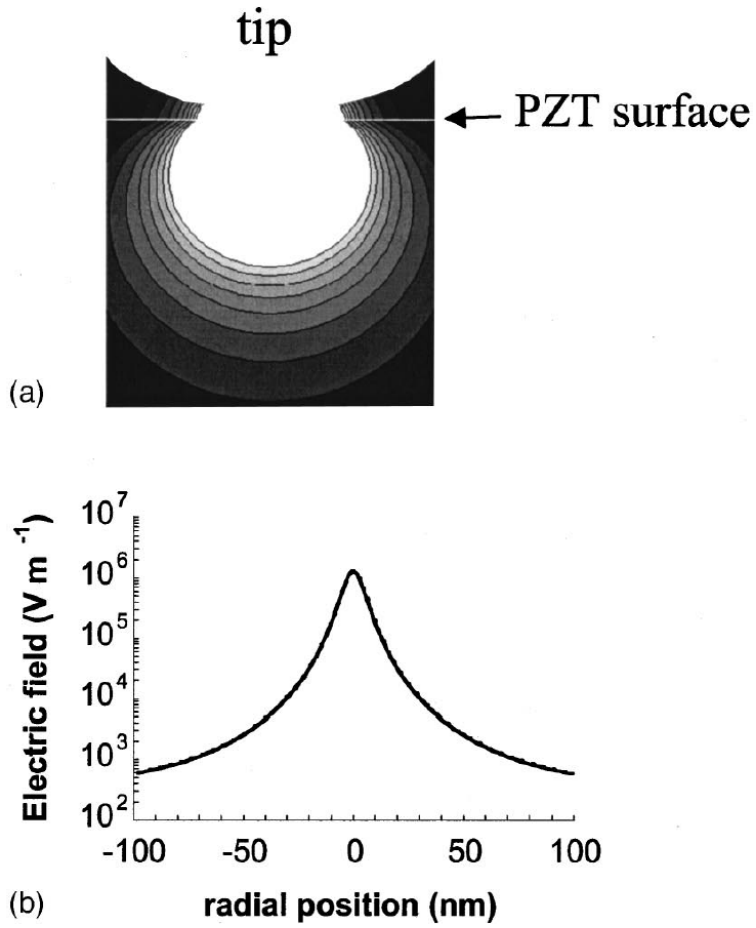

Fig. 2.9 Distribution of the displacement field ($D = \varepsilon_0 \varepsilon_r E$) in the vicinity of the tip. Figure sourced from [11].

= 6nm for all. From the calculations, the critical domain size is 30∼40nm for a tip of radius R = 50nm, written at V_{tip} = 1V. While the critical domain size that can be experimentally written and subsequently imaged is 40nm, at V_{tip} = 3V. The experimentally observed Figure 2.8 lie within the calculated curves here, though not exactly following any one curve. The purpose of section 2.4 and 2.5 is to write ferroelectric domains of the minimum size for a PZT sample. Therefore, one should use the lowest tip bias that lead to formation of a stable domain.

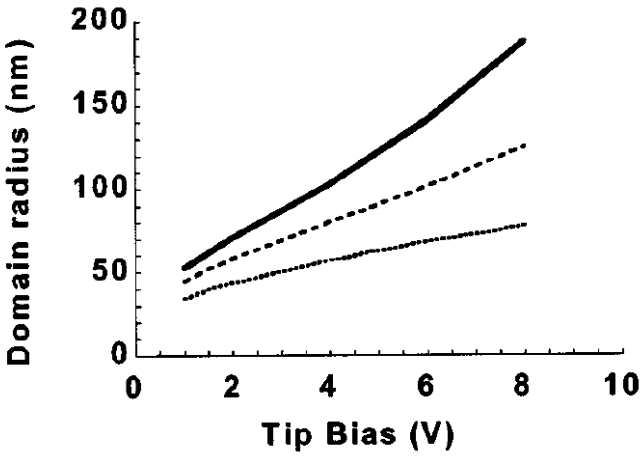

Fig. 2.10 Calculated dependence of domain radius on tip bias for different tip radii, according to the displacement field distribution in Figure 2.9. Tip radius 50nm (dotted curve), 100nm (dashed curve), 150nm (solid curve). Figure sourced from [11].

2.4 2D periodic potentials

Ferroelectric domains and polarisation were discussed in section 2.1 and the concept is going to be utilised here to realise a periodic ferroelectric domain array. A single crystal PZT ($PbZr_{0.3}Ti_{0.7}O_3$) thin film of 50nm thickness grown on doped $SrTiO_3$ substrate (also acting as the back electrode) is deployed in the work. An AFM system (NT-MDT model Solver Pro-M in PFM mode) in Durkan Lab was used with conductive AFM tips to carry out domain engineering work in this chapter. There are two steps involved in PFM lithography. The first step is to polarise a selected region (say $1\mu m \times 1\mu m$) by -10V, with special attention paid to the following points:

1. On the 50nm thick PZT single crystal sample mentioned above, the selected region should be examined by an AFM scan first to make sure the region is reasonably flat, because the later transferred single layer graphene needs to be conformal to its substrate beneath. For example, if a region of $1\mu m \times 1\mu m$ is to be polarised, one would use the guidance of keeping the height variation in the topography scan within 1nm.

2. The maximum bias voltage that can be applied to the tip is $\pm$10V in the NT-MDT PFM system used in this work. Any voltage that results in an electric field above the coercive field in the region works, as long as the voltage applied results in a change in polarisation direction. It was found that a bias voltage with magnitude greater that 4V can reverse the local polarisation direction.

3. It was found that in some cases -10 V being the bias voltage to polarise a region of PZT was too high due to tip-surface interactions. It was noticed that the application of -10 V to some unused new tips results in field evaporation of the metal coating on the tip, possibly an electrochemical phenomenon. During PFM scans those evaporated materials are moved around the surface, with deposition of materials happening in some regions. A proved solution is to raise the bias voltage by increments for all new tips, e.g. first scan -2V, then -4V, -6V, then -8V.

The second step is to write the designed pattern by applying a positive pulse voltage. The dot-to-dot distance in the array is aimed to be as small as possible in the nanometer range. And the shape of the domain formed is expected to be a circle. To achieve that, parameters that can be controlled are the applied pulse shape, pulse voltage and pulse application time. There are seven pulse shapes available from the system: triangular, square, rounded square and trapezoidal. All pulse shapes were tried at a range of pulse voltage and application time. The square pulse shape was tested to be the most reliable one across the spectrum, thus is deployed throughout this work.

Domain expansion happens during and after the pulse action. The PFM tip is used to apply the voltage, goes to defined locations and stays there for a defined period of time. This voltage results in an electric field at each dot location and changes the polarisation direction there as long as the applied field is larger than the coercive field. The electric field penetrates through the material and expand isotropically, affecting a semi-sphere shape of material beneath the tip under exposure. The volume of the polarising material and the horizontal diameter of the semi-sphere (dot diameter) therefore depend on the strength and effective time of the electric field. In other words, the magnitude and application time of the pulse.

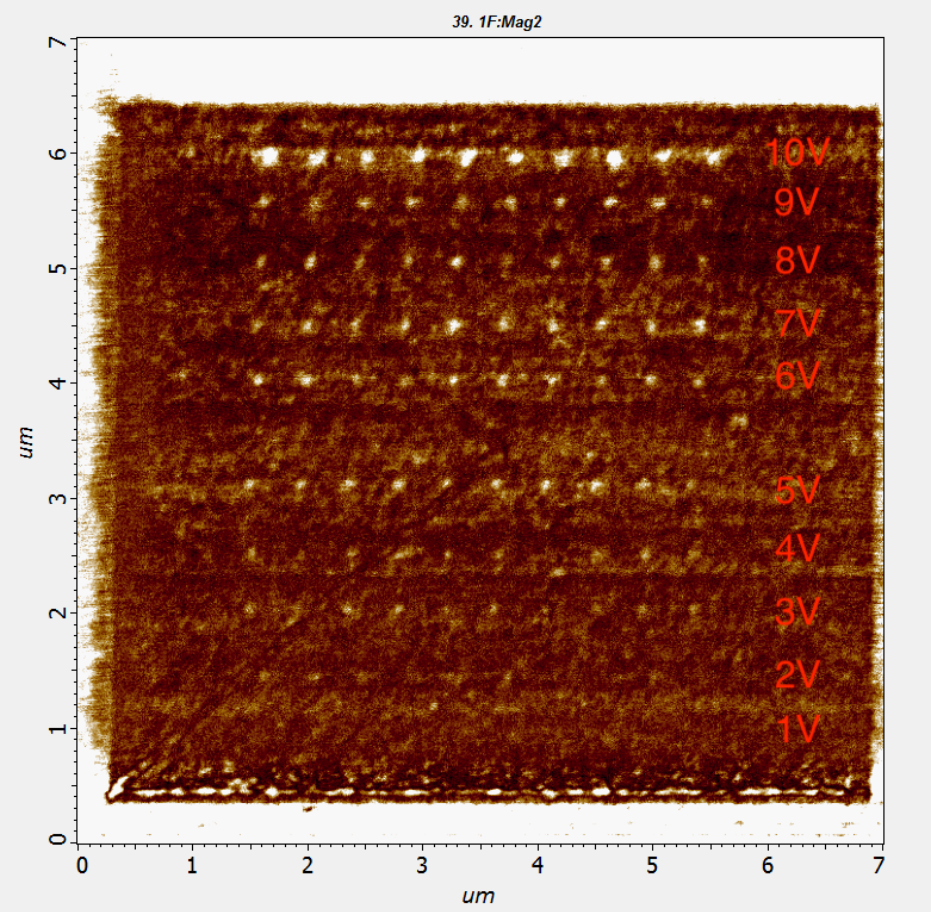

Fig. 2.11 PFM horizontal magnitude image. A selected region of $6\mu m \times 6\mu m$ was first polarised at -9V, then a 2D grid of 10×10 points were patterned at voltages +10 V, +9V, +8V,..., +2V, +1V. The voltage at each dot was applied as a square pulse, the application time was 100ms. The dot-to-dot distance is approximately 500nm. A final scan of $7\mu m \times 7\mu m$ was done to examine the pattern.

Figure 2.11 shows PFM horizontal magnitude image. A selected region of $6\mu m \times 6\mu m$ was first polarised at -9V, then a 2D grid of 10×10 points were patterned at pulse voltages +10V (highest up), +9V, +8V,..., +2V, +1V (lowest down). The dot-to-dot distance is approximately

500nm. A final scan of $7\mu m \times 7\mu m$ was done to examine the pattern. It is noticed that when the pulse voltage is below +3V, there is no evidence of domains being formed. Hence voltage below +3V results in an electric field smaller than the corresponding coercive field in that region of PZT. It is also noticed that the line of dots poled at +3V and +4V is less distinct compared to the line above.

A considerable amount of time has been spent on optimising the parameter set, on pulse voltage and application time, in order to achieve the closest dot-to-dot distance. It has been explained in section 1.5 that the size of the device is kept around 300nm due to electron coherent transport requirement, and the minimum domain size in PZT is 20nm$\sim$40nm [11, 132]. To achieve a periodic potential profile within one device of 300nm size, one needs to work on reducing the dot-to-dot distance which is 500nm in Figure 2.11. With clear dots seen at a dot-to-dot distance of 500nm (Figure 2.11), the dots were gradually brought closer and closer to each other as detailed below. Figure 2.12 shows PFM vertical magnitude and vertical phase images. A selected region of $3\mu m \times 3\mu m$ was first poled at -10 V, then an array of 20$\times$20 points were patterned at a pulse voltage +3V - +4V. Dot-to-dot distance was designed at 150nm. Pulse application time was 100ms. A PFM image of an area $4\mu m \times 3.6\mu m$ was then taken to examine the pattern.

Figure 2.13 shows PFM vertical magnitude and vertical phase images of another array patterned under the same pulse conditions as Figure 2.12, with the difference being two arrays made at two different regions on the same PZT sample. It is clearly seen that in Figure 2.13, there are fewer dots printed. Careful examinations of the two scans find that in the latter case more defects are present in the region, which show up as terraces aligning 90 degrees to each other in the magnitude image. There are local variations in the thin film, mainly defects, which leads to inconsistencies in domain switching. In such defect-rich regions to compensate for those extra pinning centres, patterning demands higher pulse voltage or longer application time. Applying same conditions as the previous defect-clean region results in fewer dots being printed.

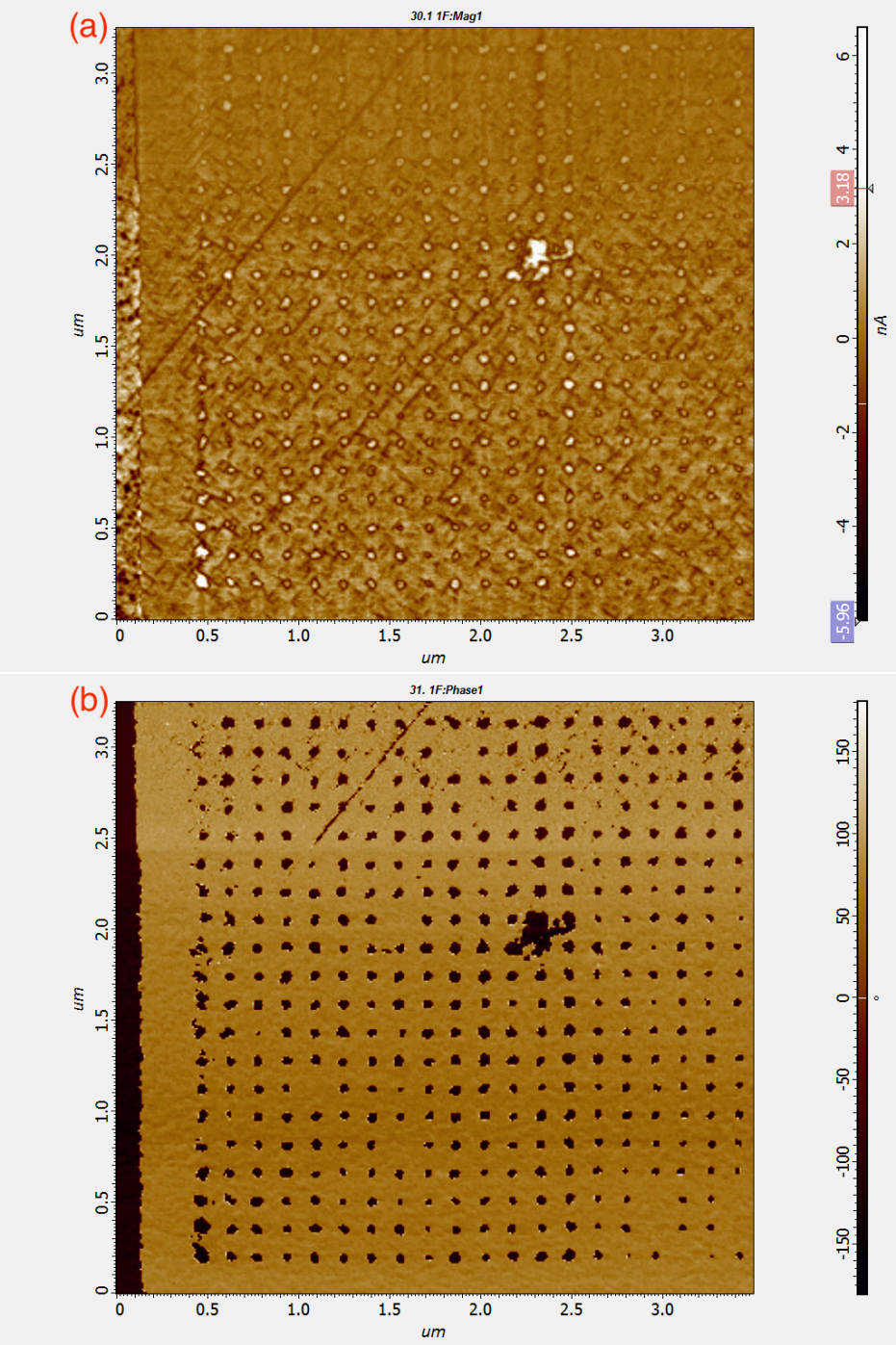

Fig. 2.12 PFM vertical images: (a) magnitude; (b) phase. A selected region of $3\mu m \times 3\mu m$ was first polarised at -10V, then an array of 20×20 points were patterned at a voltage +3V - +4V (dot-to-dot distance was designed at 150nm). The voltage at each dot were applied as a square pulse of amplitude +4V, the application time was 100ms. A final scan of $4\mu m \times 3.6\mu m$ was done to examine the pattern.

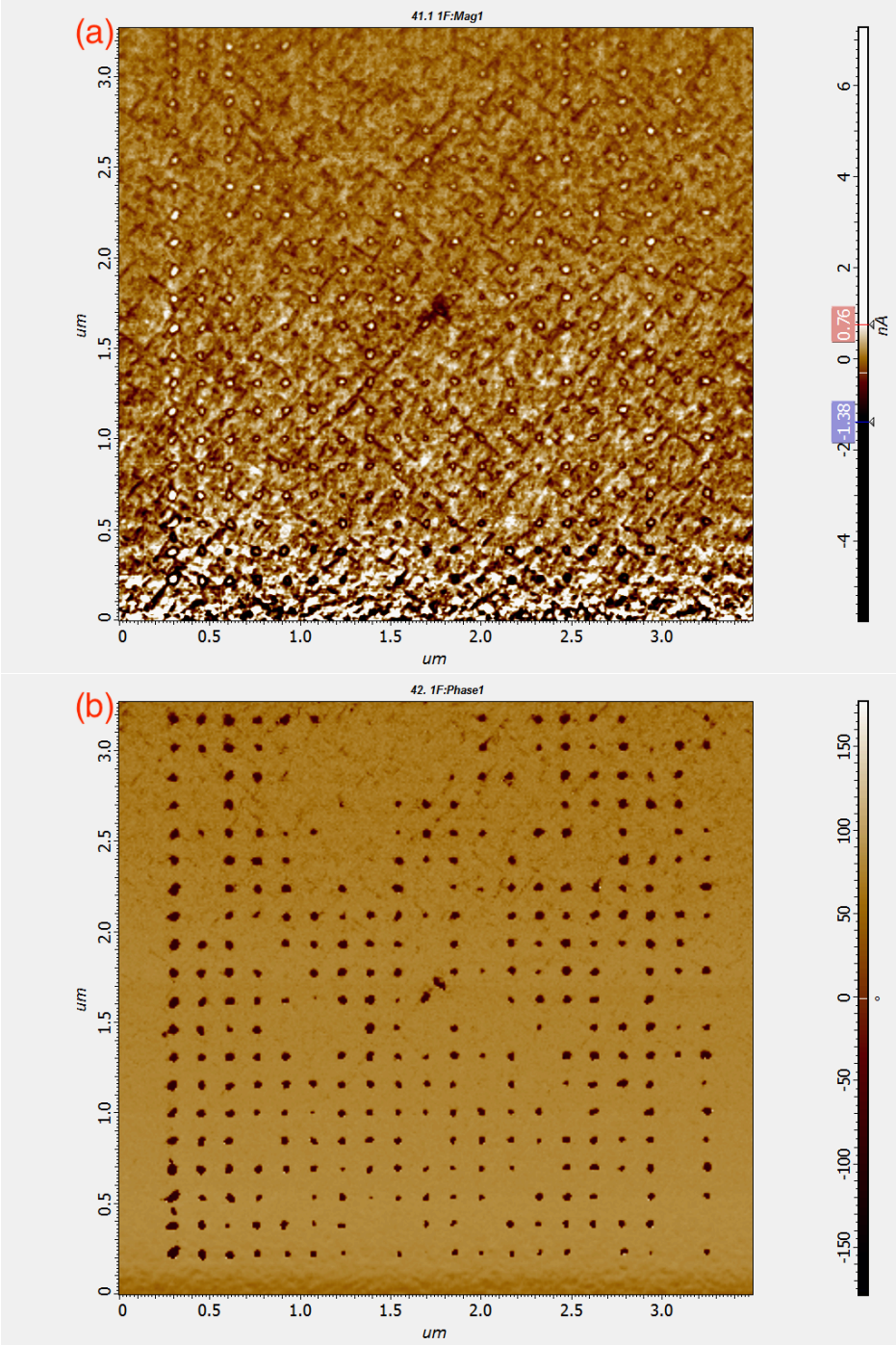

Fig. 2.13 PFM vertical images: (a) magnitude; (b) phase. A selected region of $3\mu m \times 3\mu m$ was first polarised at -10 V, then an array of 20×20 points were patterned at a voltage +3V - +4V (dot-to-dot distance was designed at 150nm). The voltage at each dot was applied as a square pulse of amplitude +4V, the application time was 100ms.

Figure 2.14(a) shows a PFM vertical phase image for an array at a modified pulse voltage +3.35V - +3.85V. It is noticeable that the dots are smaller than those in Figure 2.12 and 2.13, which were patterned at +3V - +4V. Encouraged by this, various conditions were tried with small adjustment in the pulse voltage to achieve both smaller dot size and higher percentage of printed dots at a dot-to-dot distance of 150nm. The optimised ultimate product is displayed in Figure 2.14(b). It shows a PFM vertical phase image for an array at pulse voltage +3.2V - +3.9V. This pulse voltage reliably produces arrays with the highest percentage of dots printed and smallest dot size, at the 150nm distance range.

With sufficient margin seen at 150nm, the dot-to-dot distance is pushed further down. Figure 2.15(a) shows a PFM vertical phase image for an array with dot-to-dot distance 100nm. After multiple iterations, the smallest dot-to-dot distance at which a stable 2D array can be written and subsequently imaged is found to be 39nm, as shown in Figure 2.15(b). The condition to underline here is +4.1V pulse voltage and 20ms application time.

The key goal of producing results shown from Figure 2.11 to Figure 2.15 is to narrow the distance between the points. This goal is achieved by experimenting with different lithography conditions (pulse voltage and pulse application time). The dot-to-dot distance is reduced from 500nm (Figure 2.11) to 39nm (Figure 2.15) in the end. The point behind the effort lies in the mean free path of the electrons in graphene (a few hundred nanometers under low-temperature test conditions), since graphene nano-ribbons fabricated using the same processes possess a mean free path as large as 220nm at room temperature [107]. We expect that at low temperature e.g., 10K, it will be larger. Therefore, the distance from one electrode to another is kept between 300$\sim$400nm for all fabricated devices, below the expected mean free path of graphene under low temperature. The coherence requirements together with the minimum dot-to-dot distance (39nm), determined that there is a limited number of barriers/wells (7$\sim$9) in such PZT-graphene devices.

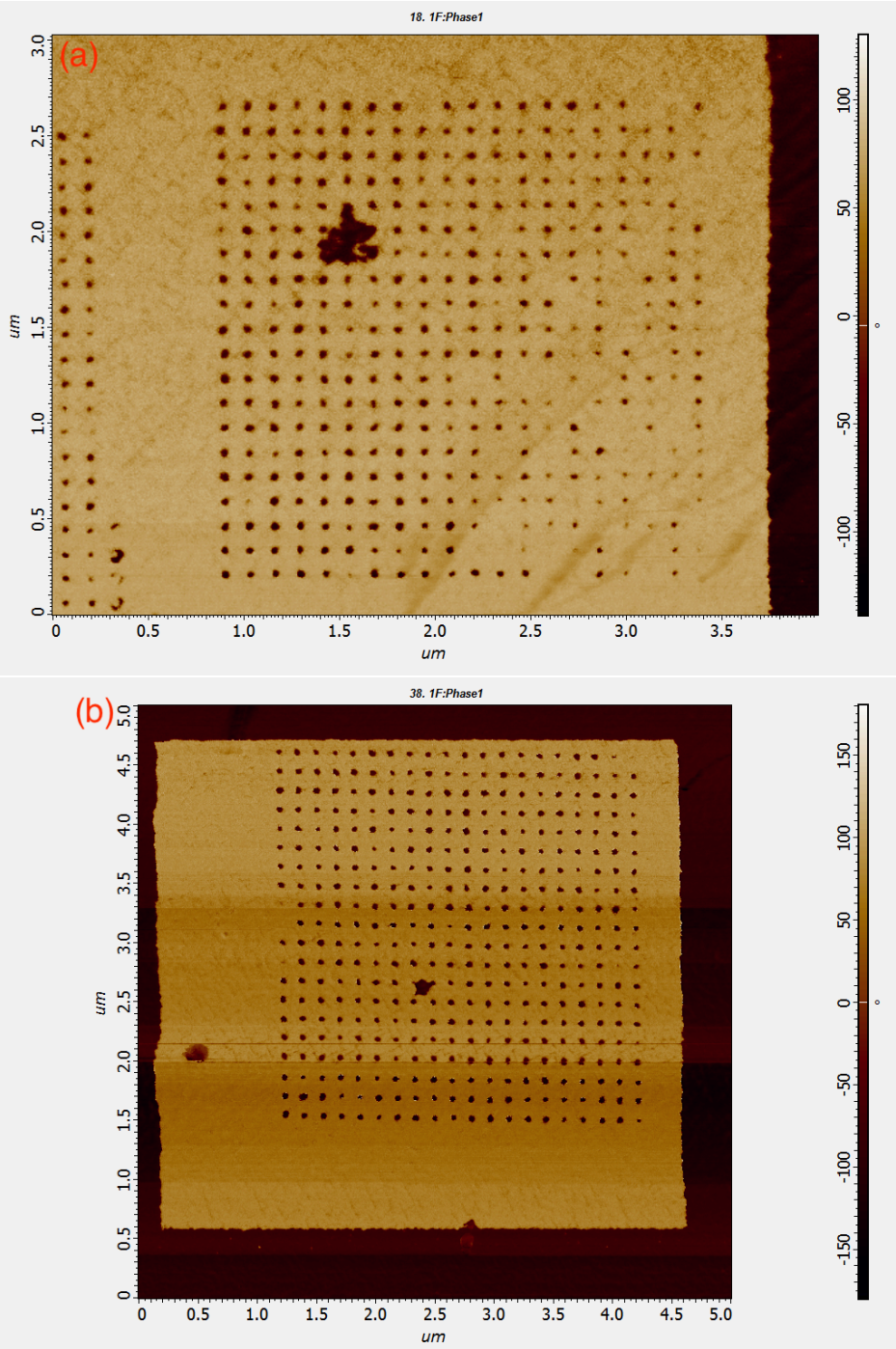

Fig. 2.14 PFM vertical phase image. A selected region of $3\mu m \times 3\mu m$ was first polarised at -10V, then an array of 20×20 points (dot-to-dot distance was designed at 150nm) were patterned at a pulse voltage: (a) +3.35V - +3.85V, dots are smaller than those in Figure 2.12(b); (b) +3.2V - +3.9V, Dots size was not much improved compared to (a). The voltage at each dot was applied as a square pulse of amplitude (a)+3.85V and (b)+3.9V, the application time was 100ms in both experiments.

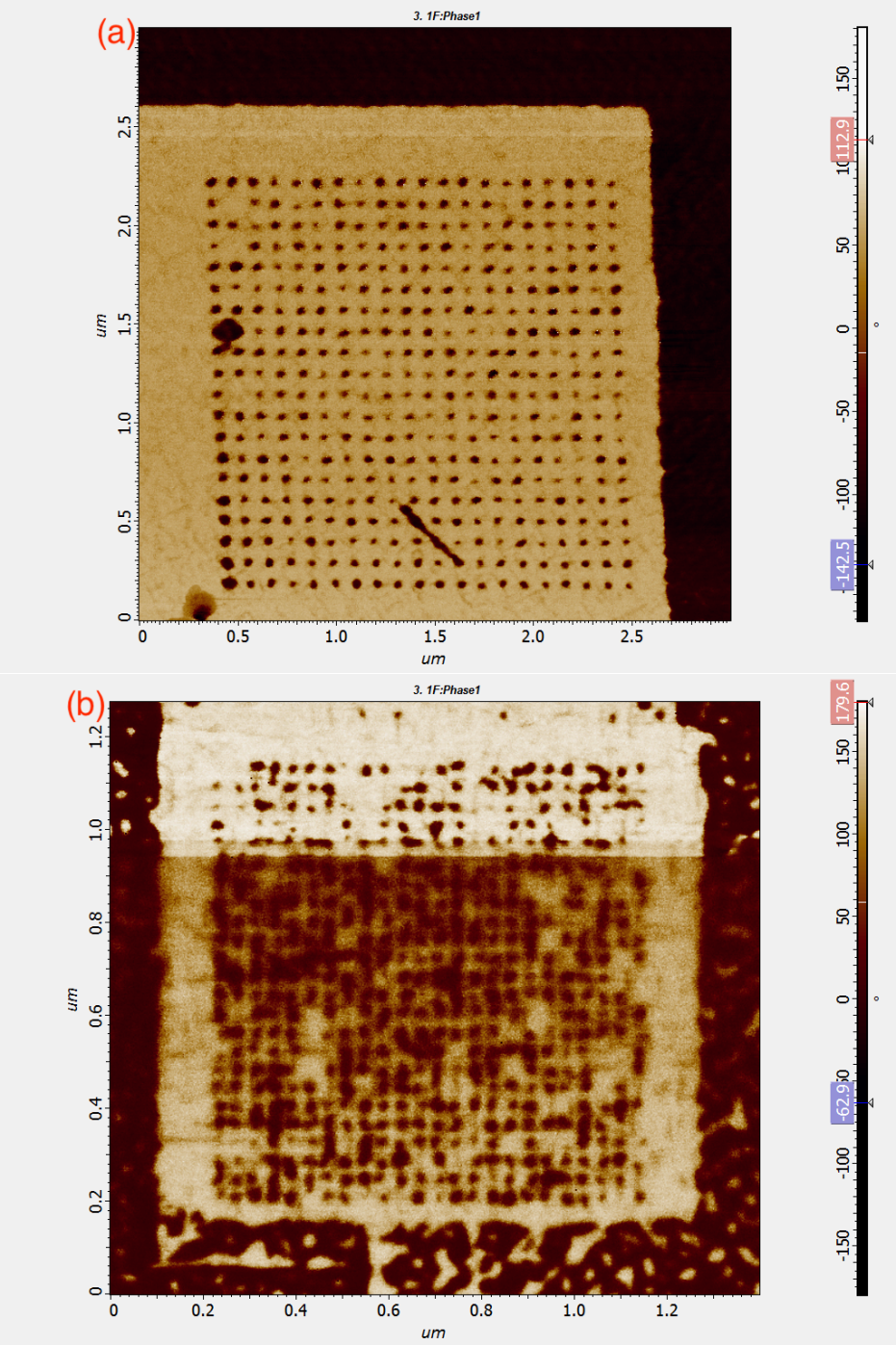

Fig. 2.15 (a) PFM vertical phase image. A selected region of $2\mu m \times 2\mu m$ was first polarised at -10V, then an array of 20×20 points were patterned at a pulse voltage +3.2V - +3.9V (dot-to-dot distance was designed at 100nm). The voltage at each dot was applied as a square pulse of amplitude +3.9V, the application time was 100ms.
(b) PFM vertical phase image. A selected region of $1\mu m \times 1\mu m$ was first polarised at -8 V, then an array of 24×24 points were patterned at an action voltage of +4.1V (dot-to-dot distance was designed at 39nm). The voltage at each dot was applied as a square pulse of amplitude +4.1V, the application time was 20ms.

2.5 1D periodic potentials

The formation of 1D periodic domains is also explored. This work starts with exploring 2D periodic potentials because it gives the possibility to explore the effect of different periods in different directions. It doubles the number of measurements we could get from a single device. Having achieved the smallest possible domains for 2D potentials, one moves on to studying 1D periodic potentials, because 1D potentials (beneath the graphene layer) stands a higher chance to result in noticeable behaviour change of electrons.
This is illustrated in Figure 2.16. Given that electrons incident on a periodic potential array can flow in all directions, in a 2D periodic potential there are two electron paths. Electrons either experience the periodic potential throughout their journey (indicated as blue arrows), or not (indicated as orange arrows). However small the periodicity is made, these gaps exist. For 2D potentials with possibly the smallest periodicity of 39nm, gaps of 10∼15nm alway exist. The existence of these gaps will make it more difficult to observe any effect on the band structure. In comparison, the choice of 1D potentials is more likely to produce a measurable effect on the band structure, as long as the size of the graphene is smaller than the region of patterned potentials.

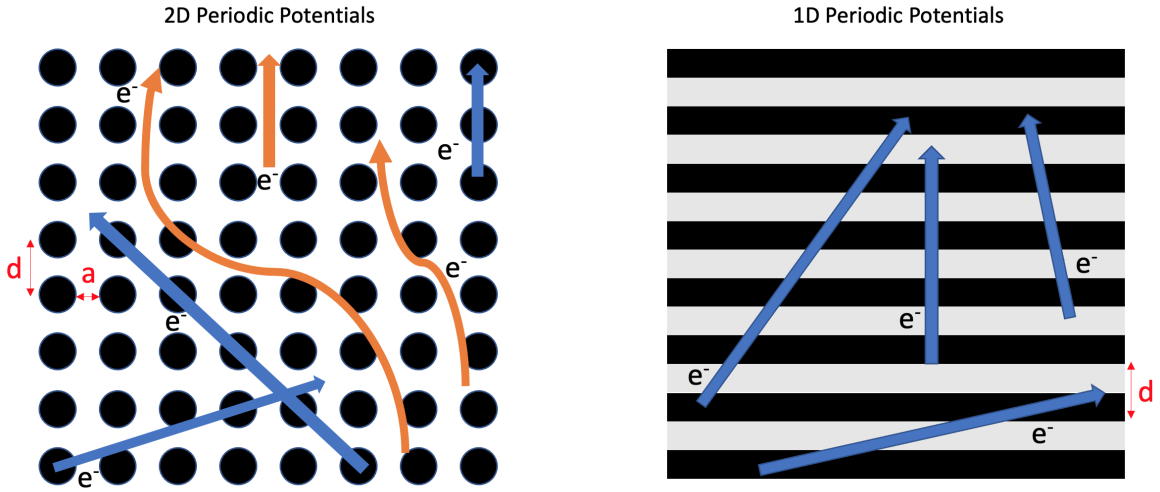

Fig. 2.16 Electrons encounters 2D potentials and 1D potentials

Experimentally, 1D potentials is achieved in a slightly different way than 2D potentials. Figure 2.17 demonstrates the steps involved in 1D domain engineering. A conductive tip carrying alternating voltages as square pulses of positive (Action1) and negative (Action2) voltage amplitudes, scans the sample surface in contact. The application time of each pulse is 20ms. Due to repetitive processing, the quality of the PZT sample deteriorates and a new dock of single crystal PZT was sourced. The sample used in this section is supplied by Dr

Ahmed Kursumovic from Prof Judith McManus-Driscoll's group in Department of Materials Science & Metallurgy, University of Cambridge. It is a single crystal PZT ($PbZr_{0.3}Ti_{0.7}O_3$) thin film of 100nm thickness grown on doped $SrTiO_3$ substrate.

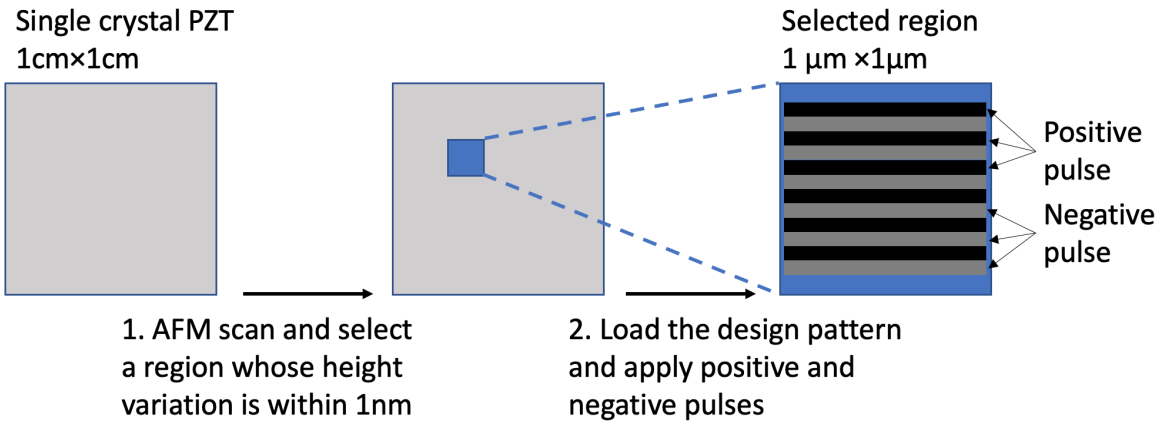

Fig. 2.17 Steps involved in 1D domain engineering. A conductive tip carrying alternating voltages as square pulses of positive (Action1) and negative (Action2) voltage amplitudes, scans the sample surface in contact. The application time of each pulse is 20ms.

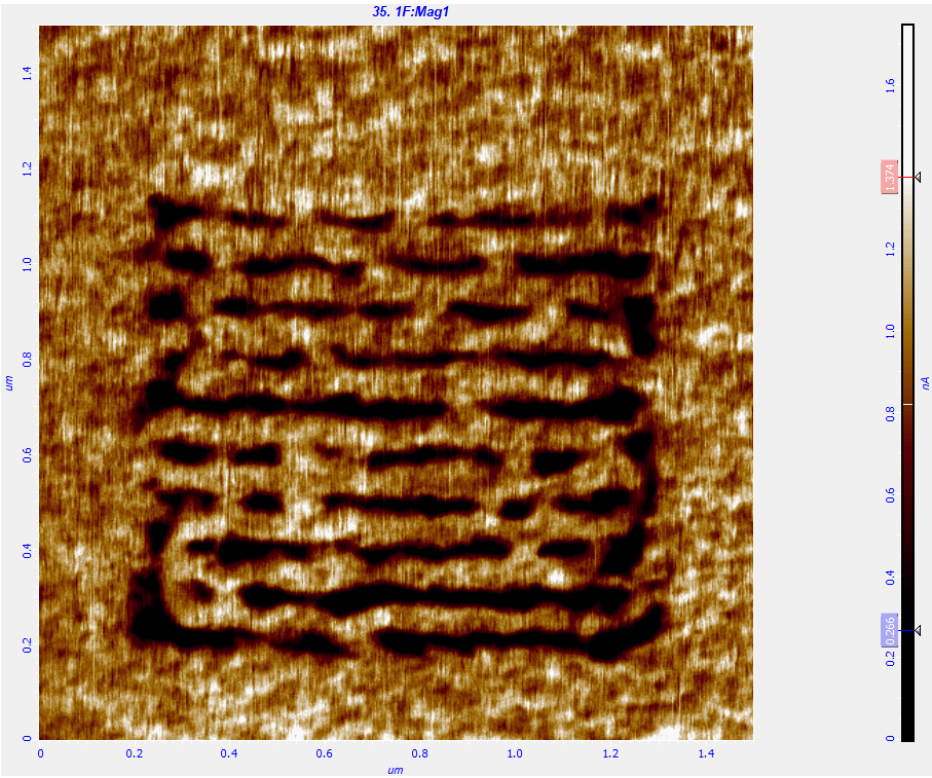

Fig. 2.18 PFM scan of a 1D potential array - discontinuous lines. Lithography condition is highlighted in medium grey in Table 2.1.

An example of the PFM magnitude scan for one poled 1D potential arrays is shown in Figure 2.18. The array is designed to be 1μm long strips, with 180° phase difference in domain polarisation. The strip width is made as 50nm, so the periodicity of this periodic potential array is 100nm. The PZT surface is polarised at alternating voltages of +5/-8V carried by a conductive AFM tip. The lithography condition is highlighted in medium grey in Table 2.1. Action1 and Action 2 correspond to positive and negative voltage amplitudes of the applied square pulse. The application time for both Action1 and Action2 pulses is 20ms.

Table 2.1 Experimented lithography conditions for PZT device 1 - 1D Potential

Pattern Dimension	**Action1 /V**	**Action2 /V**	**Periodicity**	**Result**
1μm long & 10 periods	+10.0	-10.0	100nm	discontinuous lines
1μm long & 10 periods	+3.0	-10.0	100nm	merged lines
1μm long & 10 periods	+6.0	-8.0	100nm	discontinuous lines
1μm long & 10 periods	+5.0	-8.0	100nm	discontinuous lines
1μm long & 10 periods	+4.0	-8.0	100nm	discontinuous lines
1μm long & 10 periods	+3.0	-8.0	100nm	discontinuous lines
1μm long & 10 periods	+2.0	-8.0	100nm	discontinuous lines
1μm long & 10 periods	+1.5	-8.0	100nm	continuous lines
1μm long & 10 periods	+1.5	-8.0	50nm	distorted
1μm long & 10 periods	+1.5	-8.0	60nm	distorted
1μm long & 10 periods	+1.5	-8.0	70nm	distorted
1μm long & 10 periods	+1.5	-8.0	80nm	merged lines
1μm long & 10 periods	+1.5	-8.0	90nm	discontinuous lines
1.6μm long & 10 periods	+1.5	-8.0	100nm	continuous lines
2.5μm long & 10 periods	+1.5	-8.0	100nm	continuous lines
1μm long & 10 periods	+1.5	-7.5	100nm	continuous lines
1μm long & 10 periods	+1.5	-7.5	70nm	distorted
1μm long & 10 periods	+1.5	-7.5	90nm	discontinuous lines
1μm long & 10 periods	+7.0	-6.0	100nm	discontinuous lines
1μm long & 10 periods	+3.0	-6.0	100nm	discontinuous lines

It can be seen that the domain pattern as formed is discontinuous. The discontinuity comes from the imbalance between the electric fields created by two alternating voltages of opposite

signs. A number of experiments are then carried out to find voltage combinations that produce continuous and straight parallel lines. The lithography conditions tried are summarised in Table 2.1.

One would start with the maximal voltage combination +10/-10V, which stretches to the maximum value that is allowed by the system. The outcome is discontinuous lines, similar to what is shown in Figure 2.18. In other words, domains represented by light coloured strips (in Figure 2.18) expand too big an area due to the excessive electric field created by one of the two alternating voltages. Therefore, one tries to weaken this electric field i.e. decrease the voltage applied. Bringing down the voltage to a combination +3/-10V resulted in merged lines as shown in Figure 2.19(a). This points out higher than needed reduction in the positive voltage so the corresponding electric field was weakened too much.

The above logic holds throughout the whole process of determining possible lithography conditions (outlined in Table 2.1), in order to find the right parameter sets. In the end, applying alternating voltages of +1.5/-8V was proved to be a robust condition to achieve stable 1D arrays of periodicity 100nm . 1D potential arrays made under this condition can extend as long as 2.5μm. When one tries to bring down the periodicity, inappropriate voltage combinations result in a distorted pattern, as shown in Figure 2.19(b).

Figure 2.20 exhibits 1D potential arrays of periodicities 80nm, 60nm and 50nm respectively. Their exact lithography conditions are detailed in Table 2.2, along with a number of other tested conditions. Action1 and Action 2 correspond to positive and negative voltage amplitudes of the applied square pulse. The application time for both Action1 and Action2 pulses is 20ms. Domains patterned under those conditions are the ones that finally feature in working devices. The electrical measurement under low temperature will be discussed in Chapter 4.

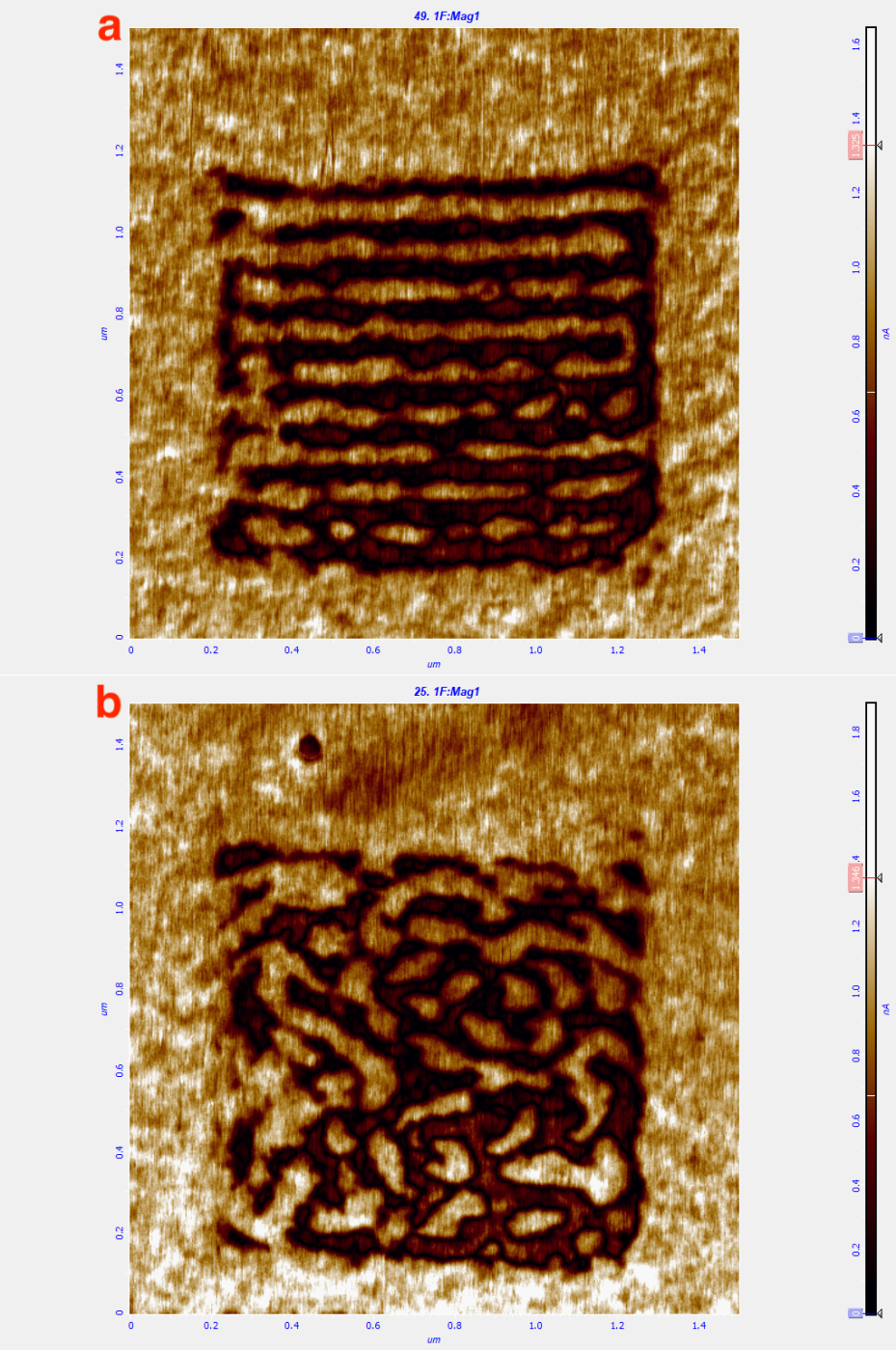

Fig. 2.19 (a) PFM scan of a 1D potential array - merged lines. Lithography condition is highlighted in light grey in Table 2.1. (b) PFM scan of a 1D potential array - distorted pattern. Lithography condition is highlighted in dark grey in Table 2.1.

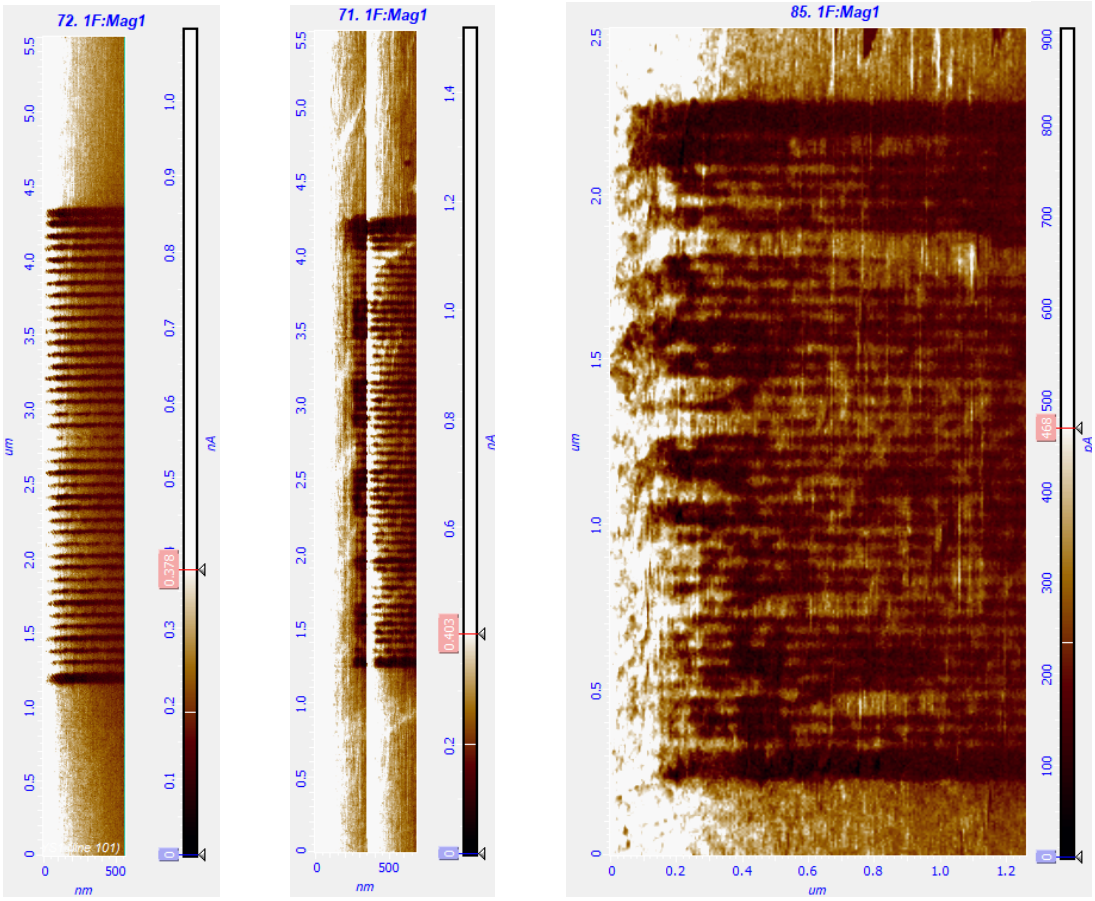

Fig. 2.20 PFM (Mag1) scans for a collection of 1D potential arrays of different periodicity. Periodicities are 80nm (left), 60nm (middle) and 50nm (right).

Table 2.2 Lithography conditions of 1D potentials for PZT device 2-4

Pattern Dimension	**Action1 /V**	**Action2 /V**	**Periodicity**	**Result**
1.6μm long & 20 periods	1.5	-8.5	80nm	continuous lines
1.6μm long & 20 periods	1.5	-9.0	80nm	continuous lines
3.2μm long & 20 periods	1.5	-8.5	80nm	continuous lines
5μm long & 40 periods	1.5	-8.5	80nm	continuous lines
3.2μm long & 20 periods	1.5	-9.0	60nm	continuous lines
3.2μm long & 40 periods	1.5	-9.5	60nm	continuous lines
3.2μm long & 40 periods	1.5	-10.0	60nm	continuous lines
5μm long & 50 periods	1.5	-9.5	60nm	continuous lines
5μm long & 50 periods	1.5	-10.0	60nm	continuous lines
3.2μm long & 40 periods	1.5	-10.0	50nm	continuous lines

2.6 Measurements of lithography-created potentials

The presence of a spontaneous polarisation within ferroelectric materials means that the thin film surface is charged, and the charge is polarisation charge bounded to the surface rather than free charge. The existence of polarisation charge puts PZT surface at certain potential, which is measurable by Kelvin Probe Force Microscopy (KPFM). This section looks at the surface potential recession of the engineered domains. Figure 2.21 exhibits the PFM vertical phase image of a 1D potential array of periodicity 130nm. The accompanying cross section phase profile shows distinct phase contrast (180° phase difference) between neighbouring domains of opposite polarisations.

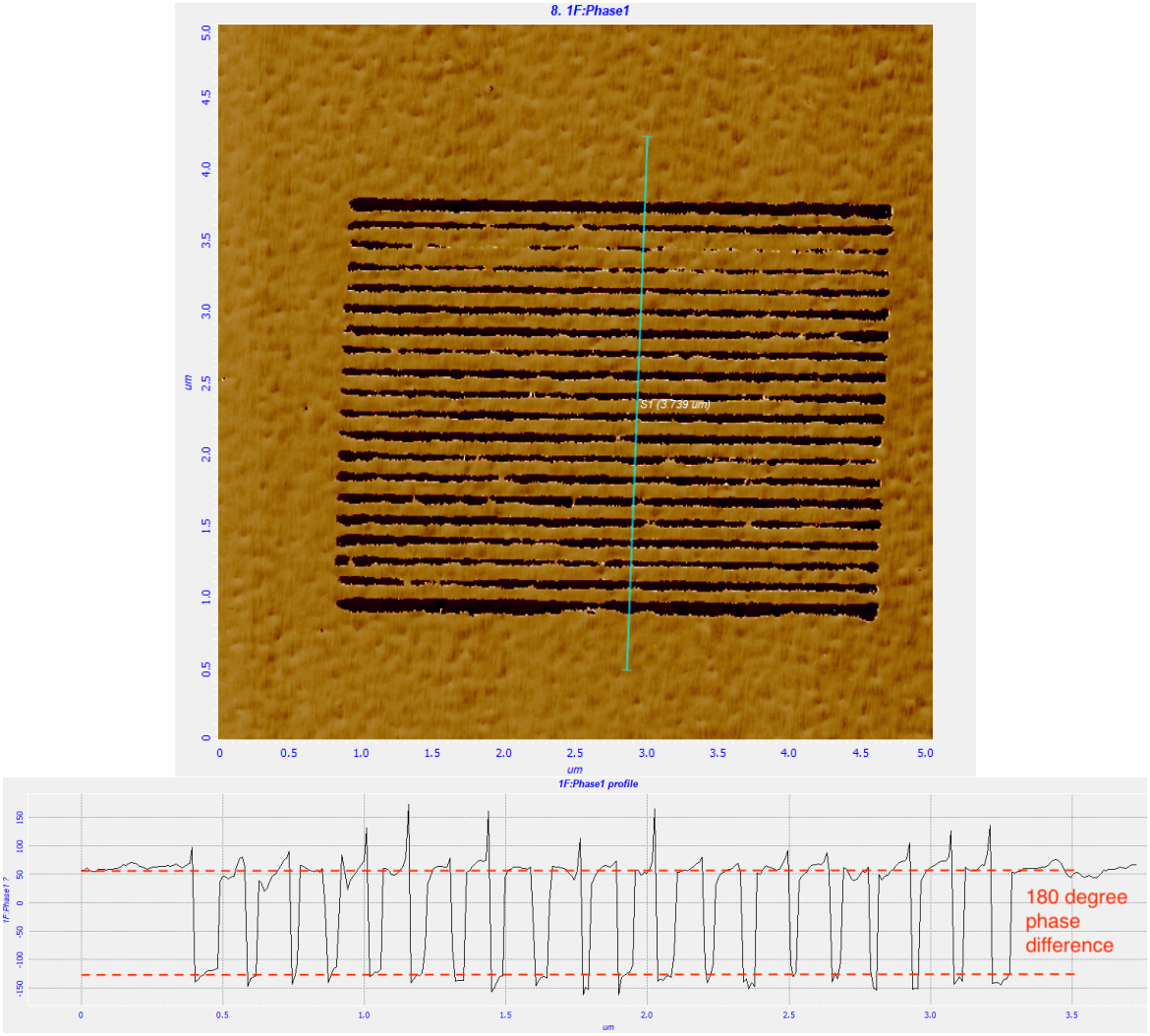

Fig. 2.21 PFM vertical phase image for a 1D periodic potential array of periodicity 130nm. The cross section phase profile shows distinct phase contrast (180° phase difference) between dark and light coloured strips. This mimics the

This will be the ideal scenario of how the potential array looks like at the time of electrical measurements i.e. periodic square barriers. The 1D electrostatic graphene superlattice effect measured in this work, depends on the periodic surface potential which is created via patterning of a ferroelectric material. However, domain relaxation takes place after the removal of external electric field and the surface potential decays over time. The discontinuity of polarisation fields within ferroelectrics gives rise to the presence of bound charge at the surface. Those screening charges create a depolarisation field opposite the direction of polarisation. While they are usually excluded in the considerations for bulk ferroelectrics, the effect is non-negligible for thin films on the nanoscale [133, 134].

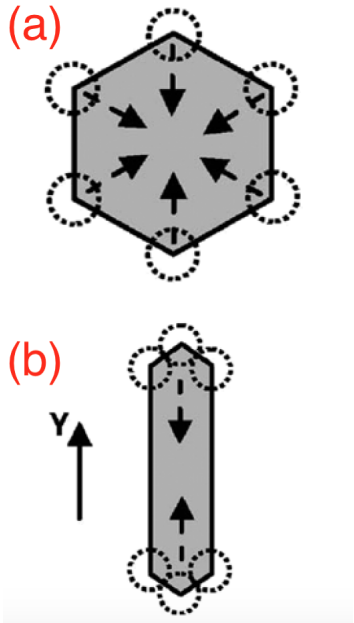

Fig. 2.22 Illustration of domain shrinkage due to heat treatment in circle domain (a) and a rectangle domain (b). The dotted circle mark domain corners and arrows show the domain shrinkage direction. Figure sourced from [12]

Forming a domain under the tip-induced electric field in PFM lithography depends on the complex interplay between the probe-induced displacement field distribution, the field dependent domain wall energy, the surface charge diffusion and the charge injection kinetics, while the domain relaxation in the absence of external fields is driven only by domain wall tension and depolarisation field [135]. It was known that low heat treatment ($\sim$100°C) is effective to accelerate domain shrinkage, indicating high mobility of the domain wall in some ferroelectric materials [12]. Therefore, after the PFM lithography step where domains are patterned, all the subsequent fabrication work is performed without heat treatment. There have been several studies of domain relaxation as a function of domain size and thin film

thickness [136, 137]. In general, the smaller is the domain size, the faster will be the domain relaxation. The thinner is the thin film thickness, the shorter lifetime the engineered domain has. Surface contamination and ion species also affects the domain stability from the creation of new pinning centres [12, 138].

Kelvin Probe Force Microscopy (KPFM) is used to investigate the polarisation charge screening mechanism of the PZT surface. It is a modified form of Atomic Force Microscopy. KPFM produces the surface potential mapping for thin film materials [139]. Upon proper calibrations, the data can be utilised to effectively image the 2D profile of differences in work functions of materials. This technique has found itself applications in fields of physics, chemistry and biology including dopant mapping, hetero-junctions imaging and etc [140]. The electrostatic force F on a surface by an AFM tip is proportional to the surface capacitance gradient in the vertical direction $\frac{\partial C}{\partial z}$ as well as the tip carried voltage V_{tip},

$$F = \frac{1}{2}\frac{\partial C}{\partial z}V_{tip}^2$$

In the case of amplitude modulated KPFM, the tip carries a superposition of dc voltage and ac voltage modulated at its resonance frequency ω,

$$V_{tip} = V_{dc} + V_{ac}\,sin\omega t$$

Therefore,

$$\begin{aligned} F &= \frac{1}{2}\frac{\partial C}{\partial z}(V_{dc} + V_{ac}\,sin\omega t)^2 \\ &= \frac{1}{2}\frac{\partial C}{\partial z}(V_{dc}^2 + V_{ac}^2\,sin^2\omega t + 2V_{dc}V_{ac}\,sin\omega t) \\ &= \frac{1}{2}\frac{\partial C}{\partial z}[(V_{dc}^2 + \frac{1}{2}V_{ac}^2) + 2V_{dc}V_{ac}\,sin\omega t - \frac{1}{2}V_{ac}^2\,cos2\omega t] \\ &= F_{dc} + F_{\omega} + F_{2\omega} \end{aligned}$$

In general, the electrostatic force F is consisted of a dc component and ac components at the first and second harmonics. For a vibrated tip at its first harmonic, V_{dc} includes the contact potential difference between the tip and sample, and the externally applied potential by a feedback loop in the case of KPFM.

$$V_{dc} = V_{CPD} - V_{applied}$$

A lock-in amplifier extracts the tip deflection A_ω at its first harmonic. The feedback loop sweeps $V_{applied}$ until the tip deflection is nullified. This externally applied value is adjusted according to the surface potentials at different locations within a scan area,

$$\text{to achieve } \; F_\omega = 0, \quad \text{so } \; V_{dc} = 0 \quad \text{i.e. } \; V_{CPD} = V_{applied}$$

As such, the surface potential difference is measured by constantly adjusting the potential offset on the tip while keeping the first harmonic vibration amplitude zero. Note that the output V_{CPD} from the system is the difference between surface potentials of the tip and sample:

$$V_{CPD} = V_{tip} - V_{sample}$$

To obtain the work function of a surface, the tip needs to be calibrated against a material whose work function is well-known such as graphite. The work function of the tip is:

$$\phi_{tip} = \phi_{graphite} + eV_{CPD/graphite}$$

The work function of the sample is calculated as,

$$\phi_{sample} = \phi_{tip} - eV_{CPD/sample}$$

This section is interested in the surface potential recession of the sample, rather than the exact work function value of the PZT surface, so deals with V_{CPD} values only. KPFM allows quantitative probing of screening phenomena in ferroelectric properties. In KPFM experiments, non-contact measurements are usually performed at tip-surface separations between 10nm and 100nm [139] which is much smaller than typical ferroelectric domains. It however suffers from both systematic errors related to feedback loops and topographical crosstalk. The resolution is limited by the tip-surface separation as well as variations of tip-surface capacitance [139]. Both have a strong dependence on the electrostatic interaction between the tip and sample.

In this section, a single crystal PZT ($PbZr_{0.3}Ti_{0.7}O_3$) thin film of 70nm thickness grown on doped $SrTiO_3$ substrate (acts as back electrode) was deployed to measure the potential time decay curve of the patterned ferroelectric domain. A $2\mu m \times 2\mu m$ area is poled at -6V first. Within that region, a $1\mu m \times 1\mu m$ area is poled at +6V. Both voltages correspond to an electric field higher than the local coercive field, and produces neighbouring domains of opposite polarisation directions. This is verified by PFM phase imaging, which shows 180° phase difference between neighbouring domains. A $3\mu m \times 3\mu m$ region was measured by KPFM to verify that the tip applied voltage results in a change in V_{CPD} values of the

engineered domains to that of the surrounding material. KFPM measurement was carried out multiple times in the next 7 days to monitor the surface potential of the engineered domains.

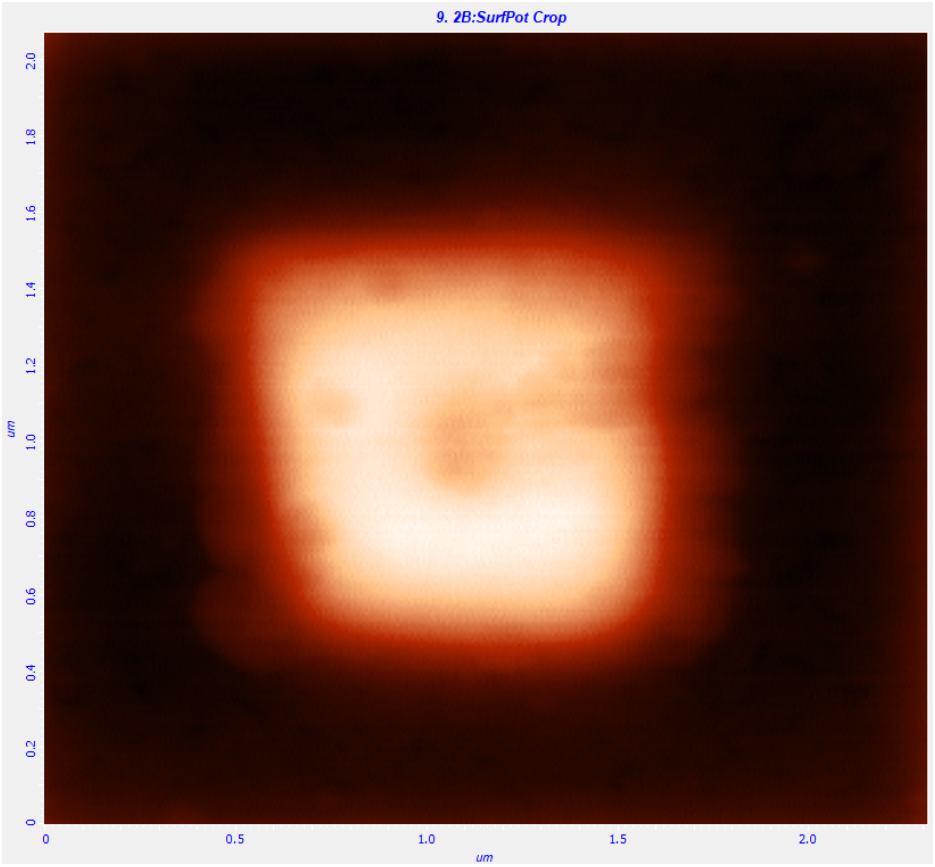

Fig. 2.23 KPFM image (surface potential) of engineered domains. The whole region is poled to -6V first. The central square region is subsequently poled to +6V. Taking surface potential distribution in this figure as a square barrier, the difference in surface potential of the positively poled region (bright) and the negatively pole region (dark) is the height of the square barrier.

Figure 2.23 shows a typical KPFM surface potential image in this experiment. The two domains here are poled at the same absolute voltages but opposite polarity, hence forming a square barrier. As mentioned before, the information in this image refers to the contact potential difference V_{CPD} between the tip and pre-planned scanning points on the sample. For the two engineered domains in Figure 2.23, the difference $V_{CPD,domain1}$ - $V_{CPD,domain2}$ is equivalent to the difference in the surface potentials $V_{sample,domain1}$ - $V_{sample,domain2}$. It is also the height of the square barrier.

Figure 2.24 illustrates the change in barrier height V_0 in seven days. In the beginning, the barrier height was 285mV. It is noticeable that the surface potential difference drops the most significantly in the first 24 hours. After 24 hours V_0 = 146.2mV, almost halved the

original value. At the end of 7 days (t = 167hr), the barrier height approached 83.3mV. The PFM lithography is followed by multiple nano fabrication steps which will be introduced in Chapter 3, and those steps takes at least 72 hours to complete. One will be interested to see the remaining value of surface potential difference at the time of electrical measurements (Chapter 4), because this value is the potential of 1D graphene superlattice. Therefore, it is helpful to know the range of barrier height in that timescale. Annotations on the figure shows that at t = 72hrs, the barrier height V_0 drops to 119.3mV. At t = 96hrs, V_0 = 101.1mV. The measured surface potential difference between neighbouring domains of opposite polarisation directions varies for different PFM tip and in different locations on the sample, hence the measurements here do not absolutely apply to the working devices that will be discussed in Chapter 4. However, it is reasonable to assume that the barrier height is of a few hundred milli volts at the time of electrical measurements.

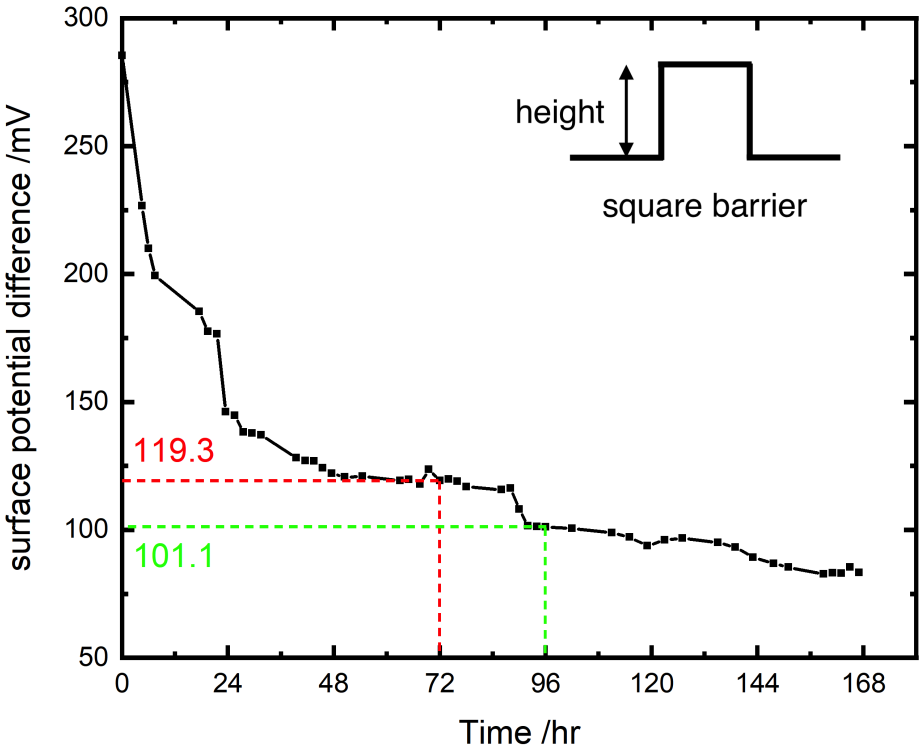

Fig. 2.24 Measured dependence of surface potential difference on time. The surface potential difference is the difference in the measured V_{CPD} values of the positively and negatively poled domains in Figure 2.23. Taking the surface potential distribution in Figure 2.23 as a square barrier, the difference in V_{CPD} values is the barrier height.

In this work, the object of concern is the surface potential contrast between positively and negatively poled domains, which was 285mV at the start. The PFM lithography and imaging are performed in the ambient environment, including applications of high voltage to a ferroelectric thin film. After the applied electric field is removed, the polarisation charges stay at the PZT surface. Relaxation of the engineered domains takes place due to depolarisation field and domain wall tension, hence reduces the surface potential contrast [141]. Externally, a range of electrochemical phenomena could also take place e.g. ionic exchange between material and liquid [142] and solid state electrochemical reactions that affect the bulk material [143]. Among them, the main path for surface discharge is the adsorption of water molecules. They then dissociate into charged species such as OH^- groups, protons, and peroxide species, which triggers the surface electronic and ionic conductivity [13]. This mechanism has been observed under different humidity and temperature environments [144–147].

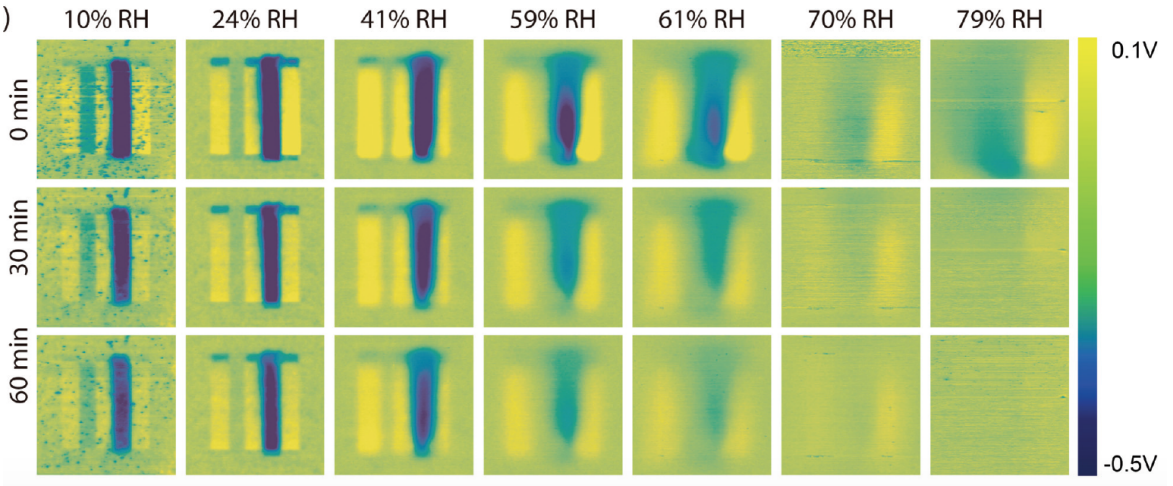

Fig. 2.25 KPFM images of different areas on a 100nm thick $Pb(Zr_{0.2}Ti_{0.8})O_3$ thin film that are poled by positive and negative voltages, as a function of relative humidity and their evolution over time. The bias voltage V for five poled strips from left to right are 8V, 0V, 8V, -8V, 8V. Figure sourced from [13]

The domain relaxation and electrolysis effect all play a part in reducing the surface potential contrast, from 285mV to 119.3mV after 72 hours and so on as monitored by KPFM measurements. Further studies are required to quantify each effect separately e.g., perform the same experiment in a vacuum chamber under a strictly monitored humidity environment. The vacuum chamber at zero humidity eliminates water electrolysis effect and allows one to determine the potential contrast change over time from the self-discharge mechanism only. The experiment can also demonstrate the potential contrast change due to different humidity environment, hence gives a rough estimate of the surface potential contrast change under certain humidity at which the domain engineering step is performed. Figure 2.25

shows an example for such experiments, the surface potential evolution on a 100nm thick $Pb(Zr_{0.2}Ti_{0.8})O_3$ thin film [13]. Though not discussed in the paper [13], it will be useful to extract and plot the surface potential contrast evolution between the third, fourth and fifth strips from the left in order to quantify the reduction of surface potential contrast under different humidity environments.

2.7 Summary

This chapter discusses the patterning of ferroelectric materials, in order to create periodic potentials (square barriers). Section 2.1 to 2.3 introduce the basis of ferroelectric material and the technique PFM to probe (reading and writting) such materials. The domain switching mechanism and the critical domain size which are essential to form engineered domains are also discussed. This work experimentally explored the formation of both 2D and 1D periodic potentials. The minimum dot-to-dot distance for a 2D array that is poled and successfully imaged is 39nm. In terms of 1D arrays, the minimum domain size (the strip width) is 25nm. Section 2.6 demonstrates surface potential measurements, effectively the barrier height. The change in surface potential is measured across 7 days. Finally, it became clear that starting with 1D periodic potentials is more sensible and likely to produce a measurable effect on the graphene band structure. All the working devices discussed in following chapters are made with 1D periodic potentials, resulting in a 1D electrostatic graphene superlattice. Note that after PFM lithography, the following fabrication steps are performed without heat treatment.

Chapter 3

Device Fabrication

This chapter describes the fabrication challenges in the project. The nature of this project, which is to create a graphene superlattice structure via the construction of alternating electric potentials on a multiferroic material (PZT), heralds an intricate device fabrication story. Graphene and PZT, are two very different materials. The main difficulties in the device fabrication are:

1. To perfectly align the periodic domains made by PFM lithography, with the subsequently patterned graphene and electrodes which are situated at pre-designed positions with an accuracy below 10nm.

2. To preserve the potentials as much as possible. Chapter 2 demonstrates that it drops to almost half of the value in 24 hours. Furthermore, It was learned from previous experiments that heating accelerates the decay of potentials and leads to distorted patterns.

3. Without oxygen plasma treatment, PZT is hydrophobic. This results in operational difficulties in the graphene transfer step, which is water-based.

4. Acids like hydrochloric acid (HCl) and hydrogen fluoride (HF), which are commonly used in cleaning transferred graphene, etch the PZT surface and shall be avoided in the process.

5. Repetitive nano processing contaminates the PZT sample. Due to the scarcity of the material, it is necessary to find a sustainable way to remove PMMA and metal residues from the PZT surface before the domain engineering step.

Bearing the above issues in mind, some common techniques in semiconductor device fabrication which jeopardise the functionality of the devices were eliminated, such as acid treatment

and hot plate heating. Eventually, a unique room temperature fabrication process mentioned in Chapter 1 was developed and put in use. The following sections will discuss the equipment and recipes involved, to form this unique process.

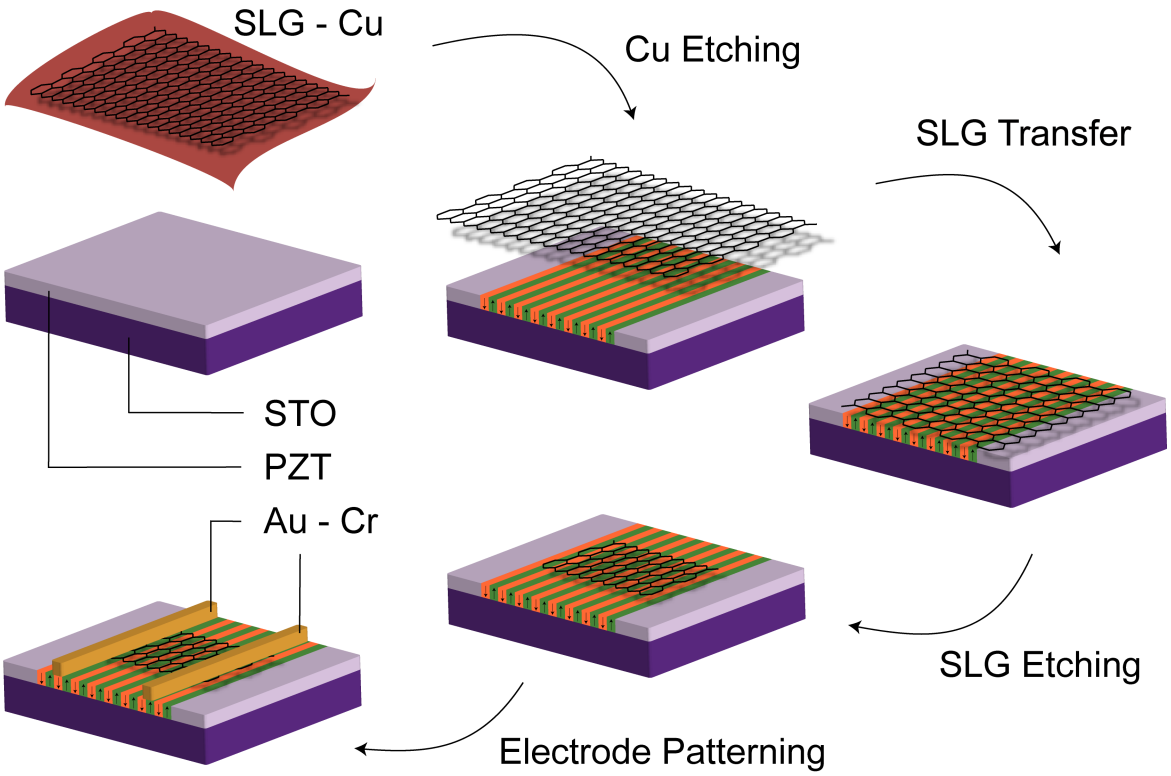

Fig. 3.1 Five Steps in PZT-graphene device fabrication. SLG-Cu: single layer graphene grown on Copper foil); PZT-STO: PZT grown on Strontium Titanate.

First of all, it is essential to outline the six steps in the PZT-graphene device fabrication as revealed in Figure 3.1. The device starts from two materials. They are single layer graphene grown on Copper foil (SLG-Cu) and PZT grown on Strontium Titanate (PZT-STO).

1. **Alignment markers**: two types of alignment markers are patterned by electron-beam lithography followed by electron-beam deposition. PFM markers help to identify the exact locations to carry out PFM lithography in step 2. E-beam alignment markers is of paramount importance to avoid mis-alignment between later e-beam lithography steps 4 and 5.

2. **PZT cleaning**: a non-destructive cleaning method is developed to remove PMMA and metal residues from the PZT surface without deteriorating sample quality.

3. **Domain engineering**: periodic potential arrays are made at multiple predefined locations by PFM lithography, refer to Chapter 2.

4. **Graphene transfer**: the backside copper is wet etched and a piece of single layer graphene is transferred onto the PZT substrate which has undergone step 2 and 3.

5. **Graphene etching**: the transferred graphene was patterned and etched at predefined locations to the designed dimensions by e-beam lithography.

6. **Electrode patterning**: metal electrodes were patterned by electron-beam lithography and deposited by electron-beam deposition on top of all etched graphene strips.

3.1 Equipment and Processes

This section will introduce the equipment deployed in the project. The project is effectively making a modified field effect transistor (FET), so lithography and metal deposition equipment are necessities. Instead of photolithography or sputtering, electron beam lithography (positive resist) and evaporation are chosen. There are a few reasons behind it. Firstly, the project involves small substrates . The size of the acquired PZT pieces are $1cm \times 1cm$ and $0.5cm \times 0.5cm$, other SiO_2 substrates are all below $1cm \times 1cm$. Because getting a good quality PZT sample is very difficult and expensive, it is crucial to plan and arrange devices carefully on the PZT substrate. It is also unavoidable to reuse the remaining space after the fabrication and measurements of each batch of devices. E-beam lithography can make very small patterns and allows changes of device design swiftly on every new batch, without costing a new photomask.
Secondly, one of the decisive points for FET performance is the ohmic contact between graphene and metal electrode. Repetitive processing involving polymers will inevitably lead to higher and higher residual levels. E-beam resist gives fewer and smaller residues than photoresist. There are three nano-lithography steps in total, and electrode patterning which makes the contact between graphene and metal is the last one. Hence, e-beam lithography is more appealing despite the high associated costs.
This section will discuss equipment and processes involved in the device fabrication. Subsection 3.1.1 introduces the electron beam lithography technique that is deployed in the alignment marker step, graphene etching step and electrode patterning step. An example of the dose test is included. Subsection 3.1.2 introduces the electron beam evaporation technique that is deployed in the alignment marker step and electrode patterning step. Subsection 3.1.3 introduces one of the dry etching techniques i.e., oxygen plasma. This is deployed in the graphene transfer step and graphene etching step.

3.1.1 Electron beam lithography

Electron beam lithography is a specialised technique for creating extremely fine patterns, in the order of nanometers. Derived from the early scanning electron microscopes, the technique consists of scanning a beam of electrons across a surface, and use the energy of the electron beam to impart a pattern into a polymer layer. The Crestec 9510CC high resolution e-beam lithography system was deployed. The beam diameter is smaller than 2nm and minimum line width is 10nm, according to specifications. A pattern design was initially done on the compatible software CABL then imported to the E-beam machine in advance.
There are two main varieties of lithography technique, parallel process and serial process. In a serial process such as e-beam lithography, the sample is kept in the chamber for a period of time as the electron beam scans across it at each designed pattern. In a parallel process such as photolithography, a mask is exposed to UV light in front of the sample so the entire sample is exposed at the same time. While electron beam lithography is a direct system that can create arbitrary patterns but photolithography needs a pre-designed mask. Figure 3.2 illustrates the patterning processing steps [14].

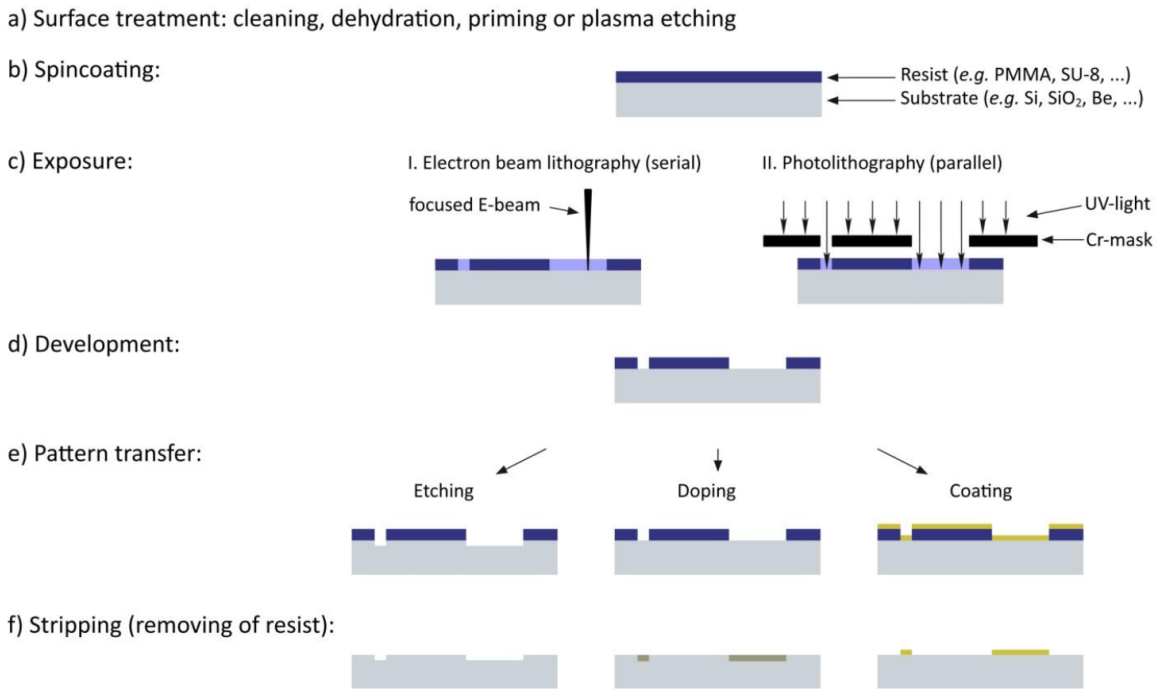

Fig. 3.2 E-beam lithography and photolithography processing steps for positive resist [14]

The sample is coated with a thin layer of e-beam resist, which is chemically modified under exposure to the electron beam [148]. In this work, the positive resist Poly(methyl methacrylate) PMMA is used, at a variety of molecular weights and concentrations, such as

495K A4 (495k Daltons, 4 wt% in anisole), 950K A2 (950k Daltons, 2 wt% in anisole) and 950K A4. The exposed areas of resist are then dissolved in a developer, leaving patterns on the bare substrate. According to different application purposes, it is either followed by metal deposition or etching. Subsequently, the remaining resist is lifted off, leaving the desired structure on the substrate. The size for an e-beam made pattern is limited by several effects [149]:

1. **Spot size** of the electron beam, which is usually a few nanometers. It is restricted by electron optics and degree of focus, position accuracy and astigmatism. At high current and low energy, mutual electrostatic repulsion between electrons within the beam is also more pronounced.

2. **forward scattering**. After the electron beam enters the sample surface, electrons collide with each other elastically and those interactions broaden the beam. It is more likely to happen in thick samples and low incident energies.

3. **backscattering**. After electrons pass through the resist film and penetrate into the substrate. A proportion of them experienced a number of large angle collisions and finally re-enter the resist, not at the same position where they left though. At large incident energies, this leads to exposure patterns appearing microns away from where they should be. Using a thinner substrate could help

4. **Proximity effect**, resulted from backscattering. It is indicative when the writing of a feature increases the exposure of another feature some distance away, leading to overexposure and pattern distortions. The density of features should be taken into account when deciding the proper exposure level.

5. **Secondary electrons**, produced by the inelastic collisions of primary electrons. They are short energy and hence short range electrons but constitute an important factor that limits the ultimate resolution.

6. **Electrostatic charging**, happens when the substrate to write on is insulating. Since there is no pathway for the electrons to escape. Charge build up within the resist and will defocus the electron beam. This can be solved by coating a thin conducting layer of metal or polymer above or below the resist.

The above unwanted interactions lead to an increase in the area of exposed material. An individual recipe to realise the desired feature should take into account the electron-resist and the electron-substrate interactions [14], which include dose time, resist type, resist thickness,

electron beam current, development time and temperature and etc. A dose test is hence necessary before any fabrication takes place on a device. Patterns made with a range of doses ($\mu C/cm^2$) are compared against each other under optical microscope for big features or scanning electron microscope (SEM) for finer structures.
Figure 3.4 shows the result of a dose test after development, under optical microscope. The design pattern in CABL software is shown in Figure 3.3. This pattern is made for the graphene etching process, a large area (coloured in blue) of graphene is exposed and etched away, with the exception of a very tiny strip (white) in the middle. Patterns in (a)-(c) are under-dosed, characterised by different levels of PMMA residues in the exposed areas. A proper dose is in the range between (d) and (f), where the exposed area is properly-dosed and the central tiny strip survives.

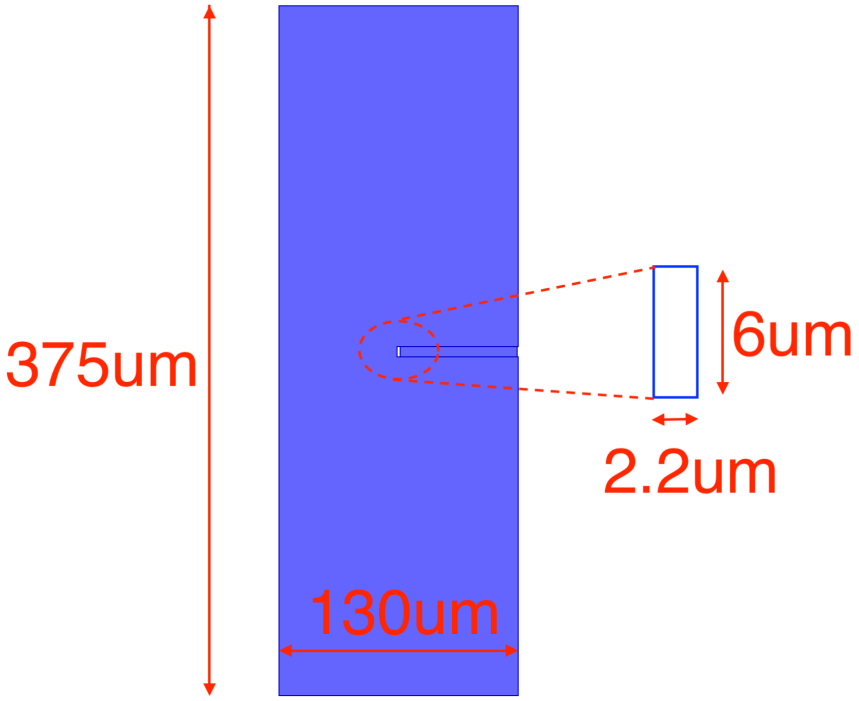

Fig. 3.3 The designed pattern for dose test demonstrated in Figure 3.4. The region coloured in blue is to be exposed and hence etched away. The remaining pattern is the graphene in the middle, of rectangular shape.

Dose (unit μC/cm^2) controls the number of electrons emitted from the electron beam to per unit area. One electron breaks one bond in the PMMA crosslinks, and the damage accumulates. One needs the dose to be high enough to ensure it breaks a sufficient number of bonds in PMMA crosslinks, such that it goes the entire way through the PMMA film. As such, the polymer under exposure can then be dissolved in the developer. Under-dosed

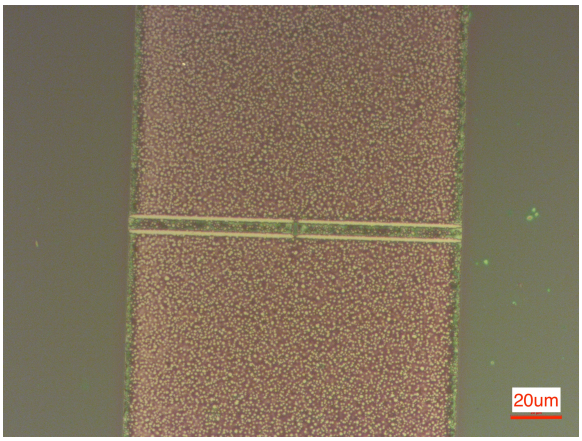

(a) dose $350\mu C/cm^2$

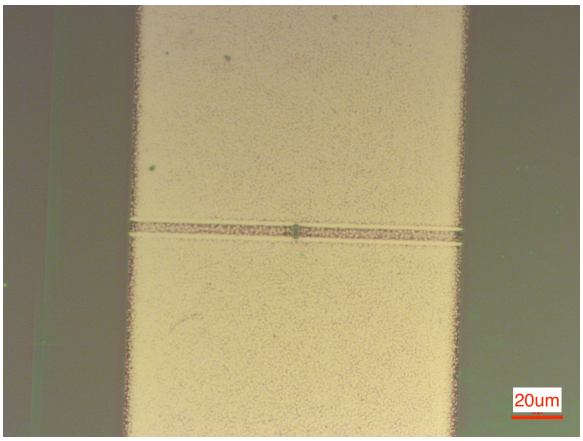

(b) dose $400\mu C/cm^2$

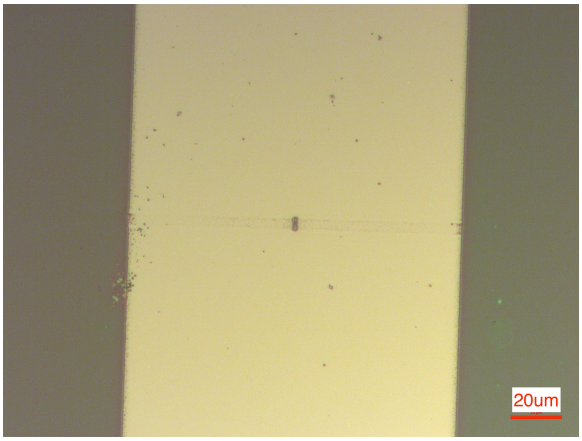

(c) dose $450\mu C/cm^2$

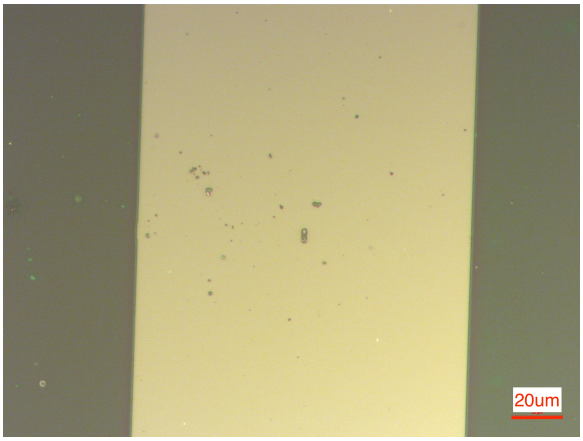

(d) dose $500\mu C/cm^2$

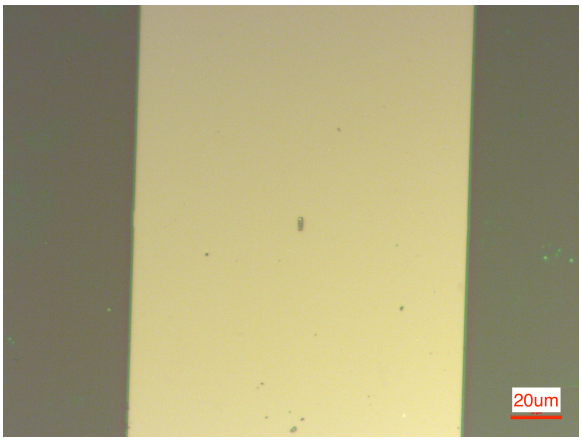

(e) dose $550\mu C/cm^2$

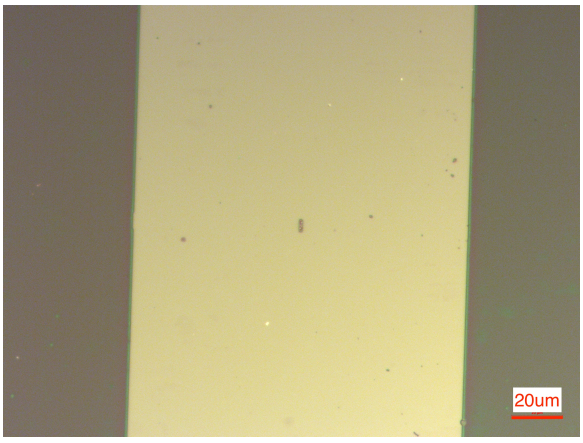

(f) dose $600\mu C/cm^2$

Fig. 3.4 The result of a dose test for graphene etching under optical microscope. The dose increases in alphabetical order. (a)-(c) are under-dosed. A proper dose is in the range between (d) and (f). Scale bars are $20\mu m$.

patterns are typically left with multiple islands of PMMA residues, or in extreme case, a continuous layer of PMMA. PMMA residues are usually several nanometers in size. Under SEM, islands of PMMA residues are clearly visible even after metal deposition takes place. Figure 3.5 shows SEM images for two patterns made by e-beam lithography, followed with metal deposition. The top pattern is properly-dosed whereas the bottom one is under-dosed. Islands of PMMA residues are noticed in the bottom pattern.

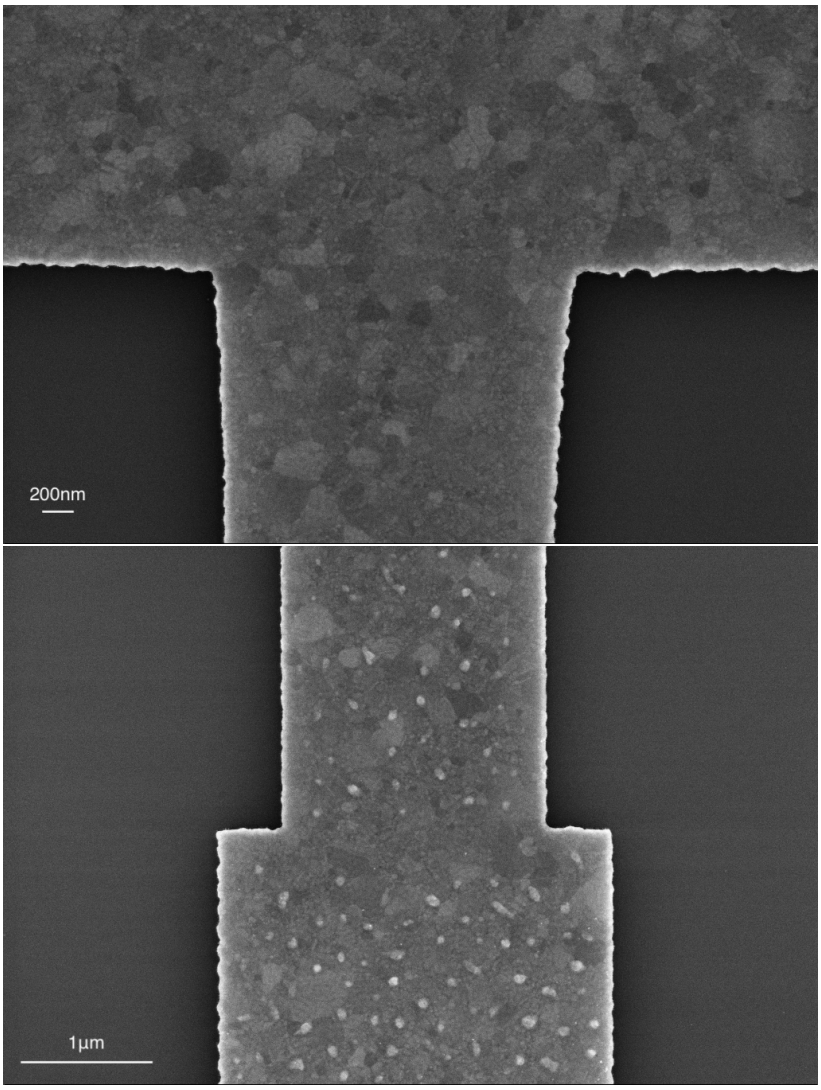

Fig. 3.5 SEM examination of two patterns. Top: properly-dosed. Bottom: under-dosed, islands of PMMA residues are spotted.

The choice of resist and its thickness depends on the applications and subsequent processes. If the lithography is followed by dry etching, the resist should be thick enough to sustain the etching process as well as not compromising the final lift-off. The electron beam current affects the beam diameter. A lower beam current corresponds to a smaller beam diameter,

leading to finer features. For example, 100pA on the Crestec system refers to a beam diameter of 2nm. However, larger beam currents is economical in making big patterns, where resolution is not the top priority. In this project, I use a mixture of 100pA, 1nA and 5nA to strike a balance between resolution and saving time. In terms of the development conditions, a mixture of MIBK and IPA at 1:3 proportion is used.

3.1.2 Electron beam evaporation

Electron beam evaporation (EB-PVD) is a form of physical vapour deposition. It refers to the process where a material within a crucible is melted by heating from a high energy electron beam, and vapour cloud of that material is created in a high vacuum chamber. A target substrate is fixed above the material crucible, at the top of the vacuum chamber. The vapour cloud condenses and forms a uniform material layer on the substrate. Compared to sputtering, EB-PVD usually leads to the formation of larger grains, and a lower adhesion to the substrate [150]. The former gives smoother surface regarding thin film deposition. The latter assists the lift-off process after metal deposition.
This project deploys the Kurt J. Lesker Electron Beam Evaporator (model PVD 75, four-crucible) in the Nanoscience Center. The parameters that can be manipulated are film thickness, deposition rate and beam current. The system can achieve high precision in thickness (0.1Å) with very good manual deposition rate control through adjusting the beam current. The minimum stable deposition rate that can be manually achieved is 0.03Å/s with an error of 0.01Å/s. In most cases, electrodes in this project are fabricated by depositing 5nm chromium (Cr) at a rate $\sim$ 0.3Å/s and 50nm gold (Au) at a rate of $\sim$ 0.5Å/s. EV-PVD is chosen over sputter due to a better deposition rate control. Also, Cr/Au layers made from sputtering required ultrasonic bath to completely lift off, which will destroy the graphene underneath.

3.1.3 Dry etching - oxygen plasma

After patterning graphene by e-beam lithography and development, etching is undertaken in the Diener Femto low power plasma system. Single layer graphene can be removed in oxygen plasma to leave the central graphene strip covered by PMMA, as shown in Figure 3.4. In most cases, the system is set at 50% O_2 concentration and etching time as 25 seconds.

3.2 Alignment markers

Alignment markers are of paramount importance to device fabrication. The device pattern design for e-beam lithography is carried out with reference to the position of alignment markers. The existence of alignment markers is like a bridge that connects between each isolated fabrication step. In step 1, two types of alignment markers are patterned by e-beam lithography followed by e-beam evaporation. One type is e-beam alignment markers. They are standard element for any process involving multiples e-beam lithography steps, hence will not be discussed much in this section. The other type is PFM markers that are specially designed for the graphene-PZT device in this work. It is to make sure that domain engineering (guided by optical microscopy in PFM) is executed at the pre-defined location for graphene etching as well as electrode patterning. Figure 3.6 shows the SEM image of a full device after probe station measurements, with a graphene strip in the center and drain/source electrodes connected to pads out of view.

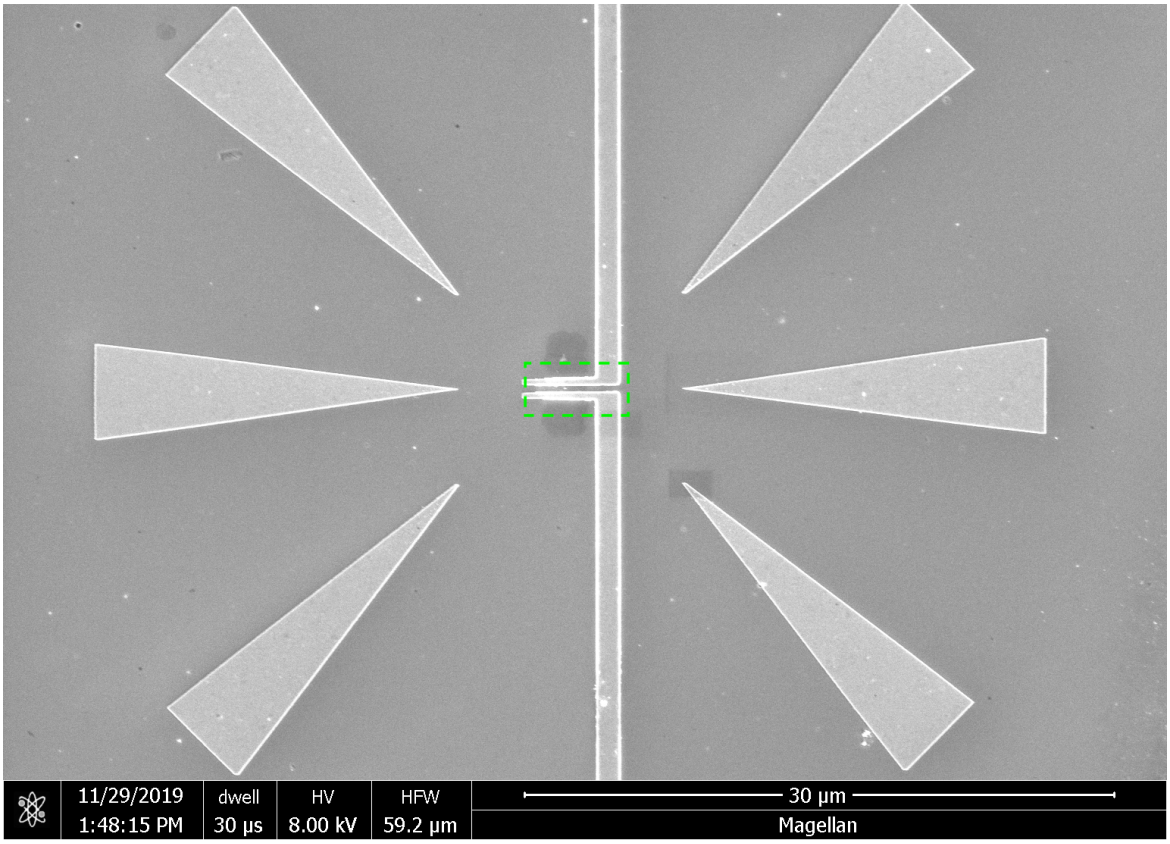

Fig. 3.6 SEM scan of a full device, featuring a six-armed PFM marker, graphene strip in the center, and drain/source electrodes connected to pads out of view. The area circled in green dashed line is where the periodic potentials are patterned.

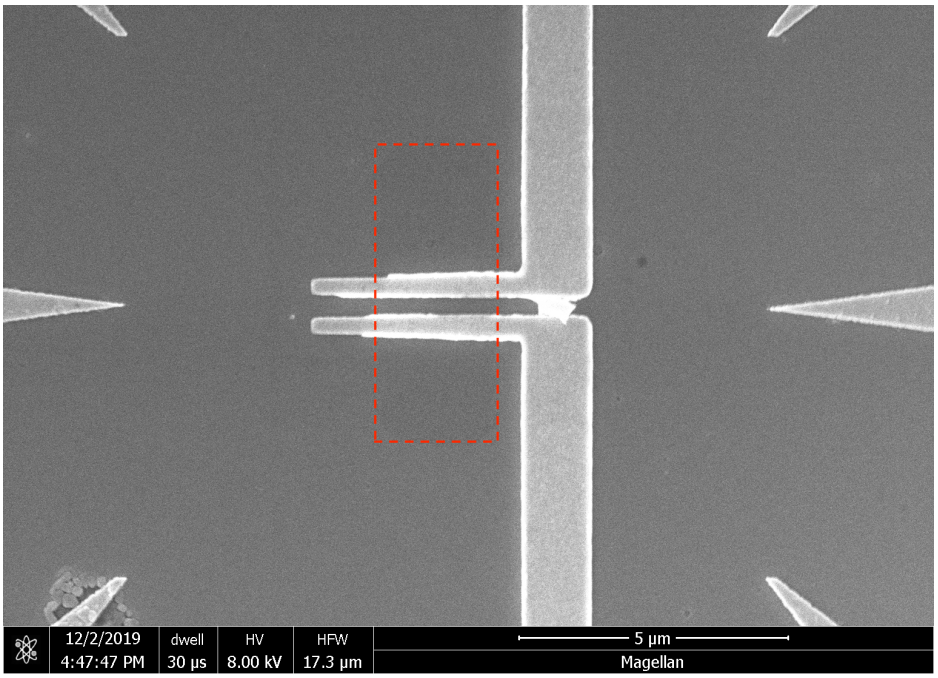

Fig. 3.7 SEM examination of a PFM marker: six apexes of the arms, very sharp and properly-dosed

A single PFM marker assembles the six-fold radial symmetry. All arms are isosceles triangles of identical geometry, with a small apex angle pointing to the center. It defines a central area of $12\mu m \times 10\mu m$. Several dose tests were conducted to compile the recipe outlined in Table 3.1 and put it to use. The resist thickness is measured to be $\sim$180nm. The dose in this recipe gives the sharpest apex as shown in Figure 3.7, which is just properly-dosed at the very edge of the apex. Choosing this dose inevitably results in under-dosed regions as it goes from the apex to the base of the triangular arm. It is shown in Figure 3.8, where PMMA residues are visible. However, the markers can always be successfully lifted off while preserving their shapes. And it does not cause any problem for subsequent processes or measurements as PFM markers don't come into contact with the graphene or periodic potentials.

Table 3.1 Recipe for PFM markers

Step	**Recipe Content**
PMMA Spincoating	950k A4 spun at 6000rpm for 60s & air-dry overnight
E-beam lithography	dose at 700 $\mu C/cm^2$
Development	105 seconds in mixed MIBK and IPA (1:3) solution
E-beam deposition	5nm Cr at 0.3Å/s and 50nm Au at 0.5Å/s
Lift-off	1 hour room temperature acetone bath

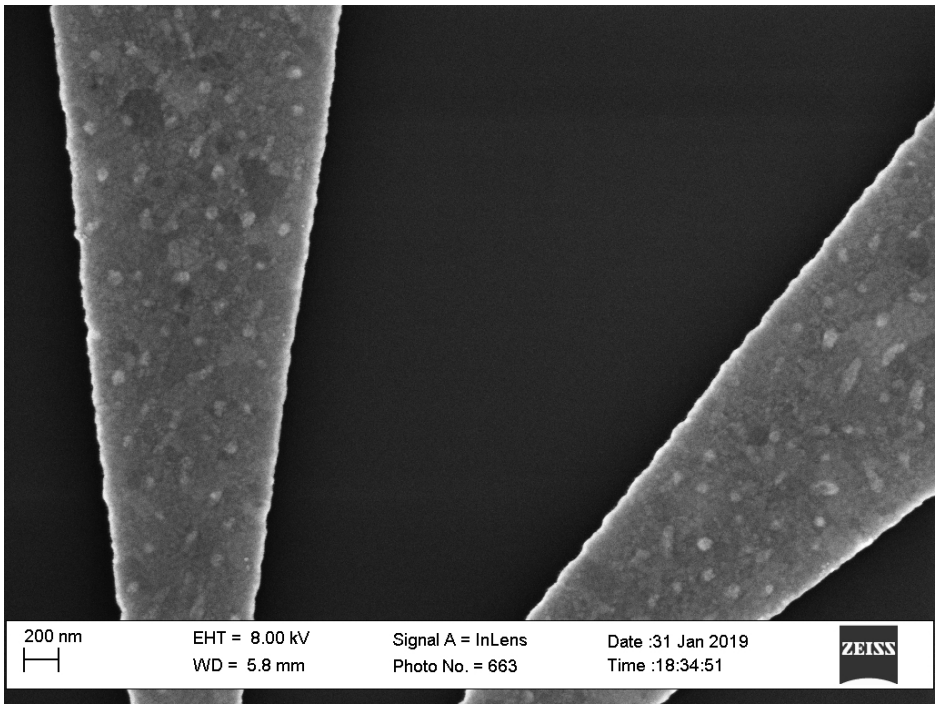

Fig. 3.8 SEM examination of a PFM marker. Top - six apexes of the arms, very sharp and properly-dosed. Bottom - under-dosed regions at the base of the triangular arm.

Figure 3.9 illustrates how to determine the location to conduct PFM lithography for a device. Firstly, the PZT sample with markers is fitted to the AFM stage. It needs to be manually adjusted to give an orthogonal orientation as shown in Figure 3.7; such that the later created 1D domains are at right angles to the etched graphene strip longitudinally, and parallel to the drain/source electrodes. This step relies on patience and operational proficiency. Secondly, a PFM marker is scanned by the AFM tapping mode (top left). Six arms of the PFM marker together point to a region of $12\mu m \times 10\mu m$ (green dashed box) in the middle of the region. Thirdly, one zooms in to select a region of $3.2\mu m \times 1.2\mu m$ (red dashed box) in the center and scan it by AFM tapping mode again. The cross sectional profile shows a height variation within $\pm$ 0.5nm. This falls below the 1nm benchmark value chosen in Chapter 2, hence is acceptable. Lastly, a pre-designed periodic pattern of 20 periods is loaded in the selected region and system executes PFM lithography.
While the $12\mu m \times 10\mu m$ region defined by the PFM marker geometry is fixed, the $3.2\mu m \times 1.2\mu m$ dimension and number of written periods are both variable from device to device. The dimension of the polarised region can be up to $5.5\mu m \times 5.5\mu m$, and the number of periods are in the range of 20 to 50, depending on the polarised region size and periodicity. It is worth mentioning that the polarised region always covers a bigger area than the etched graphene region, between drain/source electrodes. Such that an electron leaving the drain are exposed

immediately, and during its journey to the source it is only exposed to the created periodic potentials. Graphene nano-ribbons fabricated under the same recipe by the same equipment possesses a mean free path as large as 220nm at room temperature [107]. At low temperature e.g. 10K, the value could be several hundred nanometers. The distance between drain and source is between 300∼400nm for all fabricated devices, so electrons are transmitting coherently when they experience the periodic potentials underneath. Thus, it is only the created electrostatic superlattice that accounts for any change in electron transmission in this device.

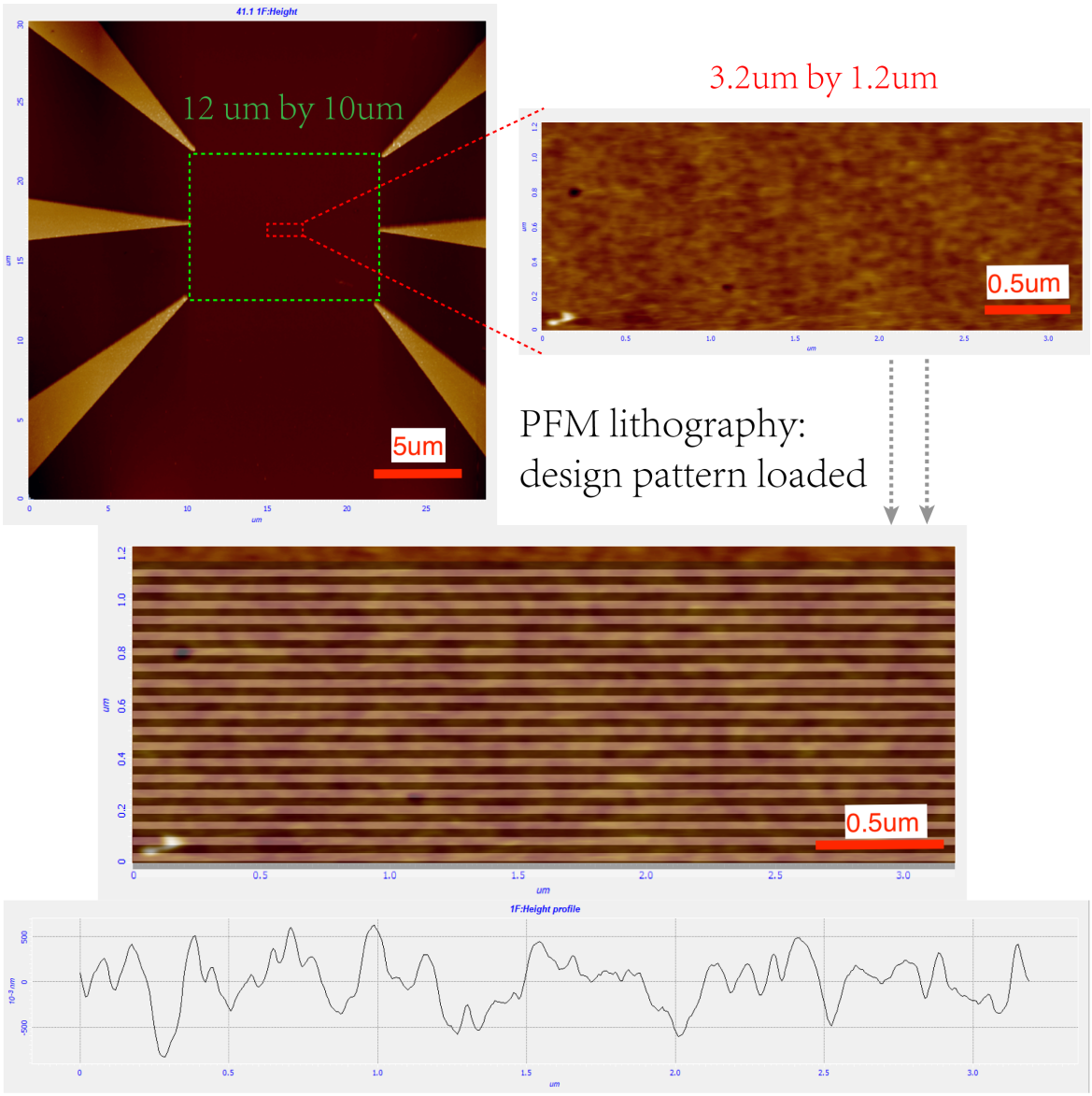

Fig. 3.9 Schematic of how one PFM marker assists in determining the location to carry out PFM lithography for a device

3.3 PZT cleaning

Repetitive processing on one sample unavoidably leads to more and denser contaminants on the PZT surface, typically PMMA and metal residues. Because PZT single crystals are very expensive and extremely difficult to acquire, it makes sense to recycle those pieces and accommodate several batches of devices on one sample. While oxygen plasma and acid treatment both deteriorate PZT sample quality, only acetone and propan-2-ol are deployed to clean the PZT afterwards. Hence, it is reasonable to re-inspect the surface with AFM at multiple locations before starting to fabricate a new batch of devices. It was found that the surfaces are covered with a lot denser contaminants, typically 2-5nm high above the surface. They are a mixture of residues and metal deposits. Figure 3.10 captured an interesting region, where the clean area (left) meets the contaminated area (right), the total scan area is 3μm$\times 3\mu$m. The blue line (showing cross section profile) cuts right through two contaminants.

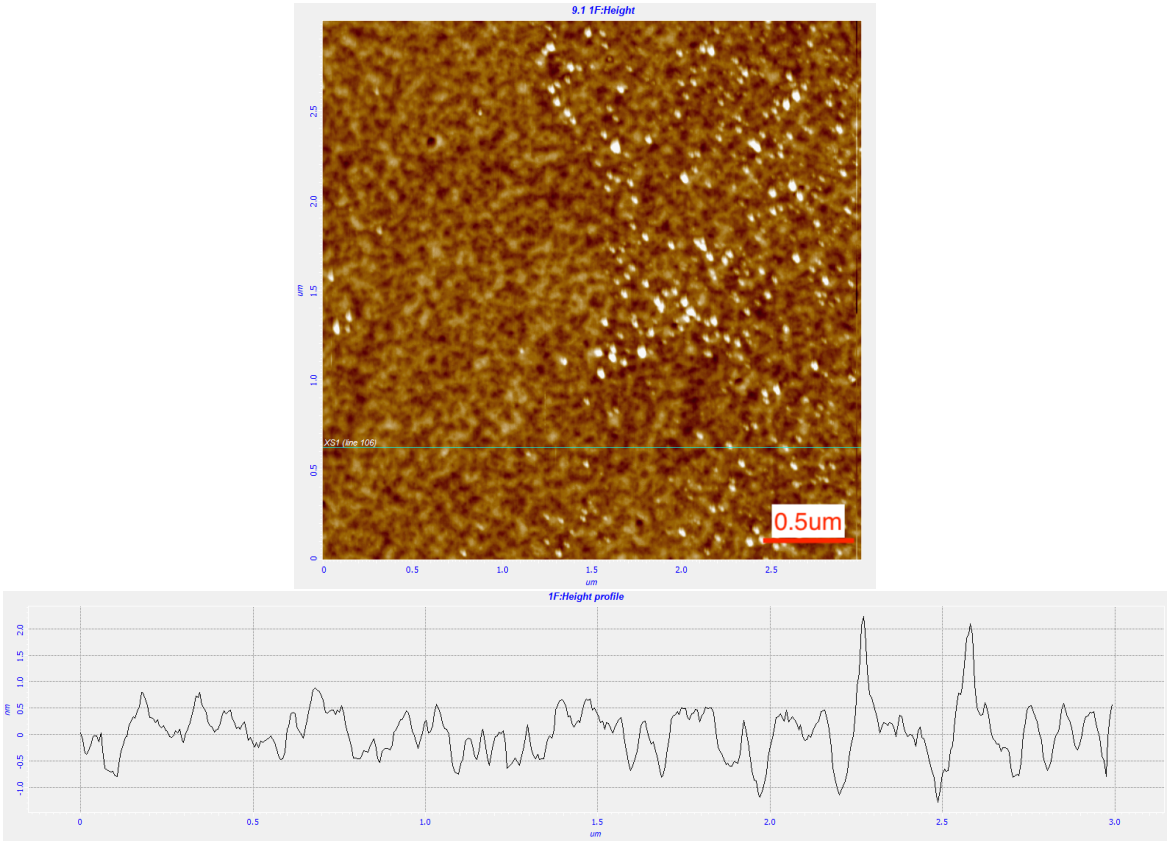

Fig. 3.10 AFM (Height) scan for PZT single crystal after fabrication dose tests. Scan area is 3μm$\times 3\mu$m. The density of bright dots (contaminants) increases significantly. A cross section (blue line location) profile cut through two contaminants and they are both higher than 2nm.

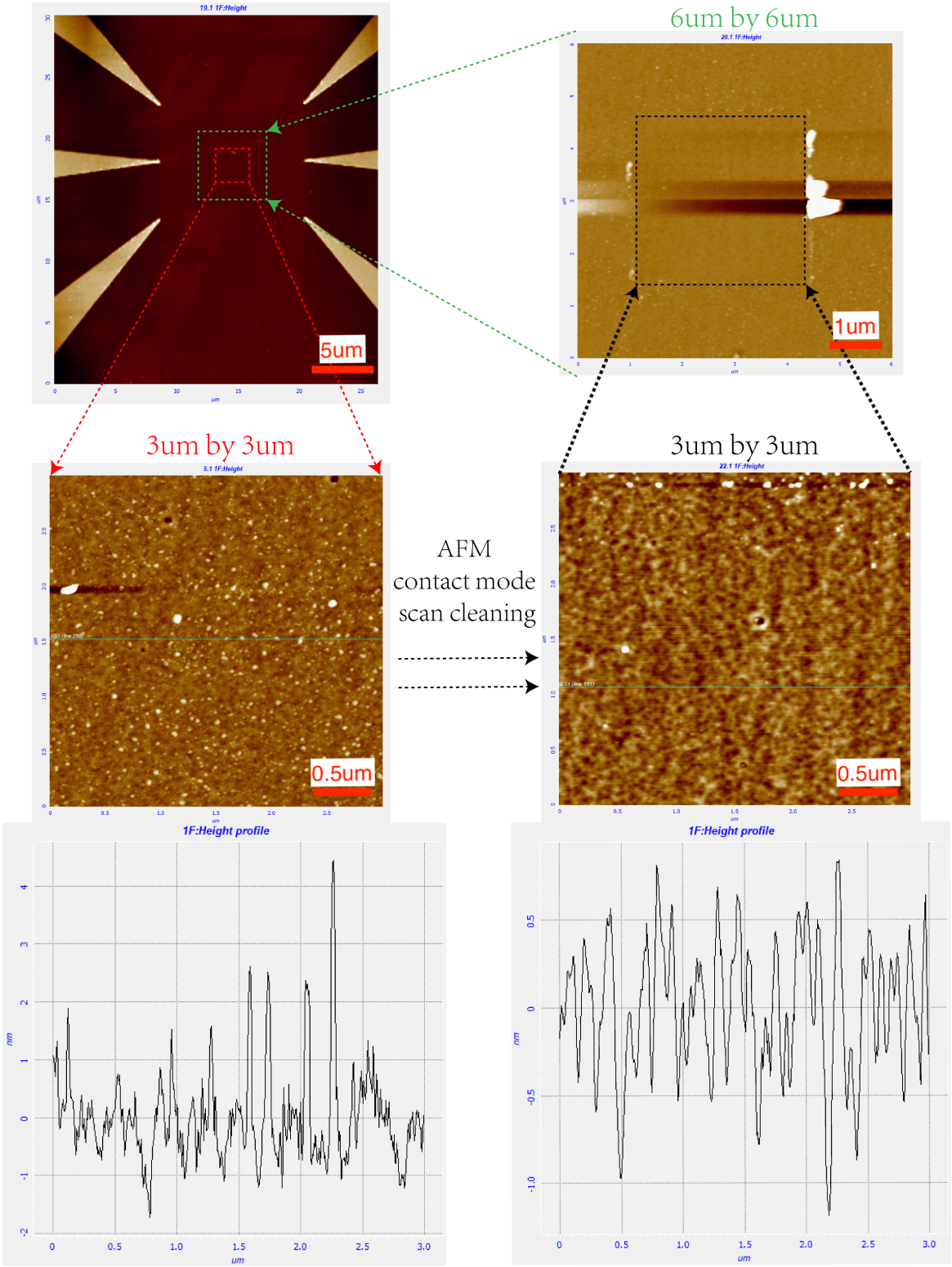

Fig. 3.11 Schematic of AFM contact mode cleaning method

To get rid of those contaminants, the sample underwent ultra-sonication in a warm Acetone bath for 1hr, then warm DI water bath for 2hrs. This removes heavy contaminants that are not stuck tightly to the surface. Then, the sample surface is rubbed on wet lint-free tissues for several rounds, to remove finer residual particles. The aforementioned procedures proved to be extremely useful in general cleaning of a PZT sample after a whole fabrication process is finished, preparing for the next batch of devices. Further cleaning is performed after the alignment marker step, before the domain engineering step starts. Figure 3.11 demonstrates this cleaning method on a dummy device.

Starting from the top left image, a region of 3μm$\times 3\mu$m in the middle of the PFM marker pattern is selected and scanned as outlined in section 3.2. AFM tapping mode imaging (bottom left image) found that the PZT surface is covered with contaminants. The cross-sectional profile (green line) shows that the height of those contaminants are 2$\sim$4nm, which are similar to those shown in Figure 3.10. Multiple chemical cleaning steps (e.g. low concentration acid and oxygen plasma) were unsuccessful in removing these particulates, so a brute-force method was applied in the end and proved useful. The AFM is then switched to contact mode, and the area is scanned again with sufficiently high force to "clean" the area, i.e. to sweep the particulates to the side. A similar work shows that the force is estimated to be between a few nN to tens of nN [151].

The bottom right image is another AFM tapping mode scan after this cleaning step, which illustrates the efficacy of this technique. The corresponding cross-section height profile (green line) revealed $\sim$1nm height variation. Figure 3.12 shows an AFM scan for the PZT single crystal before it undergoes any fabrication processes with similar height variation $\sim$1nm, indicating that this method restores the original surface. AFM images were taken at multiple locations on the sample confirming that this height variation is average across the whole sample area. There are also two noticeable contaminants in the figure. They come from the crystal growth process, whose density is very low.

It should be pointed out that these residues only appear on PZT surfaces - similar processes carried out on SiO_2/Si surfaces result in clean samples. We believe that the surface of ferroelectric materials is charged, and leads to a large electrostatic attraction with polymer and metallic residues from the fabrication processes. Ultimately, a more scaleable and acceptable method for cleaning such surfaces will be required.

Back to Figure 3.11, the top right image zooms out and looks at a 6μm$\times 6\mu$m area enclosing the cleaned region. Residues swept away accumulate only at the left and right sides of the black dashed box, since the AFM is set to scan in non-reversing positive x direction. This is beneficial for later steps in the process, as drain/source electrodes coming from top and bottom wouldn't be obstructed by the lumps which can be as high as 150nm. In practice,

a 10μm$\times$10μm region is usually cleaned in the middle of the PFM markers, as shown in Figure 3.13.

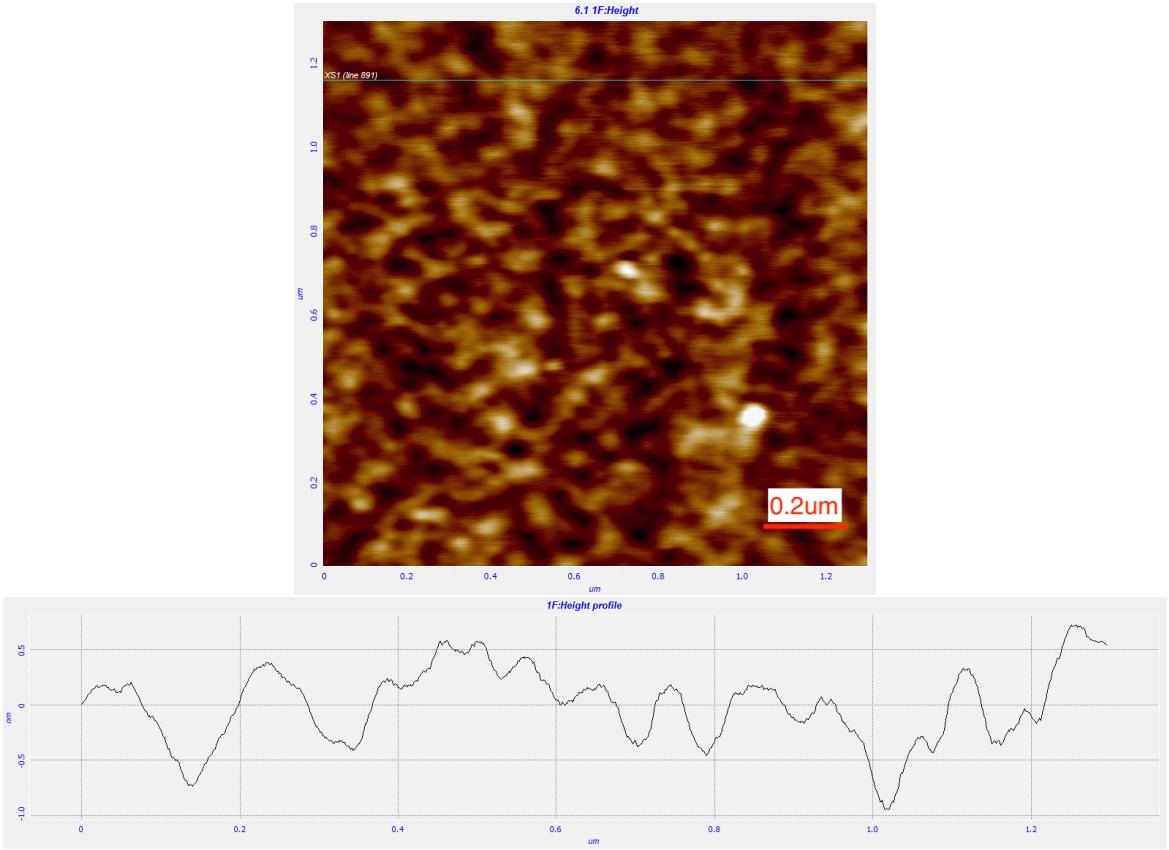

Fig. 3.12 AFM (Height) scan for PZT single crystal before any nano fabrication processes. Scan area is 1.25μm$\times$1.25μm. The two bright dots are contaminants from the crystal growth process, and the density of this kind of contaminants are very low. A cross section (blue line location) profile shows a height variation below 0.55nm.

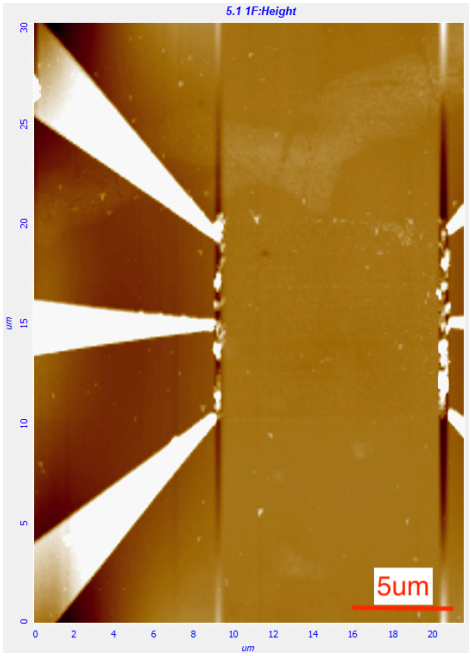

Fig. 3.13 AFM (Height) scan for a PFM marker after using contact mode to clean a 10μm$\times 10\mu$m area in the middle.

3.4 Graphene Transfer

The original method to obtain high-quality graphene samples was by mechanical exfoliation of graphite [44], which produces the highest quality graphene in terms of charge carrier mobility and defect-introduced doping. However, this process is low throughput and unlikely to be industrially scalable. On the other hand, the chemical vapour deposition method has gained more attention in producing wafer-scale monolayer graphene. The most popular substrate to grow CVD graphene on is Cu [152], other substrates of interest include Ni, Pd, Ru, Ir and SiC [153–156, 99]. The CVD grown monolayer graphene can be transferred to other destination substrates. This wet transfer process is illustrated in Figure 3.14.

1. Spin-coating of polymer-based solution onto the graphene/Cu thin film.
2. Backside Copper is etched away in wet etchant bath.
3. The polymer/graphene piece is placed in DI water bath.
4. The polymer/graphene is transferred onto the target substrate followed by heat treatment.
5. The polymer scaffold is removed by chemical dissolution or heat evaporation.
6. Polymer residues from step 5 can be removed by extra annealing.

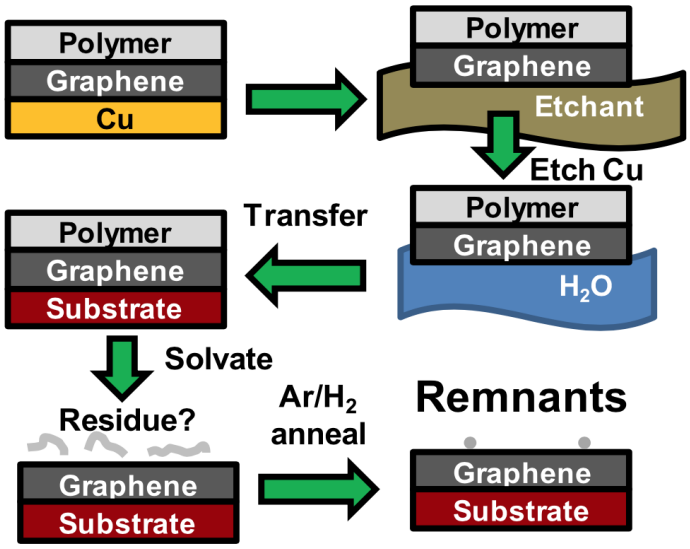

Fig. 3.14 CVD graphene transfer process flow for polymer-based scaffolds [15]

Table 3.2 Recipe to transfer CVD grown graphene on copper to PZT substrate

Step	**Recipe Content**
Material	Monolayer Graphene on Cu from Graphenea
PMMA Spin-coating	950k A4 spun at 3000rpm for 30s & heat to 200°C, 2min
Wet Etching	0.05M aqueous solution of $(NH_4)_2S_2O_8$ [157]
Water bath	2 DI water bath, 15 mins each
Transfer	Onto PZT substrate & air dry overnight
Lift off	1 hour room temperature chloroform bath

Table 3.2 illustrates the graphene transfer recipe in this work, starting from Graphenea's Monolayer Graphene on Cu product. PMMA 950K A4 (molecular weight 950 000 g/mol, 4 wt% in anisole) is picked. The spin-coating recipe will produce a polymer scaffold that is ∼210nm on the graphene/copper composite film. Other polymer-based solutions were also experimented, like PC (poly (bisphenol A carbonate)) and PMMA 950K A2 (molecular weight 950 000 g/mol, 2 wt% in anisole). While a room temperature graphene transfer process was reported to use PC scaffold (molecular weight 45 000 g/mol, 1.5wt% in Chloroform solution) and achieve the lowest residue counts among using PMMA, PLA and PC [15]. PC scaffold proves in practice very difficult to handle. Due to its lower molecular weight and concentration, PC scaffold as well as PMMA 950K A2 are thinner and less strong than PMMA 950K A4. PMMA 950K A4 is picked because it can provide firmer support to the graphene beneath, hence help reduce the possibility of wrinkles or breakage resulted from the transfer process.

Regarding concentration of the etchant, 0.05M of aqueous ammonium persulfate ($(NH_4)_2S_2O_8$) solution is used. Other popular etchant candidates ferric chloride and ferric nitrate are ruled out as they have been reported to p-dope the graphene more heavily [158]. Because the work involves fairly small graphene pieces due to the size of PZT substrate, it is sensible to start with a low concentration solution. At 0.05M, it takes 6 hours to etch a 0.5cm×0.5cm copper film. Higher etching rates are possible by raising the solution concentration. When the etchant recipe is changed to 0.1M, the etching time is reduced to 1.5 hours. In terms of device fabrication, the copper etching process is going at the same time as PZT cleaning and subsequently domain engineering steps. Hence, very large concentration (up to 1M) denoted in some literature [159, 158, 160, 161] is not necessary. Next, the residual etchant is cleaned off the PMMA/graphene film by placing the film into two consecutive water bath for 15 mins. After transferring PMMA/graphene onto PZT substrate, air dry overnight follows instead of heat treatment, as ferroelectric domains depolarise at elevated temperatures. Lastly,

chloroform is deployed to remove the PMMA scaffold since it solvates polymers better than acetone [15].

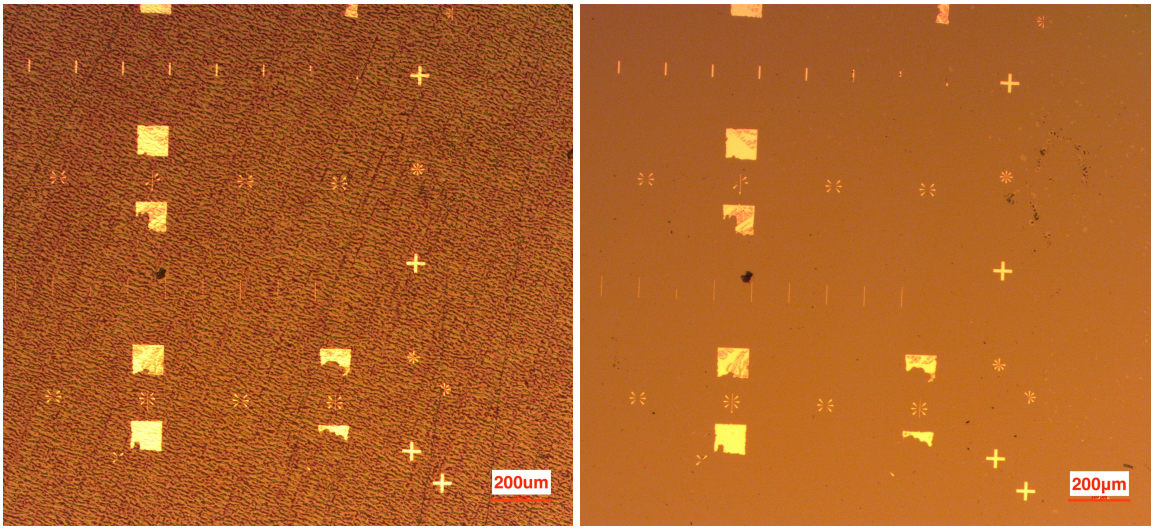

Fig. 3.15 Graphene transferred onto PZT substrate before and after lift off.

Water trapping between graphene and the substrate can be identified by AFM images. Xu *et al.* reported the first water layer of 0.37nm height between graphene and mica (hydrophilic) using AFM [162]. Melios *et al.* utilised frequency-modulated KPFM of a resolution smaller than 20nm to distinguish single layer graphene from multilayer graphene islands on SiO_2, and the surface potential difference between the two is $\sim$ 400mV [163]. This method can potentially be adopted to identify water trapped between graphene and the PZT substrate providing a reasonable surface potential difference between the two.
He *et al.* studied the effect of water droplets on the potential profile on a ferroelectric material $BaTiO_3$. They exposed a poled $BaTiO_3$ sample to an environment of 95% relative humidity for more than 120 minutes so that water droplets nucleate and grow on the ferroelectric surface to more than 10nm high. It was found that the potential difference dropped from 80mV to almost undistinguishable [164]. Another piece of work by Segura et al. suggested that the surface potential difference of a pole PZT ($PbZr_{0.2}Ti_{0.8}O_3$) reduced 20mV when the sample environment's relative humidity is changed from 10% to 80% [165]. The estimations from the literature are under extreme situations that involve extremely long exposure of the surface potential to an extremely high humidity environment. For this work, graphene wet transfer is carried out in a clean room fume hood with continuous dry air circulation. After graphene is transferred onto the PZT substrate, the sample is held vertically and air dried overnight to enable the water to drain away. Since both PZT and graphene are hydrophobic,

the negative effect from water entrapment on the 1D potential is estimated to be around a few tens of milli-volts.

This work also deploys the Monolayer Graphene on Polymer Film product from Graphenea, for which the transfer process starts from the water bath step. Figure 3.15 shows a single layer graphene transferred onto PZT substrate before and after lift off. Graphene is observed to be invisible on PZT substrate. Therefore, an extra piece of graphene is usually transferred to other substrates where graphene is visible such as a silicon wafer with 300nm SiO_2 coating. Figure 3.16 shows an SEM scan of graphene transferred onto silicon substrate. The surface topography inspected under AFM tapping mode is shown in Figure 3.17. The root-mean-square roughness of the depicted area is 0.236nm, which is excellent compared to the benchmark work in reference [166].

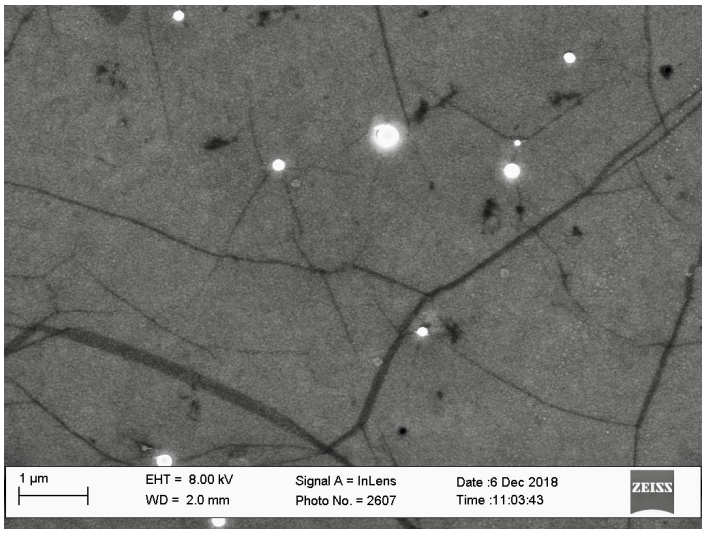

Fig. 3.16 SEM san of monolayer graphene transferred to silicon substrate

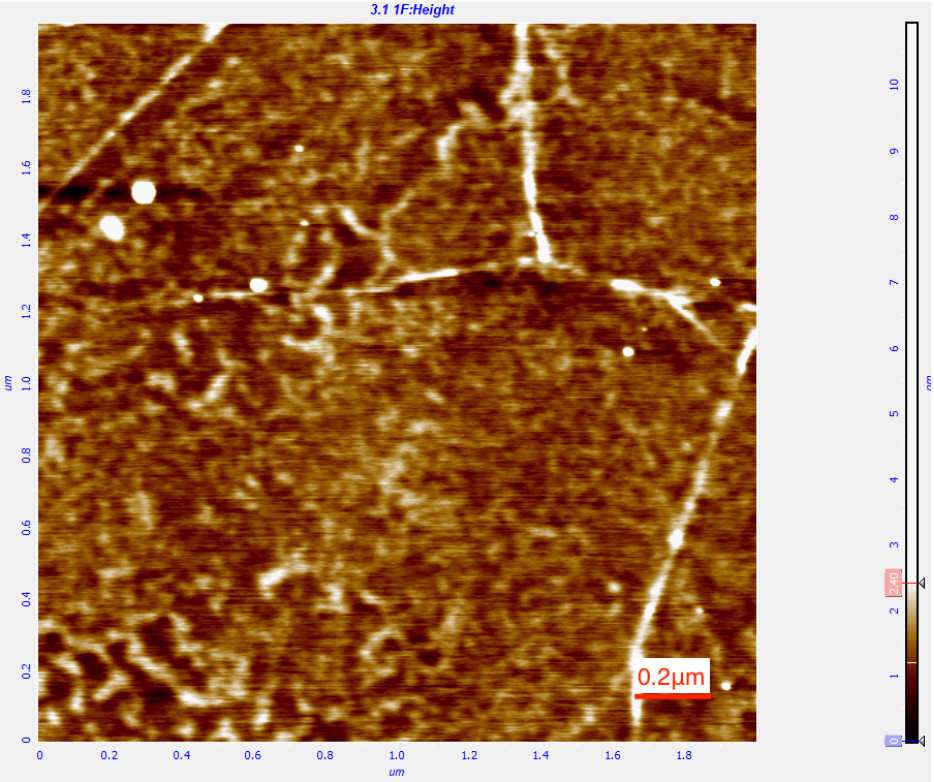

Fig. 3.17 AFM san of monolayer graphene transferred to silicon substrate

3.5 Graphene Etching

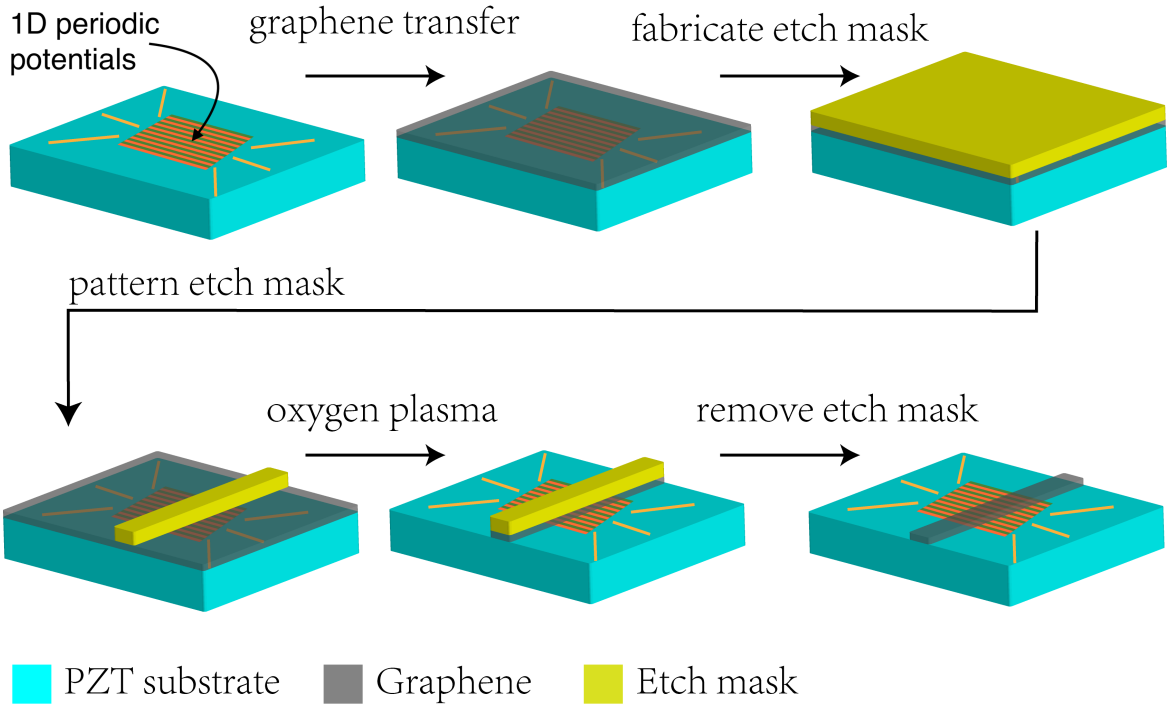

Fig. 3.18 Schematic for the graphene etching step. This step started with the top left, where the PFM alignment markers have been fabricated and the domain engineering step has produced 1D periodic potentials on the PZT surface.

Table 3.3 Recipe to pattern and etch graphene on PZT substrate

Step	**Recipe Content**
Material	Self transferred graphene on PZT substrate
PMMA etch mask	950k A4 spun at 3000rpm for 30s & air dry overnight
E-beam lithography	dose at 550 $\mu C/cm^2$
Development	105 seconds in mixed MIBK and IPA (1:3) solution
Dry Etching	50% O_2 concentration, 25s
Lift-off	1 hour room temperature acetone bath, no agitation

Figure 3.18 and Table 3.3 demonstrate the fabrication of a graphene strip and the relevant recipe. The polymer PMMA (positive resist) is deployed as the etch mask with time and complexity factors taking into account. Some researchers have reported using metal etch masks and achieved very thin graphene ribbons [167, 107]. This method would add metal deposition and extra lift off steps to the process, hence stretches the time before taking

electrical measurements on the device. The potential difference between the positive and negatively polarised domains is constantly decreasing, which then constantly reduces the electrostatic superlattice effect on the graphene. Furthermore, the graphene width requirement of this work is not down to tens of nanometer. The graphene strips just need to be narrower than the periodically patterned domains, as shown in the schematic above and also in Figure 3.1. This design guarantees that electrons between drain and source experience the periodic potentials only. Otherwise, a proportion of electrons will travel through paths where there are no periodic potentials and hence experience no graphene superlattice effect. Mixing behaviours of those two electron populations is expected to make it difficult to observe the pure graphene superlattice effect via electrical measurements. The whole etch mask is exposed to an electron beam, leaving only the thin graphene strip in the middle. Oxygen plasma is deployed in graphene dry etching, followed by standard lift off in acetone bath. Figure 3.19 shows two etched graphene strips after development.

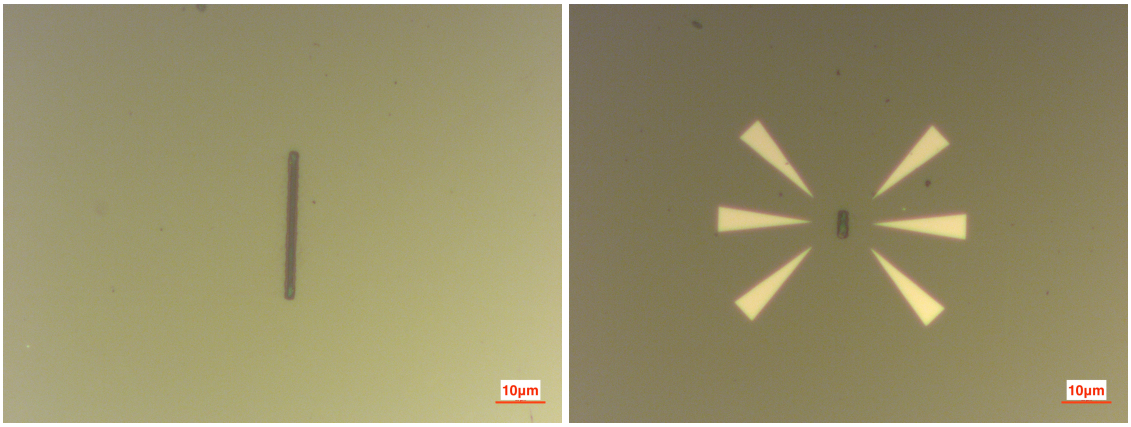

Fig. 3.19 Optical microscope images of two etched graphene strips covered by PMMA etch mask, on PZT substrate. Left: 29.885μm$\times$1.640μm strip; right: 5.438μm$\times$1.867μm strip in the center of a PFM marker pattern

3.6 Electrode Patterning

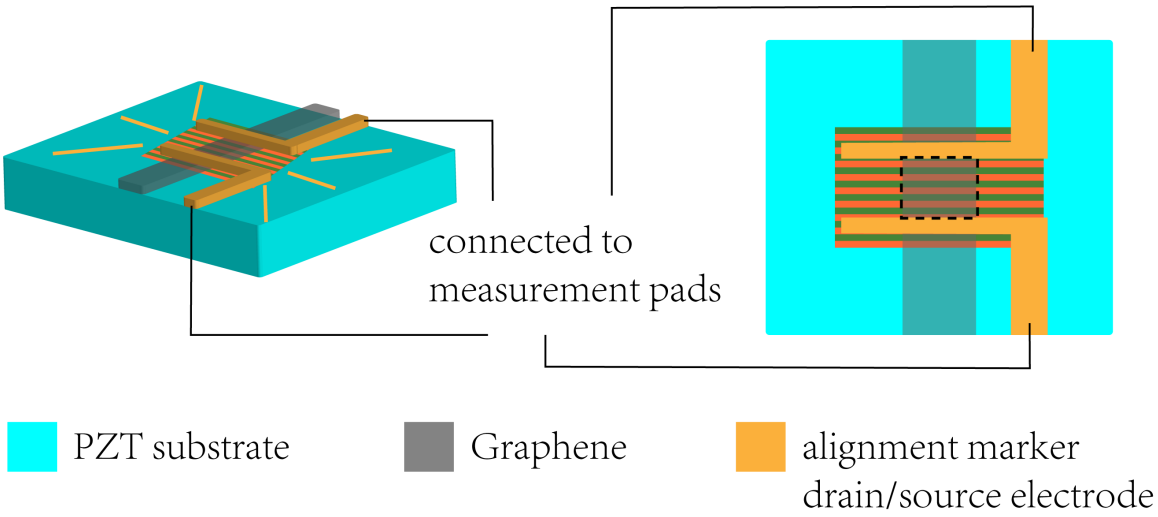

Fig. 3.20 Schematic of drain/source electrodes, 3D view (left) and top-down view (right). The alternating green and orange strips refer to 1D periodic potentials created in the domain engineering step.

The last step is to fabricate drain/source electrodes and the extended pads for electrical measurements. Figure 3.20 shows the schematic of a completed device after patterning drain/source electrodes. In the left, the 3D model is added with two electrodes on the basis of Figure 3.18. The 1D diagram in the right demonstrates that the distance between electrodes should be shorter than that of periodic domains. Hence the electrons inside the active area (circled in black dashed box) only experience the periodic potentials caused by the positive and negative polarisations of PZT beneath. This is analogous to the reason why graphene strips are narrower than the patterned domains, discussed in section 3.5.
Figure 3.21 shows a completed device fabricated following the steps shown in Figure 3.1 and 3.20. Graphene nanoribbons fabricated under the same recipe by the same equipment possess a mean free path as large as 220nm at room temperature [107]. Under low temperature e.g. 10K, it would be larger (hundreds of nanometer order). The distance between drain/source electrodes is around 300nm for this device, which is expected to be lower than the mean free path of electrons in graphene, under low temperatures. Electrons should be able to transmit coherently between the drain and source. Thus any change in their behaviours which is later observed by electrical characterisations, is purely due to the periodic disturbances exerted by the electrostatic superlattice produced from PFM lithography. The corresponding recipe is outlined in Table 3.4. The dose here (1000 $\mu C/cm^2$) is sufficiently high to ensure no PMMA residues after development, such that graphene is in ohmic contact with the electrodes.

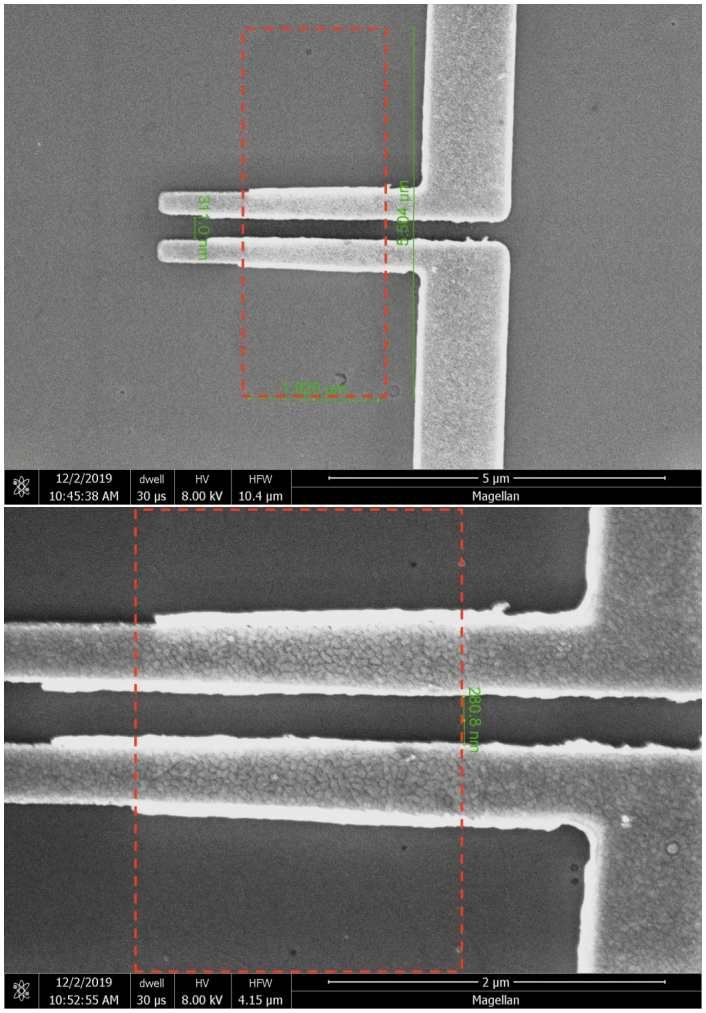

Fig. 3.21 SEM scan of a completed device. The graphene regions are emphasised by red dashed boxes. The dimension of graphene is measured at 5.438μm$\times 1.867\mu$m for this device while the distance between drain/source electrodes is measured between 280.8$\sim$311.0nm.

Table 3.4 Recipe for patterning drain/source electrodes

Step	**Recipe Content**
PMMA Spincoating	950k A4 spun at 6000rpm for 60s & air-dry overnight
E-beam lithography	dose at 1000 $\mu C/cm^2$
Development	105 seconds in mixed MIBK and IPA (1:3) solution
E-beam deposition	5nm Cr at 0.3Å/s and 50nm Au at 0.5Å/s
Lift-off	2 hour room temperature acetone bath

There are several setbacks in the fabrication process, mostly to do with the structure of the device. Firstly, in order to enable coherent transport of electrons between drain and source, the size of the device is kept around 300nm∼400nm. This distance between two electrodes is very small, and it is very tricky for a successful lift-off even for properly-dosed areas. Secondly, the fabrication steps outlined in this work produces a complicated structure including PFM alignment markers made very close to the graphene strip and patterned electrodes. Although they are necessary in integrating the domain engineering step with subsequent nano fabrication steps, the existence of them has caused challenges in the lift-off process as well. Figure 3.22 displays several SEM images on unsuccessful lift-off, where the electrode patterns are all properly-dosed. Note that graphene FET devices of similar scale fabricated on SiO_2/Si substrates do not come with so many lift-off failures. E-beam lithography followed by metal deposition is easier to lift-off on SiO_2/Si substrates. It is believed that the roughness of PZT surface has contributed to the low yield rate in device fabrication of the PZT-graphene FET devices, as well as poor contact between the deposited metal and PZT surface.

3.7 Summary

This chapter illustrates the device fabrication process for the PZT-graphene FET device in this work. There are six steps involved: alignment markers, PZT cleaning, domain engineering (refer to Chapter 2), graphene transfer, graphene etching, and electrode patterning. Detailed recipes for each step and schematics to connect between each step are all included and discussed. The self-designed PFM alignment markers in section 3.2 is essential in aligning the periodic domains created by PFM lithography, with the subsequently etched graphene and patterned electrodes which are situated at pre-designed positions. The eliminating of heating throughout the six steps helps preserve the created potentials as much as possible. A non-destructive PZT cleaning technique in section 3.3 avoids the use of harsh chemicals that would otherwise deteriorate the surface. It proved to be efficient in removing residues from previous fabrication cycles. The size of device is kept between 300nm∼400nm in this work in order for electron coherent transport between electrodes. The complicated structure and small scale of the PZT-graphene structure, together with the complexity of the PZT surface, have jointly lead to a low device yield rate.

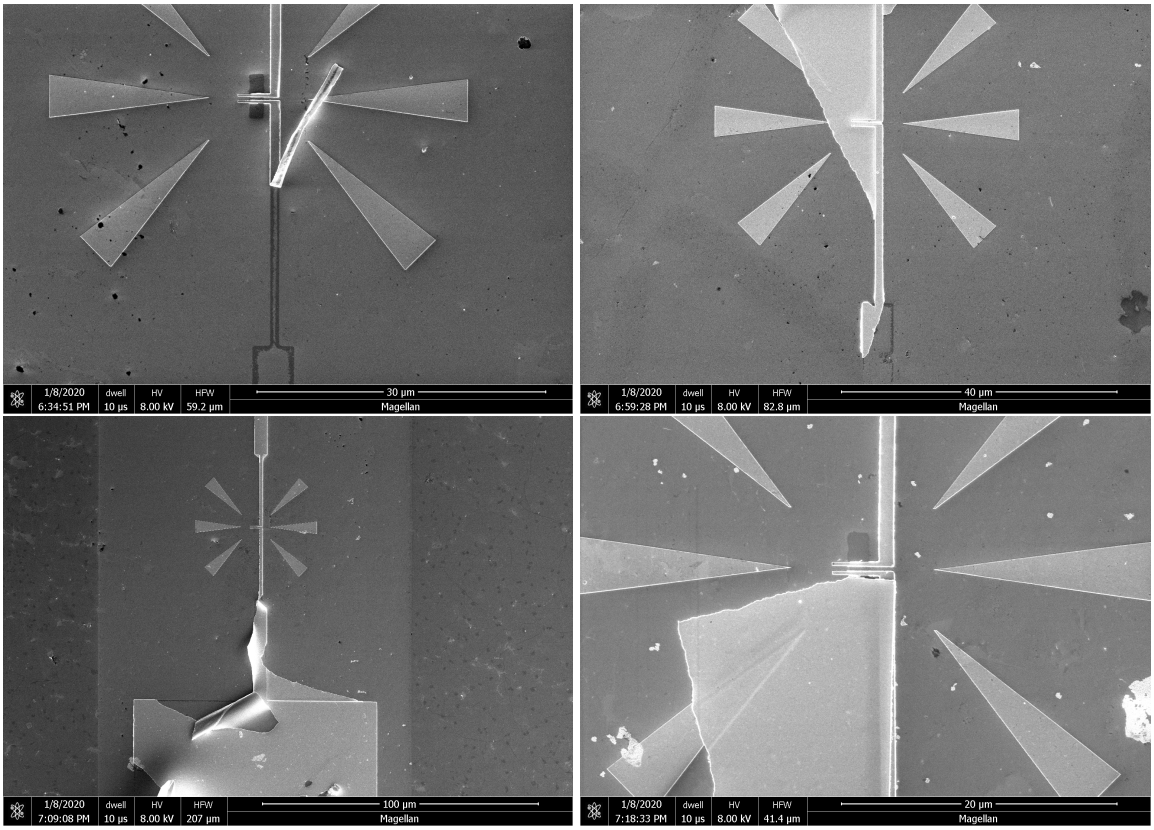

Fig. 3.22 SEM images on unsuccessful lift-off. Top left: a free-hanging electrode arm which breaks half way. Top right: the majority of the electrode area cannot be lifted off. Bottom left: an electrode arm breaks half way. Bottom right: the majority of the electrode area cannot be lifted off, which covers part of the graphene strip.

Chapter 4

Electrical Characterisation

This chapter will discuss the electrical measurement results for the PZT-graphene device. Chapter 2 and 3 have detailed preparations on the device samples, which includes ferroelectric domain engineering and complex nano-fabrication techniques to accommodate two very different materials. The end product is a PZT-graphene device as shown in Figure 4.1. A piece of single crystal thin film PZT grown on strontium titanate substrate undergoes domain engineering to create alternating rectangular regions of 180° phase difference (Figure 2.21 in Chapter 2) in polarisation directions. This leads to a periodic potential pattern. With single layer graphene transferred on top, this structure qualifies as an electrostatic graphene superlattice (EGSL).

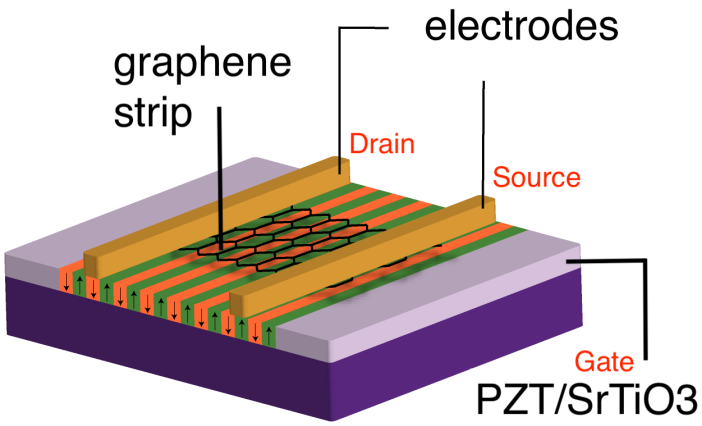

Fig. 4.1 The PZT-graphene device.

Several theoretical papers and simulation models have predicted modifications to graphene's band structure through construction of EGSLs [5, 17, 106, 168–178], amid no experimental reports. One of the effects of periodic potentials on Graphene's band structure is to introduce

an energy gap at the superlattice Brillouin Zone (SBZ). New massless Dirac fermions are generated due to the confinement effects between the barriers [106]. Additional Dirac points in the energy spectrum of graphene are created. The propagation of charge carriers through GSL is highly anisotropic, hence leads to modulation in carrier velocities and emergence of energy minibands. Collectively these will be measurable as a broadening of the current valley near the CNP point and variations in conductance.

In this work, the periodic potentials caused by periodically poled domains take the role of 1D square barriers. It has been discussed in Chapter 1 that electron transport through 1D graphene superlattice is highly anisotropic [17]. At normal incidence, electrons encountering a potential barrier transmit perfectly through it due to Klein tunnelling. Experimentally, it is difficult to control the momentum of electrons parallel (p_x) and perpendicular (p_y) to the direction of travel. As there will be a range of angles in incidence, electron transmission probability through a series of potential barriers is not 1, but will be affected to an extent. And hence the problem needs to be treated as a 2D problem despite that the periodic potential is 1D. This leads to a complex relationship between transmission probability and non-zero incident angle of electron [2, 17].

The modulation of transmission probability is manifested through a change in conductance, due to the simple relationship between the two. To make sure the change in conductance is as noticeable as possible, coherent transport should be maintained throughout the electron journey before and after the series of 1D barriers. Graphene nano-ribbons fabricated under same recipe by same equipments possesses a mean free path as large as 220nm at room temperature[107]. Under low temperature e.g. 10K, it will be larger. To maintain coherent transport between drain/source electrodes, firstly the graphene channel length between drain/source electrodes is kept between 300nm and 400nm, below the expected graphene mean free path at low temperature e.g. 10K. Such that phase randomisation by scattering between electrons is refrained in the structure to a large extent.

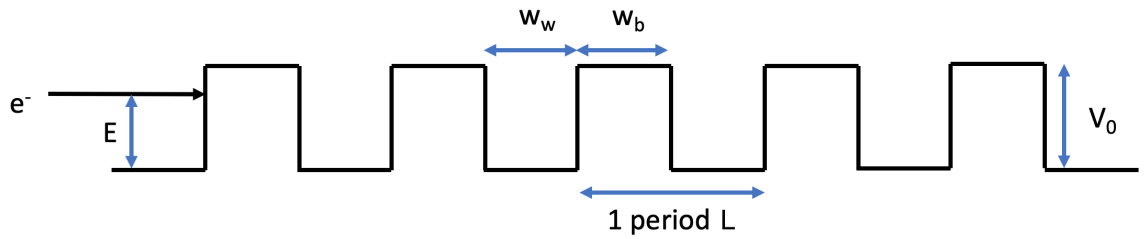

Fig. 4.2 1D Square barriers of height V_0. The barrier and well width are w_b and w_w.

Secondly, the graphene channel region is smaller than the periodic potential region to eliminate the situation that electrons avoid the barriers and take side path. The above two

points, together with the theoretical minimum ferroelectric domain size which is 20nm$\sim$40nm [11], determine the number of barriers/wells in such PZT-graphene devices. In Figure 4.2, an electron with incident energy E encounters a finite number of 1D square barriers. One period L include a barrier with width w_b and a well with width w_w. The height of the barriers is V_0. The work reported in this thesis experimentally confirmed previous theories and predictions that the presence of periodic potentials can be used to alter the band structure of single layer graphene. Electrical characterisation results of the PZT-graphene devices will be presented in this chapter, with comparison to reference devices. While reference devices are PZT-graphene devices prepared in the same way, eliminating the domain engineering step. It will be seen later that the electrostatic graphene superlattice lead to a flat region near the graphene's minimum conductivity point (the bottom of gate voltage sweep curves) along with variations in conductance.

4.1 Device measurements

The measurements are carried out in a cryogenic Lakeshore probe station connected to a semiconductor parameter analyser. Tests run under vacuum conditions (10^{-8} Torr range), at a range of temperatures from 10K to 293K. Two probes are deployed for the resistance measurement. A voltage sweep of 0 to V_1 is applied across the graphene strip between two electrodes, and the corresponding currents through graphene at each voltage values are measured. Resistance of the graphene device can be extracted from the gradient of the I-V curve, as shown in Figure 4.3. As graphene is not visible on PZT substrate, resistance measurements are deployed at the very beginning of the measurement stage, to confirm the success of fabricating each single device on the sample.

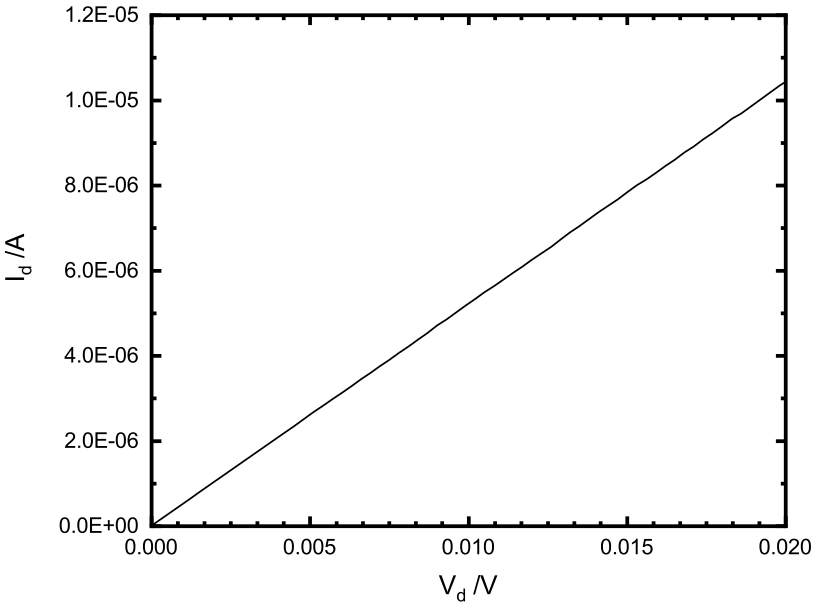

Fig. 4.3 Resistance measurement of a graphene device on PZT, the resistance is equal to V_d/I_d and is 1.92 kΩ.

Gate sweep measurements is then introduced, which deploys two probes connected to two electrodes, acting as drain and source. In this type of measurement, the voltage across drain and source (V_ds) is fixed, and the current flowing through the drain and source (I_d) is measured on sweeping the gate voltage (V_g). The gating is provided by PZT thin film sitting on a conducting strontium titanate substrate. The sample is fitted to the conductive stage which applies back gate voltage. Sweeping gate voltage modulates the charge carrier density in the graphene and moves its Fermi level along the linear dispersion spectrum. Figure 4.4

shows the linear energy dispersion of graphene, which is given by $E = \pm\hbar v_F \vec{k}$. Conduction and valence bands meet at the Dirac point. The Dirac point is the single point in the band structure which generates zero density of states. This means that there are no states to occupy here hence no carriers contributing to electronic transport. For intrinsic graphene, the fermi level sits at the Dirac point. For extrinsic graphene, the fermi level either lies in the electron conduction regime (n-type doped), or in the hole conduction regime (p-type doped). With back gate voltage, E_F is shifted away from the Dirac point, into hole or electron conduction regime. The conductance G_d increases with increase in gate voltage. This relates to the increase in carrier concentration n, which contributes to electronic transport. Therefore, measuring the gate sweep curve (I_d - V_g) is producing a curve of G_d - n.

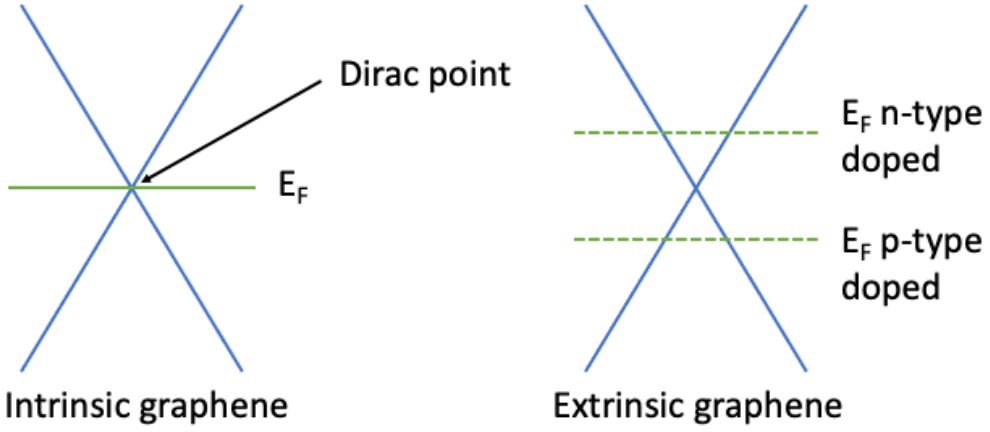

Fig. 4.4 The linear energy dispersion of graphene. For intrinsic graphene, the fermi level is at the Dirac point. For extrinsic graphene, the fermi level either lies in in the electron conduction regime (n-type doped), or in the hole conduction regime (p-type doped).

In this work, the gate voltage sweep must not extend beyond the voltage value that corresponds to the PZT coercive field, which is ∼3.5V for this sample. This is to avoid switching the poled ferroelectric domains between the drain and source electrodes during measurements. With intrinsic graphene, zero back gate voltage ($V_g = 0$) refers to the Fermi level sitting at the Dirac point, which refers to the minimum conductivity for the material. As graphene is known to be unintentionally doped in ambient environment, a non-zero gate voltage is usually required to restore its Fermi level back to the minimum conductivity. This gate voltage is known as the charge neutrality point (CNP). Figure 4.5 shows a room temperature

drain current vs gate voltage (I_d - V_g) curve on a reference GFET device. It is parabolic in shape and the CNP is characterised by the gate voltage that causes the lowest current through graphene. A positive (negative) CNP value indicates that the graphene is p-type (n-type) doped.

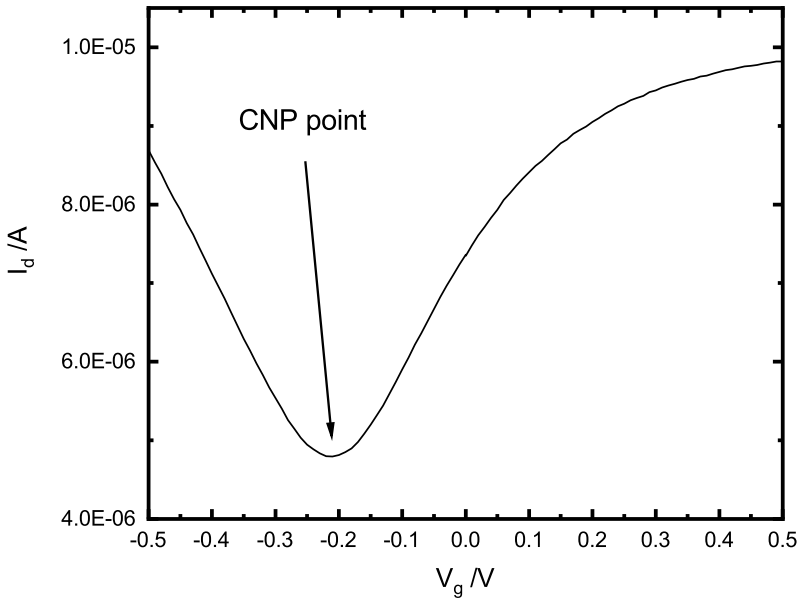

Fig. 4.5 Gate sweep measurement of a GFET device. The CNP point here is at -0.21V, indicating that the graphene is slightly n-doped.

Here, the value is -0.21V, indicating that the graphene is slightly n-doped. While graphene on SiO_2/Si substrate is usually p-doped, the graphene made on PZT substrate could be slightly n-doped or p-doped, due to the intrinsic polarisation in PZT which is different in different regions. This is because that the size of the device (300∼400nm) is comparable to a natural ferroelectric domain (several hundred nm∼μm), the doping in the graphene is likely to be affected by the polarisation charge in the PZT beneath. Note that the CNP values from PZT-graphene devices in this work are typically below $\pm$1.5V.

However, not all devices that survived the fabrication process display the normal CNP curve in Figure 4.5. Chapter 3 discussed several setbacks in the fabrication process, here in the measurement step the yield rate is further reduced by short circuits and graphene quality. In terms of the short circuit problem, Figure 4.6 shows a typical I_d - V_g measurements recorded from such devices. Varying the gate voltage has no effect on the drain current. The drain current keeps almost the same value across a range of gate voltage. While in field effect

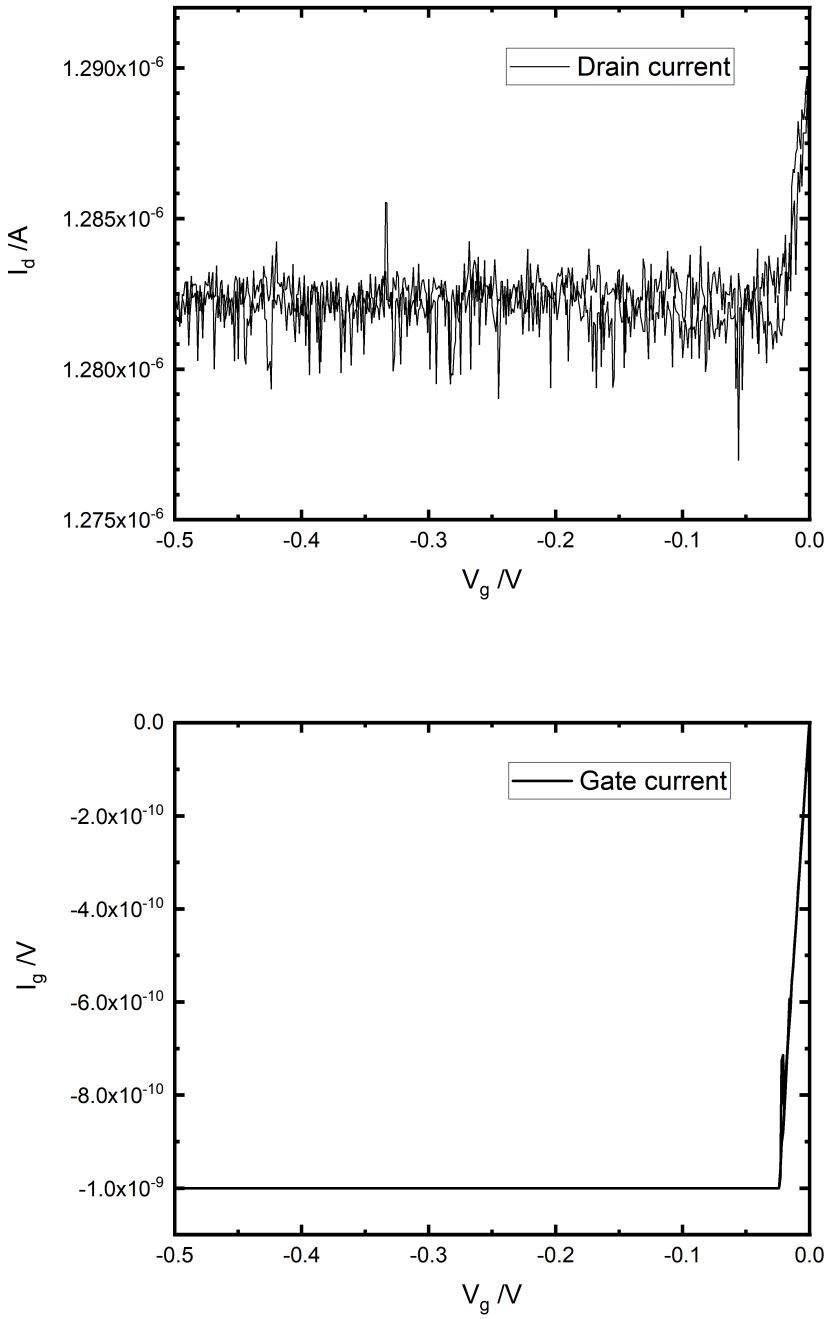

Fig. 4.6 Gate sweep measurement of a graphene device with a shorted gate. Top: changing V_g does not affect the value of I_d. Bottom: I_g reaches the preset compliance 1nA at the start of measurement. Pinholes on the PZT surface lead to short circuits between the drain/source pads and the $SrTiO_3$ substrate (Gate), and large gate current I_g which reaches the compliance at the start of measurement. Hence, there is no dependence of I_d on V_g.

transistor theories, the latter variable is supposed to control the former physical quantity. It was noticed that the gate current reached the preset compliance value 1nA at the very start of the measurement, and the increase in gate voltage caused no influence on the circuit rather than forming a higher leakage current through the gate.

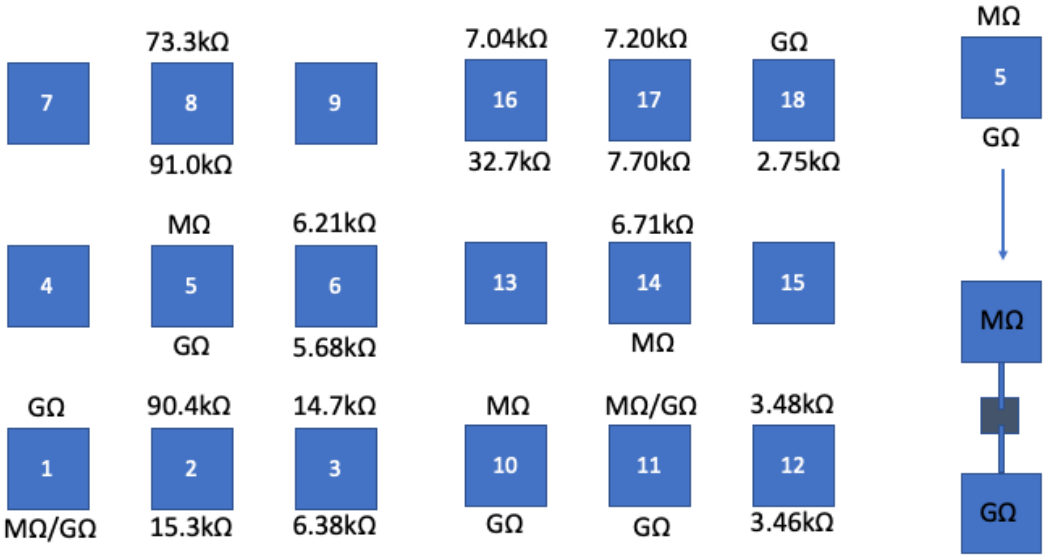

Fig. 4.7 Gate resistance values for a batch of 18 devices, from measuring the resistance between the drain/source electrode pads and the back $SrTiO_3$ surface (connected to the ground in the probe station setup). As shown in the schematic (right), the numbered square denotes a device, and the two values above and below the square point out the gate resistances of the two pads in that device, the middle grey square stands for graphene. The simple schematic is not to scale, and omits device design details. Those numbered squares without values failed in the fabrication process so weren't measured here. GΩ and MΩ means the resistance is in GΩ/MΩ range.

Measuring the device gate resistance i.e. the resistance between the drain/source electrode pads and the back $SrTiO_3$ surface (connected to the ground in the probe station setup) revealed gate resistance value as low as 2.75kΩ. In other words, the PZT thin film does not act as a promising dielectric layer anymore for those devices with leakage behaviour. And those devices failed before further measurements can even take place. The short circuit problem is attributed to small pinholes existing on the PZT thin film, which are introduced during the crystal growth process. They are subtle however detrimental if a device is planned at the same location. The two drain and source electrode pads are $100\mu m \times 100\mu m$ each. It is possible for a gold pad to cover an area with some pinholes. If one pinhole, deep enough, is covered by either drain or source electrode pad, that device will fail. And in fact, this is what

was discovered in reality. In a few failed devices, a disappointing conclusion is that only one pad is shorted. Figure 4.7 shows the measured gate resistance map for a typical batch of PZT devices.

The numbered square denotes a device, and the two values above and below are the gate resistances of the two pads in that device. The schematic on the right is an explanation on the concept, not to scale. There are some squares which display no values above or below. Those are typically devices that failed in one of the fabrication steps, e.g. poor topography hence inappropriate for PFM or AFM cleaning, and broken electrode arms or pads. Figure 4.8 shows the map of survived devices in this batch. Only device 5, 10 and 11 progressed to late measurement stages. That is a yield rate of 3 out of 18, 16.7% – very low. It should be noticed that device 1 appeared to survive the fabrication steps and were proved to be not shorted. However, one of the electrode arms did not stick tightly enough to the PZT surface. This free-hanging arm resulted in very small allowed current passing through the device. The attempt to pass a higher current blew out the device eventually.

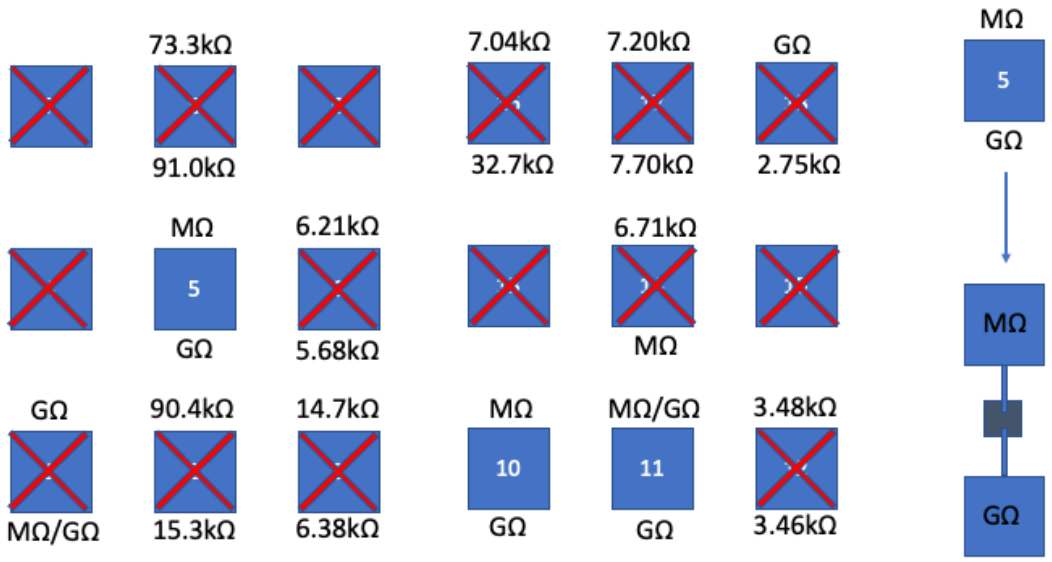

Fig. 4.8 Out of the initial planned 18 devices, only 3 devices survived in the end. Others failed either in the fabrication process, e.g. broken electrode arms or pads. Or the drain/source electrodes are shorted due to pin holes existing on the PZT thin film.

The three devices No.5, 10 and 11 are all working devices. While 8 reference devices (out of 18) were planned in this batch, none was able to provide meaningful data at this stage. As the project ran out of graphene samples after this batch, another purchase was made with the same company - Graphenea. A new batch of 15 devices (8 reference devices and 7

working devices) was fabricated, but issues come up and none of the 15 devices can provide meaningful results. In the end, a decision was made to start from the recently purchased graphene on copper samples, then self-performed the subsequent wet transfer procedures. The sudden change in experimental conditions resulted in a complete fail in fabrication of another whole batch of 22 devices, consisting of 6 working devices and 16 reference devices - 0% yield rate. Finally, just days before the lab closure, the lastest batch of 20 reference devices were fabricated and measured. Out of 20, 4 reference devices survived and all showed a clear CNP point in the gate sweep measurements. They are reference device No.4, 8, 9 and 27. The next section will discuss the results from working and reference devices.

4.2 The evidence of a band gap

At the start of the project, a lot of efforts were spent on developing the appropriate process to accommodate PZT and graphene on a single device in the first two years. In the third year many iterations of devices were measured at 78K, 100K and higher temperatures. Since 78K is the lowest temperature that can be achieved in Nanoscience center 4-terminal Lakeshore probe station. While no bandgap was observed in working devices, a decision was then made to go for lower temperatures. The 6-terminal CRX-VF Lakeshore probe station in the Cambridge Graphene Centre was later acquired and assisted the following findings. It uses a self-contained closed cycle refrigerator and is able to reach 10K in terms of temperature.

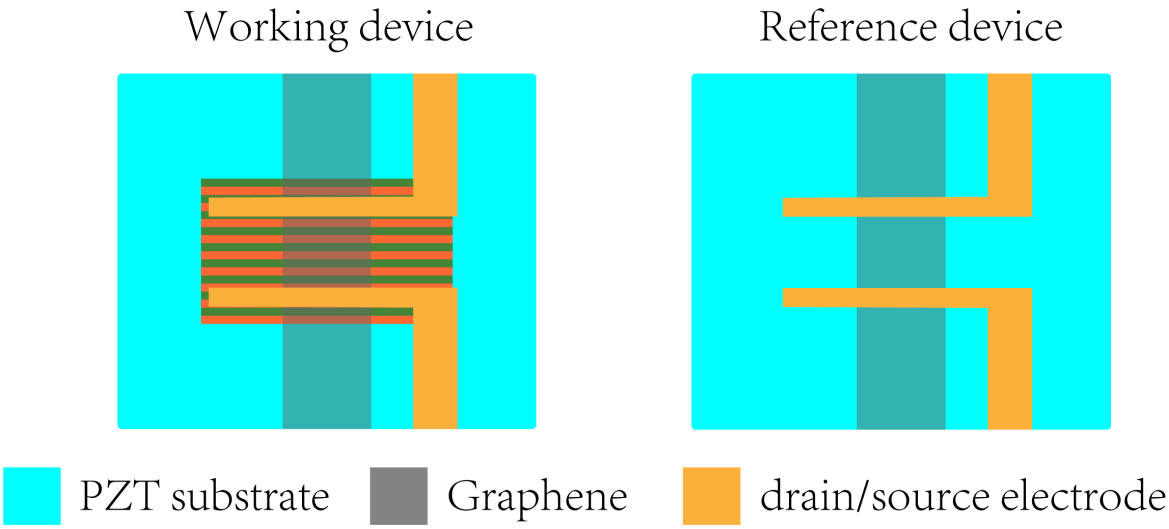

Fig. 4.9 Schematic of working and reference devices.

Figure 4.9 shows the schematic diagram of working and reference devices. In working devices, the PZT material beneath the graphene is poled to create alternating ferroelectric domains with opposite polarisation directions. This results in periodic potentials and hence a graphene superlattice effect. By comparison, in reference devices the PZT material beneath the graphene is not poled. Hence the domains beneath the graphene has random directions of polarisation. Treating the PZT-graphene device as a graphene field effect transistor (GFET), gate sweep measurements were deployed extensively in this work. The conductance (G) of graphene is gained via dividing the drain-source current (I_d) by drain-source voltage (V_d). The gate voltage values mostly stay between $\pm$3.5V throughout the work. And the DC drain-source voltage is fixed at 1mV.

Figure 4.10 shows gate sweep measurements at 10K for working device11. This working device features the central periodic potential region with L = 60nm. The gate voltage sweep range is from 0V to -3V. With V_d = 1mV, the drain current I_d is measured against the gate

voltage V_g. The drain current is measured to be in the micro ampere μ A range, and the conductance in the milli Siemens mS range. A flat region in at the bottom of the curve is noticeable in the graph, indicated by the dashed line. The flat region is estimated to be 0.295V wide, between V_g = -1.053V and V_g = -0.758V. The flat region at the bottom caused an obvious deviation in the shape of gate sweep curve from normal graphene FET (recalling Figure 4.5). It is the most direct evidence of the electrostatic graphene superlattice effect on the band structure of graphene. The superlattice created minibands and energy gaps at minizone boundaries collectively lead to a broadened current valley at the bottom of the gate sweep curve.

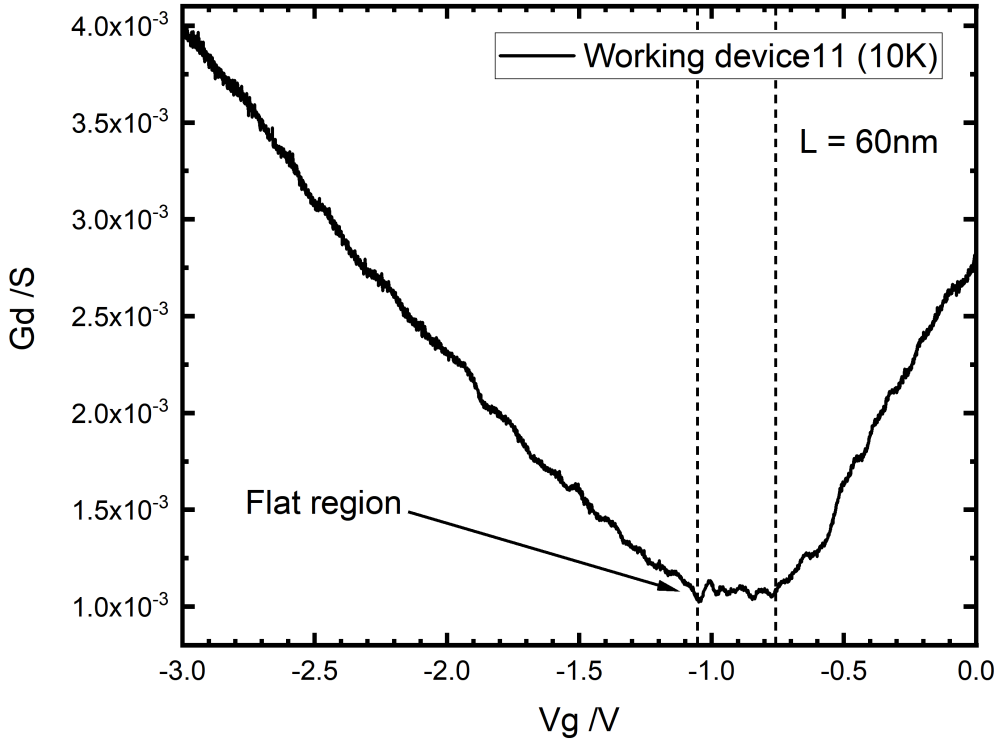

Fig. 4.10 Gate sweep measurement for working device11 at 10K. The periodic potential in this device has period L = 60nm. The barrier width w = L/2 = 30nm.

Figure 4.11 shows the gate sweep curve measured at 10K for reference device9. The PZT material beneath this device has not been through domain engineering, and the ferroelectric domains should possess random polarisation directions. A clear CNP point is featured in the graph, shown by the dashed line at V_g = 0.290V. The gate voltage sweep range is from -1V to 1V. Similar to the working device, the drain voltage V_d for this device is also fixed to 1mV.

The measured drain current I_d is a few hundred nano amperes, and the conductance G_d is a few hundred micro siemens. The values of I_d and G_d are both only one tenth of those from the above shown working device.

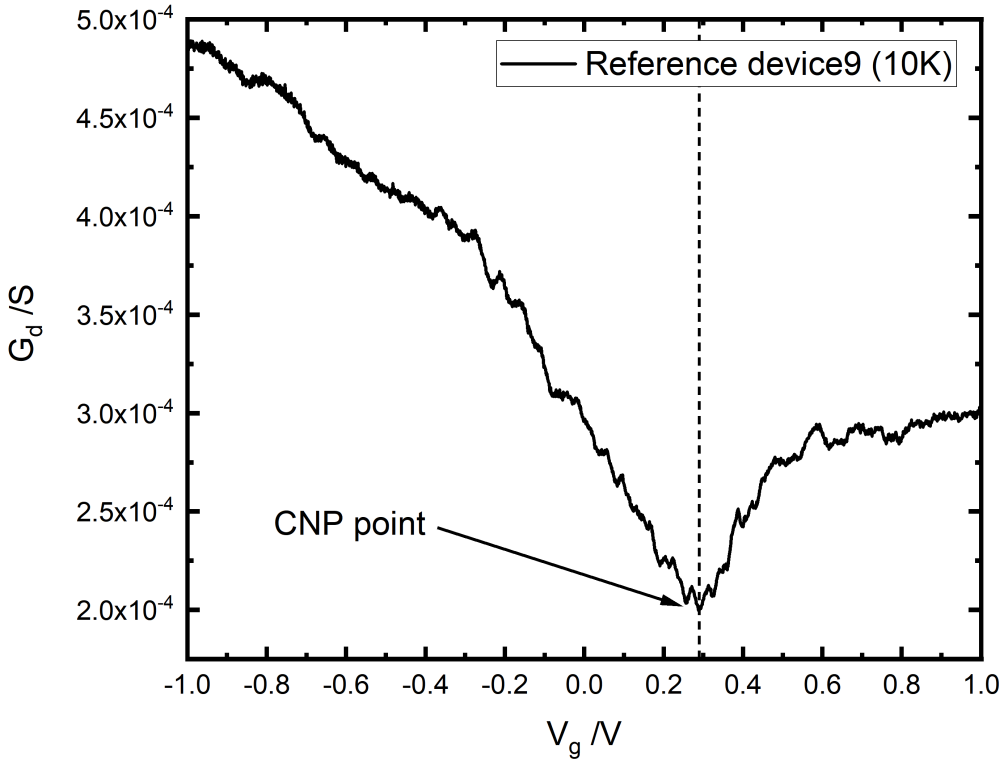

Fig. 4.11 Gate sweep measurement for reference device9 at 10K.

As previously discussed in section 4.1, multiple fabrication and sample sourcing difficulties have lead to a very low yield rate in the number of devices that display meaningful data. The 3 working devices revealed in this chapter are not made in the same batch as the 4 reference devices. In fact working device No.5, 10 and 11 are made in one batch, then reference device No.4, 8, 9 and 27 are made in another batch. A poor quality graphene sample was used in the latter batch and resulted in the difference in orders of magnitude in the conductance range. Discrepancies in graphene quality also account for a much rougher gate sweep curve for the reference devices. It is however undeniable that the reference device features a distinct CNP point and has the same shape as a normal graphene FET (recalling Figure 4.5). Such confirmation on the reference device acts as another proof to the predicted graphene superlattice effect from theory.

Figure 4.12 demonstrates the temperature dependence of electrostatic graphene superlattice effect on working device10. The gate sweep range here is 0 to 2V, and drain voltage V_d is kept at 1mV again. Gate sweep measurements were carried out at 10K, 20K, 30K and 100K. At 10K, the lowest temperature allowed by the probe station used in this project, a flat region featuring some conductance variations is spotted at the bottom of the curve roughly between 0.6V - 0.9V. At elevated temperatures, this region narrows down. It starts to disappear from 30K onward, as well as the flat region which those conductance peaks form. At 100K, a flat region can barely be characterised, and the bottom of the curve becomes rather similar to that shown in Figure 4.5. Such that a working device can hardly differentiate itself against a reference device.

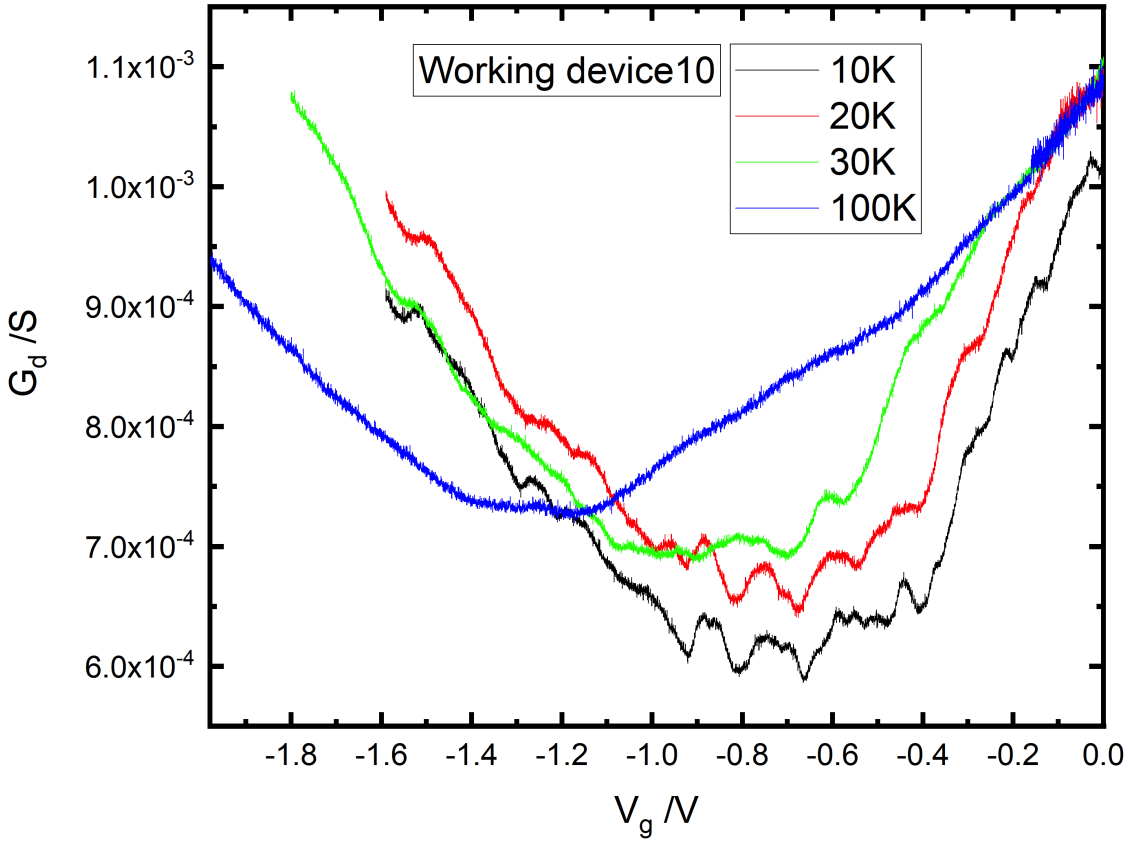

Fig. 4.12 Gate sweep measurements for a working device at four different temperatures.

Figure 4.13 shows the gate sweep measurements for reference device8 at 10K, 20K, 30K and 100K. The gate voltage sweep range is from 0 to 2V, with V_d =1mV. At all temperatures, a clear CNP point is visible (marked by dashed lines). If one only looks at the 100K curve in Figure 4.12 and 4.13, it is almost impossible to distinguish the working device from the reference. And it is exactly the dilemma facing the project in the first three years, without

the access to a probe station able to achieve low enough testing temperature. One simply cannot be convinced of any difference in the gate sweep curves from working devices against reference devices. In Figure 4.12 and 4.13, the gate sweep curves both shift to the left and become more n-doped or less p-doped as the temperature increases from 10K to 100K. This is also noted from the nanoribbon bandgap work [26] in section 1.3. The reason could be that as the measurement chamber is heated to raise the temperature, water molecules which have a hole-doping effect on graphene desorb from the graphene surface. The curtailment of p-dopants causes the gate sweep curve of graphene to shift to the left [179].

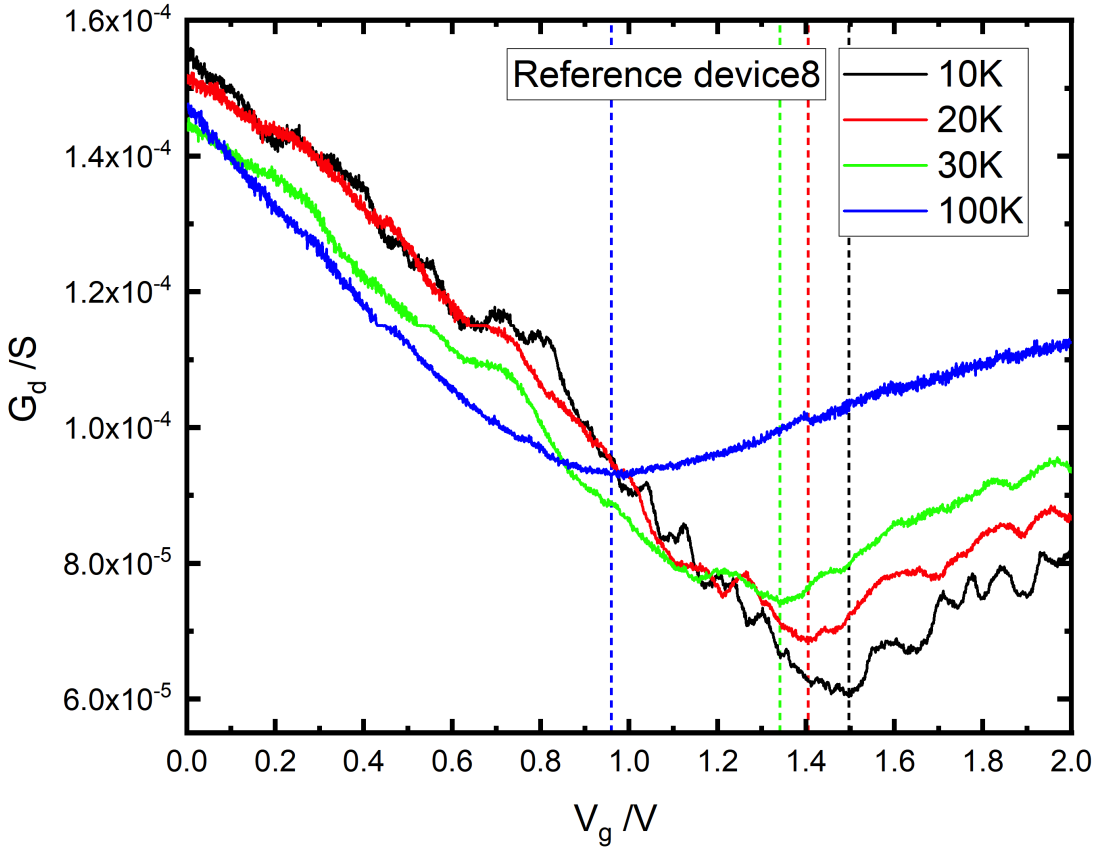

Fig. 4.13 Gate sweep measurements for a reference device at four different temperatures

When the temperature goes down from 100K to 30K, the mean potential caused by the thermal motion of electrons (kT/e, k = 8.6173 $\times$ 10^{-5}eV) goes down from 8.617mV to 2.585mV. It drops further to 0.862mV when the temperature is further reduced to 10K. Given that the 1D superlattice potential is estimated to be at least 100mV, it should be possible to observe energy gap effects.

Louie's group predicted an energy gap at the superlattice Brillouin zone (SBZ) of a 1D graphene superlattice of period L, and the first minizone boundary is at $k_x = \pm\frac{\pi}{L}$ [17]. Where

k_x is the component of the wavevector $\vec{k}$ parallel to the periodic potential direction, at a fixed k_y value. In Figure 4.10, the period L is 60nm. So the energy gap between the first and second miniband at the first minizone boundary, is created at $k_x = \pm\ 0.005236\ \text{Å}^{-1}$. This value refers to a band very close to the center of the original Brillouin zone. It was demonstrated that new massless Dirac fermions are generated when a periodic potential is applied to graphene [169], which are different from the original massless Dirac fermions. In 1D rectangular graphene superlattices, the features of these new massless Dirac fermions are obscured by other states existing around the new Dirac point energy. The net effect of this is that the magnitude of the energy gap will be less than the amplitude of the potential [169].

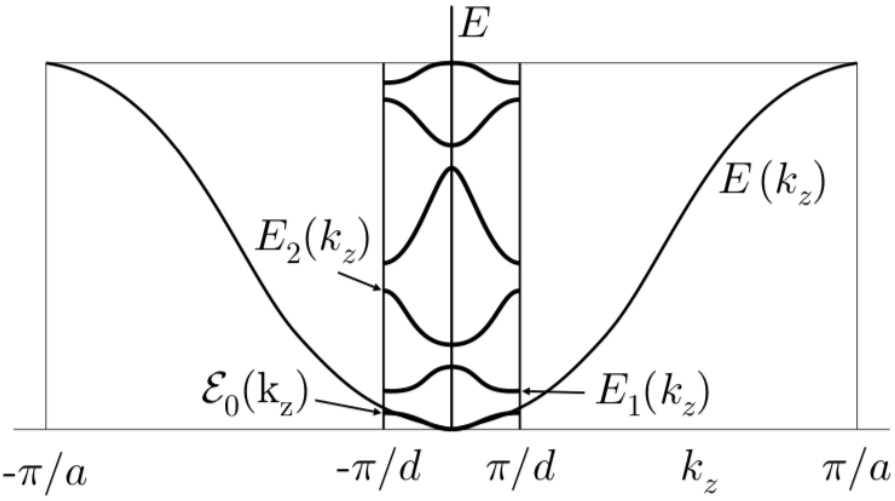

Fig. 4.14 Minibands and minigaps in a superlattice. Here, $\frac{\pi}{a}$ denotes the Brillouin zone boundary of the superlattice; $E(k_z)$ represents the unperturbed, original bulk band. The effect of the superlattice, of period d, is to introduce new "mini Brillouin zones" with boundaries at $\pm\frac{\pi}{d}$. The band is split into minibands with dispersion relationships labelled by $E_0(k_z)$, $E_1(k_z)$, $E_2(k_z)$ etc. Figure sourced from [16]

The overall effect of 1D periodic potential in this work is manifested through the occurrence of a slightly broadened bottom region on the gate sweep curve with a series of conductance oscillation peaks. Those peaks correspond to the opening and narrowing of the minibands resulting from the periodic potentials. It should be pointed out that as the energy gap is created at the superlattice Brillouin zone, instead of the original Dirac point. Figure 4.14 shows minibands and energy gaps between those minibands resulted by a superlattice [16]. If it were created at the original Dirac point as in reference [26], recalling Figure 1.18 in Chapter 1, the gate sweep curve of a 24nm wide nanoribbon exhibits an extensive flattened region due to quantum size effect.

4.3 The size of the "flat region"

Flat regions of different size were observed at the bottom of the gate sweep curves for all working devices. A clear minimum value in conductance is seen for all reference devices, namely the CNP point. This contrast is due to the periodic potentials under graphene on the working devices. This section will look at the gate sweep measurements of three working devices in terms of the flat region size. A fitting analysis using a parabola is adopted in the analysis, in order to contrast the flat region caused by the graphene superlattice effect. Figure 4.15 shows the parabola fitting result for a reference GFET device without the 1D periodic potential (Figure 4.5 of section 4.1). While the measured gate sweep curve is asymmetric, the largest possible and also relatively symmetric segment was chosen to carry out the fitting analysis. The fitting is able to take care of the most characteristic part of the curve.

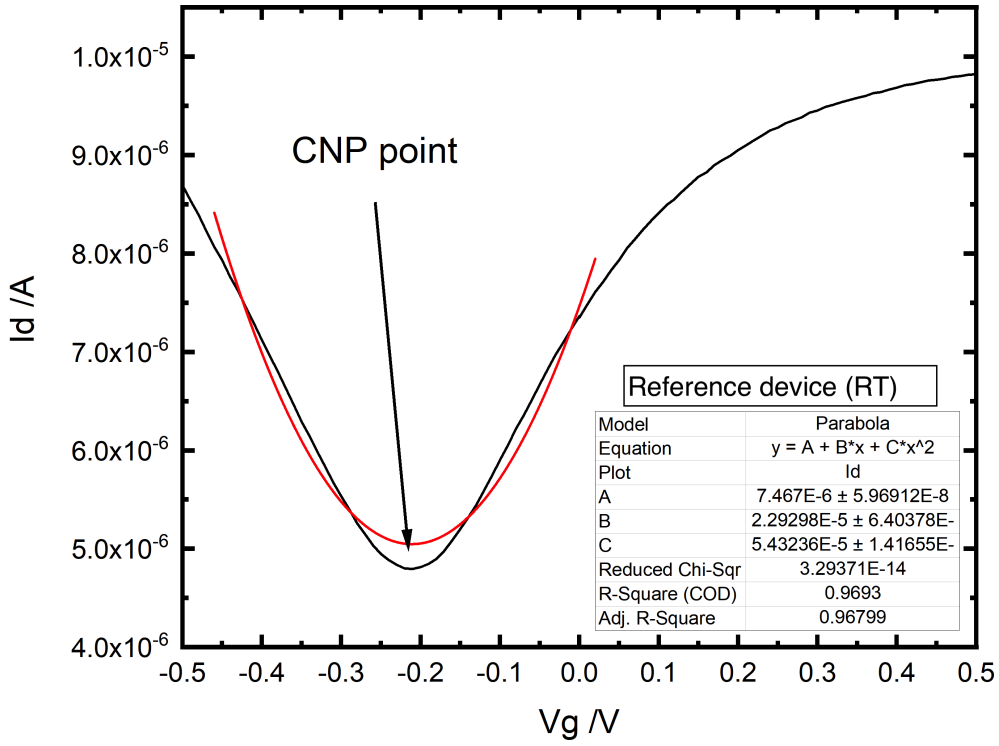

Fig. 4.15 Fitting parabola to Figure 4.5. The graph is gate sweep measurement of a reference GFET device at the room temperature. The CNP point here is at -0.21V, indicating that the graphene is slightly n-doped.

In fact, almost all gate sweep curves measured in this project are asymmetric. This includes the simplest graphene FET made on silicon substrate, as shown in Figure 4.15. In the following fitting analysis for working devices data, a relatively symmetric part of the curve is chosen as the fitting window. It was also ensured that the fitting takes care of as large part of the curve as possible. Figure 4.16, 4.17 and 4.18 illustrate the parabola fitting analysis for working device No.5, 10 and 11 respectively.
In each figure, the top fitting graph considers the overall gate sweep curve. It produces a fit of the general shape of each gate sweep curve to a parabola. It is worth mentioning that the working device data are generally more asymmetric than that of reference device or the simplest GFET shown in Figure 4.15. This accords with theory predictions and is a result of the graphene superlattice effect. The effect is reflected as a sudden drop in conductance G_d at certain (V_g - V_{CNP}) value, i.e. kinks in the gate sweep curve. The locations and width of those kinks relate to the created minibands and energy gap between two minizone boundaries, which will be addressed in the next section. Those kinks and change in the curve shape have led to extra challenges in the parabola fitting analysis. In order to get a quantitative view of the flat region size, a two-step fitting analysis is carried out, which results in the top and bottom graph in each figure.
In each top figure, the bottom of the fitted parabola is always at a much higher distance than Figure 4.15 from the bottom of the measured curve, because conductance is reduced by energy gaps at minizone boundaries. The fitting window selection for the top figure is based on finding the symmetric part of the curve in order to give a best fit parabola. The fitted parabola intercepts with the measured data twice in the top figure, as marked by black dashed lines. The region enclosed by those black dashed lines is selected as the fitting window for the bottom figure. In the bottom figure, the gate sweep curve and the fitted parabola intercept twice as well. The value of two V_g - V_{CNP} interceptions is looked up on the graph, and the difference between the two values is the flat region width as annotated on each bottom figure.

The underlying approach here is to exclude the central flat region and fit parabola on the selection of low energy region. If the flat region is not excluded, the algorithm will include those data in the fitting calculations. Forcing the fitting calculations to include the flat region gives a poorly fitted curve, which is understandable as parabola does not feature a flat region. Also, it contradicts the aim of this analysis, which is to know how the curve looks without the flat region. Bearing the asymmetry and miniband kinks in this analysis, one would say that parabola is not the single absolute formula for the fitting. It is though still the closet one that can describe the measurements. The primary focus of the fitting analysis is to laterally

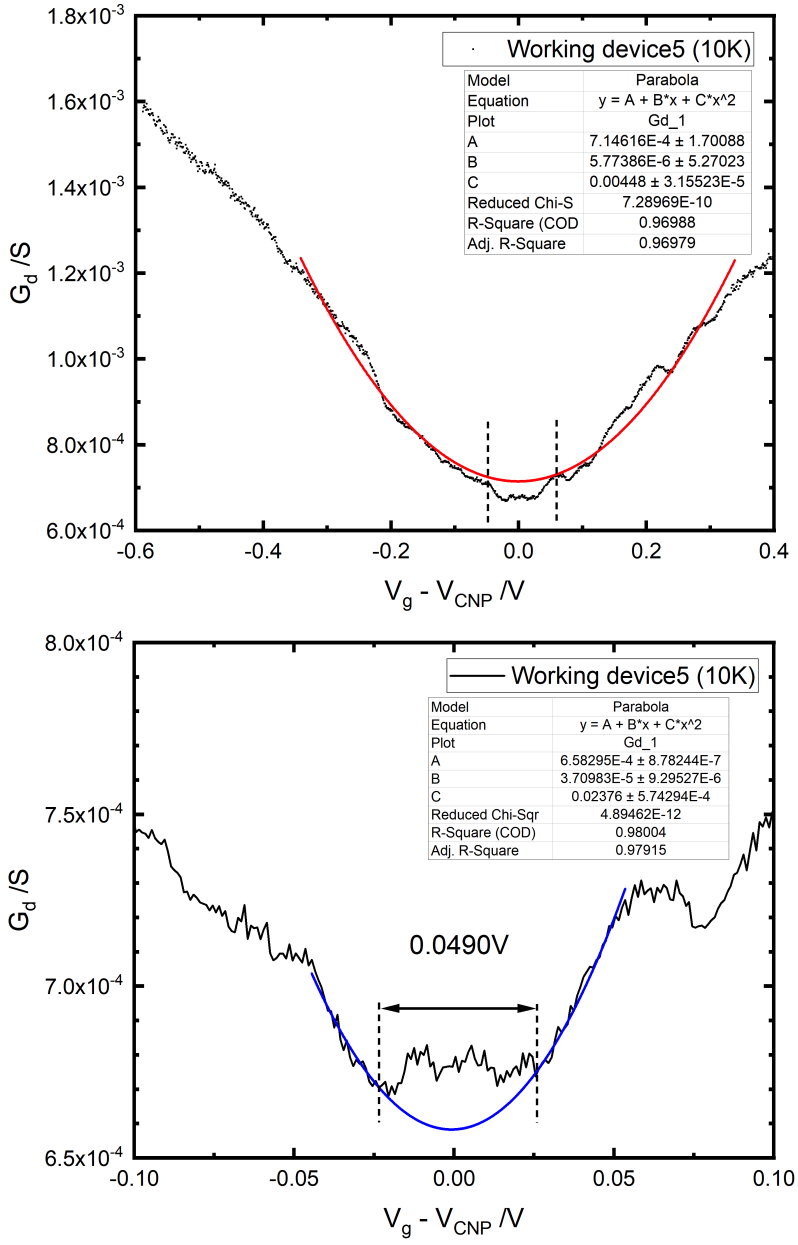

Fig. 4.16 Fitting parabola to the gate sweep curve of working device 5, L = 80nm, w = 40nm. Top: fitting consider the overall curve which results in the chosen window between black dashed lines. Bottom: another parabola fitting is carried out within the window marked in the top graph. The flat region size is 0.0490V.

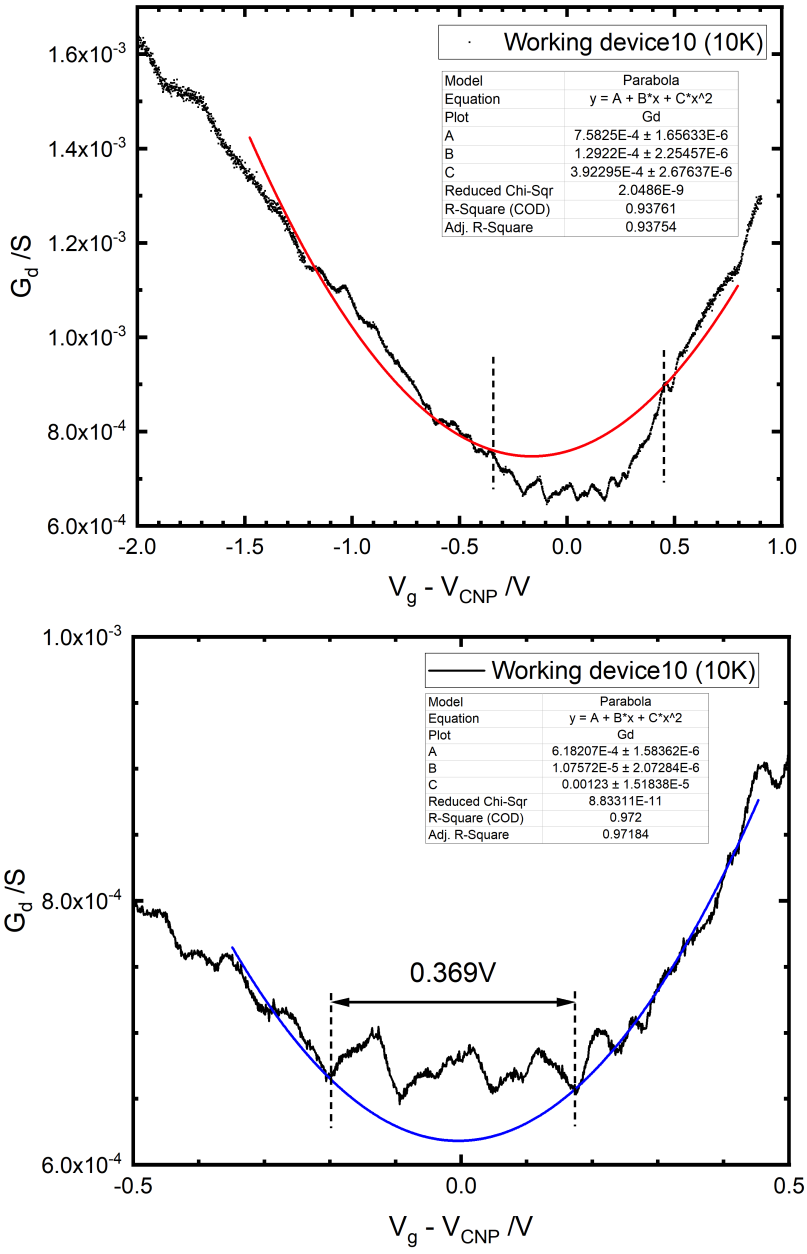

Fig. 4.17 Fitting parabola to the gate sweep curve of working device 10, L = 60nm, w = 30nm. Top: fitting consider the overall curve which results in the chosen window between black dashed lines. Bottom: another parabola fitting is carried out within the window marked in the top graph. The flat region size is 0.369V.

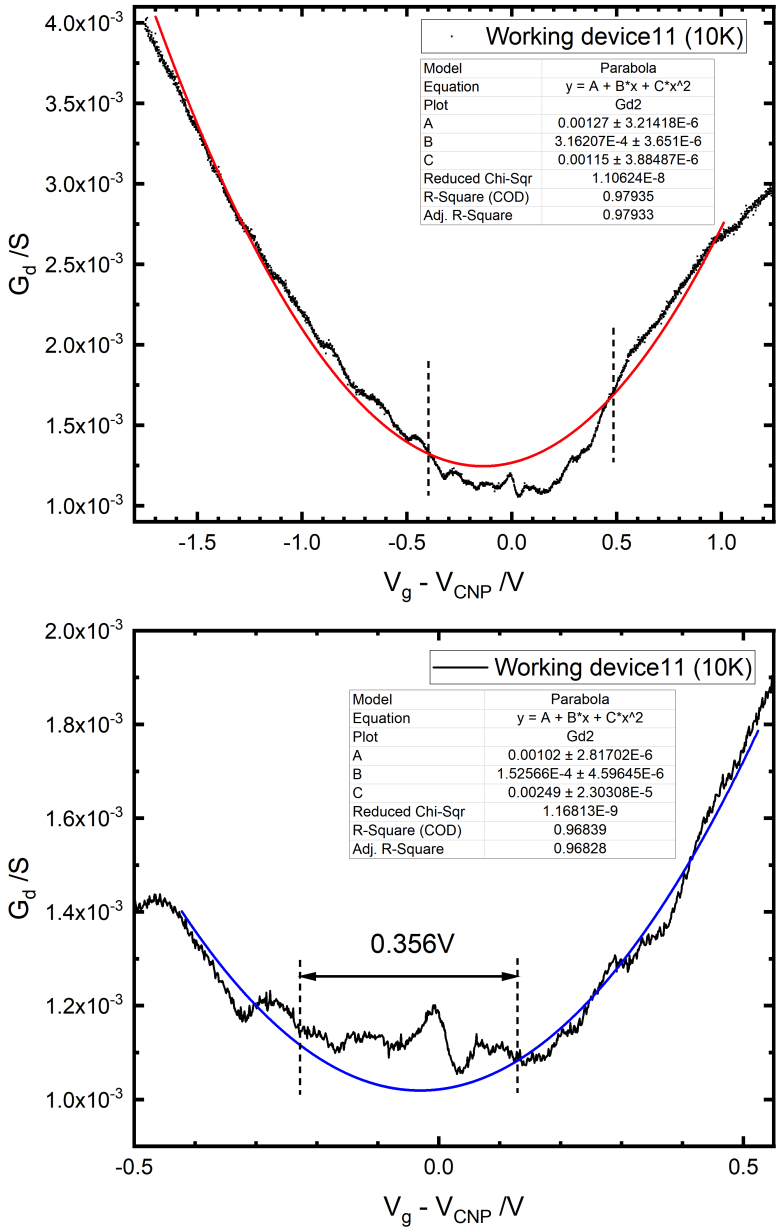

Fig. 4.18 Fitting parabola to the gate sweep curve of working device 11, L = 60nm, w = 30nm. Top: fitting consider the overall curve which results in the chosen window between black dashed lines. Bottom: another parabola fitting is carried out within the window marked in the top graph. The flat region size is 0.356V.

compare the flat region width between data of three working devices. And using parabola in the fitting is sufficient to achieve such aim.

The fitting results from Figure 4.16 to 4.18 are summarised in table 4.1. The basic idea is to systematically characterise the effect caused by the electrostatic graphene superlattice, in comparison to the reference devices. The width of the flat region is 0.0490V for working device No.5, which features the L = 80nm superlattice. And the value is 0.369V and 0.356V, similar for working device No.10 and 11 that both feature L = 80nm superlattice. While one may think that the size of the flat region agrees with the superlattice parameters designed for three devices. It is worth mentioning that the periodic potentials for working device No.5 was patterned more than 8 hours before those in working device No.10 and 11. Recalling Figure 2.24, the surface potential, starting at 270mV, dropped by more than 100mV in the first 10 hours. In other words, the 1D barrier potential in working device No.5 could be a lot lower than those of working device No.10 and 11 at the time of electrical characterisation. It is believed that barrier potential is the most important factor that affects the flat region width here.

Table 4.1 Fitting results for working device 5, 10 and 11

Working device	**Domain engineeirng time**	**Periodicity**	**Flat region size**
5	Hour 1	80nm	0.0490V
10	Hour 9	60nm	0.369V
11	Hour 9	60nm	0.356V

4.4 The computation on minibands and energy gaps

In pristine graphene, the charge carriers are described by the massless Dirac equation. They have a linear energy dispersion that is symmetric near the Dirac point in the Brillouin zone. The energy of graphene charge carrier E, in terms of the wavevector $\vec{k} = (k_x, k_y)$ with respect to Dirac points is governed by

$$E = s\hbar v_0 k \tag{4.1}$$

where s = ± 1, and Fermi velocity of the charge carrier in graphene v_0 = 8.5 $\times$ 10^5 m/s. The Plank constant $\hbar$ = 6.5821 $\times$ 10^{-16} eV· s. Those values give

$$\begin{aligned} E &= \pm 5.595 \times 10^{-10}\, \vec{k}\, eV \\ &= \pm 5.595\, \vec{k}\, eV \qquad\qquad \vec{k} \text{ is in the unit of } \text{Å}^{-1} \end{aligned} \tag{4.2}$$

The above formulae and following discussions apply to states in proximity to the Dirac points. Those states out of the linear energy spectrum regime is out of scope in this project. When an external periodic potential is applied to graphene, the group velocity of energy states is renormalised, and the renormalisation effect is anisotropic in different directions. Figure 1.20 shows Dirac cones for pristine graphene and that affected by a 1D graphene superlattice. In subfigure b, the periodic potential array has a spatial period L, barrier width w and potential U_{1D}. The energy spectrum along any line in the wavevector $\vec{k}$ space with respect to the Dirac point is linear, but there are different group velocities in different directions.

The periodic potential is in the x-direction in the figure, the group velocity $v_{||}$ for a carrier moving in this direction is not renormalised. A carrier with wavevector (k_x, 0), equivalent to slicing the Dirac cones in subfigure b at $k_y = 0$, the energy dispersion still follows formulae 4.1 and 4.2. For a particle moving in the y-direction, which is perpendicular to the periodic potential propagation, the group velocity $v_\perp$ is reduced the most. According to the model in ref [17], the renormalised group velocity v_k is a strong function of the direction of wavevector $\vec{k}$. The effect of renormalisation depends on length parameters L and w, and the size U_1D of periodic potentials. Under the condition $U_1D = 0.5eV$, L = 10nm, w = 5nm, the group velocity v_k along a certain direction can be reduced to less than 40% of the original value v_0, while retaining v_0 along some direction [17].

Figure 4.19 illustrates the first minizone boundary (MB) and the corresponding energy gap of a 1D graphene superlattice. The energy dispersion of charge carriers in a 1D graphene superlattice is plotted versus the component of wavevector k_x, while fixing k_y. The direction of k_x is parallel to the direction of periodic potential in Figure 1.20, it is also in the same direction as $\hat{x}$. The red curve stands for the energy spectrum while $k_y = 0$, it is expressed mathematically as $E = \pm\, 5.595\ k_x\ eV \cdot$ Å. The blue curve indicates the graphene energy spectrum affected by an 1D graphene superlattice. The first minizone boundary is at $k_x = \pm\frac{\pi}{L}$. For $k_y = 0.012$ Å^{-1}, the energy gap ΔE at this minizone boundary is also mapped onto the graph.

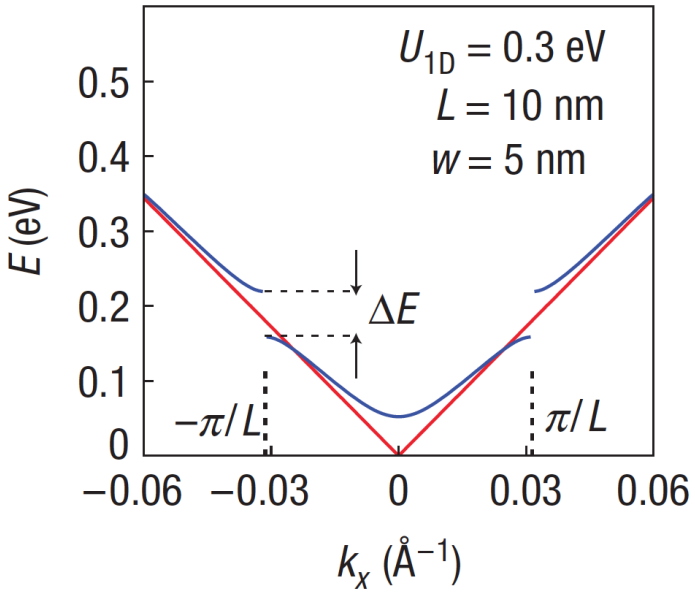

Fig. 4.19 Energy gap at the superlattice Brillouin zone or minizone boundary (MB) of a 1D graphene superlattice. U_{1D} = 0.3eV, L = 10nm and w = 5nm. Energy of charge carriers in a 1D graphene superlattice versus the component of the wavevector k_x at a fixed k_y. Dashed vertical lines indicate minizone boundaries ($k_x = \pm\frac{\pi}{L}$). ΔE is the energy gap at the minizone boundary for a given k_y. Red and blue lines correspond to k_y being zero and 0.012 Å^{-1}, respectively. Figure sourced from [17]

By fixing one component of the wavevector k_y, it is possible to plot energy E versus k_x and find the minizone boundary locations. As the Fourier series of a square wave is composed of sine waves of odd integer periods, the minizone boundaries resulted from such graphene superlattice are at $\pm\frac{\pi}{L}, \pm\frac{3\pi}{L}, \pm\frac{5\pi}{L}, \pm\frac{7\pi}{L}$ etc. Figure 4.20 used the above k_x values to find the corresponding energy E values on the red curve which is the energy spectrum under the 1D graphene superlattice in Figure 4.19, fixing $k_y = 0$. This linear energy spectrum of E versus k_x is equivalent to that of pristine graphene, because under 1D periodic potentials the group

velocity $v_{||}$ of states parallel to the direction of the periodic potential is not renormalised. The energy dispersion follows formulae 4.1 and 4.2. By defining minizone boundary locations on Figure 4.20, one is able to find the corresponding energy values at which the minibands occur. It should be noticed that all calculations involved in this Figure are done with respect to the Dirac point.

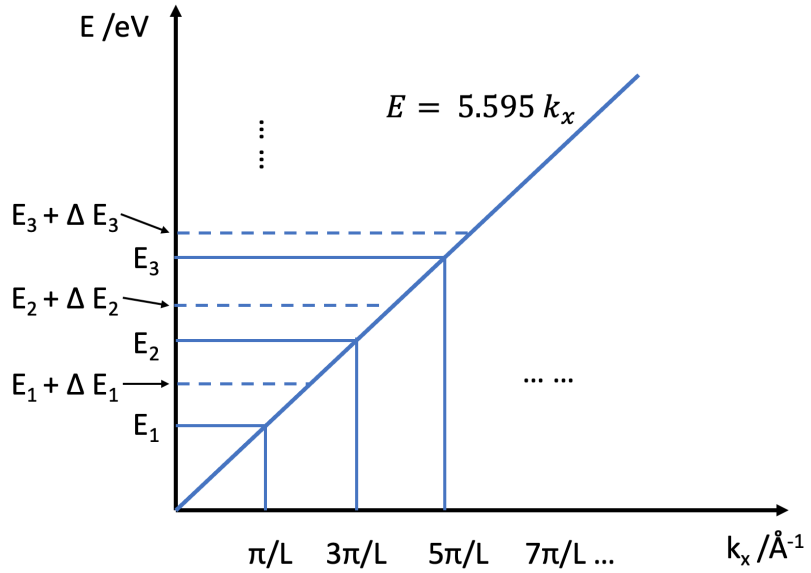

Fig. 4.20 The linear energy spectrum of graphene. The minizone boundaries resulted from the 1D periodic potentials are at locations of $\frac{\pi}{L}$, $\frac{3\pi}{L}$, $\frac{5\pi}{L}$, $\frac{7\pi}{L}$ etc. The corresponding energy E values can be found.

In terms of the size of the bandgap at the minizone boundary in Figure 4.19, reference [17] shows that for a Kronig-Penney type rectangular potential barrier 1D graphene superlattice, the energy gap at the minizone boundary (MB) can be expressed with the following equation in terms of superlattice parameters as

$$\Delta E = \frac{2}{\pi} |U_{1D} \sin(\frac{\pi w}{L}) \sin\theta_{\vec{k},\hat{x}}| \tag{4.3}$$

where U_{1D} is the amplitude of the potential, w is the barrier height, L is the period and $\theta_{\vec{k},\hat{x}}$ is the polar angle between the wavevector $\vec{k}$ and direction $\hat{x}$. The periodic potential described in their analysis is alternating between zero and U_{1D} = 0.3eV, with a period L = 10nm and barrier width w = 5nm. While k_y = 0.012 Å^{-1}, at the first minizone boundary location $k_x = \pm\frac{\pi}{10nm} = \pm 0.0314$Å^{-1}, the size of bandgap

$$\Delta E_1 = \frac{2}{\pi} |\, 0.3eV \times \sin\frac{\pi}{2} \times \sin(\tan^{-1}\frac{0.012}{0.0314})\,| = 0.0681eV.$$

The energy gap at the second, third and higher number minizone boundaries ΔE_2, ΔE_3 etc can be calculated in a similar fashion by substituting the $\frac{2}{\pi} \cdot U_{1D}$ coefficient by the corresponding Fourier term coefficients. Keeping k_y fixed, the sine value of the polar angle between $\vec{k}$ and $\hat{x}$ should also be adjusted at each minizone boundary. Those energy values are also mapped onto Figure 4.20. The segment between E_n and $E_n + \Delta E_n$ represents the energy gap between two adjacent minibands created by the graphene superlattice.
Since the data collected from the experiments are gate sweep measurements, the energy E and energy gap ΔE are then converted to gate voltage, illustrated in Figure 4.21. It should again be noticed that all calculations involved in Figure 4.21 are done with the gate voltage adjusted by the charge neutrality point (CNP) value. The segment of the gate sweep curve between $\frac{E_n}{e}$ and $\frac{E_n}{e} + \frac{\Delta E_n}{e}$ corresponds to the superlattice created miniband in Figure 4.20. By mapping the created minibands from the energy spectrum (E-k relationship) to the gate sweep curve(I-V relationship), one is able to construct the theoretically predicted effect from a 1D graphene superlattice on a G_d versus (V_g - V_{CNP}) graph. Such that overlapping those theoretical predictions with the measured gate sweep curve will give a comparison between theories and experiments, and have a better understanding of the 1D graphene superlattice effect.

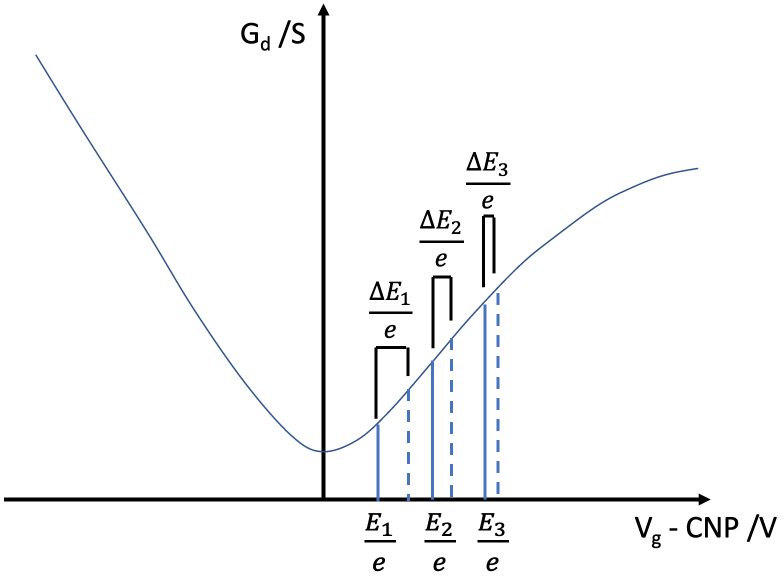

Fig. 4.21 Map the minizone boundary locations and the relevent energy gap onto the gate sweep measurements. The curve is not to scale, and acts as a simple representation of graphene gate sweep measurement.

In this project, the periodic potential is constructed by alternating ferroelectric domains of opposite polarisation directions. Hence, the 1D periodic potential is alternating between

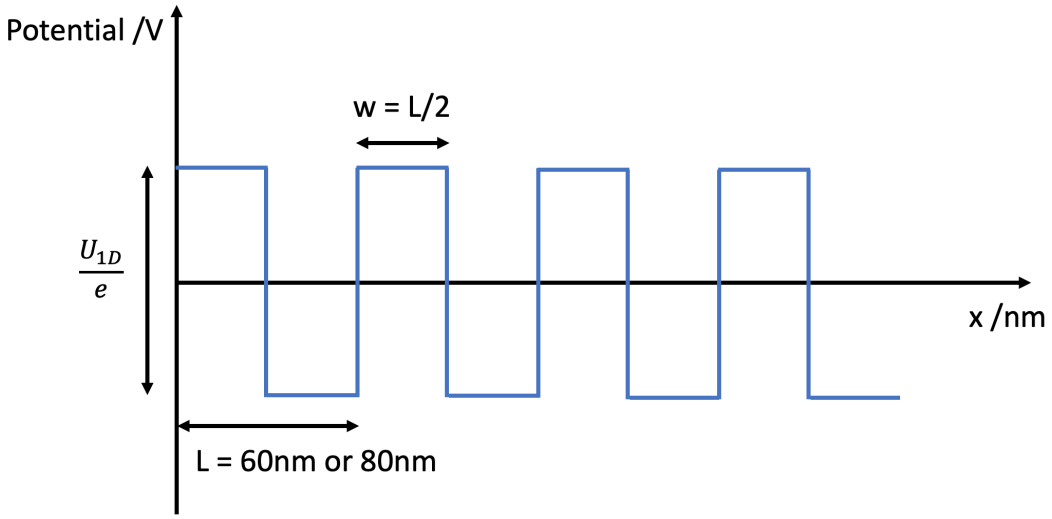

Fig. 4.22 The 1D periodic potentials in this project: potential $\frac{U_1D}{e}$, period L = 60nm or 80nm, barrier width w = $\frac{L}{2}$.

negative and positive values. This is demonstrated in Figure 4.22, with potential $\frac{U_1D}{e}$ and period L = 60nm or 80nm for working devices. The barrier width w is always designed to be half of the period, so this 1D periodic potential is a finite square wave. Writing it in Fourier series,

$$\begin{aligned} f(x) &= U_{1D} \sum_{n=1,3,5\ldots}^{\infty} \frac{2}{n\pi} \sin \frac{n\pi x}{L/2} \\ &= U_{1D} \left(\frac{2}{\pi} \sin \frac{2\pi x}{L} + \frac{2}{3\pi} \sin \frac{6\pi x}{L} + \frac{2}{5\pi} \sin \frac{10\pi x}{L} + \ldots \right) \end{aligned} \tag{4.4}$$

By substituting the $\frac{2}{\pi} \cdot \mathrm{U}_{1D}$ coefficient in formula 4.3 by Fourier terms, the energy gap at each minizone boundary can be calculated

$$\begin{aligned} k_x &= \pm \frac{\pi}{L} & \Delta E &= \frac{2}{\pi} |U_{1D} \sin \theta_{\vec{k},\hat{x}}| \\ k_x &= \pm \frac{3\pi}{L} & \Delta E &= \frac{2}{3\pi} |U_{1D} \sin \theta_{\vec{k},\hat{x}}| \\ k_x &= \pm \frac{5\pi}{L} & \Delta E &= \frac{2}{5\pi} |U_{1D} \sin \theta_{\vec{k},\hat{x}}| \\ k_x &= \pm \frac{7\pi}{L} & \Delta E &= \frac{2}{7\pi} |U_{1D} \sin \theta_{\vec{k},\hat{x}}| \\ &\ldots & &\ldots \end{aligned}$$

It is not possible to measure U_{1D} at the time of gate sweep measurements. The surface potential resulted from alternating ferroelectric domains of opposite polarisation directions can only be measured by KPFM, which can not be carried out with the device structure built above the PZT surface. The KPFM time decay measurement in section 2.6 Figure 2.24 provides an estimate on the order of magnitude of the U_{1D} value at the time of electrical measurements. Figure 2.24 shows the result of time decay measurements on the surface potential on the PZT across 7 days. An area on the PZT surface is poled by a metal tip to result in positively and negatively polarised domains. The sample was then regularly examined by KPFM to reveal how the surface potential changed in that area.

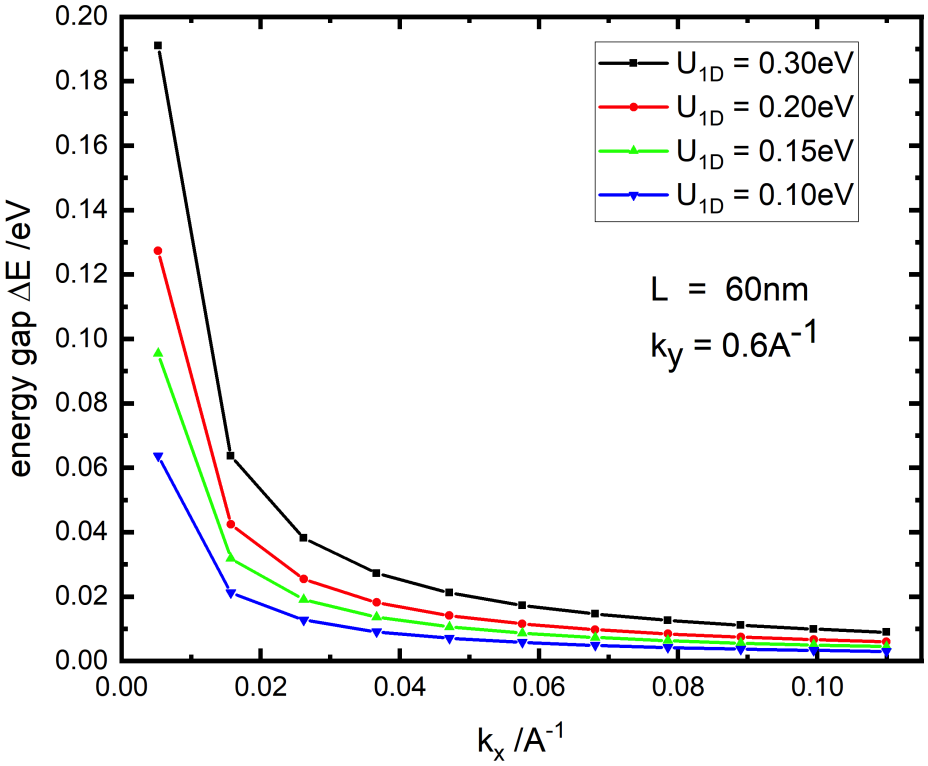

Fig. 4.23 Energy gap ΔE at the first eleven minizone boundaries for graphene superlattice of period L = 60nm. The graph is plotted at $k_y = 0.6\text{Å}^{-1}$, while U_{1D} = 0.3eV, 0.2eV, 0.15eV and 0.1eV. Barrier width w = 30nm.

It takes at least 72 hours from the time when the last polarised domain is made, to the time when the first measurement in the probe station under 10K is made. According to Figure 2.24, 72 hours refers to $\sim$ 120mV surface potential remained. This potential value is not absolute for every patterned domain, because the surface potential created by PFM lithography does vary from one tip to the other, and from one area to the other. It is fair to assume that the surface potential remained on PZT surface at the time of electrical measurement is a few hundred milli volts, thus U_{1D} is a few hundred meV. The energy gap ΔE is proportional to the

barrier potential U_{1D}. Figure 4.23 and 4.24 plot ΔE at each minizone boundary for different U_{1D} values 300meV, 200meV, 150meV and 100meV while keeping $k_y = 0.6Å^{-1}$.
The energy gaps of the first eleven minizone boundaries are plotted for each periodicity. While the size of the energy gap does not vary a lot between two different periodicity, the k_x ($=\frac{n\pi}{L}$) range does. For L = 60nm, k_x is between $0.00524Å^{-1}$ to $0.10996Å^{-1}$ in Figure 4.23. For L = 80nm, k_x is between $0.00393Å^{-1}$ to $0.08247Å^{-1}$ in Figure 4.24. A drastic drop in energy gap between the first and second minizone boundaries is also obvious. Taking 60nm periodicity and 0.3eV potential as an example, the energy gap decreases from 0.19098eV (1st MB) to 0.06364eV (2nd MB), that is a factor of three drop. After the second MB, the change in energy gap is more moderate.

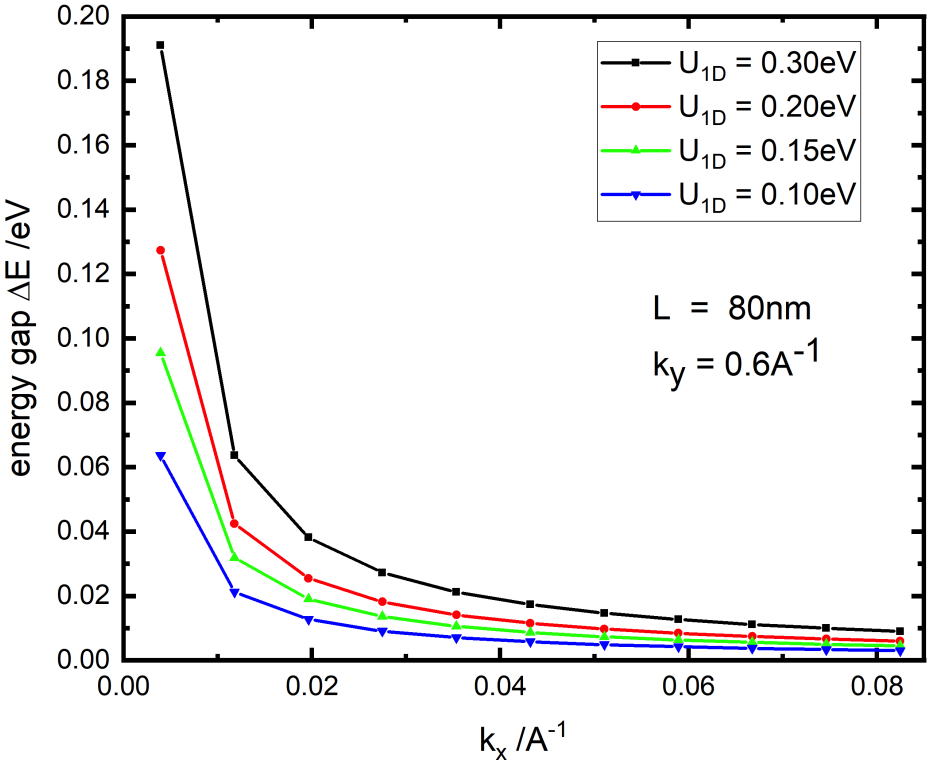

Fig. 4.24 Energy gap ΔE at the first eleven minizone boundaries for graphene superlattice of period L = 80nm. The graph is plotted at $k_y = 0.6Å^{-1}$, while U_{1D} = 0.3eV, 0.2eV, 0.15eV and 0.1eV. Barrier width w = 40nm.

$k_y = 0.6Å^{-1}$ corresponds to $\theta_{\vec{k},\hat{x}} = 89.5°$, it is the polar angle where the k_y component is much greater than the k_x component. The 1D electrostatic graphene superlattice effect is enlarged than k_y of smaller values, so when one presents Figure 4.23 and 4.24 of energy gap ΔE at the first eleven minizone boundaries it is easier to illustrate the effect of U_{1D} and the contrast in size of ΔE between different minizone boundaries. The energy gap ΔE

is also proportional to $\sin\theta_{\vec{k},\hat{x}}$. Although 1D graphene superlattice is considered here, it is still a 2D problem. And this 2D nature is blended into the problem by $\vec{k}$ = (k_x, k_y). In addition to looking at different values of U_{1D} in Figure 4.23 and 4.24, a few k_y values are also considered including k_y = 0.6Å^{-1}, 0.00908Å^{-1}, 0.00524Å^{-1} and 0.00303 Å^{-1}. Those values are chosen to reflect polar angle $\theta_{\vec{k},\hat{x}}$ = 89.5°, 60°, 45° and 30° at the first minizone boundary, for the L = 60nm graphene superlattice. Figure 4.25 demonstrates the effect on the energy gap ΔE at the first eleven minizone boundaries by varying k_y. It can be noticed that for k_y = 0.00908Å^{-1} ($\theta_{\vec{k},\hat{x}}$ = 60°), 0.00524Å^{-1} (45°) and 0.00303 Å^{-1} (30°), from the fifth minizone boundary onward the energy gaps ΔE are similar between the three k_y values. They are all very close to zero. In comparison, from the second minizone boundary onward the energy gaps ΔE at k_y = 0.6Å^{-1} ($\theta_{\vec{k},\hat{x}}$ = 89.5°) is always at least twice of those of k_y = 0.00908Å^{-1} ($\theta_{\vec{k},\hat{x}}$ = 60°), 0.00524Å^{-1} (45°) and 0.00303 Å^{-1} (30°).

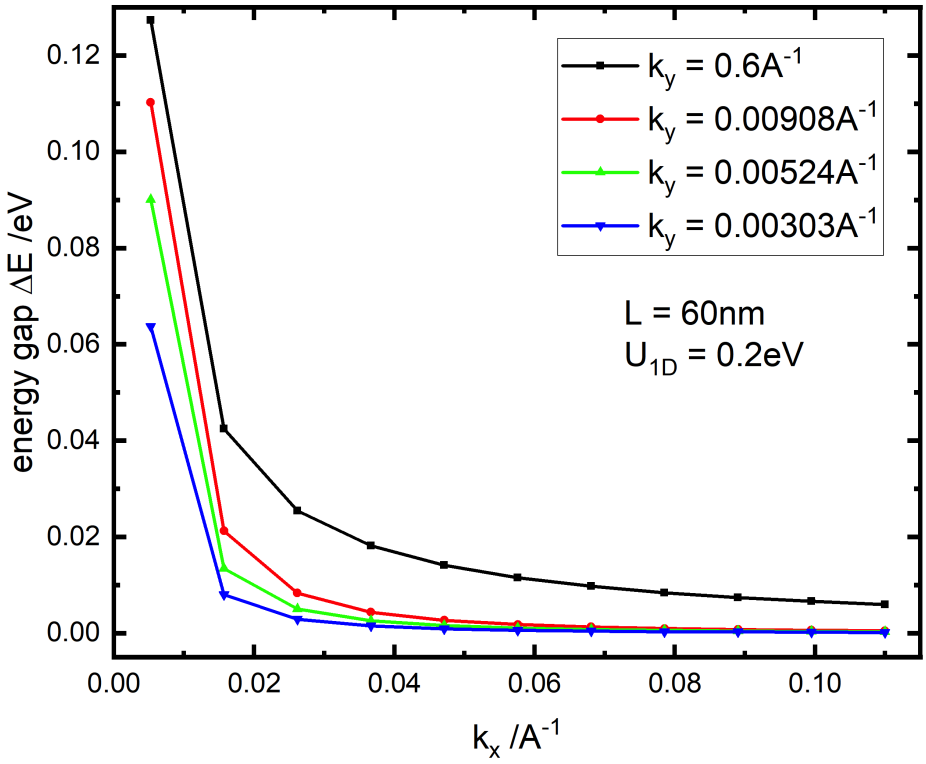

Fig. 4.25 Energy gap ΔE at the first eleven minizone boundaries for graphene superlattice of period L = 60nm. The graph is plotted at U_{1D} = 0.2eV, while k_y = 0.6Å^{-1}, 0.00908Å^{-1}, 0.00524Å^{-1} and 0.00303 Å^{-1}. Barrier width w = 30nm.

4.5 The match with experimental observations

In this work, the creation of minibands via the interaction of single-layer graphene with periodic electrostatic potentials is experimentally demonstrated. The electrostatic potential is produced by the means of a periodically poled ferroelectric substrate. For purely normal incidence of electrons, Klein tunnelling leads to perfect transmission owing to the suppression of back-scattering process for massless Dirac fermions. However, despite the collimation effect from the barriers [170], in reality the current will flow at a range of angles centred on normal, between the drain and source electrodes; such that the incidence on the barriers are mixed with normal and oblique angles. Therefore, there is a possibility that certain population of electrons are confined in the potential wells between two barriers, and the spectrum of those bound states give arise to multiple minibands. Moreover, the variations in conductance are noted as kinks in the gate sweep curves.

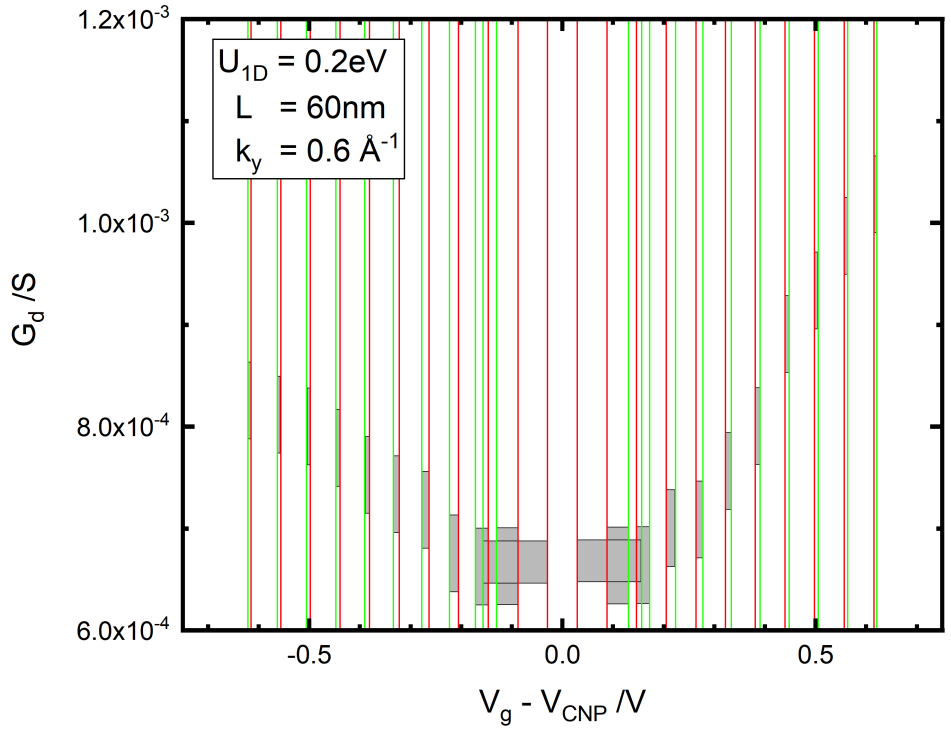

Fig. 4.26 A G_d versus (V_g - V_{CNP}) plot maps minizone boundaries and energy gaps between two adjacent minibands for a superlattice L = 60nm, U_{1D} = 0.2eV, k_y is fixed at 0.6Å^{-1}. This corresponds to 89.5° at the first minizone boundary. Red lines indicates the first eleven minizone boundaries for this superlattice. Shade boxes between red and green lines indicates energy gaps between adjacent minibands. The energy gap at the first minizone boundary is so large that it extends into the second and third minibands.

From the method outlined in section 4.4, a G_d versus (V_g - V_{CNP}) map which includes minizone boundaries and energy gaps between two adjacent minibands can be computed at different barrier potential U_{1D} and wavevector component k_y. An example is demonstrated in Figure 4.26, for a superlattice with L = 60nm and U_{1D} = 0.2eV. Red lines indicates the first eleven minizone boundaries for this superlattice. Shade boxes are between red and green lines, which refer to energy gaps between adjacent minibands. The first shaded box covers an extensive region in which the second shaded box sits. This means that under the above superlattice condition, the first energy gap is so big that it extends into the second and third minibands, such that the second and third minibands starts before the energy gap between the first and second minibands finishes.

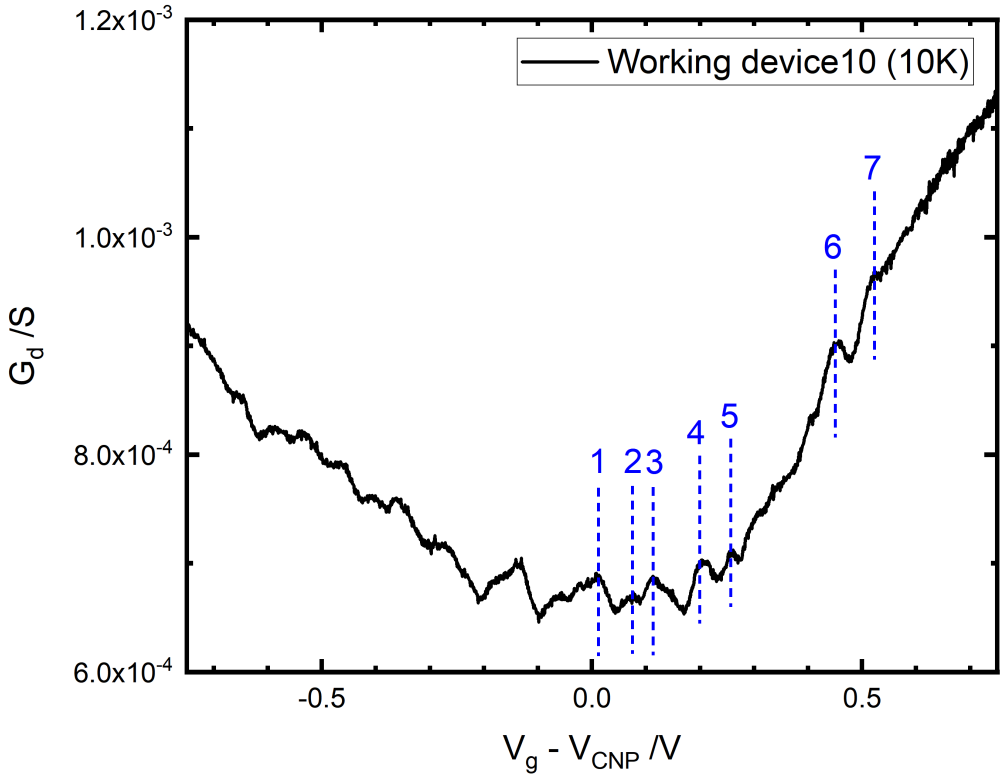

Fig. 4.27 Gate sweep measurements of working device 10, whose period L for the potentials underneath is 60nm. Blue dashed lines mark the locations of a sudden drop in conductance G_d

In theory, the conductance should reduce within an energy gap between adjacent minibands. In other words, G_d should drop within the shaded boxes on the MB map, and increases out of them. Figure 4.27 shows the gate sweep measurements of working device No.10. Blue dashed lines mark the locations of a sudden drop in G_d. One would like to overlap the MB map in Figure 4.27 and the measured gate sweep curve in Figure 4.27.

The result is shown in Figure 4.28. The conductance drop location No.1, 3, 4, 5 (number shaded in green) refer to good matches between grey shaded boxes and blue dashed lines. That is, the theory predicted drop in conductance due to energy gap at the minizone boundary and the drop in G_d on the measured gate sweep curve. The conductance is expected to start dropping from the left side of a shaded box, and start rising from the right side of a shade box until it meets another shaded box. While conductance drop location No.6 and 7 are half way between two predicted energy gaps.

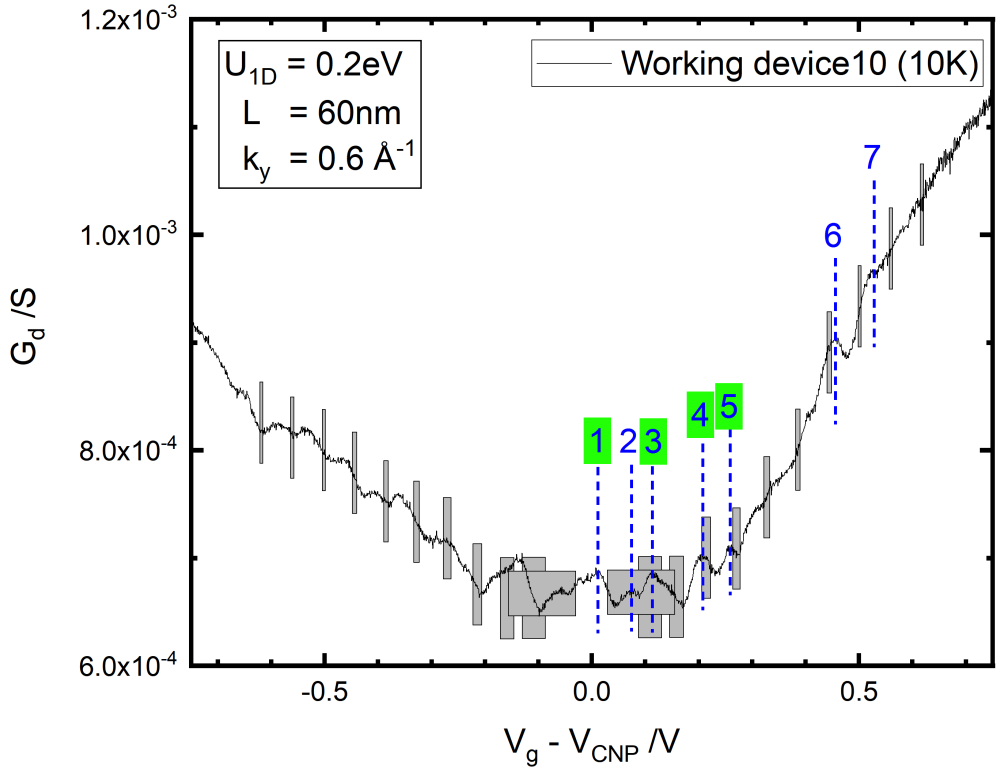

Fig. 4.28 Overlap of Figure 4.26 with Figure 4.27. The conductance drop location No.1, 3, 4, 5 (number shaded in green) refer to good matches between the theory predicted drop in conductance due to energy gap at the minizone boundary and the drop in G_d on the measured gate sweep curve.

Not all conductance drop locations are matched with theoretical predictions. The map in Figure 4.26 is based on a fixed k_y value 0.6Å^{-1} which represents the polar angle $\theta_{\vec{k},\hat{x}} = 89.5°$. Hence, the predicted map is for one single polar angle. While the electrons can travel at all angles between two electrodes, one needs to integrate the energy gap for polar angle between -90° and 90° at every minizone boundaries to get an accurate prediction. Because the graphene is not infinite, the length parameters of the graphene region shall also be taken into account of in the integral calculations.

When the polar angle $\theta_{\vec{k},\hat{x}}$ is close to $\pm 90°$, where the electron momentum has a k_y component much larger than k_x component, the electron experiences the strongest graphene superlattice effect. As the angle $\theta_{\vec{k},\hat{x}}$ approaches zero, the graphene superlattice effect disappears. This is also illustrated in Figure 4.25 of section 4.4. The map shown in Figure 4.23 is produced for barrier potential U_{1D} = 0.1, 0.15, 0.2 and 0.3eV for L = 60nm, keeping k_y fixed. The same is done for different k_y values that correspond to $\theta_{\vec{k},\hat{x}} = \pm 89.5°$, $\pm 60°$, $\pm 45°$ and $\pm 30°$ at the first minizone boundary. By overlapping those 12 maps with the measured data, the best match is shown in Figure 4.28. The same approach was undertaken for working device No.11. The top graph in Figure 4.29 shows the gate sweep measurements, with blue dashed lines marking the locations of drop in G_d. The bottom figure overlap the measured data with the theory prediction from a graphene superlattice (U_{1D} = 0.15eV and $k_y = 0.6 Å^{-1}$).
The conductance drop location No.1, 2, 3, 5, 6 in the measured data can be matched with that predicted by theory. While location No.4 is again within a predicted miniband between two shaded boxes. The periodic potentials is designed to be a square barrier with barrier width equal to 30nm, such design is also assumed in the analysis. But the PFM lithography will not produce exactly 30nm size of domain each time, bearing some equipment error. At the same time, the Fourier series included in the energy gap ΔE calculations assumes the square wave to be infinite. But the number of square barrier in each working device is between 4 to 5. The above two assumptions may not hold perfectly in experiments, and may cause discrepancies between theory and experimental data; such that the minizone boundary locations are not uniquely defined, or there are peaks near some minizone boundaries. Both are already observed in working device No.10 and 11.

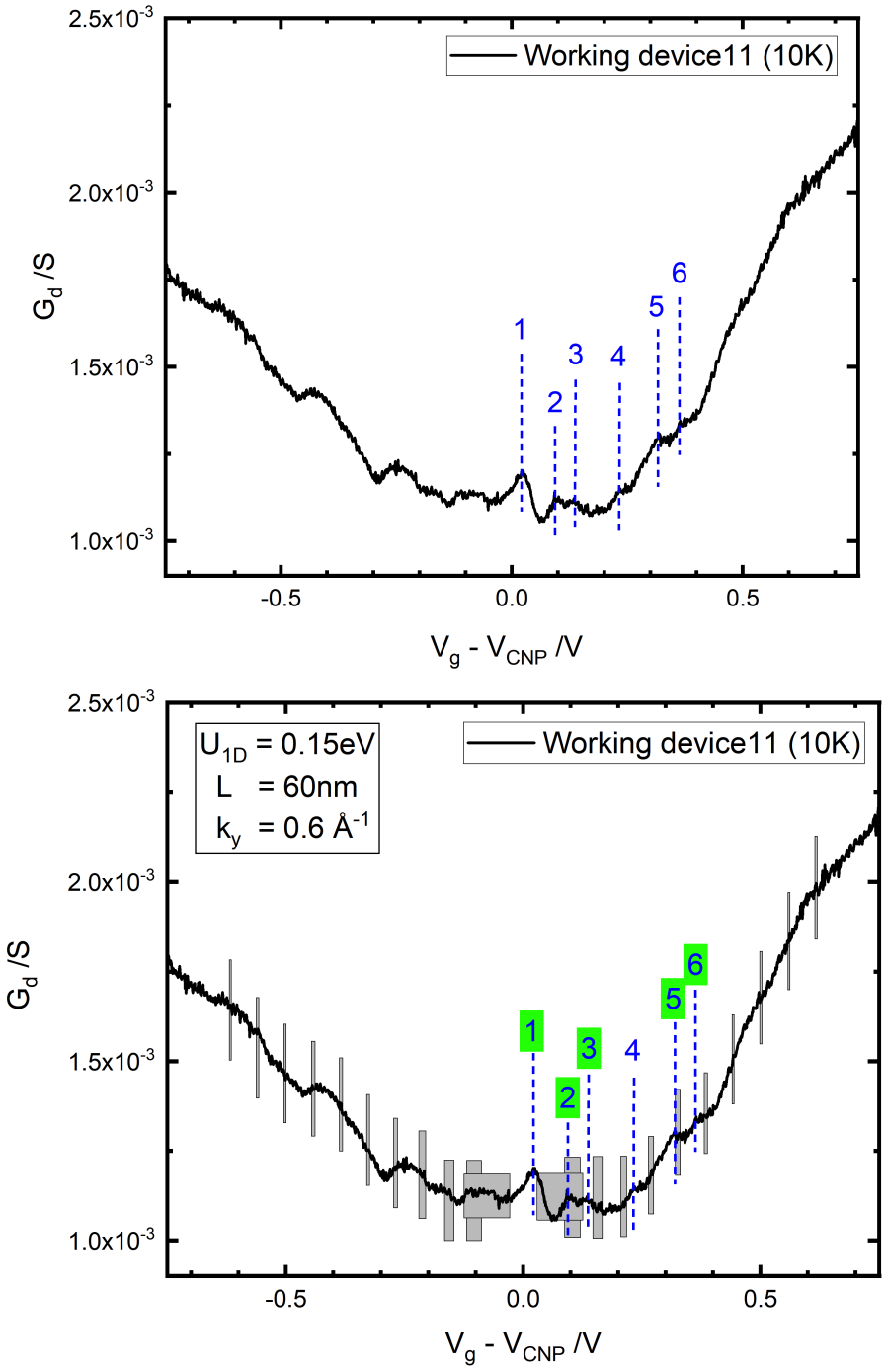

Fig. 4.29 Top: Gate sweep measurements of working device 11, whose period L for the potentials underneath is 60nm. Blue dashed lines mark the locations of a sudden drop in conductance G_d. Bottom: Overlap of theory predictions form a graphene superlattice with Figure 4.27. The conductance drop location No.1, 2, 3, 5, 6 (number shaded in green) refer to good matches between the theory predicted drop in conductance due to energy gap at the minizone boundary and the drop in G_d on the measured gate sweep curve.

It was observed that the gate sweep curve for reference devices also features with some variations in conductance, marked in Figure 4.30. One may wonder why the reference device exhibits similar behaviour to working devices. This is within our expectations due to the material used in this project, to produce periodic potentials. The ferroelectric material PZT has random domains built in from the crystal growth stage, whose directions of polarisation are usually random. If one is to measure the surface potential of a fresh PZT sample, the value is usually a few tens of milli volts. The PFM lithography step taken for the working devices firstly erases those built in domains with random polarisation directions, then replaces them with periodic domains with opposite polarisation directions. This step is omitted for reference devices, and thus leaves the PZT materials underneath graphene with domains of random polarisation directions.

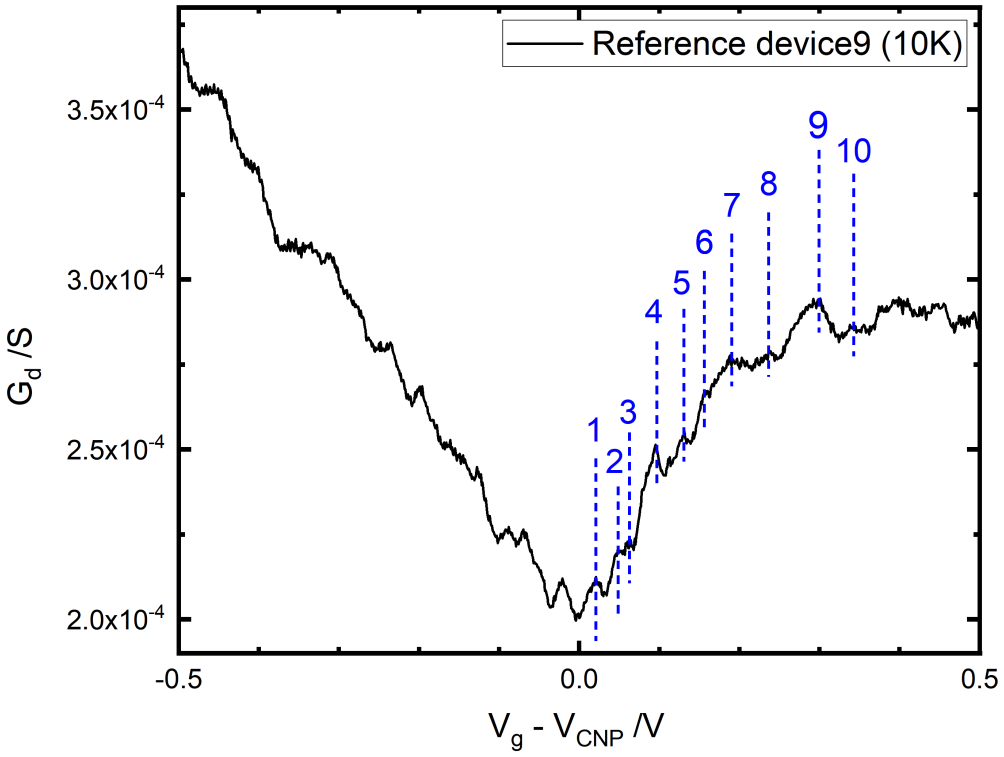

Fig. 4.30 Gate sweep measurements of working device 10, whose period L for the potentials underneath is 60nm. Blue dashed lines mark the locations of a sudden drop in conductance G_d

The distance of the square barriers i.e. the distance between drain and source electrodes, is ∼300nm. If there is a built in domain of size 100nm or above beneath the graphene region, it is very likely to cause effects similar to that from a graphene superlattice. Hence, a similar approach to that above was undertaken, and MB maps are produced for barrier potential

U_{1D} = 0.01, 0.20 and 0.30eV for L = 100nm, 115nm and 120nm, keeping k_y fixed. By overlapping those 9 maps with the measured data, the best match one is shown in Figure 4.31. The conductance drop location No.1, 2, 6, 7, 9 (number shaded in green) refer to good matches to a graphene superlattice of U_{1D} = 0.03eV and L = 100nm.

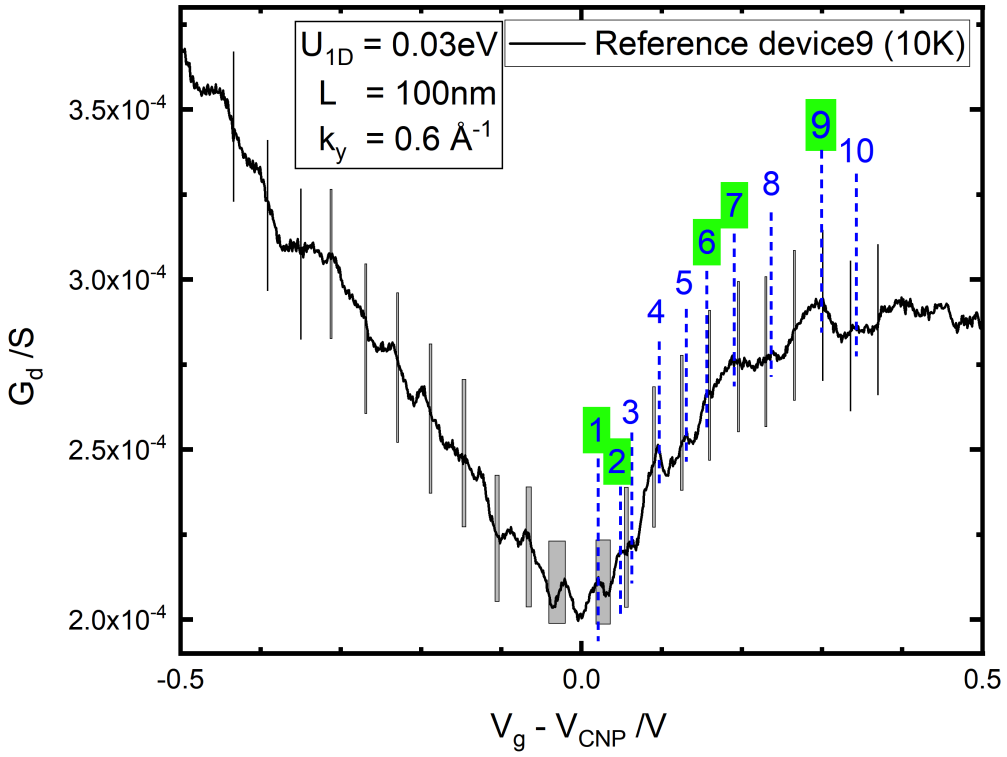

Fig. 4.31 Overlap of Figure 4.26 with Figure 4.27. The conductance drop location No.1, 2, 6, 7, 9 (number shaded in green) refer to good matches between the theory predicted drop in conductance due to energy gap at the minizone boundary and the drop in G_d on the measured gate sweep curve.

The condition in Figure 4.31 above is L=100nm, U_1D=0.03eV, which is reflected in surface potential measurements for intrinsic domains in PZT. Figure 4.32 shows a PFM magnitude image for the PZT surface. A square region in the center is poled at -10V. The surrounding materials are not poled, thus showing the intrinsic domain distribution. It is observed that natural domains in PZT are a few hundred nanometers range, and the variations in surface potential is a few tens of mV. The spontaneous domain between drain/source electrodes is very likely to cause a step barrier. Given that the size of device is 300∼400nm, comparable to intrinsic domain size, it is not surprising to see variations in conductance which are of a similar nature caused by a 1D superlattice, such as that shown in Figure 4.31.

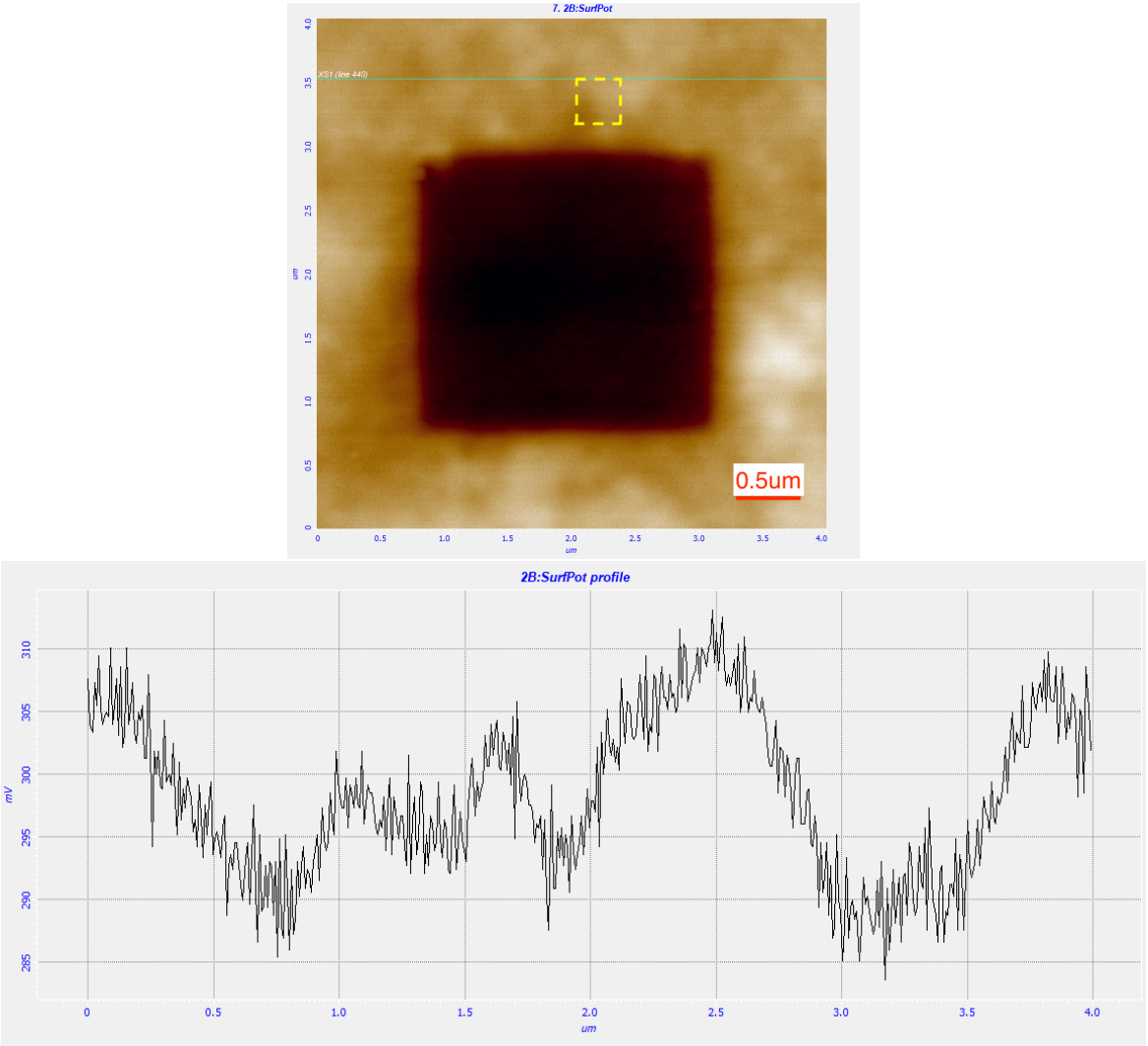

Fig. 4.32 KPFM surface potential measurement for the PZT surface: a square region is poled by -10V in the center. The surrounding material is unpoled, representing the intrinsic domains. The size of intrinsic domains is a few hundred nanometers, and the variations in surface potential is a few tens of mV. The yellow dashed square indicates the size of the PZT-graphene device.

4.6 Summary

This chapter will discuss the electrical measurement results for the PZT-graphene device. The 1D electrostatic graphene superlattice (EGSL) effect in the PZT-graphene device will be measurable as a broadening of the current valley near the CNP point and variations in conductance. Device fabrication together with pinholes on the PZT surface have lead to a low device yield rate in this work. A flat region is observed at the bottom of the gate sweep curve for working devices, while a clear CNP point is observed for reference devices (4.2). The measurements were fitted by a parabola in section 4.3 to laterally compare the size of the flat region. In section 4.4, the locations of minizone boundary and the corresponding energy gaps are computed, inspired by reference [17]. Overlapping the modelled MB map with experimental data in section 4.5 demonstrates the match between the theory and experiment. The deficiency of the model is also discussed as it did not integrate the superlattice effect at all polar angles or take into account of the length parameters of graphene.
A more inclusive model would take into account the EGSL effect at all polar angles i.e., integrate the energy gap for polar angle between -90° and 90° at every minizone boundary. Moreover, the device geometry should be involved in the theoretical calculations. In other words, instead of assuming the graphene area as infinite, the length parameters of the graphene region in the fabricated device are factored in because they affect the polar angle of the electrons travelling in the 1D periodic potential. Those improvements lead to a tailored model hence a tailored MB map for every single device to predict the 1D electrostatic graphene superlattice effect in that device.

Chapter 5

Conclusion and Future work

This work experimentally explores the effect of periodic potential modulation on the band structure of graphene. The periodic potentials are created via domain engineering in a ferroelectric material PZT. A PZT-graphene field effect device is designed, fabricated, and electrically characterised at different temperatures. Evidence of a bandgap is observed, and the measurements prove to match a theoretical predictions on 1D electrostatic graphene superlattice effect. This thesis aims to experimentally prove the idea that artificial periodic potentials created beneath a 2D material result in modifications of the band structure.

Chapter 1 introduces the basic band structure knowledge of Schrödinger's electrons as well as the chiral and massless Dirac fermions in graphene. Starting from the chemical bonding in graphene crystal lattice, a molecular orbital model was used to derived the band structure of graphene. Fermions inside graphene follows conical energy spectrum, and the resulting unusual properties such as zero mass of charge carriers near the Dirac points and Klein tunnelling are discussed. Several methods that have been proved to create energy gaps in graphene were demonstrated. Theoretical predictions on the modification of graphene band structure from 1D periodic potential perturbations, which support this work is presented.

Chapter 2 focuses on the patterning of ferroelectric materials. PZT, as a ferroelectric material, is utilised in this work as the media to produce 1D periodic potentials beneath a single layer graphene. The domain switching mechanism and the critical domain size which are essential to form engineered domains is discussed. Piezoresponse Force Microscopy (PFM) is deployed in poling periodic domains of opposite polarisation directions on the PZT surface. This chapter describes the steps taken to create and optimise of both 2D and 1D periodic potentials. The minimum dot-to-dot distance for a 2D array that was poled and successfully imaged was 39nm. In terms of 1D arrays, the minimum domain size (the strip width) was

25nm. Domains with opposite polarisation directions, when measured by the KPFM, exhibits surface potentials of opposite signs. Two domains poled by -6V and +6V are created and their surface potential difference was measured across seven days, which is effectively the barrier height. It became clear that starting with 1D periodic potentials is more sensible and likely to produce a measurable effect on the graphene band structure. All the working devices discussed in following chapters are made with 1D periodic potentials, resulting in a 1D electrostatic graphene superlattice.

Chapter 3 solves nano fabrication challenges for the PZT-graphene FET device. In order to ensure electron coherence transport between drain/source electrodes, the device size is kept around 300$\sim$400nm. Furthermore, the graphene between two electrodes is kept narrower than that of periodic potentials. Bearing constraints set by the nature of the work, some common techniques in semiconductor device fabrication which jeopardise the functionality of the devices were eliminated, such as acid treatment and heating. Eventually, a unique room temperature fabrication process was developed and put in use. There are six steps involved: alignment markers, PZT cleaning, domain engineering (refer to Chapter 2), graphene transfer, graphene etching, and electrode patterning. Detailed recipes for each step and schematics to connect between each step are all discussed. The self-designed PFM alignment markers is essential in aligning the periodic domains created by PFM lithography, with the subsequently etched graphene and patterned electrodes which are situated at pre-designed positions. A non-destructive PZT cleaning technique proved to be efficient in removing residues from previous fabrication cycles. The device structure and the intricacy in integrating PZT and graphene, have jointly lead to a low device yield rate.

Chapter 4 discusses the electrical measurement results for the PZT-graphene device. In this work, a piece of single crystal thin film PZT undergoes domain engineering to create periodic potentials. With single layer graphene transferred on top, this structure qualifies as a 1D electrostatic graphene superlattice (EGSL), whose effect is measurable as a broadening of the current valley near the CNP point and variations in conductance collectively. The mean potential caused by the thermal motion of electrons drops to 0.862mV when the temperature is reduced to 10K. Given that the 1D superlattice potential is estimated to be at least 100mV, it should be possible to observe energy gap effects. Flat regions of different size are observed at the bottom of the gate sweep curves for all working devices. A clear minimum value in conductance is seen for all reference devices, namely the CNP point. The discussed fitting analysis is able to take care of the most characteristic part of the curve, in order to contrast the flat region caused by the graphene superlattice effect. The locations of minizone boundary

and the corresponding energy gaps are computed, in order to work out a MB map at multiple conditions of superlattice potential U_{1D} and polar angle $\theta_{\vec{k},\hat{x}}$. Overlapping the modelled MB map with experimental data demonstrates the match between the theory and experiment.

The work in this thesis opens a lot of opportunities for future work. Periodic potentials are proved to be an interesting tool to explore the properties of graphene, there is a lot more to be done in this field. Firstly, it is worth to measure the PZT-graphene device at a temperature lower than 10K. The Lakeshore CPX probe station is able to achieve 1.6K in temperature while the Advanced Research Systems probe station can go down to 1.5K. Using such equipment may help discover further findings and understand the 1D electrostatic graphene superlattice effect better. Secondly, since the remained potential on the PZT substrate affects the measurability of the electrostatic graphene superlattice effect, one way to improve the domain engineering work in Chapter 2 is to extend the time decay curve. For example, having the domain engineering work carried out in vacuum can avoid the electrochemical phenomena to a large extent. It will also be beneficial to carry out further studies to separately quantify the effect from domain relaxation and water electrolysis on the surface potential contrast resulted from the domain engineering step in Chapter 2.

Thirdly, based on the knowledge learnt in Chapter 2, one is invited to fabricate devices based on 2D periodic potentials as outlined in the chapter to explore the 2D electrostatic graphene superlattice effect. The computation of minizone boundaries and energy gaps can be extended to the 2D graphene superlattice. Furthermore, it shall be noted that a 2D graphene superlattice can be considered as two 1D superlattices of different periodicity situated perpendicularly to each other, given that two groups of electrode pads are arranged perpendicularly to each other. It provides an opportunity to assess the effect of superlattice parameter e.g., periodicity and the number of barriers and wells on the electron behaviour at the same location of the sample.

Fourthly, regarding the graphene wet transfer method outlined in Chapter 3 it would be beneficial to add a study of the water layer between graphene and PZT and quantify the effect on the 1D periodic potential as well as the MB map interpretation. Fifthly, in Chapter 4 a more inclusive model would not only consider the EGSL effect at all polar angles i.e., integrate the energy gap for polar angle between -90° and 90° at every minizone boundary, but also involve the device geometry because the graphene length and width limit the range of polar angles of travelling electrons in the 1D potential. Lastly, it would be interesting to look at ways of creating 1D graphene superlattice in a more controlled manner. For example,

one can use substrates other than ferroelectric materials to realise periodic potentials e.g., growing or arranging two alternating materials of different work functions periodically on a substrate.

References

[1] Charles Kittel. Introduction to Solid State Physics, 8th edition. *Wiley & Sons, New York, NY*, 2004.

[2] Michaël Barbier, F. M. Peeters, P. Vasilopoulos, and J. Milton Pereira. Dirac and Klein-Gordon particles in one-dimensional periodic potentials. *Physical Review B - Condensed Matter and Materials Physics*, 77(11):1–9, 2008.

[3] M Polini, F Guinea, M Lewenstein, H C Manoharan, and V Pellegrini. Artificial honeycomb lattices for electrons, atoms and photons. *Nat Nanotechnol*, 8(9):625–633, 2013.

[4] W J Zhu, T Low, V Perebeinos, a a Bol, Y Zhu, H G Yan, J Tersoff, and P Avouris. Structure and Electronic Transport in Graphene Wrinkles. *Nano Letters*, 12:3431–3436, 2012.

[5] J. A. Briones-Torres, J. Madrigal-Melchor, J. C. Martínez-Orozco, and I. Rodríguez-Vargas. Electrostatic and substrate-based monolayer graphene superlattices: Energy minibands and its relation with the characteristics of the conductance curves. *Superlattices and Microstructures*, 73:98–112, 2014.

[6] Ralph C. Smith, Stefan Seelecke, Zoubeida Ounaies, and Joshua Smith. A Free Energy Model for Hysteresis in Ferroelectric Materials. *Journal of Intelligent Material Systems and Structures*, 2003.

[7] Yachin Ivry. *Nano Ferroelectrics*. PhD thesis, University of Cambridge, 2011.

[8] Franz J. Giessibl. Advances in atomic force microscopy, 2003.

[9] A. Gruverman, B. J. Rodriguez, C. Dehoff, J. D. Waldrep, A. I. Kingon, R. J. Nemanich, and J. S. Cross. Direct studies of domain switching dynamics in thin film ferroelectric capacitors. *Applied Physics Letters*, 87(8), 2005.

[10] Ramesh Nath, Seungbum Hong, Jeffrey A. Klug, Alexandra Imre, Michael J. Bedzyk, Ram S. Katiyar, and Orlando Auciello. Effects of cantilever buckling on vector piezoresponse force microscopy imaging of ferroelectric domains in BiFeO[sub 3] nanostructures. *Applied Physics Letters*, 96(16):163101, 2010.

[11] C. Durkan, M. E. Welland, D. P. Chu, and P. Migliorato. Probing domains at the nanometer scale in piezoelectric thin films. *Physical Review B*, 60(23):16198–16204, dec 1999.

[12] Xiaoyan Liu, Kenji Kitamura, and Kazuya Terabe. Thermal stability of LiTaO3 domains engineered by scanning force microscopy. *Applied Physics Letters*, 2006.

[13] Neus Domingo, Iaroslav Gaponenko, Kumara Cordero-Edwards, Nicolas Stucki, Virginia Pérez-Dieste, Carlos Escudero, Elzbieta Pach, Albert Verdaguer, and Patrycja Paruch. Surface charged species and electrochemistry of ferroelectric thin films. *Nanoscale*, 11(38), 2019.

[14] Microsystems Technology and F O R Molecular. MICROSYSTEMS TECHNOLOGY FOR MOLECULAR BIOENGINEERING LAB COURSE - ELECTRON BEAM LITHOGRAPHY Supervisors :. 2011.

[15] Joshua D Wood, Gregory P Doidge, Enrique A Carrion, Justin C Koepke, Joshua A Kaitz, Isha Datye, Ashkan Behnam, Jayan Hewaparakrama, Basil Aruin, Yaofeng Chen, Hefei Dong, Richard T Haasch, Joseph W Lyding, and Eric Pop. Annealing free, clean graphene transfer using alternative polymer scaffolds. *Nanotechnology*, 26(5):055302, 2015.

[16] Raphael Tsu. *Superlattice to Nanoelectronics*. 2011.

[17] Cheol Hwan Park, Li Yang, Young Woo Son, Marvin L Cohen, and Steven G Louie. Anisotropic behaviours of massless Dirac fermions in graphene under periodic potentials0. *Nature Physics*, 4(3):213–217, 2008.

[18] Changgu Lee, Xiaoding Wei, Jeffrey W. Kysar, and James Hone. Measurement of the elastic properties and intrinsic strength of monolayer graphene. *Science*, 2008.

[19] E.L. Wolf. *Graphene: A new Paradigm in Condensed Matter and Device Physics*. Oxford University Press, 1st edition, 2014.

[20] Koichi Saito, Jun Nakamura, and Akiko Natori. Ballistic thermal conductance of a graphene sheet. *Physical Review B - Condensed Matter and Materials Physics*, 2007.

[21] N. Mingo and D. A. Broido. Carbon nanotube ballistic thermal conductance and its limits. *Physical Review Letters*, 2005.

[22] K. S. Novoselov, A. K. Geim, S. V. Morozov, D. Jiang, Y. Zhang, S. V. Dubonos, I. V. Grigorieva, and A. A. Firsov. Electric field in atomically thin carbon films. *Science*, 2004.

[23] Keun Soo Kim, Yue Zhao, Houk Jang, Sang Yoon Lee, Jong Min Kim, Kwang S. Kim, Jong Hyun Ahn, Philip Kim, Jae Young Choi, and Byung Hee Hong. Large-scale pattern growth of graphene films for stretchable transparent electrodes. *Nature*, 2009.

[24] S. V. Morozov, K. S. Novoselov, M. I. Katsnelson, F. Schedin, D. C. Elias, J. A. Jaszczak, and A. K. Geim. Giant intrinsic carrier mobilities in graphene and its bilayer. *Physical Review Letters*, 2008.

[25] P. Blake, E. W. Hill, A. H. Castro Neto, K. S. Novoselov, D. Jiang, R. Yang, T. J. Booth, and A. K. Geim. Making graphene visible. *Applied Physics Letters*, 2007.

[26] Melinda Y. Han, Barbaros Özyilmaz, Yuanbo Zhang, and Philip Kim. Energy Band-Gap Engineering of Graphene Nanoribbons. *Physical Review Letters*, 98(20):206805, may 2007.

[27] Gui Gui, Jin Li, and Jianxin Zhong. Band structure engineering of graphene by strain: First-principles calculations. *Physical Review B - Condensed Matter and Materials Physics*, 2008.

[28] Urbano Oseguera. Classical Kronig–Penney model. *American Journal of Physics*, 60(2):127, 1992.

[29] G. A. Luna-Acosta, F. M. Izrailev, N. M. Makarov, U. Kuhl, and H. J. St??ckmann. One dimensional Kronig-Penney model with positional disorder: Theory versus experiment. *Physical Review B - Condensed Matter and Materials Physics*, 80(11), 2009.

[30] S. Gattenlöhner, W. Belzig, and M. Titov. Dirac-Kronig-Penney model for strain-engineered graphene. *Physical Review B - Condensed Matter and Materials Physics*, 82(15), 2010.

[31] Maxim Drabkin, Werner Kirsch, and Hermann Schulz-Baldes. Transport in the random Kronig-Penney model. *Journal of Mathematical Physics*, 53(12), 2012.

[32] Joo Hyoung Lee and Jeffrey C. Grossman. Energy gap of Kronig-Penney-type hydrogenated graphene superlattices. *Physical Review B - Condensed Matter and Materials Physics*, 84(11), 2011.

[33] Donald a. McQuarrie. The Kronig-Penney Model: A Single Lecture Illustrating the Band Structure of Solids. *The Chemical Educator*, 1(1):1–10, 1996.

[34] Ben G Streetman and Sanjay Banerjee. Solid state electronic devices, 2000.

[35] Akihiko Yoshikawa, Hiroyuki Matsunami, and Yasushi Nanishi. Development and applications of wide bandgap semiconductors. In *Wide Bandgap Semiconductors: Fundamental Properties and Modern Photonic and Electronic Devices*. Springer, 2007.

[36] E. Schrödinger. An undulatory theory of the mechanics of atoms and molecules. *Physical Review*, 1926.

[37] E. Schrödinger. Quantisierung als Eigenwertproblem. *Annalen der Physik*, 1926.

[38] E. Schrödinger. Quantisierung als Eigenwertproblem. *Annalen der Physik*, 1926.

[39] E. Schrödinger. Quantisierung als Eigenwertproblem. *Annalen der Physik*, 1926.

[40] E. Schrödinger. Der stetige Übergang von der Mikro- zur Makromechanik. *Die Naturwissenschaften*, 1926.

[41] E. Schrödinger. Quantisierung als Eigenwertproblem. *Annalen der Physik*, 1926.

[42] M Barbier, P Vasilopoulos, and F M Peeters. Dirac electrons in a Kronig-Penney potential: Dispersion relation and transmission periodic in the strength of the barriers. pages 3–7, 2009.

[43] P R Wallace. The band theory of graphite. *Physical Review*, 71(9):622–634, 1947.

[44] K S Novoselov, A K Geim, S V Morozov, D Jiang, Y Zhang, S V Dubonos, I V Grigorieva, and A A Firsov. Electric Field Effect in Atomically Thin Carbon Films. *Science*, 306(5696):666–669, 2004.

[45] Wheeler Conover. Chemistry, 8th Edition (by Stephen S. Zumdahl and Susan A. Zumdahl). *Journal of Chemical Education*, 2009.

[46] A H Castro Neto, F Guinea, N M R Peres, K S Novoselov, and A K Geim. The electronic properties of graphene. *Rev. Mod. Phys.*, 81(1):109–162, jan 2009.

[47] Yuanbo Zhang, Yan Wen Tan, Horst L. Stormer, and Philip Kim. Experimental observation of the quantum Hall effect and Berry's phase in graphene. *Nature*, 2005.

[48] S Reich, J Maultzsch, C Thomsen, and P Ordejón. Tight-binding description of graphene. *Phys. Rev. B*, 66(3):35412, jul 2002.

[49] J. C. Slonczewski and P. R. Weiss. Band structure of graphite. *Physical Review*, 1958.

[50] K S Novoselov, A K Geim, S V Morozov, D Jiang, M I Katsnelson, I V Grigorieva, S V Dubonos, and A A Firsov. Two-dimensional gas of massless Dirac fermions in graphene. *Nature*, 438(7065):197–200, 2005.

[51] F. D.M. Haldane. Model for a quantum hall effect without landau levels: Condensed-matter realization of the "parity anomaly". *Physical Review Letters*, 1988.

[52] Gordon W. Semenoff. Condensed-Matter simulation of a three-Dimensional anomaly. *Physical Review Letters*, 1984.

[53] A. K. Geim and K. S. Novoselov. The rise of graphene. *Nature Materials*, 2007.

[54] A. Calogeracos and N. Dombey. History and physics of the Klein paradox. *Contemporary Physics*, 1999.

[55] Choongyu Hwang, David A. Siegel, Sung Kwan Mo, William Regan, Ariel Ismach, Yuegang Zhang, Alex Zettl, and Alessandra Lanzara. Fermi velocity engineering in graphene by substrate modification. *Scientific Reports*, 2012.

[56] D. C. Elias, R. V. Gorbachev, A. S. Mayorov, S. V. Morozov, A. A. Zhukov, P. Blake, L. A. Ponomarenko, I. V. Grigorieva, K. S. Novoselov, F. Guinea, and A. K. Geim. Dirac cones reshaped by interaction effects in suspended graphene. *Nature Physics*, 2011.

[57] N. Dombey and A. Calogeracos. Seventy years of the Klein paradox. *Physics Report*, 1999.

[58] M I Katsnelson, K S Novoselov, and A K Geim. Chiral tunnelling and the Klein paradox in graphene. *Nature Physics*, 2(9):620–625, 2006.

[59] Alexander A. Balandin, Suchismita Ghosh, Wenzhong Bao, Irene Calizo, Desalegne Teweldebrhan, Feng Miao, and Chun Ning Lau. Superior thermal conductivity of single-layer graphene. *Nano Letters*, 2008.

[60] Jae Hun Seol, Insun Jo, Arden L. Moore, Lucas Lindsay, Zachary H. Aitken, Michael T. Pettes, Xuesong Li, Zhen Yao, Rui Huang, David Broido, Natalio Mingo, Rodney S. Ruoff, and Li Shi. Two-dimensional phonon transport in supported graphene. *Science*, 2010.

[61] Eric Pop, Vikas Varshney, and Ajit K. Roy. Thermal properties of graphene: Fundamentals and applications. *MRS Bulletin*, 2012.

[62] Albert D. Liao, Justin Z. Wu, Xinran Wang, Kristof Tahy, Debdeep Jena, Hongjie Dai, and Eric Pop. Thermally limited current carrying ability of graphene nanoribbons. *Physical Review Letters*, 2011.

[63] Alberto Cortijo and María A.H. Vozmediano. Effects of topological defects and local curvature on the electronic properties of planar graphene. *Nuclear Physics B*, 2007.

[64] G. M. Rutter, J. N. Crain, N. P. Guisinger, T. Li, P. N. First, and J. A. Stroscio. Scattering and interference in epitaxial graphene. *Science*, 2007.

[65] S. Das Sarma, Shaffique Adam, E. H. Hwang, and Enrico Rossi. Electronic transport in two-dimensional graphene. *Reviews of Modern Physics*, 2011.

[66] C. Casiraghi, A. Hartschuh, E. Lidorikis, H. Qian, H. Harutyunyan, T. Gokus, K. S. Novoselov, and A. C. Ferrari. Rayleigh imaging of graphene and graphene layers. *Nano Letters*, 2007.

[67] Matthew J Allen, Vincent C Tung, and Richard B Kaner. Honeycomb Carbon: A Review of Graphene. *Chemical Reviews*, 110(1):132–145, jan 2010.

[68] Yuanbo Zhang, Victor W. Brar, Caglar Girit, Alex Zettl, and Michael F. Crommie. Origin of spatial charge inhomogeneity in graphene. *Nature Physics*, 6(1):74–74, 2010.

[69] K. S. Novoselov, E. McCann, S. V. Morozov, V. I. Falko, M. I. Katsnelson, U. Zeitler, D. Jiang, F. Schedin, and a. K. Geim. Unconventional quantum Hall effect and Berry's phase of 2pi in bilayer graphene. *Nat. Phys.*, 180:177–180, 2006.

[70] Edward McCann. Interlayer asymmetry gap in the electronic band structure of bilayer graphene. In *Physica Status Solidi (B) Basic Research*, volume 244, pages 4112–4117, 2007.

[71] Irene Palacio, Arlensi?? Celis, Maya N. Nair, Alexandre Gloter, Alberto Zobelli, Muriel Sicot, Daniel Malterre, Meredith S. Nevius, Walt A. De Heer, Claire Berger, Edward H. Conrad, Amina Taleb-Ibrahimi, and Antonio Tejeda. Atomic structure of epitaxial graphene sidewall nanoribbons: Flat graphene, miniribbons, and the confinement gap. *Nano Letters*, 15(1):182–189, 2015.

[72] Katsunori Wakabayashi, Mitsutaka Fujita, Hiroshi Ajiki, and Manfred Sigrist. Electronic and magnetic properties of nanographite ribbons. *Physical Review B*, 59(12):8271, 1999.

[73] Young Woo Son, Marvin L. Cohen, and Steven G. Louie. Energy gaps in graphene nanoribbons. *Physical Review Letters*, 97(21), 2006.

[74] L. Brey and H. A. Fertig. Electronic states of graphene nanoribbons studied with the Dirac equation. *Physical Review B*, 73(23):2–6, 2006.

[75] K Nakada, M Fujita, G Dresselhaus, and M S Dresselhaus. Edge state in graphene ribbons: Nanometer size effect and edge shape dependence. *Physical Review B*, 54(24):17954–17961, 1996.

[76] Denis A. Areshkin, Daniel Gunlycke, and Carter T. White. Ballistic transport in graphene nanostrips in the presence of disorder: Importance of edge effects. *Nano Letters*, 7(1):204–210, 2007.

[77] V Barone, O Hod, and G E Scuseria. Electronic structure and stability of semiconducting graphene nanoribbons. *Nano Lett*, 6(12):2748–2754, 2006.

[78] Li Yang, Cheol Hwan Park, Young Woo Son, Marvin L. Cohen, and Steven G. Louie. Quasiparticle energies and band gaps in graphene nanoribbons. *Physical Review Letters*, 2007.

[79] T. Low, F. Guinea, and M. I. Katsnelson. Gaps tunable by electrostatic gates in strained graphene. *Physical Review B - Condensed Matter and Materials Physics*, 2011.

[80] Vitor M. Pereira, A. H. Castro Neto, H. Y. Liang, and L. Mahadevan. Geometry, mechanics, and electronics of singular structures and wrinkles in graphene. *Physical Review Letters*, 2010.

[81] Zhihong Chen, Yu-Ming Lin, Michael J. Rooks, and Phaedon Avouris. Graphene nano-ribbon electronics. *Physica E: Low-dimensional Systems and Nanostructures*, 40(2):228–232, dec 2007.

[82] Barbaros Özyilmaz, Pablo Jarillo-Herrero, Dmitri Efetov, and Philip Kim. Electronic transport in locally gated graphene nanoconstrictions. *Applied Physics Letters*, 2007.

[83] Xiaolin Li, Xinran Wang, Li Zhang, Sangwon Lee, and Hongjie Dai. Chemically derived, ultrasmooth graphene nanoribbon semiconductors. *Science*, 2008.

[84] J. Hicks, A. Tejeda, A. Taleb-Ibrahimi, M. S. Nevius, F. Wang, K. Shepperd, J. Palmer, F. Bertran, P. Le Fèvre, J. Kunc, W. a. de Heer, C. Berger, and E. H. Conrad. A wide-bandgap metal-semiconductor-metal nanostructure made entirely from graphene. *Nature Physics*, 9(1):49–54, 2013.

[85] Irene Palacio, Arlensiú Celis, Maya N. Nair, Alexandre Gloter, Alberto Zobelli, Muriel Sicot, Daniel Malterre, Meredith S. Nevius, Walt A. De Heer, Claire Berger, Edward H. Conrad, Amina Taleb-Ibrahimi, and Antonio Tejeda. Atomic structure of epitaxial graphene sidewall nanoribbons: Flat graphene, miniribbons, and the confinement gap. *Nano Letters*, 2015.

[86] TSU LESAKIR. SUPERLATTICE AND NEGATIVE DIFFERENTIAL CONDUCTIVITY IN SEMICONDUCTOR. *IBM Journal of Research and Development*, 1970.

[87] D. Weiss, K. V. Klitzing, K. Ploog, and G. Weimann. Magnetoresistance oscillations in a two-dimensional electron gas induced by a submicrometer periodic potential. *EPL*, 1989.

[88] Till Schlösser, Klaus Ensslin, Jörg P. Kotthaus, and Martin Holland. Landau subbands generated by a lateral electrostatic superlattice - Chasing the Hofstadter butterfly. *Semiconductor Science and Technology*, 1996.

[89] C. Albrecht, J. H. Smet, K. Von Klitzing, D. Weiss, V. Umansky, and H. Schweizer. Evidence of Hofstadter's fractal energy spectrum in the quantized Hall conductance. *Physical Review Letters*, 2001.

[90] Thomas G. Pedersen, Christian Flindt, Jesper Pedersen, Niels Asger Mortensen, Antti Pekka Jauho, and Kjeld Pedersen. Graphene antidot lattices: Designed defects and spin qubits. *Physical Review Letters*, 100(13), 2008.

[91] L. A. Chernozatonskiĭ, P. B. Sorokin, E. É. Belova, J. Brüning, and A. S. Fedorov. Superlattices consisting of "lines" of adsorbed hydrogen atom pairs on graphene. *JETP Letters*, 85(1):77–81, 2007.

[92] Elizabeth J. Duplock, Matthias Scheffler, and Philip J D Lindan. Hallmark of perfect graphene. *Physical Review Letters*, 92(22):225502–1, 2004.

[93] Jorge O. Sofo, Ajay S. Chaudhari, and Greg D. Barber. Graphane: A two-dimensional hydrocarbon. *Physical Review B - Condensed Matter and Materials Physics*, 2007.

[94] Jian Zhou, Miao Miao Wu, Xiao Zhou, and Qiang Sun. Tuning electronic and magnetic properties of graphene by surface modification. *Applied Physics Letters*, 2009.

[95] Richard Balog, Bjarke Jørgensen, Louis Nilsson, Mie Andersen, Emile Rienks, Marco Bianchi, M Fanetti, Erik Lægsgaard, Alessandro Baraldi, Silvano Lizzit, Zeljko Sljivancanin, Flemming Besenbacher, Bjørk Hammer, Thomas G Pedersen, Philip Hofmann, and Liv Hornekær. Bandgap opening in graphene induced by patterned hydrogen adsorption. *Nature Materials*, 9(4):315–319, 2010.

[96] Carlos Forsythe, Xiaodong Zhou, Kenji Watanabe, Takashi Taniguchi, Abhay Pasupathy, Pilkyung Moon, Mikito Koshino, Philip Kim, and Cory R. Dean. Band structure engineering of 2D materials using patterned dielectric superlattices. *Nature Nanotechnology*, 2018.

[97] Eli Rotenberg, Aaron Bostwick, Taisuke Ohta, Jessica L McChesney, Thomas Seyller, and Karsten Horn. Origin of the energy bandgap in epitaxial graphene. *Nature materials*, 7(4):258–259; author reply 259–260, 2008.

[98] George Alexandru Nemnes, Daniela Dragoman, and Mircea Dragoman. Graphene bandgap induced by ferroelectric Pca 21 HfO2 substrates: A first-principles study. *Physical Chemistry Chemical Physics*, 2019.

[99] S Y Zhou, G-H Gweon, a V Fedorov, P N First, W a de Heer, D-H Lee, F Guinea, a H Castro Neto, and a Lanzara. Substrate-induced bandgap opening in epitaxial graphene. *Nature materials*, 6(10):770–775, 2007.

[100] Marco Gobbi, Sara Bonacchi, Jian X. Lian, Yi Liu, Xiao Ye Wang, Marc Antoine Stoeckel, Marco A. Squillaci, Gabriele D'Avino, Akimitsu Narita, Klaus Müllen, Xinliang Feng, Yoann Olivier, David Beljonne, Paolo Samorì, and Emanuele Orgiu. Periodic potentials in hybrid van der Waals heterostructures formed by supramolecular lattices on graphene. *Nature Communications*, 2017.

[101] Maya N. Nair, Irene Palacio, Arlensiú Celis, Alberto Zobelli, Alexandre Gloter, Stefan Kubsky, Jean Philippe Turmaud, Matthew Conrad, Claire Berger, Walter De Heer, Edward H. Conrad, Amina Taleb-Ibrahimi, and Antonio Tejeda. Band Gap Opening Induced by the Structural Periodicity in Epitaxial Graphene Buffer Layer. *Nano Letters*, 17(4):2681–2689, 2017.

[102] Matthew Yankowitz, Jeil Jung, Evan Laksono, Nicolas Leconte, Bheema L. Chittari, K. Watanabe, T. Taniguchi, Shaffique Adam, David Graf, and Cory R. Dean. Dynamic band-structure tuning of graphene moiré superlattices with pressure. *Nature*, 2018.

[103] Tsuneya Ando and Takeshi Nakanishi. Impurity Scattering in Carbon Nanotubes - Absence of Back Scattering. *Journal of the Physical Society of Japan*, 1998.

[104] Tsuneya Ando, Takeshi Nakanishi, and Riichiro Saito. Berry's Phase and Absence of Back Scattering in Carbon Nanotubes. *Journal of the Physical Society of Japan*, 1998.

[105] Paul L. Mc Euen, Marc Bockrath, David H. Cobden, Young Gui Yoon, and Steven G. Louie. Disorder, pseudospins, and backscattering in carbon nanotubes. *Physical Review Letters*, 1999.

[106] I. Rodríguez-Vargas, J. Madrigal-Melchor, and O. Oubram. Resonant tunneling through double barrier graphene systems: A comparative study of Klein and non-Klein tunneling structures. *Journal of Applied Physics*, 112(7), 2012.

[107] Z. Xiao and C. Durkan. Size effects in the resistivity of graphene nanoribbons. *Nanotechnology*, 2019.

[108] M. E Lines and A. M Glass. Applications of Ferroelectrics. In *Principles and Applications of Ferroelectrics and Related Materials*, pages 1–43. 2001.

[109] D J Griffiths. *Introduction to electrodynamics,Griffith-3ed.pdf*, volume 3. 2010.

[110] GH Haertling. Ferroelectric ceramics: history and technology. *J. Am. Ceram. Soc.*, 82(4):718–818, 1999.

[111] Draean Damjanovic. Ferroelectric, dielectric and piezoelectric properties of ferroelectric thin films and ceramics. *Reports on Progress in Physics*, 1998.

[112] Joseph Valasek. Note on the piezo-electric effect in Rochelle salt crystals. *Science*, 1927.

[113] C. B. Sawyer and C. H. Tower. Rochelle salt as a dielectric. *Physical Review*, 35(3):269–273, 1930.

[114] Yachin Ivry, Nan Wang, and Colm Durkan. High-frequency programmable acoustic wave device realized through ferroelectric domain engineering. *Applied Physics Letters*, 104(13), 2014.

[115] G. Arlt. Twinning in ferroelectric and ferroelastic ceramics: stress relief, 1990.

[116] A. L. Kholkin, S. V. Kalinin, A. Roelofs, and A. Gruverman. Review of ferroelectric domain imaging by piezoresponse force microscopy. In *Scanning Probe Microscopy*. 2007.

[117] Yachin Ivry, Nan Wang, Daping Chu, and Colm Durkan. 90° Domain Dynamics and Relaxation in Thin Ferroelectric/Ferroelastic Films. *Physical Review B - Condensed Matter and Materials Physics*, 81(17):1–8, 2010.

[118] Jose Angel and Garcia Melendrez. Ferroelectric and Ferroelastic phenomena in PZT thin films. (April), 2014.

[119] Yachin Ivry, D P Chu, and Colm Durkan. Bundles of polytwins as meta-elastic domains in the thin polycrystalline simple multi-ferroic system PZT. *Nanotechnology*, 21(6):065702, 2010.

[120] C Durkan, D P Chu, P Migliorato, M E Welland, C Durkan, D P Chu, P Migliorato, and M E Welland. Investigations into local piezoelectric properties by atomic force microscopy Investigations into local piezoelectric properties by atomic force microscopy. 366(2000):31–34, 2016.

[121] Yachin Ivry, James F. Scott, Ekhard K H Salje, and Colm Durkan. Nucleation, growth, and control of ferroelectric-ferroelastic domains in thin polycrystalline films. *Physical Review B - Condensed Matter and Materials Physics*, 86(20):1–6, 2012.

[122] Y. Ivry, D. P. Chu, J. F. Scott, and C. Durkan. Flux closure vortexlike domain structures in ferroelectric thin films. *Physical Review Letters*, 104(20):1–4, 2010.

[123] Yachin Ivry, Daping Chu, and Colm Durkan. Nanometer resolution piezoresponse force microscopy to study deep submicron ferroelectric and ferroelastic domains. *Applied Physics Letters*, 94(16), 2009.

[124] R J a Steenwelle. Characterization of piezo- and ferroelectric thin films by Scanning Probe Techniques. (September):0–58, 2007.

[125] A. Garcia-Melendrez and C. Durkan. Reversible nanoscale switching of polytwin orientation in a ferroelectric thin film induced by a local electric field. *Applied Physics Letters*, 103(9), 2013.

[126] Yachin Ivry, Colm Durkan, Daping Chu, and James F. Scott. Nano-domain pinning in ferroelastic-ferroelectrics by extended structural defects. *Advanced Functional Materials*, 24(35):5567–5574, 2014.

[127] Sergei V Kalinin, Brian J Rodriguez, Stephen Jesse, Junsoo Shin, Arthur P Baddorf, Pradyumna Gupta, Himanshu Jain, David B Williams, and Alexei Gruverman. Vector piezoresponse force microscopy. *Microscopy and microanalysis : the official journal of Microscopy Society of America, Microbeam Analysis Society, Microscopical Society of Canada*, 12(3):206–220, 2006.

[128] Colm Durkan, Jose Angel Garcia-Melendrez, and Long Ding. On the Manipulation of Ferroelectric and Ferroelastic Domains at the Nanoscale. *Journal of Electronic Materials*, 44(7):2230–2242, 2015.

[129] C Durkan, M E Welland, D P Chu, and P Migliorato. Scaling of piezoelectric properties in nanometre to micrometre scale. *Electronics Letters*, 36(18):1538–1539, 2000.

[130] Stephen Jesse, Brian J Rodriguez, Samrat Choudhury, Arthur P Baddorf, Ionela Vrejoiu, Dietrich Hesse, Marin Alexe, Eugene a Eliseev, Anna N Morozovska, Jingxian Zhang, Long-Qing Chen, and Sergei V Kalinin. Direct imaging of the spatial and energy distribution of nucleation centres in ferroelectric materials. *Nature materials*, 7:209–215, 2008.

[131] L M Eng, H J Guntherodt, G a Schneider, U Kopke, and J M Saldana. Nanoscale reconstruction of surface crystallography from three-dimensional polarization distribution in ferroelectric barium-titanate ceramics. *Applied Physics Letters*, 74(2):233–235, 1999.

[132] Rolf Landauer. Electrostatic considerations in BaTiO3 domain formation during polarization reversal. *Journal of Applied Physics*, 1957.

[133] M. Dawber, P. Chandra, P. B. Littlewood, and J. F. Scott. Depolarization corrections to the coercive field in thin-film ferroelectrics. *Journal of Physics Condensed Matter*, 2003.

[134] G. Catalan, A. Schilling, J. F. Scott, and J. M. Gregg. Domains in three-dimensional ferroelectric nanostructures: Theory and experiment. *Journal of Physics Condensed Matter*, 19(13), 2007.

[135] Sergei V. Kalinin, Anna N. Morozovska, Long Qing Chen, and Brian J. Rodriguez. Local polarization dynamics in ferroelectric materials. *Reports on Progress in Physics*, 2010.

[136] Yi Kan, Xiaomei Lu, Huifeng Bo, Fengzhen Huang, Xiaobo Wu, and Jinsong Zhu. Critical radii of ferroelectric domains for different decay processes in LiNb O3 crystals. *Applied Physics Letters*, 2007.

[137] Yi Kan, Huifeng Bo, Xiaomei Lu, Wei Cai, Yunfei Liu, and Jinsong Zhu. Growth evolution and decay properties of the abnormally switched domains in LiNb O3 crystals. *Applied Physics Letters*, 2008.

[138] Xijun Li, Kazuya Terabe, Hideki Hatano, and Kenji Kitamura. Nano-domain engineering in LiNbO3 by focused ion beam. *Japanese Journal of Applied Physics, Part 2: Letters*, 2005.

[139] Sergei V. Kalinin, Yunseok Kim, Dillon D. Fong, and Anna N. Morozovska. Surface-screening mechanisms in ferroelectric thin films and their effect on polarization dynamics and domain structures, 2018.

[140] Min-Jung Lee, Tae-Il Lee, Jinhyong Lim, Jungsik Bang, Woong Lee, Taeyoon Lee, and Jae-Min Myoung. Effect of the deposition temperature and a hydrogen post-annealing treatment on the structural, electrical, and optical properties of Ga-doped ZnO films. *Electronic Materials Letters*, 2009.

[141] Junjiang Tian, Zhengwei Tan, Zhen Fan, Dongfeng Zheng, Yadong Wang, Zoufei Chen, Fei Sun, Deyang Chen, Minghui Qin, Min Zeng, Xubing Lu, Xingsen Gao, and Jun Ming Liu. Depolarization-Field-Induced Retention Loss in Ferroelectric Diodes. *Physical Review Applied*, 11(2), 2019.

[142] F. Laurell, M. G. Roelofs, and H. Hsiung. Loss of optical nonlinearity in proton-exchanged LiNbO3 waveguides. *Applied Physics Letters*, 1992.

[143] Joachim Maier. *Physical Chemistry of Ionic Materials: Ions and Electrons in Solids*. 2004.

[144] Sergei V. Kalinin and Dawn A. Bonnell. Local potential and polarization screening on ferroelectric surfaces. *Physical Review B - Condensed Matter and Materials Physics*, 63(12), 2001.

[145] Sergei V. Kalinin, C. Y. Johnson, and Dawn A. Bonnell. Domain polarity and temperature induced potential inversion on the BaTiO 3(100) surface. *Journal of Applied Physics*, 91(6), 2002.

[146] Sergei V. Kalinin and Dawn A. Bonnell. Screening phenomena on oxide surfaces and its implications for local electrostatic and transport measurements. *Nano Letters*, 4(4), 2004.

[147] M. Debska. Surface potential decay on triglycine sulfate crystal. *Journal of Electrostatics*, 63(11), 2005.

[148] Boštjan Berčič. Introduction to Electron Beam Lithography. *Scanning Electron Microscopy*.

[149] Maria Stepanova and Steven Dew. *Nanofabrication: Techniques and principles*. 2014.

[150] A. Baptista, F. J.G. Silva, J. Porteiro, J. L. Míguez, G. Pinto, and L. Fernandes. On the Physical Vapour Deposition (PVD): Evolution of Magnetron Sputtering Processes for Industrial Applications. In *Procedia Manufacturing*, 2018.

[151] Woosuk Choi, Muhammad Arslan Shehzad, Sanghoon Park, and Yongho Seo. Influence of removing PMMA residues on surface of CVD graphene using a contact-mode atomic force microscope. *RSC Advances*, 7(12), 2017.

[152] X. Li, W. Cai, J. An, S. Kim, J. Nah, D. Yang, R. Piner, A. Velamakanni, I. Jung, E. Tutuc, S.K. Banerjee, L. Colombo, and R.S. Ruoff. Large area synthesis of high quality and uniform graphene films on copper foils. *Science*, 324(5932):1312–1314, 2009.

[153] A Reina, X T Jia, J Ho, D Nezich, H B Son, V Bulovic, M S Dresselhaus, and J Kong. Large Area, Few-Layer Graphene Films on Arbitrary Substrates by Chemical Vapor Deposition. *Nano Letters*, 9(1):30–35, 2009.

[154] Soon Yong Kwon, Cristian V. Ciobanu, Vania Petrova, Vivek B. Shenoy, Javier Bareño, Vincent Gambin, Ivan Petrov, and Suneel Kodambaka. Growth of semiconducting graphene on palladium. *Nano Letters*, 9(12):3985–3990, 2009.

[155] Peter W Sutter, Jan-Ingo Flege, and Eli a Sutter. Epitaxial graphene on ruthenium. *Nature materials*, 7(5):406–11, 2008.

[156] Johann Coraux, Alpha T. N'Diaye, Carsten Busse, and Thomas Michely. Structural coherency of graphene on Ir(111). *Nano Letters*, 8(2):565–570, 2008.

[157] Xingyi Wu, Guofang Zhong, Lorenzo D'Arsié, Hisashi Sugime, Santiago Esconjauregui, Alex W. Robertson, and John Robertson. Growth of Continuous Monolayer Graphene with Millimeter-sized Domains Using Industrially Safe Conditions. *Scientific Reports*, 2016.

[158] Zhang Ting Wu, Wei Wei Zhao, Wei Yu Chen, Jie Jiang, Hai Yan Nan, Xi Tao Guo, Zheng Liang, Yu Ming Chen, Yun Fei Chen, and Zhen Hua Ni. The influence of chemical solvents on the properties of CVD graphene. *Journal of Raman Spectroscopy*, 2015.

[159] Morton L. Heilig. United States Patent Office. *ACM SIGGRAPH Computer Graphics*, 28(2):131–134, 1994.

[160] Grzegorz Lupina, Julia Kitzmann, Ioan Costina, Mindaugas Lukosius, Christian Wenger, Andre Wolff, Sam Vaziri, Mikael Östling, Iwona Pasternak, Aleksandra Krajewska, Wlodek Strupinski, Satender Kataria, Amit Gahoi, Max C. Lemme, Guenther Ruhl, Guenther Zoth, Oliver Luxenhofer, and Wolfgang Mehr. Residual metallic contamination of transferred chemical vapor deposited graphene. *ACS Nano*, 2015.

[161] Ahmed Ibrahim, Ghaith Nadhreen, Sultan Akhtar, Feras M. Kafiah, and Tahar Laoui. Study of the impact of chemical etching on Cu surface morphology, graphene growth and transfer on SiO2/Si substrate. *Carbon*, 2017.

[162] Ke Xu, Peigen Cao, and James R. Heath. Graphene visualizes the first water adlayers on mica at ambient conditions. *Science*, 329(5996), 2010.

[163] C. Melios, C. E. Giusca, V. Panchal, and O. Kazakova. Water on graphene: Review of recent progress, 2018.

[164] D. Y. He, L. J. Qiao, Alex A. Volinsky, Y. Bai, M. Wu, and W. Y. Chu. Humidity effects on (001) BaTiO3 single crystal surface water adsorption. *Applied Physics Letters*, 98(6), 2011.

[165] J. J. Segura, N. Domingo, J. Fraxedas, and A. Verdaguer. Surface screening of written ferroelectric domains in ambient conditions. *Journal of Applied Physics*, 113(18), 2013.

[166] Zhuocong Xiao, Qifang Wan, and Colm Durkan. Cleaning Transferred Graphene for Optimization of Device Performance. *Advanced Materials Interfaces*, 2019.

[167] Shishir Kumar, Nikos Peltekis, Kangho Lee, Hye Young Kim, and Georg Stefan Duesberg. Reliable processing of graphene using metal etchmasks. *Nanoscale Research Letters*, 2011.

[168] Michaël Barbier, F. M. Peeters, P. Vasilopoulos, and J. Milton Pereira. Dirac and Klein-Gordon particles in one-dimensional periodic potentials. *Physical Review B - Condensed Matter and Materials Physics*, 77(11):1–9, 2008.

[169] Cheol-Hwan Park, Li Yang, Young-Woo Son, Marvin L. Cohen, and Steven G. Louie. New Generation of Massless Dirac Fermions in Graphene under External Periodic Potentials. *Physical Review Letters*, 101(12):126804, 2008.

[170] Cheol Hwan Park, Young Woo Son, Li Yang, Marvin L. Cohen, and Steven G. Louie. Electron beam supercollimation in graphene superlattices. *Nano Letters*, 8(9):2920–2924, 2008.

[171] Rakesh P. Tiwari and D. Stroud. Tunable band gap in graphene with a noncentrosymmetric superlattice potential. *Physical Review B - Condensed Matter and Materials Physics*, 79(20):1–5, 2009.

[172] M. Barbier, P. Vasilopoulos, and F. M. Peeters. Extra Dirac points in the energy spectrum for superlattices on single-layer graphene. *Physical Review B - Condensed Matter and Materials Physics*, 81(7):1–7, 2010.

[173] Li Gang Wang and Shi Yao Zhu. Electronic band gaps and transport properties in graphene superlattices with one-dimensional periodic potentials of square barriers. *Physical Review B - Condensed Matter and Materials Physics*, 2010.

[174] Cheol Hwan Park, Liang Zheng Tan, and Steven G. Louie. Theory of the electronic and transport properties of graphene under a periodic electric or magnetic field. *Physica E: Low-Dimensional Systems and Nanostructures*, 43(3):651–656, 2011.

[175] E. S. Azarova and G. M. Maksimova. Transport in graphene nanostructures with spatially modulated gap and potential. *Physica E: Low-Dimensional Systems and Nanostructures*, 61:118–124, 2014.

[176] Yi Xu, Ying He, and Yanfang Yang. Resonant peak splitting in graphene superlattices with one-dimensional periodic potentials. *Applied Physics A: Materials Science and Processing*, 115(3):721–729, 2014.

[177] Yi Xu, Ying He, and Yanfang Yang. Transmission gaps in graphene superlattices with periodic potential patterns. *Physica B: Condensed Matter*, 457:188–193, 2015.

[178] H. García-Cervantes, L. M. Gaggero-Sager, O. Sotolongo-Costa, G. G. Naumis, and I. Rodríguez-Vargas. Angle-dependent bandgap engineering in gated graphene superlattices. *AIP Advances*, 6(3), 2016.

[179] Tingting Feng, Dan Xie, Gang Li, Jianlong Xu, Haiming Zhao, Tianling Ren, and Hongwei Zhu. Temperature and gate voltage dependent electrical properties of graphene field-effect transistors. *Carbon*, 78, 2014.